STRUCTURES, STRUCTURAL TRANSFORMATIONS AND PROPERTIES OF SELECTED ELEMENTAL AND EXTENDED SOLIDS

A Thesis submitted to the College of

Graduate and Postdoctoral Studies

In Partial fulfilment of the requirements

for the Degree of Doctor of Philosophy

In the Department of Physics and Engineering Physics

University of Saskatchewan

Saskatoon

By

Adebayo Abayomi Adeleke

PERMISSION TO USE

In presenting this thesis in partial fulfillment of the requirements for a Postgraduate degree from the University of Saskatchewan, I agree that the Libraries of this University may make it freely available for inspection. I further agree that permission for copying of this thesis in any manner, in whole or in part, for scholarly purposes may be granted by the professor or professors who supervised my thesis work or, in their absence, by the Head of the Department or the Dean of the College in which my thesis work was done. It is understood that any copying or publication or use of this thesis or parts thereof for financial gain shall not be allowed without my written permission. It is also understood that due recognition shall be given to me and to the University of Saskatchewan in any scholarly use which may be made of any material in my thesis.

DISCLAIMER

Reference in this thesis to any specific commercial products, process, or service by trade name, trademark, manufacturer, or otherwise, does not constitute or imply its endorsement, recommendation, or favoring by the University of Saskatchewan. The views and opinions of the author expressed herein do not state or reflect those of the University of Saskatchewan and shall not be used for advertising or product endorsement purposes.

Requests for permission to copy or to make other uses of materials in this thesis in whole or part should be addressed to:

Head of the Department of Physics and Engineering Physics

116 Science Place

University of Saskatchewan

Saskatoon, Saskatchewan S7N 5E2

Canada

OR

Dean College of Graduate and Postdoctoral Studies

University of Saskatchewan

116 Thorvaldson Building, 110 Science Place

Saskatoon, Saskatchewan S7N 5C9

Canada

ABSTRACT

The current boom in computer power has created avenue to study materials' properties under extreme thermodynamic conditions where experimental characterization is very challenging. This thesis is an aggregation of several objectives ranging from the study of elemental as well as extended materials for technological, high energy density (HED), and geophysical applications; all at high pressure. The density functional theory (DFT), ab initio metadynamics and ab initio molecular dynamics (AIMD) methods have been employed to analyze structural phase transitions, electronic, vibrational, and mechanical properties of selected materials at high pressure. Where available, high-pressure-high-temperature (HPHT) experiments were combined with the various theoretical methods for complete elucidation of the system.

The first set of projects in this thesis involve study of structural phase transition in two elements: carbon (C) and nitrogen (N). The first part presents the results of structural phase transition in a two-dimensional polymeric C_{60} after being subjected to uniaxial compression at high temperature in a metadynamics simulation. The new structure exhibits a mixed sp^2/sp^3 hybridization. The structure is stable at ambient condition and exhibits superior mechanical performance than most of widely used hard ceramics. The second part presents theoretical results on the identification, and characterization of single bonded nitrogen in crystal structure isostructural to black phosphorus (BP-N) at 146 GPa and 2200 K. The crystal structure exhibits a unique puckered two-dimensional layer exhibiting exciting physical and chemical phenomena including prospect for high energy density (HED) applications. Synchrotron x-ray diffraction and Raman spectroscopy were used for experimental characterization of the BP-N. First-principles methods were employed in the theoretical characterization.

The second set of projects involve the theoretical studies of transition metal (TM) -TM alloys/compounds. The first part of the chapter investigates structural phase transition leading to shape memory loss in the shape memory alloy NiTi. The second part investigates the formation of Au-Fe compounds at high pressure. A detailed analysis of the transition kinetics and dynamical pathway in NiTi using the metadynamics method reveals the possibility of the B19′ phase of NiTi losing its shape memory when subjected to high stress conditions and heated above a critical

temperature (T_c) of 700 K. Using the particle swarm-intelligence optimization algorithm interfaced with first principles methods, we predicted the formation of bulk intermetallic compounds of two bulk-immiscible components, Fe and Au. the systems are stabilized by pressure and notable electron transfer.

Next, the results of theoretical studies of the formation of noble gas element - TM compound were presented. The identification of a thermodynamically stable compound of Argon (Ar) and nickel (Ni) under thermodynamic conditions representative of the Earth's core using density functional calculations were presented. The study present evidence of the reactability of Ar with one of the Earth's core's main constituents, Ni. The compound of Ar and Ni was identified as ArNi with a $L1_1$ Laves structure. It was found that ArNi compound is stabilized by notable electron transfer from Ni to Ar.

The final project is an extensive theoretical study of the formation of alkali metal-transition metal intermetallic compounds at high pressure and temperature relevant to the upper mantle and the core of the Earth. These studies were carried out using particle swarm-intelligence optimization and genetic algorithms interfaced with first principles methods. The first part investigates the formation of K-Fe compounds at thermodynamics conditions relevant to the Earth's interior while the second part investigates the formation of K-Ni compounds in the Earth's interior. It was found that K and Fe can form intermetallic compounds that are stabilized by high pressure and energy reordering of atomic orbital. Phase transitions were also reported and the instabilities that induce them were also investigated. Furthermore, the study on K-Ni systems identify the crystal structure for the long-sought structure of the only experimentally known K-Ni compound to date. The identified K_2Ni exhibits a semiconducting ground state with an indirect bandgap. The results of both studies indicate that the chemical properties of elements can change dramatically under extreme conditions and could have significant implications for understanding the Earth's interior.

STATEMENT OF CO-AUTHORSHIP

While I only present my contributions, the research in this thesis is a result of collaborations between the author, Adebayo Abayomi Adeleke, thesis advisor, Prof. Yansun Yao of the Department of Physics and Engineering Physics at the University of Saskatchewan, Saskatoon, Drs. Elissaios Stavrou, and Stanimir A. Bonev of Lawrence Livermore National Laboratory, California and Drs. Cheng Ji, and H-k Mao of the Center for High Pressure Science and Technology Advanced Research, Beijing, whose contributions are described below:

Chapter 1 described the underlying theory and computational tools employed in this thesis and was written solely by Adebayo Abayomi Adeleke.

Chapter 2 is based on the papers '*o*-C_{240}: A new sp^3-dominated allotrope of Carbon' published in the *Journal of Physics: Condensed Matter* and 'Nitrogen in Black Phosphorus Structure' published in *Science Advances*. Experimental data for the nitrogen project was supplied by Dr. Cheng Ji and theoretical Calculations and theoretical analyses were carried out by Adebayo Abayomi Adeleke and Prof. Yansun Yao. The crystal structure of *o*-C_{240} was predicted by Prof. Yansun Yao, phonon dispersion calculation was performed by Adebayo O. Adeniyi and all other Calculations were carried out by Adebayo Abayomi Adeleke. Analyses and manuscript drafting for the carbon project were performed by Adebayo Abayomi Adeleke with contribution from Prof. Yansun Yao and all authors contributed to the interpretation of results. The manuscript drafting for the nitrogen project was done by Prof. Yansun Yao, Dr. H-k Mao, and Dr. Cheng Ji with contribution from Adebayo Abayomi Adeleke.

Chapter 3 is based on the papers 'High temperature shape memory loss in nitinol: A first principles study' published in the *Physical Chemistry Chemical Physics* and 'Aurum reservoir deep down: stable compounds of two bulk-immiscible metals in the core?' is being drafted. All Calculations were carried out by Adebayo Abayomi Adeleke. Analyses and manuscript drafting were performed by Adebayo Abayomi Adeleke. All authors contributed to the interpretation of results.

Chapter 4 is based on the paper 'High-pressure compound of argon and nickel: noble gas in the Earth's core?' published in *ACS Earth and Space Chemistry*. Calculations were carried out

by Adebayo Abayomi Adeleke. Analyses and manuscript drafting was performed by Adebayo Abayomi Adeleke, Experimental data were supplied by Dr. Elissaios Stavrou. All authors contributed to the interpretation of results and advanced writing of the manuscript.

Chapter 5 is based on the papers 'Formation of stable compounds of potassium and iron under pressure' published in the *Journal of Physical Chemistry A* and 'Two good metals make a semiconductor: A potassium-nickel compound under pressure' published in *Physical Review B.* All Theoretical calculations and manuscript writing for the K-Fe project were carried out by Adebayo Abayomi Adeleke. The crystal structure and the XRD of the $P2_1/m$-K_2Ni were predicted by Prof. Yansun Yao. Experimental XRD of K-Ni compound was extracted from Ref. [227] by Prof. Yansun Yao. The experimental XRD peaks of the K-III was collected by Dr. Elissaios Stavrou. All other theoretical calculations for the K-Ni project reported in this thesis were performed by Adebayo Abayomi Adeleke. The K-Ni Manuscript drafting was performed by Adebayo Abayomi Adeleke and Prof. Yansun Yao and all authors contributed to the interpretation of results.

Chapter 6 is a general conclusion of the thesis and is solely written by Adebayo Abayomi Adeleke.

ACKNOWLEDGEMENTS

I would like to start by acknowledging my gratitude to the University of Saskatchewan, located on Treaty 6 Territory and the Homeland of the Métis.

I would like to express my profound appreciation to Prof. Yansun Yao, for his support and encouragement as my thesis advisor; thank you for your useful critiques and for sharing your expertise. I also appreciate the supportive role of my advisory committee members: Prof. Rob Pywell, Prof. Lenaic Couedel, Dr. Ning Chen and Prof. John S. Tse: my PhD training would not have been successful without their constant and enormous support.

I am thankful to the Dr. Theodore R. Hartz Graduate Scholarship and the Dr. Gerhard Herzberg Memorial Scholarship that funded a major part of my PhD. I also gratefully acknowledge the financial support of Canadian Natural Sciences and Engineering Research Council (NSERC) and the Department of Physics and Engineering Physics. I acknowledge access to high-performance computers: Compute Canada (Westgrid), Plato at the University of Saskatchewan on which most of the research reported in this thesis were performed. I also appreciate the invaluable support and guidance of Dr. Stanimir Bonev and access to high-performance computers: Quartz and the Oslic at the Lawrence Livermore National Laboratory, CA, USA, on which part of the research reported in this thesis were performed.

Needless to say, that without the unending support, tremendous patience and unconditional love of my wife, my son, my wife's family, and mine, none of these would have been possible – thank you all for holding the fort when it was and wasn't convenient. Indeed, the last days of my programme made me realize that nothing is as genuine or be compared to the love and support of family. Lest I forget, a big thanks to my friend, Adedayo Oke, for always having my back. I will also like to thank everyone that I have met in the course of my programme: y'all made my decision to do a PhD training at the University of Saskatchewan one of the best decisions of my life.

Ìyàsímímọ́

To my wife, Dr. Abisola Adeleke and
my son, Albert Adeleke, for always being there.

TABLE OF CONTENTS

LIST OF TABLES

LIST OF FIGURES

LIST OF ABBREVIATIONS

1D ……. One dimension

2D ……. Two dimension

3D ……. Three dimension

AIMD …….. *ab initio* Molecular Dynamics

APW ……. Augmented Plane Wave

B3LYP ……... Becke, 3-parameter, Lee-Yang-Parr

B88 ……. Becke

BCC ……. Body centred cubic

BMGs ……. Bulk metallic glasses

BO ……. Born-Oppenheimer

BP ……. Black phosphorus

BSE ……. Bulk silicate Earth

BZ ……. Brillouin zone

CALYPSO …… Crystal structure AnaLYsis by Particle Swarm Optimization

CBM ……. Conduction band minimum

CMB ……. Core-mantle boundary

CEL …… Crystal Energy Landscape

Cg ……. Cubic Gauche

CNT ……. Carbon Nanotube

CV ……. Collective variable

DAC ……. Diamond anvil cell

DFPT …….……. Density functional perturbation theory

DFT ……. Density functional theory

DOS ……..…… Density of states

ELF ……..……. Electron localization function

EOS …….……. Equations of state

ETT …….…….. Electron Topological Transition

eV ……..…..…… Electron volt

FC …….……. Force constant

FCC ……..……. Face centred cubic

FES …….……..……. Free Energy Surface

FFT …….……..……. Fast Fourier Transform

FP-LAPW ……..... Full Potential Linearized Augmented Plane Wave

fs ……..…… Femtosecond

GA …….……...…….. Genetic Algorithm

GGA …….……. Generalized-gradient approximations

GPa …….……. GigaPascal

HCP …….……..…..……. Hexagonal close packed

HEDM …….…...……. High-energy-density material

HK …….……...……. Hohenberg-Kohn

HLP ……...…….…….. Hexagonal layered-polymeric

HSE ……..…… Heyd-Scuseria-Ernzerhof

HPHT ……..…….. High pressure-high temperature

HTHP …….…….…….. High temperature-high pressure

H_v ……..…….……. Vickers hardness

IFC …….……. Interatomic force constant

K ……..……..……..……. Kelvin

keV ……..……..… Kilo electron volt

KS …….…….……. Kohn-Sham

LAPW …….……...……. Linearized Augmented Plane Wave

LDA ……...……. Local density approximation

LP …….……. Layered-polymeric

LR …….……. Long range

LSDA …….……. Local spin density approximation

MD …….…….. Molecular dynamics

MP …….……..……. Monkhorst and Pack

MPa ……..……..……...…. Megapascal

MSD ……..……..… Mean-squared displacement

NCPP ……..……..……. Norm conserving pseudopotential

NH ……...……. Nose-Hover

NPT …….……..……. Isothermal-isobaric ensemble

ns ……..……... Nanosecond

NVE ……..……. Constant volume-constant energy (microcanonical) ensemble

NVT …….…… Constant volume –constant temperature (canonical) ensemble

PAW …….……..……. Projector augmented wave

PBC ……. Periodic boundary condition

PBE ……..……..……. Perdew, Burke and Enzerhof

PES ……..……..……. Photoelectron spectroscopy

PREM ……..…… Preliminary Reference Earth model

ps ……..……... Picosecond

psc ……..……..…. Pseudosimple cubic

PSO ……..……...……. Particle swarm-intelligence optimization

P-T ……..…...……. Pressure-Temperature

PW ……...……..……. Plane wave

PW91 ……..……..……. Perdew and Wang

QE ……..……. Quantum Espresso

RS ……..……..…… Random Searching

RTA ……..……..…… Relaxation time approximation

sc ….……..……..…….. Simple cubic

SCF ……...……. Self-consistent field

SR ……..……..…… Short range

SXRD ……..……...…. Single-crystal x-ray diffraction

TDDFT ……...…… Time-dependent density functional theory

THz ……...…..…….. TeraHertz

TM ……... Transition metal

TPa ……..……. TeraPascal

U ……..……. Hubbard correction

USPP ……..……. Ultra soft pseudopotential

VASP ……...……. Vienna Ab-initio Simulation Package

VBM ……..……...……. Valence band maximum

*v*DOS …….……..……. Vibrational density of states

vdW …….…….…… van der Waals

VF .…….……..……..……. Verlet Leapfrog

VRH …….…… Voigt-Reuss-Hill

VV .…….……..……..……. Velocity Verlet

XC .…….…….……..……. Exchange correlation

XRD ..……..……. X-ray diffraction

ZPE ..…….……. Zero-point energy

CHAPTER 1

INTRODUCTION AND THEORETICAL METHODS

The advent of powerful computers has opened the way for the study of materials' properties under extreme thermodynamic conditions that are beyond the reach of laboratory experiments. These [extreme] conditions naturally exist in the earth's interior. The origin, mechanism of accretion, growth, composition, and state of Earth's core remain significantly uncertain and theoretical calculations could in principle improve our understanding of them, most especially the crystal structure and the chemical composition of the inner core and possible stratification of the outer core. Therefore, the formation and the working of the earth's interior can be studied non-invasively by constructing models, that on one hand, mimic physical and chemical processes in the earth and on the other hand, are understandable by computer. Generally, the development of robust models of planets requires (among other things) the knowledge of various minerals that exist inside planets and their physical properties such as thermal conductivity, density, viscosity e.t.c [1-5]. The reliability of the results of any of these models are as good as the underlying theory, and so is their computer simulation. Many of these theories are difficult, if not impossible, to solve exactly and an alternative in term of numerical approximations are employed. Formulating simulation models from fundamental laws of physics reduces the number of approximations needed in the computer simulation, thereby increasing the accuracy of the results and reliability of the emerging predictions. The whole computer simulation process creates a virtual laboratory where experiments can be done at faster rate, cheaper cost and extreme conditions can be easily accessible.

Physical properties of solids at high pressure have been a major highlight of fundamental research in geophysics and planetary physics. Thermodynamic instabilities develop in ambient-pressure materials as the pressure is raised, inducing transition into new phases with higher densities. Such new phases can possess a variety of novel and interesting electronic states such as super-ionic, super-hard, superconducting, and metallic states. Contrary to miniaturization required to experimentally generate pressures in the gigapascal (GPa) regime, such high pressures can be achieved in numerical simulation by adjusting the size and/or shape of unit cell. With the current boost in computational power and advanced material simulation Softwares, studies of materials with diverse complexities are becoming possible with unprecedented precisions and accuracy. In

fact, there is now great synergy between numerical simulations and experiments at high pressure: Numerical simulation can guide experiments and can also be used to understand complex experimental results. As exploration continues on the experiment front, more complex results emerge which require development of more robust and sophisticated theories as well as numerical algorithms to model, solve and understand them.

In stable materials, high pressure and temperature provides compression energies ($p\Delta V$) and thermal energies ($T\Delta S$) large enough to break intermolecular or intramolecular interactions within it and to overcome energy barriers. The breaking of such interactions causes instability to develop with in the materials and as such drive the materials into a new thermodynamically stable configuration, in other words, transform to a new phase. Some classic examples include the compression of graphite into diamond [6], compression of hexagonal boron nitride into cubic boron nitride [7] and compression of wurtzite GaN into rocksalt GaN [8] under diverse thermodynamic conditions.

Strictly speaking, a lot can be understood about solid materials (typically composed of atomic nuclei and electrons) by examining their crystal structures and chemical bonding. Thus, physical, and chemical theories of solid materials are generally formulated to capture the motion of the nuclei, electrons, including instances where the motion of both are correlated, quantum mechanically. In this dispensation, such theories can be effectively translated into computer simulation algorithms that explicitly concern themselves with electronic structures and those relating to nuclear motions. Simple monatomic systems have been successfully studied using the exact solution of the Schrödinger equation, however, difficulties set in when treating bigger systems with several atoms, for which the problem complexity grows to non-trivial, many body problems. Over time, several approximate solution methods to the many body problems have evolved. One of such methods that have received wide acceptance from the community of materials scientists is the density functional theory (DFT) in which solutions to the Schrödinger equation describing a material are derived self consistently without input parameters from experiments. This method is also popularly referred as first-principles or *ab initio* method [9]. These methods are discussed in detail in subsequent sections.

Experimentally, high static pressure (to few hundreds of GPa) can be generated within a diamond anvil cell (DAC) and dynamic high pressures are generated through shock waves [10]. These pressure media generally support *in situ* generation and measurement of experimental

observables such as pressure and to some extent, temperature. They further support analytical technique such as X-ray powder diffraction (XRD) and *in situ* spectroscopy such as Raman and infrared spectroscopy. High pressures in the terapascal (TPa) regime [10] are not readily achievable by DACs because of the level of miniaturisation of sample required for such pressures – a major set back to the DAC method. First-principles density functional theory are then combined with these experimental methods to explore pressure and density regions on the phase diagram of materials that otherwise would remain unexplored by experiments alone. For instance, laboratory experiments can be done at few hundreds of GPa using DAC after which observed properties such as phase stability and excitation modes are theoretically modelled and then extrapolated into the TPa regime. Furthermore, transferable models (constructed from low pressure experimental observations) can also be used for direct study of materials at the TPa regime without extrapolation; especially in instances where there are sparse or no experimental data to guide a reasonable extrapolation. Therefore, First-principles density functional theory calculations can provide a deeper insight into, and further assist in the understanding of experimental observations.

Crystal structure of materials can be determined from experimental XRD data. Also, crystal structure searching algorithms can be combined with DFT calculations to explore high pressure regions for which there are no sufficient XRD data for accurate structure determination. Seemingly complex free-energy surface of various functional materials can be explored for structural configurations that corresponds to a local energy minimum (colloquially referred as metastable structural configuration) or global energy minimum (colloquially referred as ground-state structural configuration). These algorithms range (in their capabilities) from those that requires only the knowledge of the chemical composition to those that require starting experimental or theoretical structures, to identify the thermodynamically stable structure of interest under pressure. This remarkable predictive power benefits experimentalists in solving the structure of complex materials whose crystal structure deviate from standard simple structures [11]. Several efficient structure searching schemes for predicting stable crystal structures have been developed based on energy barrier cross-over or global energy minimization. These schemes include simulated annealing [12], minima hopping [13], *ab initio* molecular dynamics [14-15], metadynamics method [16] designed to overcome energy barriers. The global minimization methods include random sampling [17], genetic algorithms [18-20], particle swarm-intelligence optimization [21]

and so on. Some of these methods will be discussed in detail in the following sections and will be discussed further in subsequent chapters where they have been applied to solve various problems.

Different crystal structure searching algorithms have been combined with DAC-based spectroscopies to demonstrate the synthesis of stable Xe (Fe, Fe/Ni)$_x$ systems [22], rare earth elements (REE) and Ni, Co or Fe systems [23], iron-nickel systems [24] and alkali metal and Ni/Fe systems [25-27] at thermodynamic conditions of the Earth's core. These studies revealed unusual chemical and electronic changes in the reactants, resulting in different physical, optical and chemical properties exhibited by the final products. It was found that in some instance, the crystal structure of the compound is related to the crystal structures of the reactants [22] while in others, the compound adopts a completely different, and sometimes complex, crystal structures [24].

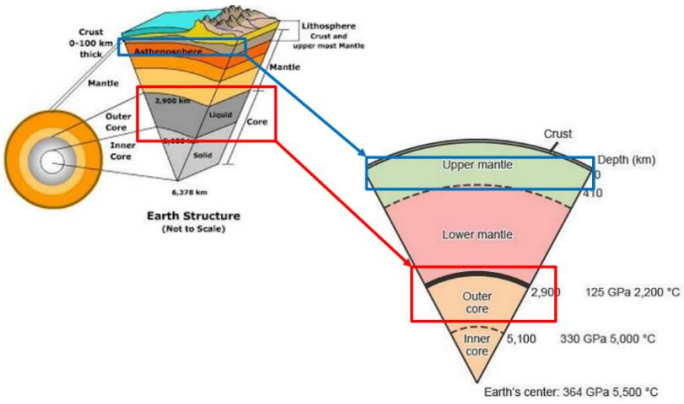

Figure 1.1. A cross-section of the Earth showing its interior profile. The blue and the red boxes are used to clearly mark out the pressure regions covered in this thesis. This figure is adapted for illustration from ref. [28].

The Earth's core (shown and marked out in Fig 1.1) constituents made up 32% of the mass of the Earth and 16% of its volume. The core is subject to very high pressure and temperature (*P-T*) conditions beyond 136 GPa and ~4000 K. Meanwhile, the exact composition of the core remains uncertain because of technical challenges involved in high *P-T* experiments. High pressure experimental data as well as state-of-the-art theoretical predictions have been used to establish stable crystal structures, solid-solid phase transitions, elemental partitioning and melting temperature of iron and iron alloys in the core [29]. Other properties including sound velocities, densities, electrical and thermal conductivities are also being measured and modeled theoretically at high *P-T* relevant to the Earth's core conditions. The nature and physical properties of stable

crystalline phases of iron and nickel are strongly affected by light elements (elements lighter than iron) alloying in the core. In 1952, it was proposed that the core contains of order 10 wt% light alloys, in addition to iron and nickel because the seismological constrained density of the liquid outer core is substantially lower than that of pure iron at the Earth's core *P*-*T*. The core is therefore thought to contain a considerable amount of one or more light elements such as K, Si, O, and/or C [30]. Specifically, K could produce significant amount of heat in the Earth's core thereby contributing to the working of the Earth's geodynamo. Significant experimental and theoretical works have been done in examining and establishing the presence of Si-Fe/Ni [30], O-Fe/Ni [31], and C-Fe/Ni [30] alloys in the core; but K-Fe/Ni study is scarce. Therefore, one of the objectives of this thesis is to study the K-Fe/Ni system and use them to understand some part of the Earth's interior.

The radioactivity of the Earth is an important parameter for the understanding of the Earth's internal energy budget, the evolution, and dynamics of the planet's crust-mantle-core system. Attempts to estimate the overall radioactivity of the planet over the past few decades using geophysical and geochemistry tools has witness incremental success due to fundamental limitations in observing the Earth. Thus, so far, we have only some model-dependent estimates of the radioactive content of the Earth's mantle and core. The crust and the upper mantle are accessible for sampling, as such, the radioactive contents of this part of the Earth's interior can be reliably estimated. The dynamic activity of the Earth is driven by the heat produced in the interior of the Earth by decay of radioactive isotopes U, Th, and K. The heavy, heat-producing elements U and Th are believed to have been left in the mantle during the Earth's differentiation, since their estimated concentrations in bulk silicate Earth (BSE) are consistent with the compositions of undifferentiated protoplanetary materials (CI chondrites). Thus, investigation of the radioactive heating from the Earth's core has been focused on the ^{40}K [32]. Therefore, it will be interesting to demonstrate that the radioactive decay product of the ^{40}K can be retained in the Earth's core and to also show in what form (compound) it will be retained. If a significant amount of ^{40}K $\rightarrow$Ar is to stay in the core, it has to somehow chemically bond to Fe and/or Ni. Hence, another objective of this thesis is to study the ^{40}K $\rightarrow$Ar-Ni system with the aim to understand the Earth's core.

Among other slightly heavy noble metals, the Earth crust is known to be depleted of siderophile gold (Au) which is believed to be transported from the mantle to the crust. An amount of Au that cannot be explained by its content in the mantle's magma is also suggested to be

depleted in the mantle [33,34]. The distribution of the depleted mantle Au within the Earth's interior is therefore worth investigating. The inclusion of siderophile light elements such as S, O, Si and C into various Earth's models could not exhaustively explain the mass and density deficit observed as density jump across the inner core boundary (ICB) in seismic data. In general, the reactivity of Au and Earth's core relevant element, such as Fe is scarce in literature. As a first step, plausibility of stable compound formation without considering its implication for the Earth's inner core dynamics is a good start. Therefore, it will be interesting to demonstrate that Au can form chemical compound with Fe, the main constituent of the Earth's core under pressure. Furthermore, the fact that Au and Fe are two immiscible solids makes it more interesting. Hence, another objective of this thesis is to study the Au-Fe system with the aim to understand the physics and chemistry of their formation at high pressures.

The knowledge of crystal structure is of great importance for estimating physical properties and phase equilibria in the Earth's core. Such knowledge is also important for understanding the origin of seismic anisotropy and the dynamics of the core. While both experimental and theoretical methods were employed to study the crystal structure of iron and nickel at high *P-T* conditions, the extrapolated results have been very controversial [30]. Even though synchrotron XRD measurements at inner core *P-T* conditions were successfully performed, yet the phase diagram of neither pure iron nor nickel could exhaustively explain the phase diagram profile of the Earth's interior. This disagreement, thus, points to the need to revisit the composition of the Earth's interior, especially the core and understand how it helps to explain the Earth's evolution, profile, internal energy budget and its implication on the working of the Earth's geodynamo.

Elemental systems are very important both from fundamental and applied sciences point of view. For example, cubic diamond (*c*-diamond), an allotrope of carbon is the hardest naturally existing materials [35-38] but highly insulating. For technological applications in electronics, carbon is continually being sought in a superhard form like the *c*-diamond but with semiconducting state up to metallic state like in graphite. Also, nitrogen, if compressed to high enough pressure, its bonds could be used to store significantly high energy (high energy density (HED)) that is released at will [39,40], but as the first element of group V, it has never been found in the black phosphorous structure. If nitrogen is found in black phosphorous structure, it could provide a firm base for exploring new type of HED nitrogen. Another objective of this thesis, therefore, is to predict new allotropes of carbon with an optimum combination of hardness and a relatively small

energy band gap compared to the *c*-diamond, that could outperform the present-day ceramics. Also, to find nitrogen in the black phosphorus structure there by completing the structural motif for the group V elements while improving our knowledge of the properties of HED materials.

In this thesis, various theoretical and experimental techniques have been used to study the crystal structure and structural phase transitions in functional materials at high pressures. We also determine their electronic, thermodynamic, and other properties. Materials examined include those that are relevant to our understanding of the Earth and its interior, and those with technological implications such as high energy density materials (HEDM), shape memory alloys (other wise referred as smart alloys) and superhard materials. The following body of work have been reported in this thesis: (i) *ab initio* study of elemental solids for application in electronics, superhard materials and HEDM. Using *ab initio* methods, a new allotrope of carbon was predicted and characterized. Furthermore, the long-sought black phosphorous (BP) phase of Nitrogen was identified from experimental data and theoretically characterized [41,42]. (ii) *ab initio* study of transition metal-transition metal alloy for application in smart alloy systems and in understanding effects of high pressure on their formation. Using *ab initio* methods, shape memory loss was predicted in nitinol (NiTi) at temperature above 700 K while gold (Au) was predicted to form iron (Fe)-rich compounds under high pressure condition [43]. (iii) *ab initio* and experimental study of noble gas element-transition metal alloy for understanding of the Earth's core. Combining *ab initio* methods and in situ X-ray diffraction techniques, it was shown that argon (Ar), a natural radioactive decay product of potassium (^{40}K) form stable compound with nickel (Ni) at 140 GPa, 2500 K; a thermodynamics condition relevant to the Earth's interior [44], and the last project reported is (iv) *ab initio* study of alkali metal-transition metal alloy for understanding of the Earth's interior. Using *ab initio* methods, alkali metal, K, was predicted to form stable compounds with core dominant elements: Fe and Ni, under high pressure condition [45,46]. First-principles density functional theory, crystal structure searching methods, *ab initio* molecular dynamics (AIMD), metadynamics and in situ XRD methods have been extensively applied to unearth structures of these materials and elucidate some interesting properties as well.

1.1 Density Functional Theory

The description of the structures and dynamics of many-electron system is one of the early but basic problems in theoretical physics and chemistry; like Dirac stated [47], *The underlying*

physical laws necessary for the mathematical theory of a large part of physics and the whole of chemistry are thus completely known, and the difficulty is only that the exact application of these laws lead to equations much too complicated to be soluble. Still, the seemingly insurmountable challenge of solving the Schrödinger wave equation for realistic (many-particle) systems has opened a whole new area in modern day physics and chemistry and the way we understand chemical systems. As introduced in 1964 by Kohn *et al.* [48], Density functional theory (DFT) [49-51] is an effective approach to obtain approximate solutions to the many-particle problems. DFT is conceptually rooted in the Thomas-Fermi model of a uniform electron gas [52], coupled with the Slater local exchange approximation [53]. Within the DFT framework, the ground state of a system is mapped to the ground-state electron density in a way that the Schrödinger wave equation,

$$\hat{H}\psi(\boldsymbol{r}_1, \dots, \boldsymbol{r}_N) = E\psi(\boldsymbol{r}_1, \dots, \boldsymbol{r}_N), \tag{1.1}$$

in which N is the number of electrons at positions $\boldsymbol{r}_1, \dots, \boldsymbol{r}_N$, is satisfied for many-particle system.

Although many DFT methods are *ab initio* because they are based on finding the energy eigenvalue of the Schrödinger wave equation from the wavefunction, others use the electronic density to obtain the energy eigenvalue. The latter could come as a semiempirical DFT method if functionals have been fitted to experimental data. *Ab initio* (first principles) theory embraces all essentially non-empirical and wavefunction-based methods of solving the Eq. (1.1) for many-particle systems [54]. The Schrödinger wave equation for many-particle system is called the Kohn-Sham (KS) equation [48]. Particles in many-particle systems continually interact, which make constructing analytical solutions to the KS equation close to impossible. Thus, development of approximate-solution schemes has evolved with each scheme having its own assumptions. Interesting properties ranging from electronic structure, lattice vibration, superconductivity, magnetic properties, to bonds and bond characterization were successfully studied using DFT [15].

1.1.1 Schrödinger Equation and Born-Oppenheimer Approximation

Given a molecular system of N-electron and M nuclei, the Schrödinger wave equation is given by the Eq. (1.1) where the Hamiltonian operator $\hat{H}$ is defined according to:

$$\hat{H} = \hat{T}_{ee} + \hat{T}_{NN} + \hat{V}_{ext} + \hat{V}_{ee} + \hat{V}_{NN} \ , \tag{1.2}$$

where $\hat{T}_{ee}$ is the kinetic energy operator for electrons, $\hat{T}_{NN}$ is the kinetic energy operator for the nuclei, $\hat{V}_{ext}$ is the external potential operator, $\hat{V}_{ee}$ is the operator describing the potential due to electron-electron interaction and $\hat{V}_{NN}$ is the operator describing the potential due to nuclei-nuclei interaction. The $\psi(\boldsymbol{r}_1, \ldots, \boldsymbol{r}_N)$ is also a function of the spin coordinates of all N electrons $(s_1, s_2, \ldots, s_N)$. In principle, the spin dependence of the wavefunction is implicitly assumed and so through out this thesis, we shall invoke this assumption.

The Born-Oppenheimer approximation was built on the premise that atomic nuclei are much heavier than individual electrons; each proton in a nucleus has more than 1800 times the rest mass of an electron, justifying the treatment of the nucleus as stationary relative to the electron. Thus, the many-particle system can be simplified by separating the nuclei and electrons into separate mathematical problems [54] and the $\hat{T}_{NN}$ term in Eq. (1.2) can be ignored. The ground-state electron density which is the only physical observable of the DFT is then built from the solutions to the KS equations (KS orbitals) of each electron.

1.1.2 Hohenberg-Kohn Theorem

DFT is usually implemented through the KS equations whose validity, conceptually, depends on the validity of the statement of existence by Hohenberg and Kohn, referred to as the Hohenberg-Kohn (HK) theorem [51]. The first HK theorem is an existence theorem which states that 'the ground state of any interacting many-particle system with a given fixed inter-particle interaction is a unique functional of the electron density $\rho(r)$'. Although the first Hohenberg–Kohn theorem rigorously proves that a functional of the electron density $E[\rho_0]$ exists, the theorem says nothing about the actual form of the functional. The HK theorem neither formulate a mathematical description of the mapping nor the form of the functional and all its associated approximations. The two HK theorems can be stated as:

Theorem 1.1.2.1 ([48,51])**.** *The ground-state energy from Schrödinger's equation is a unique functional of the electron density.*

Proof. Consider the electron density ρ for the ground state electron density of some N-electron system. If we assume that there are two external potentials V_{ext} and V'_{ext}, different by more than a constant and suppose the two external potentials give the same ρ for its ground state, then there

exists two Hamiltonians $\widehat{H}$ and $\widehat{H'}$ corresponding to the same ground state density but different normalized N-electron wavefunctions ψ and ψ'. If we designate ψ' as a trial function for the Hamiltonian $\widehat{H}$, we can construct a proof by contradiction as follows

$$E_0 < \langle\psi'|\widehat{H}|\psi'\rangle = \langle\psi'|\widehat{H'}|\psi'\rangle + \langle\psi'|\widehat{H} - \widehat{H'}|\psi'\rangle = E_0' + \int \rho(\boldsymbol{r})\,[V_{ext}(\boldsymbol{r}) - V'_{ext}(\boldsymbol{r})]d\boldsymbol{r}, \quad (1.3)$$

where E_0 and E_0' are the ground-state energies corresponding to $\widehat{H}$ and $\widehat{H'}$, respectively. Repeating the procedure above with a trial function ψ for the Hamiltonian $\widehat{H'}$, yields:

$$E_0' < \langle\psi|\widehat{H'}|\psi\rangle = \langle\psi|\widehat{H}|\psi\rangle + \langle\psi|\widehat{H'} - \widehat{H}|\psi\rangle = E_0 + \int \rho(\boldsymbol{r})\,[V'_{ext}(\boldsymbol{r}) - V_{ext}(\boldsymbol{r})]d\boldsymbol{r}\,. \quad (1.4)$$

Adding Eqs. (1.3) and (1.4), yield the contradiction $E_0 + E_0' < E_0 + E_0'$, thus there cannot be two different V_{ext} corresponding to the same ρ for their ground states. It then follows that the ground-state energy from Schrödinger's equation is a unique functional of the electron density [48,51].

□

The second Hohenberg–Kohn theorem defines an important property of the functional and states that:

Theorem 1.1.2.2 ([48,51])**.** *The electron density that minimizes the energy of the overall functional is the true electron density corresponding to the full solution of the Schrödinger equation.*

Proof. The proof of second HK theorem is restricted to densities $\rho(\boldsymbol{r})$ that are ground state densities of the electron Hamiltonian with some external potential V_{ext}. This defines a space of possible densities within which one can construct functionals of the density. Since all properties such as the kinetic energy, e.t.c., are uniquely determined if $\rho(\boldsymbol{r})$ is specified, then each such property can be viewed as a functional of $\rho(\boldsymbol{r})$, including the total energy functional:

$$E_{HK}[\rho] = T[\rho] + E_{int}[\rho] + \int V_{ext}(\boldsymbol{r})\rho(\boldsymbol{r})d\boldsymbol{r} + E_{II} \equiv F_{HK}[\rho] + \int V_{ext}(\boldsymbol{r})\rho(\boldsymbol{r})d\boldsymbol{r} + E_{II}, \quad (1.5)$$

where $T[\rho]$ is the kinetic energy functional, $E_{int}[\rho]$ is the electron-electron interaction energy functional and E_{II} is the interaction energy of the nuclei. The functional $F_{HK}[\rho] = T[\rho] + E_{int}[\rho]$ includes all internal energies, kinetic and potential, of the interacting electron system, which must be universal by construction.

If we now, consider a system with the ground state density $\rho^{(1)}(\boldsymbol{r})$ corresponding to external potential $V_{ext}^{(1)}(\boldsymbol{r})$, the HK functional is equal to the expectation value of the Hamiltonian in the unique ground state, which has wavefunction $\psi^{(1)}$

$$E^{(1)} = E_{HK}\left[\rho^{(1)}\right] = \left\langle \psi^{(1)} \middle| \widehat{H^{(1)}} \middle| \psi^{(1)} \right\rangle . \tag{1.6}$$

Furthermore, we consider a different density, say $\rho^{(2)}(\boldsymbol{r})$, which corresponds to a different wavefunction $\psi^{(2)}$. It then follows that the energy

$$E^{(2)} = E_{HK}\left[\rho^{(2)}\right] = \left\langle \psi^{(2)} \middle| \widehat{H^{(1)}} \middle| \psi^{(2)} \right\rangle \tag{1.7}$$

of the state is greater than $E^{(1)}$, since

$$E^{(1)} = \left\langle \psi^{(1)} \middle| \widehat{H^{(1)}} \middle| \psi^{(1)} \right\rangle < \left\langle \psi^{(2)} \middle| \widehat{H^{(1)}} \middle| \psi^{(2)} \right\rangle = E^{(2)} . \tag{1.8}$$

Thus, the energy given by Eq. (1.5) in terms of the HK functional evaluated for the correct ground state density $\rho_0(\boldsymbol{r})$ is indeed lower than the value of this expression for any other density $\rho(\boldsymbol{r})$. It then follows that if the functional $F_{HK}[\rho]$ was known, then by minimizing the total energy of the system, Eq. (1.5), with respect to variation in density function $\rho(\boldsymbol{r})$, one would find the exact ground state density and energy [48,51].

□

In a nutshell, if the true functional form is known, then one can try to minimize the energy by varying the electron density, to find the ground state electron density. Once the ground state electron density is known, all the properties can be calculated.

1.1.3 Kohn-Sham formulation of DFT

Kohn and Sham [48] assume that the ground state density of an interacting, many-particle system is equal to that of some chosen non-interacting system. With Born-Oppenheimer's approximation invoked, this ansatz leads to more solvable independent-particle equations for non-interacting system. We are going to assume the atomic unit throughout this thesis, with $\hbar = 1$, $m_e = 1$ and $e = 1$. This means that an interacting, many-particle system obeying the Hamiltonian for the system of electrons and nuclei,

$$\hat{H} = -\frac{1}{2}\sum_{i} \nabla_i^2 - \sum_{i,I} \frac{Z_I}{|\boldsymbol{r}_i - \boldsymbol{R}_I|} + \frac{1}{2}\sum_{i \neq j} \frac{1}{|\boldsymbol{r}_i - \boldsymbol{r}_j|} + \frac{1}{2}\sum_{I \neq J} \frac{Z_I Z_J}{|\boldsymbol{R}_I - \boldsymbol{R}_J|} \ , \qquad (1.9)$$

where electrons are denoted by lower case subscripts and nuclei, with charge Z_I, denoted by upper case subscripts, was replaced with a different auxiliary system that can be solved more easily. If we make the following definition:

$$\hat{T} = -\frac{1}{2}\sum_{i=1}^{N} \boldsymbol{\nabla}_i^2 \ , \hat{V}_{ee} = \frac{1}{2}\sum_{i \neq j} \frac{1}{|\boldsymbol{r}_i - \boldsymbol{r}_j|} \ , \hat{V}_{ext} = -\sum_{i,I} \frac{Z_I}{|\boldsymbol{r}_i - \boldsymbol{R}_I|} \ , \hat{V}_{NN} = \frac{1}{2}\sum_{I \neq J} \frac{Z_I Z_J}{|\boldsymbol{R}_I - \boldsymbol{R}_J|} \ . \quad (1.10)$$

Then, Eq. (1.9) can be re-written as:

$$\hat{H} = \hat{T} + \hat{V}_{ext} + \hat{V}_{ee} + \hat{V}_{NN} \ . \qquad (1.11)$$

Furthermore, $\boldsymbol{r}_i$ is the position of the *i-th* electron, $V_{ext}(\boldsymbol{r})$ is a measure of Coulomb interaction, in term of potential between the electrons and the nuclei. N is the number of electrons in the system, $\hat{V}_{ee}$ is the electron-electron repulsion term and $\hat{T}$ is the kinetic energy operator.

As a build-up on the first HK theorem, Kohn and Sham [48] assumes that the ground state density of the original interacting system is equal to that of some chosen non-interacting (auxiliary) system. This decouples the interacting-system problem to independent-particle equations for non-interacting system with all the cumbersome many-body interaction terms dumped into an exchange correlation functional of the density. Essentially, DFT can be viewed as a powerful method in which the knowledge of electron density,

$$\rho(\boldsymbol{r}) = \sum_{i=1}^{N} |\psi_i(\boldsymbol{r})|^2, \qquad (1.12)$$

implies knowledge of the wavefunction, the potential and all other observables that can be derived from them. In principle, many-particle wavefunction depends on 3N variables, and each of the N particles depend on three spatial variables, making it a 3N-dimentional problem. However, in practice, DFT is only a function of the density which has three variables, thereby reducing the complexity that arise for system with large value of N to 3-dimensional problem solved N time.

The first HK theorem can be written in terms of the Hamiltonian in Eq. (1.11) and the electron density in Eq. (1.12) as:

$$E[\rho] = T[\rho] + V_{ee}[\rho] + V_{NN}[\rho] + V_{ext}[\rho]. \tag{1.13}$$

The external potential term can be written explicitly in terms of the density as:

$$V_{ext}[\rho] = \int \hat{V}_{ext}(\boldsymbol{r}) \cdot \rho(\boldsymbol{r}) d^3\boldsymbol{r} \ . \tag{1.14}$$

The universal functionals $T[\rho]$, $V_{ee}[\rho]$ and $V_{NN}[\rho]$ are unknown for a given system configuration while the system dependent functional $V_{ext}[\rho]$ is specified. If we have a system for which the external potential $V_{ext}(\boldsymbol{r})$ is known, substituting Eq. (1.14) into (1.13) and assuming the second HK theorem holds true, it suffices to write:

$$E[\rho] = T[\rho] + V_{ee}[\rho] + V_{NN}[\rho] + \int \hat{V}_{ext}(\boldsymbol{r}) \cdot \rho(\boldsymbol{r}) d^3\boldsymbol{r} \ , \tag{1.15}$$

and the ground-state energy of the system is derived by minimizing Eq. (1.15) with respect to the electron density $\rho(\boldsymbol{r})$ [48,55].

Now, we attempt to write the functional described by the HK theorem in terms of single particle wavefunctions, $\psi_i(\boldsymbol{r})$, bearing in mind that Eq. (1.12) defines the electron density. The energy functional can be formulated as:

$$E[\{\psi_i\}] = E_{analytic}[\{\psi_i\}] + E_{XC}[\{\psi_i\}], \tag{1.16}$$

where $E_{analytic}$ is a collection of terms whose analytical form is completely known and every other term including all the quantum mechanical effects not described by the analytical form are represented as E_{XC}. We can explicitly define the analytic term in terms of contribution from various particles' interaction as:

$$E_{analytic}[\{\psi_i\}] = -\frac{1}{2}\sum_i \int \psi_i^* \boldsymbol{\nabla}^2 \psi_i d^3r + \int V(\boldsymbol{r})\rho(\boldsymbol{r}) d^3r$$

$$+\frac{1}{2}\iint \frac{\rho(\boldsymbol{r})\rho(\boldsymbol{r}')}{|\boldsymbol{r}-\boldsymbol{r}'|} d^3r d^3r' + E_{NN} \ . \tag{1.17}$$

E_{NN} in Eq. (1.17) is the Coulomb interactions between pair of nuclei, the first, second and third terms are the electron kinetic energies, the electrons - nuclei Coulomb interactions and the electron interaction with the mean field created by electrons, respectively [48,51,55]. Finding the right

electron density, according to Kohn and Sham, can be done by solving a set of equations in which each equation only involves single electron. The KS equation thus take the form:

$$\left[-\frac{1}{2}\boldsymbol{\nabla}^2 + V_{ext}(\boldsymbol{r}) + V_H(\boldsymbol{r}) + V_{XC}(\boldsymbol{r})\right]\psi_i(\boldsymbol{r}) = \varepsilon_i\psi_i(\boldsymbol{r})\,. \tag{1.18}$$

The solutions to equation (1.18) are single particle wavefunctions that are dependent on three spatial variables only. The potential $V_{ext}(\boldsymbol{r})$ defines the interactions between an electron and the collection of atomic nuclei. The Hartree potential, $V_H(\boldsymbol{r})$, is the Coulomb repulsion between the effective electron density of all electrons and the *i-th* electron being considered in the KS equation. The $V_H(\boldsymbol{r})$ already captures the self-interaction contribution, since the *i-th* electron as well contribute to the effective electron density. The analytical expression for the Hartree potential is:

$$V_H(\boldsymbol{r}) = \int \frac{\rho(\boldsymbol{r}')}{|\boldsymbol{r} - \boldsymbol{r}'|} d^3r'. \tag{1.19}$$

The exchange-correlation term, $V_{XC}(\boldsymbol{r})$, yield an exchange-correlation energy functional $E_{XC}[\rho(\boldsymbol{r})]$ which can be separated into the exchange part $E_X[\rho(\boldsymbol{r})]$ and the correlation part $E_C[\rho(\boldsymbol{r})]$. The analytical definition of $V_{XC}(\boldsymbol{r})$ is given as:

$$V_{XC}(\boldsymbol{r}) = \frac{\delta E_{XC}[\rho(\boldsymbol{r})]}{\delta\rho(\boldsymbol{r})}\,. \tag{1.20}$$

Putting Eqs. (1.19) and (1.20) into Eq. (1.18) yields:

$$\left[-\frac{1}{2}\boldsymbol{\nabla}^2 + V(\boldsymbol{r}) + \int \frac{\rho(\boldsymbol{r}')}{|\boldsymbol{r} - \boldsymbol{r}'|} d^3r' + \frac{\delta E_{XC}[\rho(\boldsymbol{r})]}{\delta\rho(\boldsymbol{r})}\right]\psi_i(\boldsymbol{r}) = \varepsilon_i\psi_i(\boldsymbol{r})\,. \tag{1.21}$$

We have established that the problem of a system of interacting particles can be approximated by an auxiliary system of non-interacting particles if their ground state energy can be mapped (HK theorems). Furthermore, we found that the predicting power and accuracy of the auxiliary system depends on the performance of the map. Also, that the KS equations gives the mechanics of the auxiliary system. Solving the KS equations requires the knowledge of the Hartree potential, which requires the knowledge of electron density. The knowledge of the electron density requires the knowledge of the single particle wavefunctions, which requires solving the KS

equation. Hence, constructing solutions for this type of problem requires an iterative method [48,51,55].

1.1.4 Functionals forms of Exchange Correlation

The DFT within the KS formalism is continually being employed in electronic structure studies and in the study of other properties of materials and solids because of the success of approximate functionals implemented within it. The KS-DFT calculations were able to reproduce experimental observations to a significant degree of accuracy. As beautiful and compact as the KS formalism is, finding analytical solution to it remain daunting because of the presence of an exchange-correlation ($E_{XC}(\rho)$) term (see Eq. (1.21)). To make the construction of solutions to this equation less cumbersome and achievable, approximations were made for the $E_{XC}(\rho)$ term whose exact form is unknown [55-57]. So far, great progress has been made with the following remarkable approximations:

1.1.4.1 The local spin density approximation (LSDA)

Kohn and Sham [48] put forward an assumption that solids are close to the limit of homogeneous electron gas making the effects of exchange and correlation to be local in character. Consequent on this assumption, we can make an approximation about the local spin density being constant over all space as in a homogeneous electron gas. Thus, exchange-correlation energy functional takes the form

$$E_{XC}^{LSDA}\left[\rho^{\uparrow},\rho^{\downarrow}\right]=\int d^{3}r\;\rho(\boldsymbol{r})\epsilon_{XC}^{uniform}\left(\rho^{\uparrow}(\boldsymbol{r}),\rho^{\downarrow}(\boldsymbol{r})\right). \tag{1.22}$$

The exchange-correlation term can be written as a direct sum of the exchange energy per electron, which is known exactly in its analytic form, and the correlation term as follows:

$$E_{XC}^{LSDA}\left[\rho^{\uparrow},\rho^{\downarrow}\right]=\int d^{3}r\;\rho(\boldsymbol{r})\left[\epsilon_{X}^{uniform}\left(\rho^{\uparrow}(\boldsymbol{r}),\rho^{\downarrow}(\boldsymbol{r})\right)+\epsilon_{C}^{uniform}\left(\rho^{\uparrow}(\boldsymbol{r}),\rho^{\downarrow}(\boldsymbol{r})\right)\right]. \tag{1.23}$$

The problem of double-counting of interaction in the exchange contribution to average energy per electron is solved by multiplying the contribution to energy eigenvalue by a factor of $\frac{1}{2}$, thereby yielding

$$\epsilon_X = -\frac{1}{2}\frac{3}{2\pi}k_F^\sigma = -\frac{3}{4}\left(\frac{6}{\pi}\rho^\sigma\right)^{1/3}, \tag{1.24}$$

where k_F^σ is the spin-polarized Fermi wave number as a function of spin-polarized electron density ρ^σ. The correlation energy to a great accuracy have been calculated using Monte Carlo methods for homogeneous electron gas with different kind of electron densities [56,57]. The LSDA is expected to be best for systems that behave like a homogeneous gas, such as a nearly-free-electron metal. However, this approximation performs poorly for systems of atoms where the density must go continuously to zero outside the atom. This significant draw back of the LSDA has stimulated ideas for constructing functionals that are expected to perform better for systems in which the LSDA failed [57].

1.1.4.2 The generalized-gradient approximations (GGA)

Another form of approximation to the KS functional expected to achieve better results than the LSDA is the generalized-gradient approximation. The approximation is based on the fact that real materials do not have a uniform electron density, rather, they have a slowly varying one. Therefore, the GGA functional is expressed using both the local electron density and the spatial variation in the electron density included through the density gradient. The generalized form of the GGA functional is

$$\begin{aligned} E_{XC}^{GGA}\left[\rho^\uparrow,\rho^\downarrow\right] &= \int d^3r\, \rho(\boldsymbol{r})\epsilon_X(\rho^\uparrow,\rho^\downarrow,\left|\boldsymbol{\nabla}\rho^\uparrow\right|,\left|\boldsymbol{\nabla}\rho^\downarrow\right|,\dots) + E_C^{GGA}\left[\rho^\uparrow,\rho^\downarrow\right] \\ &\equiv \int d^3r\, \rho(\boldsymbol{r})\epsilon_X^{uniform}(\rho)F_X(\rho^\uparrow,\rho^\downarrow,\left|\boldsymbol{\nabla}\rho^\uparrow\right|,\left|\boldsymbol{\nabla}\rho^\downarrow\right|,\dots) + E_C^{GGA}\left[\rho^\uparrow,\rho^\downarrow\right], \end{aligned} \tag{1.25}$$

where $\epsilon_X^{uniform}(\rho)$ is the exchange energy of the unpolarised gas and F_X is the exchange enhancement factor. The F_X is a function of the dimensionless reduced density gradients of m_{th} order. The reduced density is given as:

$$S_m(\boldsymbol{r}) = \frac{|\boldsymbol{\nabla}^m \rho(\boldsymbol{r})|}{(2k_F)^m \rho(\boldsymbol{r})} \,. \tag{1.26}$$

Here, the k_F is the Fermi wave vector. The value of F_{XC} varies with different types of approximation in use. Available approximations include but not limited to the Becke (B88) [58,59], Perdew and Wang (PW91) [60], and Perdew, Burke and Enzerhof (PBE) [61]. However, the most widely used approximation is the PBE. The improvements of PBE over PW91 include an accurate description of the linear response of the uniform electron gas, correct behavior under uniform scaling and a smoother potential. The formalism of PBE was started with the GGA for correlation in the form

$$E_C^{PBE}\left[\rho^{\uparrow}, \rho^{\downarrow}\right] = E_C^{GGA}\left[\rho^{\uparrow}, \rho^{\downarrow}\right] = \int d^3r \; \rho[\epsilon_C^{uniform}(r_s\,, \zeta) + H(r_s, \zeta, t)] \,, \tag{1.27}$$

where r_s is the local Seitz radius, $\rho = 3/(4\pi r_s^3) = k_F^3/3\pi^2$, $\zeta = (\rho^{\uparrow} - \rho^{\downarrow})/\rho$ is the relative spin polarization, $\epsilon_C^{uniform}(r_s, \zeta)$ is the correlation energy of the homogeneous electron gas, and $t(\boldsymbol{r}) = |\boldsymbol{\nabla}\rho(\boldsymbol{r})|/2\phi\, k_s \rho(\boldsymbol{r})$ is a dimensionless density gradient [58-59,61-63]. $\phi(\zeta) = \left[(1+\zeta)^{2/3} + (1-\zeta)^{2/3}\right]/2$ is a spin scaling factor and $k_s = 2\sqrt{k_F/\pi}$ is the Thomas-Fermi screening wave number. The gradient contribution $H(t, r_s, \zeta)$ was constructed from three conditions:

(a) In the slowly varying limit ($t \to 0$), $H(t, r_s, \zeta)$ is given by its second-order gradient expansion [57-59]

$$H(t, r_s, \zeta) \to \beta \phi^3 t^2 \,, \tag{1.28}$$

where $\beta \cong 0.066725$.

(b) In the rapidly varying limit $t \to \infty$, $H(t, r_s, \zeta) \to -\epsilon_C^{uniform}$, this makes correlation to vanish.

(c) Under uniform scaling to the high-density limit, the correlation energy must scale to a constant [57]. Thus, $H(t, r_s, \zeta) \to \gamma\phi^3 \ln t^2$, where $\gamma = (1 - \ln 2)/\pi^2 \cong 0.031091$.

Hence, conditions (a) – (c) are satisfied by

$$H(t, r_s, \zeta) = \gamma\phi^3 \ln\left\{1 + \frac{\beta}{\gamma} t^2 \left[\frac{1+At^2}{1+At^2+A^2t^4}\right]\right\} , \tag{1.29}$$

where

$$A = \frac{\beta}{\gamma}\left[\exp\left\{\frac{-\epsilon_C^{uniform}}{\gamma\phi^3}\right\} - 1\right]^{-1} . \quad (1.30)$$

The GGA for the exchange energy was also constructed [61] and the expression, for $\zeta = 0$ everywhere, was derived to be

$$E_X^{PBE} = E_X^{GGA} = \int d^3r\, \rho\epsilon_X^{uniform}(\rho)F_X^{PBE}(s) , \quad (1.31)$$

where $\epsilon_X^{uniform} = -3k_F/4\pi$ and $F_X^{PBE}(s) = 1 + \kappa - \frac{\kappa}{(1+\mu s^2/\kappa)}$, with $\kappa = 0.804$, $\mu = 0.235$.

The implementation of the GGA approximation (Perdew-Burke-Ernzerhof, PBE [61]) have been successfully used in the study of structural geometry, atomic total energy and vibrational properties of systems whose electron density varies slowly in space [64]. This success is owed to the inclusion of more physical ingredient than the LSDA. The efficacy of PBE functional in structural parameters prediction is demonstrated in the study of systems of O, Si, C [65], where such predictions were shown to agree very well with experimental observations.

1.1.4.3 The hybrid functional

The hybrid functional, introduced in 1993 by Axel Becke [66], is a class of approximation for the exchange-correlation functional as a mixture of a fraction of exact exchange from Hartree-Fock theory with local or semilocal exchange. The hybrid functional improves the description of the energy band gap in semiconductors and insulators, but the results critically depend on the amount of Hartree-Fock exchange included in the functional. The Hartree-Fock theory is an improvement of the self-consistent field method introduced by D. R. Hartree in 1927 [50]. Hartree proposed solving the Schrodinger wave equation for many-body system using a trial wave function that is defined as the product of single particle functions. However, Hartree's trial function do not consider the antisymmetric nature of wavefunction and do not also ignores the correlation between electrons. Hartree and V. A. Fock included the electron exchange interaction term to the self-consistent field method. Although, the correlation between electrons is still not accounted for. The analytical term for the Hartree-Fock exchange interaction is given in form, as

$\sum_{i<j}^{N} \int d^3r d^3r' \frac{|\phi_i(r)|^2 |\phi_j(r')|^2}{|r-r'|} - \sum_{i<j}^{N} \int d^3r d^3r' \frac{\phi_i^*(r)\phi_j^*(r)\phi_i(r')\phi_j(r')}{|r-r'|}$ [50]. In the last few decades, different hybrid functionals have been developed such as B3LYP [67,68], PBE0 [69] and HSE [70] with each of them constrained by the number of parameters that control the fraction of Hartree-Fock exchange that is mixed with other simple *ab initio* functionals.

1.1.4.3.1 The Heyd–Scuseria–Ernzerhof (HSE) functional

Heyd, Scuseria and Ernzerhof [70] proposed a new hybrid functional which perform the exact exchange mixing for short-range interactions only, in both Hartree-Fock and DFT. The mixing for the short-range interaction allows the exchange hole to be delocalized among neighbors within a short range from a reference point while nothing is known beyond the circumference. The HSE functional is an extension of the PBE0 [69] hybrid functional which is based on the PBE exchange correlation functional. The PBE0 hybrid functional assumes an exchange-correlation energy of the form

$$E_{XC}^{PBE0} = aE_X^{HF} + (1-a)E_X^{PBE} + E_C^{PBE} \,, \tag{1.32}$$

where the mixing coefficient $a = 1/4$ as determined from perturbation theory. The formulation of the HSE functional extend the expression for the exchange energy in Eq. (1.32), splitting all terms into their short- and long-range components according to $\frac{1}{r} = \frac{1-\mathrm{erf}(\omega r)}{r} + \frac{\mathrm{erf}(\omega r)}{r}$, where the first term is the short-range (SR) and the second term is the long-range (LR) yield:

$$E_X^{PBE0} = aE_X^{HF} + (1-a)E_X^{PBE} = aE_X^{HF,SR}(\omega) + aE_X^{HF,LR}(\omega)$$

$$+(1-a)E_X^{PBE,SR}(\omega) + E_X^{PBE,LR}(\omega) - aE_X^{PBE,LR}(\omega) \,. \tag{1.33}$$

A Carefully chosen value of $\omega = 0.15$ ensures that long-range exchange contributions of both the PBE and Hartree-Fock functionals to the exchange energy are very small, negligible and tends to cancel out [71]. Therefore, a screened Coulomb potential hybrid density functional is obtained, of the form:

$$E_X^{\omega PBEh} = aE_X^{HF,SR}(\omega) + (1-a)E_X^{PBE,SR}(\omega) + E_X^{PBE,LR}(\omega) + E_C^{PBE} \,, \tag{1.34}$$

where ω is an adjustable parameter that determine the extent of short-range interactions. In the limit of $\omega = 0$, ωPBEh $\rightarrow$ PBE0 and in the limit $\omega \rightarrow \infty$, ωPBEh $\rightarrow$ PBE. The HSE06 variant of the HSE hybrid functional (in which $a = 0.25\ and\ \omega = 0.2$) was used for hybrid functional calculation in this work since it has been shown to give good results for most systems [71].

1.1.4.4 DFT+U

Accurate description and determination of the electronic, magnetic properties and magnetic order of transition metals (with *d* and *f* electrons) depends, to a great extent, on the accuracy of the exchange-correlation functional. The conventional, approximate LSDA and GGA functionals do not correct for orbital-dependent interactions as well as self-interaction of electrons. It is good to note that the self-interaction of an electron in the Hartree interaction is canceled in exact treatments of exchange, as in Hartree-Fock. The acronym DFT+U represent methods that involve the LSDA- or GGA-type calculation for which orbital-dependent interactions are corrected for. The additional interaction is usually considered only for highly localized atomic-like orbitals on the same site for which orbital energies are shifted by occupations. The Hubbard like parameter "U" is often taken from a fitting to constrained density functional calculations (such as LSDA calculations), making it fully *ab initio*. Alternatively, the LSDA calculation results may be compared with the corresponding mean-field solution for the modelled Hamiltonian. In the implementation, a modification is made in the one electron Hamiltonian. A U parameter is added to take care of the strong electron-electron interaction. The on-site U parameter describes the effective electron-electron interaction (Coulomb interaction) in a solid-state environment. When the DFT calculation is provided with appropriate U parameter, spin states and energy gap between filled and empty *d* or *f* states are accurately predicted [72].

1.1.4.5 Calculation of the Hubbard U parameter

The expression of DFT+U energy functional from Hubbard model (a model Hamiltonian) is constructed with theoretical framework to adequately describe strongly correlated materials. The extent to which *d* and *f* wavefunction change in space is proportional to the number of *d* and *f*

electrons [72-73]. The "U" parameter is the sum of the energy differences between two excited configurations Θ^{n+1}, Θ^{n-1} and the ground state configuration Θ^{n}. Hence, in terms of the Coulomb energy of the *d* orbital, we define the U as

$$U = E(\rho_\Theta + 1) + E(\rho_\Theta - 1) - 2E(\rho_\Theta)\,, \tag{1.35}$$

where ρ_Θ is the occupation number, $\rho_\Theta \pm 1$ is the deviation from ρ_Θ. The energy due to inter-electronic interactions between *d*- electrons is accounted for in the Hamiltonian through $E^U = \frac{1}{2} U \sum_{i \neq j} \rho_i \rho_j$. The parameters $\rho_i \rho_j$ ($\rho = 0$ or 1) is the atomic orbital occupation of the ith and jth localized *d* orbital of the atom experiencing the "Hubbard" term. Therefore, the total energy of a system is written as

$$E^{DFT+U} = E^{DFT} + E^U - E^{DC}\,. \tag{1.36}$$

The last term of Eq. (1.36) is subtracted in order to avoid double counting the interaction contained in the E^U term and in some average way, the E^{DFT}. The E^{DC} is expressed as the mean value of the Hubbard term U, so that the E^{DC} without the orbital polarization effect can be written as

$$E^{DC}(\rho_D) = \frac{1}{2} U \varrho_D(\varrho_D - 1) - \frac{1}{2} J \varrho_D(\varrho_D - 1)\,, \tag{1.37}$$

where $\varrho_D = \sum_i \rho_i$ is the total number of *d*-electrons. The on-site exchange parameter J can be determined by fitting the Eq. (1.37) for the electron-electron interaction to the result of constrained LSDA calculations. This new addition to the one electron Hamiltonian improves the results significantly. It should be noted that increasing the pressure of a system causes little changes in the bare Coulomb interactions which suggests that compression slightly modifies electron-electron interaction being compensated by the "U" parameter [72-73] For this reason, we do not consider pressure dependence of "U" in pressure dependence calculations involving *d*-block materials.

1.1.5 The periodic boundary condition

Application of the KS DFT to a real solid system or other condensed matter poses significant challenge because of the large number of non-interacting electrons (on the order of Avogadro's number) involved. The one-electron wave functions are supposed to extend for the

whole systems, thus the basis sets needed for the expansion of the Kohn Sham orbitals should ideally be infinite. Meanwhile, crystalline solids are composed of spatially repeating units. Thus, solving the Schrödinger equation in a unit cell suffices for the whole crystalline solid by taking advantage of the periodicity of the crystal. This leads to the use of periodic boundary condition (PBC) formulated through the Bloch theorem. The Bloch theorem states that the wavefunctions of the crystal Hamiltonian can be written as

$$\psi_i(\boldsymbol{k},\boldsymbol{r}) = e^{i\boldsymbol{k}\cdot\boldsymbol{r}}u_i(\boldsymbol{k},\boldsymbol{r}), \tag{1.38}$$

where $u_i(\boldsymbol{k},\boldsymbol{r})$ denote the periodic functions also known as the Bloch wavefunctions for which $u_i(\boldsymbol{k},\boldsymbol{r}) = u_i(\boldsymbol{k},\boldsymbol{r}+\boldsymbol{R})$ for all lattice vector $\boldsymbol{R}$. The Bloch wavefunctions extend on the whole crystals and thus have a delocalized nature [74]. This theorem is derived from the translational symmetry of the crystal which satisfies

$$\psi_i(\boldsymbol{k},\boldsymbol{r}+\boldsymbol{R}) = e^{i\boldsymbol{k}\cdot\boldsymbol{R}}\psi_i(\boldsymbol{k},\boldsymbol{r})\,. \tag{1.39}$$

In the above Eq. (1.39), i is the band index, $\boldsymbol{k}$ is the wave vector of the electron in the first Brillouin zone (BZ). On substituting $\psi_i(\boldsymbol{k},\boldsymbol{r}+\boldsymbol{R})$ into the KS equation, i.e., Eq. (1.21), a new set of eigen-equations are obtained for a given $\boldsymbol{k}$. The computation is thus made much more plausible by considering one electron rather than the order of Avogadro's number, since each electron occupies an electronic state of definite wave vector $\boldsymbol{k}$. The complete solution is given by simply multiplying a wave vector $\boldsymbol{k}$ to the phase factor of the solutions in a single reciprocal unit cell. Electronic wave functions at *k* points close to each other are almost identical. Therefore, only a finite number of *k* points in a small region of the reciprocal lattice are required to determine the total ground state energy of a solid, decreasing the computational cost [55,74].

1.1.6 The planewave basis set

Generally, an infinite number of plane wave (PW) basis set is required to fulfil the Bloch theorem expansion which starts with the periodicity of the crystal lattice. However, the right-hand side of Eq. (1.39) can be expanded into a finite number of plane waves for which wave vectors correspond to the reciprocal lattice vectors of the crystal. Thus, each electronic wavefunction,

representing the eigen-function of the KS equation, is a sum of plane waves, with normalization constant ϖ :

$$\psi_i(\boldsymbol{k},\boldsymbol{r}) = \frac{1}{\sqrt{\varpi}}\sum_{\boldsymbol{G}} c_{i,\boldsymbol{k}+\boldsymbol{G}} \cdot e^{\boldsymbol{i}(\boldsymbol{k}+\boldsymbol{G})\cdot\boldsymbol{r}} \ . \tag{1.40}$$

During implementation, the coefficient, $C_{\boldsymbol{i},\boldsymbol{k}+\boldsymbol{G}}$ (where $\boldsymbol{G}$ are reciprocal lattice vectors) which corresponds to small kinetic (band) energies $|\boldsymbol{k}+\boldsymbol{G}|^2$ are more important in the Bloch expansion than those with large kinetic energies. Therefore, the PW basis set can be truncated to include only plane waves that have kinetic energies that are smaller than a particular cutoff energy. This criterion requires that the kinetic energies of the basis set be less than the cutoff energy,

$$\frac{1}{2}|\boldsymbol{k}+\boldsymbol{G}|^2 < E_{cut}. \tag{1.41}$$

The idea of choosing cutoff energy often leads to an error in the calculated total energy and its derivatives. Hence, during implementation, cutoff energy is increased until the calculated total energy converges within the required tolerance. This ensures that the error introduced through an incomplete basis set because of plane wave energy cutoff is reduced to within some tolerance [55,75-76].

1.1.7 The Pseudopotential approximation

In the region near a nucleus there is a strong bonding between the nucleus and the electron which give rise to a localized wavefunctions in the region near the nucleus – the core states. The task of expanding a localized (core) wavefunction is computationally expensive; at the same time, the need to include relativistic (through spin orbit coupling for heavy elements) and other effects in DFT calculation is on the rise, making such task more expensive. This peculiar situation calls for an approximation that can improve DFT calculations, reduce the basis set size while conserving computer time and resources. It is well known that physical properties of most matter depend more on the bonding system between atoms that make up the matter and in turn, the bonding depends on the valence (not the core) electrons. Hence, an approximation that consider only the wavefunctions of valence electrons outside the core during PW expansion is not unphysical. Furthermore, nearest neighbor atoms do not have their cores interact significantly and for this

reason, the electronic structure is gently influenced. The advantage of these assumptions and approximation is that the very high energy cutoff E_{cut} required for the PW expansion in the localized region can be avoided without giving up the physical details of the system under study. The approximations were implemented [75-77] by replacing the core electrons and the ionic potentials by pseudopotential which acts on set of pseudo wavefunctions instead of the true valence wavefunctions. Orthogonality of the pseudo wavefunctions with the core wavefunctions is not necessarily required which leads to the possibility of representing the core wavefunction by a nodeless function. Consequently, very few PWs are required in the pseudo wavefunction's expansion. The description of pseudopotential approximation is shown schematically in Fig. 1.2.

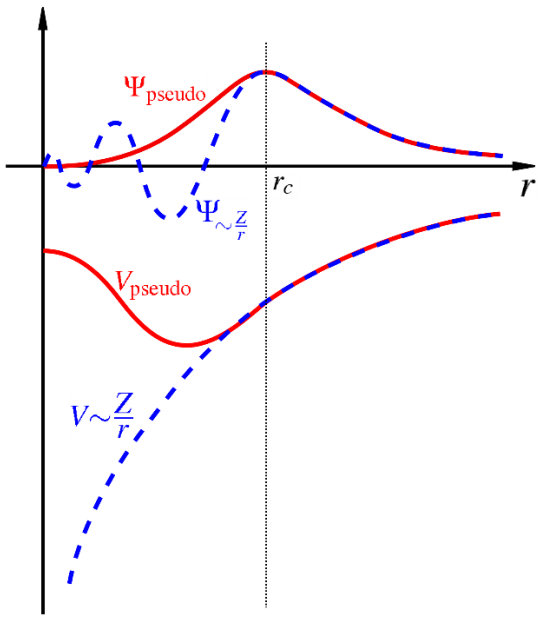

Figure 1.2. An all-electron valence wavefunction and electronic potential (dotted-blue curves) of the nucleus plotted against distance, r, from the atomic nucleus. Beyond the cutoff radius r_c, the pseudo wavefunction and pseudo potential are identical to the all-electron valence wavefunction and potential, respectively. Ref. [78].

There are basically two forms of pseudopotentials, namely the norm conserving (NCPP) and the ultra-soft (USPP). NCPP are constructed to fulfil two conditions which are

1. Inside the cutoff radius r_c, the norm of each pseudo wavefunction must be identical to its corresponding all-electron wavefunction.

$$\int_{r<r_c} d^3r\, \psi_{R,i}(\boldsymbol{r})\, \psi_{R,j}(\boldsymbol{r}) = \int_{r<r_c} d^3r\, \psi_{pseudo_{R,i}}(\boldsymbol{r}) \psi_{pseudo_{R,j}}(\boldsymbol{r}) \tag{1.42}$$

where $\psi_{R,i}$ and $\psi_{pseudo_{R,i}}$ are the all-electron and pseudo reference states, respectively, for the pseudopotential on atom R [55].

2. All-electron and pseudo wavefunctions are identical outside the cutoff radius, r_c.

The USPP can achieve a reduced basis set size by introducing a generalized eigenvalue problem with a non-zero difference in norms, so that a normalized eigenstate of the pseudo-Hamiltonian obeys the generalized equation

$$\hat{H}\left|\psi_i(\boldsymbol{r})\right\rangle = \varepsilon_i \hat{S}\left|\psi_i(\boldsymbol{r})\right\rangle, \tag{1.43}$$

where

$$\hat{S} = 1 + \sum_{R,i,j} |P_{R,i}\rangle q_{R,ij} \langle P_{R,j}| \;,\; q_{R,ij} = \langle \psi_{R,i}(\boldsymbol{r}) | \psi_{R,j}(\boldsymbol{r}) \rangle - \left\langle \psi_{pseudo_{R,i}}(\boldsymbol{r}) \middle| \psi_{pseudo_{R,j}}(\boldsymbol{r}) \right\rangle$$

and $P_{R,i}$ are projectors that form a dual basis with the pseudo reference states within the cutoff radius and zero outside, such that

$$\left\langle P_{R,i} \middle| \psi_{pseudo_{R,j}}(\boldsymbol{r}) \right\rangle_{r<r_c} = \delta_{ij} \;. \tag{1.44}$$

Consequently, USPP are usually characterized by longer cutoff radius than the NCPP [55].

1.1.8 The PAW method

The Projector Augmented Waves (PAW), which is an all-electron scheme, was developed by Blöchl in 1994 [77]. The scheme allows an all-electron wave function to be constructed as a sum of the pseudo-wave function outside the core region (where pseudo-wave function is equivalent to all-electron wave function) and the partial wave function inside the core region less by the corresponding pseudo partial wavefunction in the core region. So, if we define the all-electron partial waves as $\psi_n^\sigma(\boldsymbol{r})$ and the pseudo waves as $\tilde{\psi}_n^\sigma(\boldsymbol{r})$, then the reconstructed KS wave function can be written as

$$\psi_n(\boldsymbol{r}) = \tilde{\psi}_n(\boldsymbol{r}) - \tilde{\psi}_n^{\sigma}(\boldsymbol{r}) + \psi_n^{\sigma}(\boldsymbol{r}) \tag{1.45}$$

The PAW method is different from the all-electron method in the treatment of the core electrons. The PAW method treats the core of an atom as a "frozen core". Thus, it has the advantages of pseudopotential methods but retain the physics of an all-electron calculation [55].

Unless otherwise specified in the methodology, electronic structure calculations in this thesis are performed using the PAW method. A pictorial illustration of this construction process is shown in Fig. 1.3.

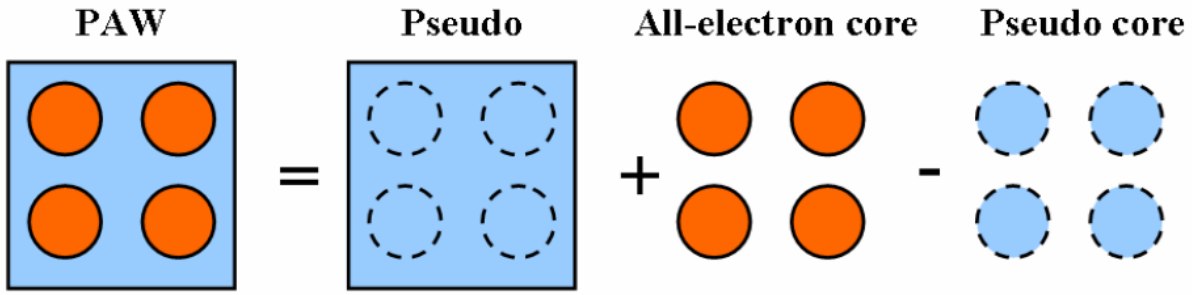

Figure 1.3. A simplified schematic of the procedures involved in the construction of PAW wave function. Ref. [78].

1.1.9 Self-consistence cycle and ground-state total energy

Solving the KS equations requires the knowledge of other parameters (such as electron density, ground-state total energy) that also depends on the solutions (KS wavefunctions) themselves. Thus, one can solve the KS equations self consistently. The procedure used throughout this thesis for the calculation of electronic structure of various materials studied is illustrated schematically in Fig. 1.4. We start the self-consistent field (SCF) calculation with an educated initial guess of the electron density $\rho(\boldsymbol{r})$. A good guess would be the atomic density of chemical species that make up the system. The KS equations are then constructed using the guessed density and effective potential. The KS equation in k-space is given as $\sum_{\boldsymbol{G}'}\left[\frac{1}{2}|\boldsymbol{k}+\boldsymbol{G}|^2\delta_{\boldsymbol{G}\boldsymbol{G}'} + V_{NN}(\boldsymbol{G}-\boldsymbol{G}') + V_{XC}(\boldsymbol{G}-\boldsymbol{G}') + V_H(\boldsymbol{G}-\boldsymbol{G}')\right]\psi_{i,\boldsymbol{k}+\boldsymbol{G}'} = \in_i \psi_{i,\boldsymbol{k}+\boldsymbol{G}}$, where $\boldsymbol{G}$ is the reciprocal lattice vector and $\psi_{i,\boldsymbol{k}+\boldsymbol{G}}$ is the plane wave coefficient. The KS equation is solved numerically at each *k*-point throughout the BZ yielding a set of pseudo-wavefunctions. The pseudo-wavefunctions,

which correspond to the KS orbitals, are used to calculate a new electron density $\rho_N(\boldsymbol{r}) = \sum_i |\psi_i(\boldsymbol{r})|^2$. The newly calculated electron density $\rho_N(\boldsymbol{r})$ is compared with the initially guessed density, $\rho(\boldsymbol{r})$, for convergence. Convergence is achieved when the difference $|\rho(\boldsymbol{r}) - \rho_N(\boldsymbol{r})|$ is less than some set tolerance, Ξ. If the tolerance criterion is not satisfied, the process is repeated until the criterion is satisfied. Once convergence is achieved, the resulting electron density is used to calculate the ground-state total energy, which in turn is used to calculate the pseudo-wavefunction, energies (atomic energy levels / bands) as well as the force on each atom (using Hellmann-Feynman's theorem) [79]. It is important to state that the pseudo-wavefunction contains information about other physical properties of the system being studied in the ground state. Hence, other physical properties of the system can be extracted from the pseudo-wavefunction.

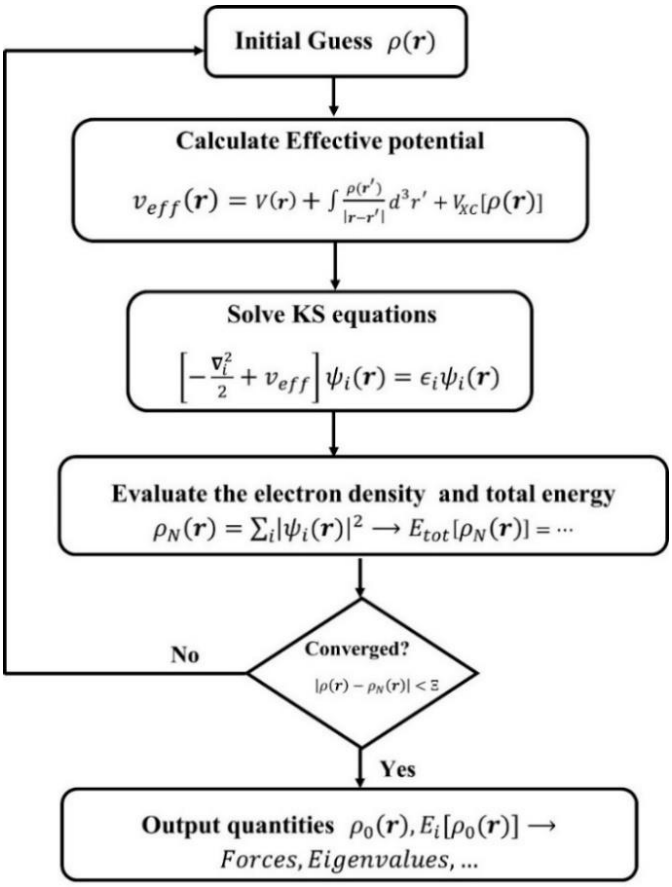

Figure 1.4. A flowchart illustrating how the self-consistent calculation proceeds step by step using DFT with PW basis set.

1.1.10 The Full-Potential Linearized Augmented Plane Wave (FP-LAPW) method

The linearized augmented plane wave (LAPW) method is a modification of the Slater's augmented plane wave method (APW). The APW method was motivated by the fact that the potential and wavefunctions near an atomic nucleus are like those in an atom as they are strongly changing but almost spherical. Meanwhile, the potential and wavefunctions are smoother in the interstitial space between the atoms. Accordingly, unit cell is partitioned atomic sphere and interstitial regions in which different basis expansions are used in these regions: radial solutions of Schrödinger's equation inside non-overlapping atomic spheres and planewaves in the remaining interstitial region [80]. See illustration in Fig. 1.5 below.

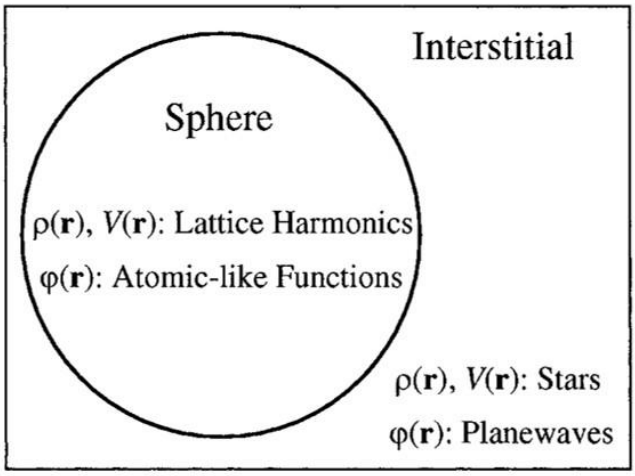

Figure 1.5. The dual representation of the APW and the LAPW methods. Stars and lattice harmonics are symmetrized plane waves and spherical harmonics used to represent the density and potential [80].

$$\varphi(\boldsymbol{r}) = \begin{cases} \dfrac{1}{\sqrt{\Omega}} \sum_{\boldsymbol{G}} c_{\boldsymbol{G}} e^{i(\boldsymbol{G}+\boldsymbol{k})\cdot\boldsymbol{r}} & \boldsymbol{r} \in I \\ \sum_{\ell m} A_{\ell m} u_{\ell}(r) Y_{\ell m}(\hat{\boldsymbol{r}}) & \boldsymbol{r} \in S \end{cases}, \tag{1.46}$$

where φ is a wavefunction, Ω is the cell volume, u_ℓ is the regular solution of

$$\left[-\frac{d^2}{dr^2}+\frac{\ell(\ell+1)}{r^2}+V(r)-E_\ell\right]ru_\ell(r)=0\,. \tag{1.47}$$

Here, $c_{\boldsymbol{G}}$ and $A_{\ell m}$ are expansion coefficients, E_ℓ is a parameter, V is the spherical component of the potential in the sphere. The coefficient $A_{\ell m}$ is defined as

$$A_{\ell m}=\frac{4\pi i^\ell}{\sqrt{\Omega}u_\ell(R)}\sum_{\boldsymbol{G}}c_{\boldsymbol{G}}j\ell(|\boldsymbol{k}+\boldsymbol{G}|R)Y^*_{\ell m}(\boldsymbol{k}+\boldsymbol{G})\,, \tag{1.48}$$

where the origin is taken at the center of the sphere and R is the sphere radius and $j\ell$ is Bessel function coefficients. Thus, the $A_{\ell m}$ are completely determined by the planewave coefficients, $c_{\boldsymbol{G}}$,and the energy parameters, E_ℓ. These are the variational coefficients in the APW method. However, in this APW formalism, there are values of the energy parameter, E_ℓ for which u_ℓ vanishes on the sphere boundary [80]. At these energies, the planewaves and radial functions become decoupled. This is called the asymptote problem.

Andersen [81] extended this work by proposing a method in which the basis functions and their derivatives are made continuous by matching planewave to a radial function at fixed E_ℓ plus its derivative with respect to E_ℓ. This choice circumvents the problems with the APW method, mentioned above, as well as providing a flexible and accurate band structure method. This is the LAPW method. In the LAPW method, the basis functions inside the spheres are linear combinations of radial functions, $u_\ell(r)Y_{\ell m}(\hat{\boldsymbol{r}})$ and their derivatives with respect to the linearization parameters, E_ℓ. The u_ℓ are defined exactly as in the APW method (Eq. (1.47)), with a fixed E_ℓ. The energy derivative, $\dot{u}_\ell(r)Y_{\ell m}(\hat{\boldsymbol{r}})$, satisfies

$$\left[-\frac{d^2}{dr^2}+\frac{\ell(\ell+1)}{r^2}+V(r)-E_\ell\right]r\dot{u}_\ell(r)=0\,, \tag{1.49}$$

in the non-relativistic case. These functions are matched to the values and derivatives of the planewaves on the sphere boundaries. Planewaves, augmented in this way, are the LAPW basis functions. In terms of this basis, the wavefunctions are

$$\varphi(\boldsymbol{r}) = \begin{cases} \frac{1}{\sqrt{\Omega}} \sum_{\boldsymbol{G}} c_{\boldsymbol{G}} e^{i(\boldsymbol{G}+\boldsymbol{k})\cdot\boldsymbol{r}} & \boldsymbol{r} \in I \\ \sum_{\ell m} A_{\ell m} u_{\ell}(r) + B_{\ell m} \dot{u}_{\ell}(r) Y_{\ell m}(\hat{\boldsymbol{r}}) & \boldsymbol{r} \in S \end{cases}, \tag{1.50}$$

where the $B_{\ell m}$ are coefficients for the energy derivative, like the $A_{\ell m}$. The LAPW basis are just planewaves in the interstitial, as in the APW method. Inside the spheres the LAPW basis have more variational freedom than APW basis [81]. The LAPW-based calculations were performed in this thesis using the wien2k code [82].

1.2 Crystal Structure Prediction

Crystal structure prediction at 0 K is important in understanding the crystallization processes in materials. Several available methods for 0 K structure prediction are energy-based in which energetically viable crystal structures are uncovered by scanning the multidimensional energy hypersurface. This is performed by computing lattice energy changes with respect to parameters such as unit cell dimension, space group symmetry and atomic coordinates with the purpose of identifying all possible energy minima. These computations completely ignore entropic and kinetic contribution to energy as well as the zero-point vibrational energy correction, unless otherwise specifically computed for system(s) of interest. The reason being the expensive computational cost of computing vibrational free energy, entropic and kinetic contributions of all possible structures. The distribution of virtual crystal structures and their relative energies is referred to as the crystal energy landscape (CEL) or the potential energy surface (PES). The last few decades have ushered in some novel way of systematically exploring the PES for a given element, compound, or elemental compositions whose computational cost is known to increase exponentially with number of constituents. Few of the methods relevant to the work reported in this thesis will be subsequently discussed.

1.2.1. Random Search Method

The random searching (RS) method gives the widest and unbiased coverage of the PES. The RS method is particularly useful in situations where nothing is known about the low-energy

structures except its constituents. Even though the name suggest that the algorithm generates crystal structures from random numbers, yet, few constraints (such as symmetry, bond lengths) are imposed to improve efficiency and ensure that random structures generated are physically 'random sensible structures'. In the RS method, a random set of unit cell lengths (*a, b, c*) and angles (*α, β, γ*) is generated and the cell volume is renormalized to a random value within ±50% (or thereabout) of a chosen mean volume. One can determine the appropriate mean volume from known structures composed of the same atoms, by adding up atomic volumes, or by relaxing a few 'handmade' structures. In addition to symmetry and bond lengths, the RS method can be biased by specifying range of stoichiometries and number of formular units. However, this will preclude the discovery of structures beyond the number of units specified, which may hold the global energy minimum structure for the system being studied. The RS method is a powerful crystal structure prediction tool if one has no *a priori* knowledge of the likely structure and the predictions can be systematically improved by imposing few constraints [83].

1.2.2. Genetic Algorithm Method

Since crystal structure prediction requires searching and distinguishing a huge number of energy minima on the PES, then, more intelligent algorithm that goes beyond RS method is a pressing need. The genetic algorithm (GA) is a global optimization method of 'intelligently' exploring the PES. The GA method is a RS method equipped with self-learning capabilities that mimic the Charles Darwin's theory of natural evolution. In the GA method, crystal structure population from a cell volume-constrained-RS method (trial structures) are iteratively operated upon by evolution operators such as cross over operator and mutation operator rather than the traditional 'slice and paste'. The workflow in GA method is shown in Fig. 1.6. The generation of random structures ensures unbiased sampling of the PES. In a case where some a priori crystal structure data are available, small percentage of the random structure population can be produced by 'seed'. The initial simulation cell size can be evaluated as:

$$V_i = V_0 \cdot (1 \pm \varepsilon)\,, \tag{1.51}$$

where $V_0 = \sum_{i=0}^{n} a \cdot R_i^3$, $\varepsilon = \sigma \cdot e^{-\left(\frac{\zeta}{2}\right)^2}$. R_i is the atomic radius of each atom, a is an adjustable parameter that determines the average cell volume, ζ is a random number between ± 1, σ is the

tolerance range of the cell size. Crystal structure refinement is performed after every optimization loop including symmetrization to have diverse population.

The cross over operation is performed on refined crystal structures by creating child structures from slices of two parent structures cut using periodic planar slabs. The cut can be made along the periodic boundaries or along the cell. The cross over operation is performed according to:

$$\begin{pmatrix} a_x & 0 & 0 \\ b_x & b_y & 0 \\ c_x & c_y & c_z \end{pmatrix} = \frac{1}{F_{pi} + F_{pj}} \left[F_{pi} \begin{pmatrix} a_{xi} & 0 & 0 \\ b_{xi} & b_{yi} & 0 \\ c_{xi} & c_{yi} & c_{zi} \end{pmatrix} + F_{pj} \begin{pmatrix} a_{xj} & 0 & 0 \\ b_{xj} & b_{yj} & 0 \\ c_{xj} & c_{yj} & c_{zj} \end{pmatrix} \right], \quad (1.52)$$

where F_p is the fitness values of parent crystal structures and a, b, c are lattice vectors. In a case where cross over operation is not efficient, mutation operation is applied. This method involves swapping several different atomic positions in pairs, especially where different species of atoms with similar properties are involved. It is important to note that mutation operator is not usually applied to randomly shifted atomic positions because such locations may lack orientation and may diverge the trajectory of the structure search [84]. Crystal structure predictions using GA in this thesis was implemented within an inhouse program interfaced with a DFT code.

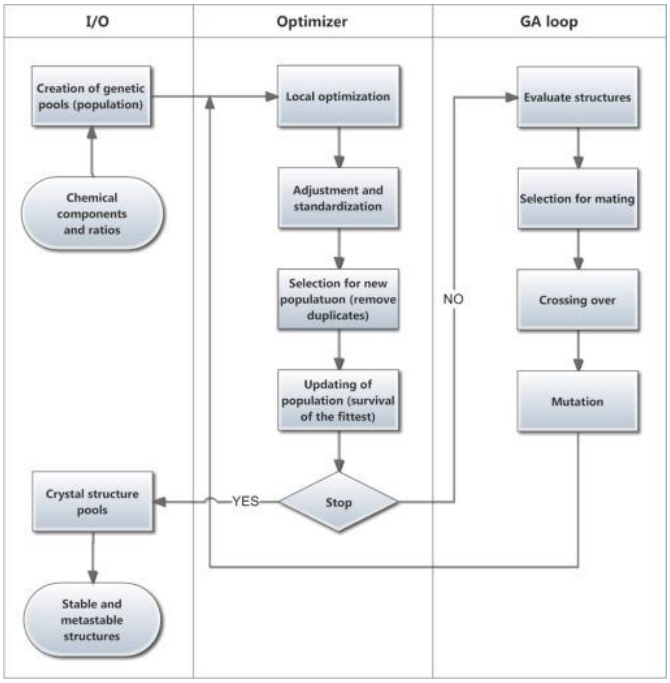

Figure 1.6. General flowchart illustrating the basic processes of a genetic algorithm [84].

1.2.3. Particle swarm-intelligence optimization

The particle swarm-intelligence optimization (PSO) is a global optimization, population-based evolutionary algorithm for dealing with problems in which a best solution can be represented as a point or surface in an N-dimensional space. The PSO algorithm is inspired from the swarm behavior such as birds flocking in nature. Thus, particles move through the solution space and are evaluated according to some fitness criterion after each time step. For every iteration in the PSO method, each particle is updated by following two "best" values. The first one is the best solution (fitness) it has achieved so far, called *pbest* and the second-best value is a global best, called *gbest*. The social interaction between neighboring particles is captured through the evaluation of fitness within a specified radial space. The neighborhood bests (*lbest*) allow parallel exploration of the search space and reduce the tendency of the PSO falling into local minima, but slow down convergence speed. The PSO method is applied in crystal structure prediction as follows: (1) random crystal structures are generated with constraint of symmetry within the 230 space groups (2) the constrained random structures are optimized to evaluate the energies of the local minimum-energy configurations. The local optimization increases the computational cost of the method while reducing the noise of the CEL, enhancing comparability between different structures (3) identification of unique local minima by geometrical structure parameter. This is achieved by removing identical or duplicate structures to speed up convergence to the global minimum. Here, the bond lengths in two structures are compared according to

$$\Delta d = \sqrt{\sum_{i,j} \left(d_i - d_j'\right)^2 \delta_{ij}} \ , \tag{1.53}$$

Where d_i and d_j' are the bond lengths in the two structures, respectively and δ_{ij} is a delta function. If the deviation (Δd) is less than certain preset tolerance, the two structures are considered equivalent and are removed (4) new structures are generated by PSO for further iteration: a new evolutionary generation. Here, the position of each particle is updated using its velocity vector according to

$$x_{i,j}^{t+1} = x_{i,j}^{t} + v_{i,j}^{t+1} \tag{1.54}$$

where $v_{i,j}^{t+1} = \omega v_{i,j}^{t} + c_1 r_1 \left(\text{pbest}_{i,j}^{t} - x_{i,j}^{t}\right) + c_2 r_2 \left(\text{gbest}_{i,j}^{t} - x_{i,j}^{t}\right)$, $j \in \{1,2,3\}$, c_1 and c_2 are the particle's self-confidence and swarm-confidence factor, respectively (typically, $c_1 = c_2 = 2$). ω is the inertia weight of the particle with high value (0.9) inducing global search and low value (0.4) inducing local search [85]. r_1 and r_2 are two separately generated random numbers between 0 and 1. The velocity update formula includes random parameters (r_1 and r_2) to ensure better coverage of the searching space and avoid being trapped in local optima. The flow chart in Fig. 1.7 summarizes the implementation of PSO method used in this thesis.

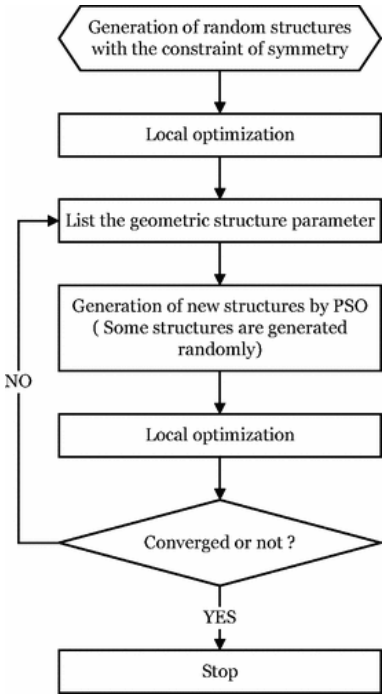

Figure 1.7. General flowchart illustrating the basic processes of a particle swarm-intelligence optimization algorithm [85].

1.3 Molecular Dynamics

Molecular dynamics (MD) is a computational approach in which the classical Newton's equations of motion are solved numerically for atoms and molecules placed in a simulation box. Atoms and molecules interact as an ensemble for a fixed period of time leading to the evolution of a dynamic chemical system in the phase space. During an MD simulation, the potential energy surface of the chemical system is systematically sampled and the nuclear dynamics under the influence of temperature is calculated. The macroscopic thermodynamic properties are defined as

an ensemble average, which is an average over a large number of microstates of the ensemble. Thus, an MD simulation generates a set of points in the phase space as a function of time according to the ensemble [15,86-88]. Assuming ergodicity, properties calculated from the MD trajectory are time-average based. Therefore, sampling over enough phase space for long enough time, the experimentally relevant information about structural dynamics and thermodynamic properties can be calculated. Depending on the experimentally relevant condition we are interested in, MD simulation can be performed in a microcanonical ensemble (*NVE*), canonical ensemble (*NVT*) and isothermal-isobaric (*NpT*) ensemble. The MD simulation carried out in this thesis were mostly performed in an *NpT* ensemble unless otherwise stated in the computational details.

1.3.1 A Simple Molecular Dynamics algorithm

A general flow chart of a typical MD simulation is shown in Fig. 1.8. The ease with which an MD algorithm runs benefitted from the assumption that nuclei can be treated as point particles that follow classical Newtonian dynamics.

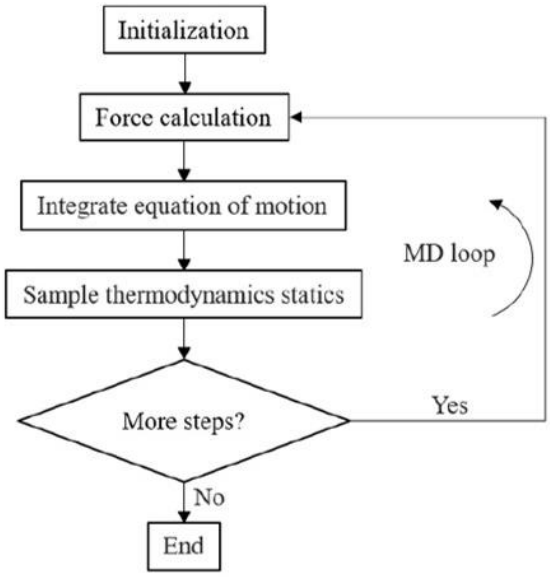

Figure 1.8. General flowchart illustrating the basic processes of an MD algorithm [88].

From Fig. 1.8, an MD simulation starts with the initialization of particles with initial positions and velocities at time t = 0 following a specific statistical distribution. The initial

velocities are set according to the Maxwellian distribution of equipartition relationship, $K_B T(t_0) = \sum_i^N \frac{m v_{\alpha,i}^2(t_0)}{N_f}$, where K_B is the Boltzmann constant, $T(t_0)$ is the temperature at time t_0. Furthermore, $v_{\alpha,i}(t_0)$ is the $\alpha = (x, y, z)$ component of velocity for atom i at time t_0, and N_f is the number of degrees of freedom. Then, the forces on each atom are calculated by taking the gradient of the electronic potential energy. Once the forces are obtained, one can integrate the Newton's equation of motion to get the positions and velocities. Over time, different algorithms have been developed for the implementation of MD with each one improving the routine for integrating the Newton's equation of motion. Analytically, Newton's equation of motion is a second order differential equation that numerically simplifies into two coupled first order differential equations involving position and velocity. Thus, the two commonly used numerical algorithms for the integration are, the Velocity Verlet (VV) algorithm and the Verlet Leapfrog (VF) algorithm. Both schemes can simultaneously integrate the velocity and position in time. The equations of the VV algorithm from Taylor series expansion of position and velocity are written as:

$$\boldsymbol{v}_{t+1/2} = \boldsymbol{v}_t + \frac{\boldsymbol{f}_t \cdot \Delta t}{2m}\,, \tag{1.55}$$

$$\boldsymbol{r}_{t+1} = \boldsymbol{r}_t + \boldsymbol{v}_{t+1/2} \cdot \Delta t\,, \tag{1.56}$$

$$\boldsymbol{v}_{t+1} = \boldsymbol{v}_{t+1/2} + \frac{\boldsymbol{f}_{t+1} \cdot \Delta t}{2m}\,, \tag{1.57}$$

where Δt is the time step. The half-step velocity calculated from the force is used as the mean velocity between steps t and $t + 1$ to update the velocity and position. A similar approach is used for the VF algorithm which also makes use of the half-step velocity. The VF is time-reversal symmetric and conserve energy. The velocity in the VF algorithm is given by

$$\boldsymbol{v}_{t+1/2} = \boldsymbol{v}_{t-1} + \frac{\boldsymbol{f}_t \cdot \Delta t}{2m}\,. \tag{1.58}$$

The new position and velocity at the $(t + 1)$th step are then given by,

$$\boldsymbol{r}_{t+1} = \boldsymbol{r}_t + \boldsymbol{v}_{t+1} \cdot \Delta t \tag{1.59}$$

$$\boldsymbol{v}_{t+1} = \boldsymbol{v}_{t+1/2} + \boldsymbol{v}_{t-1/2} \tag{1.60}$$

A general rule of thumb is to choose Δt to be small enough to resolve the fastest event in a crystal structure such as bond bending and bond stretching. The simulation is also run long enough to a time length (physical enough) for the desired event to occur. Therefore, from MD simulation, a time dependent trajectory (position and velocity at each time step) of the atoms of the system under study is determined from successive integration of the steps. The total time depends on the event time scale, in the order of picosecond (ps) to nanosecond (ns). Once the trajectory is obtained, exploiting the ergodic hypothesis, many microscopic and macroscopic properties of the system are calculated from the time average. An MD calculation runs in a loop until the number of desired times steps is reached [88].

1.3.2 Ab initio Molecular Dynamics

In principle, the nuclei of most atoms can be treated as classical point-like particles, and their motions can be studied by Newton's laws; this forms the basis for classical MD. The forces on the atoms can be calculated quantum mechanically using the Hellmann-Feynman theorem, and this method is known as *ab initio* MD (AIMD). In this formalism, the electrons are optimized self-consistently to a configuration that minimizes the system energy. Thus, the electrons are assumed to move with the nuclei and the force on the nuclei can be calculated. In AIMD the forces are calculated from the Hellmann-Feynman Theorem and is written as

$$\boldsymbol{F} = -\frac{dE(\boldsymbol{R})}{d\boldsymbol{R}}\,, \tag{1.61}$$

where $\boldsymbol{R}$ is the nuclear spatial coordinate and the energy E can be obtained by solving the KS equations:

$$E = \langle\psi|H|\psi\rangle\,. \tag{1.62}$$

We recall the Hellmann-Feynman theorem which states that the first derivative of the eigenvalues of a Hamiltonian, $H\lambda$, that depends on a parameter λ is given by the expectation value of the derivative of the Hamiltonian:

$$\frac{\partial E_\lambda}{\partial \lambda} = \left\langle \psi_\lambda \middle| \frac{\partial H_\lambda}{\partial \lambda} \middle| \psi_\lambda \right\rangle \tag{1.63}$$

where ψ_λ is the eigenfunction of H_λ corresponding to the E_λ eigenvalue. For the AIMD, we say that nuclear coordinates are the parameters of the electronic Hamiltonian, H. We can therefore derive the force acting on the I_{th} nucleus in the electronic ground state as:

$$\boldsymbol{F}_I = -\frac{\partial E(\boldsymbol{R})}{\partial \boldsymbol{R}_I} = -\left\langle \psi(\boldsymbol{R}) \middle| \frac{\partial H(\boldsymbol{R})}{\partial \boldsymbol{R}_I} \middle| \psi(\boldsymbol{R}) \right\rangle , \tag{1.64}$$

where $\psi(\boldsymbol{R})$ is the electronic ground state wave function of the Hamiltonian $H(\boldsymbol{R})$. Eq. (1.64) is an expression of the force on an ion, which is given by the expectation value of the gradient of the electronic Hamiltonian in the ground state. The calculations are based on direct minimization of the KS equations at each time step. The electronic information from previous MD step can provide a good initial approximation for the ground state of the updated nuclear potion, enabling the energy and forces for a new time step to be computed in an efficient way [88]. All the AIMD simulations reported in this thesis were performed using VASP.

1.3.3 Metadynamics

The trajectories from an *ab initio* MD simulation are informative only if the run is long enough for the system to visit all energetically relevant configurations, thereby satisfying the ergodic condition in the time scale of the simulation for a dynamic system evolving in phase space. This highlight the fact that *ab initio* MD is drawn back by time scale problem, if one is to resolve properly the fastest motion of the system – bond stretching and bond bending. In most chemical reactions or phase transitions, one frequent source of difficulty is the separation of relevant configuration by high free-energy barriers that are insurmountable by thermal fluctuation from increasing the temperature of the system. Thus, transition from one metastable state to another can only be activated by rare, but high-enough fluctuations to take the system over the free energy barrier. In principle, such high energy barriers could be crossed by over pressurizing the system so that the contribution from the *p*V term increases the Gibbs energy. But such over pressurization often leads to mechanical and dynamic instability [89] in addition to missing some of the intermediate metastable phases, thereby smearing out more details about intermediate structures. To achieve this high fluctuation without inducing instabilities, additional history-dependent bias potential (or force) is required on selected number of degrees of freedom often referred to as

collective variables (CVs), adaptatively constructed in the CVs space. This constrained molecular dynamic is referred to as metadynamics. Metadynamics is a technique for speeding up configuration sampling in molecular dynamics simulation and reconstructing the free energy surface (FES) as a function of CVs [90,91]. The potential in metadynamics is written as sum of Gaussians which are added to the Hamiltonian of the system and are deposited along the system trajectory as it evolves. The Gaussians, while pushing the system out of the local free energy minima, prevent it from revisiting configurations that have already been sampled.

For the system prepared in the local minimum B (in Fig. 1.9), *ab initio* MD is not capable of pushing it out of the minimum because the barriers are larger than thermal fluctuations. Metadynamics, on the other hand, deposits Gaussians in the potential basin as the simulation progress, causing the bias potential to grow until the system is eventually pushed out of the basin B. The natural route will be transition into the basin A (local minimum, corresponding to a metastable configuration) where the system is, again, trapped. The process of filling the basin continues in the basin A until it is completely filled and the dynamics in the system become diffusive in the region between the basin A and B. Further filling of the diffusive state with Gaussians while the simulation progress makes the basin C (global minimum, corresponding to a ground state configuration) accessible.

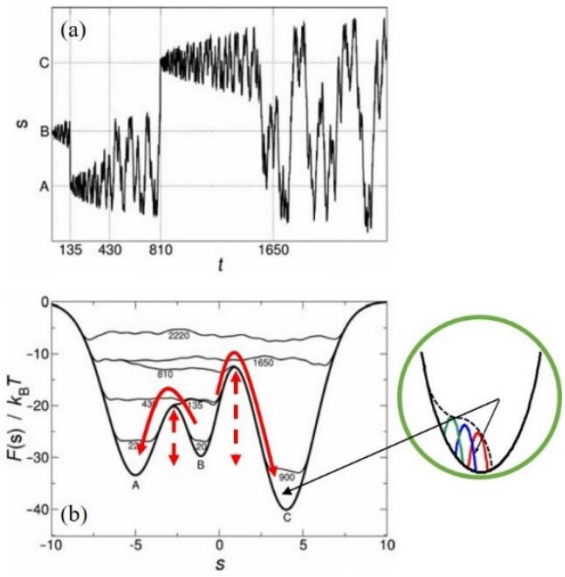

Figure 1.9. Underlying principle of the metadynamics method of crossing the energy barriers in a one-dimensional model potential (a) Time evolution of the CVs during the simulation (b)

Schematic representation of the progressive filling of the potential well with Gaussian to overcome the energy barrier [78,91]. I have modified this figure for illustrations.

The choice of order parameters in metadynamics simulation are always informed by the properties of interest. In the implementation of metadynamics used in this thesis, the dynamics of the simulation box is assumed to be correlated with the motion of the atoms in it. Thus, it suffices to describe the order parameter in terms of the six degrees of freedom of the simulation box: the 3 cell lengths and 3 angles. The global rotations of the box can be avoided by freezing them through construction of an upper triangular edge matrix, $\mathbf{h} = (\mathbf{a}, \mathbf{b}, \mathbf{c})$, comprising of the variable cell parameters of the simulation box. The **h** matrix, after fixing the simulation box from rotation, becomes:

$$\begin{pmatrix} h_{11} & 0 & 0 \\ h_{12} & h_{22} & 0 \\ h_{13} & h_{23} & h_{33} \end{pmatrix} . \tag{1.65}$$

The driving force for the simulation depends on the history-dependent Gibbs free energy G according to $\phi^t = -\frac{\partial G^t}{\partial \mathbf{h}}$. The set of order parameters evolve during the simulation according to:

$$\mathbf{h}^{t+1} = \mathbf{h}^t + \delta h \frac{\phi^t}{|\phi^t|} . \tag{1.66}$$

The Gibbs free energy is a function of the box edges, such that on varying the box edges, a thermodynamic state is reached. This history-dependent Gibbs potential, which is written in term of a Gaussian function is given as:

$$G^t(h) = G(h) + \sum_{t'<t} We^{-\frac{\left|\mathbf{h}-\mathbf{h}^{t'}\right|^2}{2\delta h^2}} , \tag{1.67}$$

where δ and W are the width and the height of the Gaussian, respectively. The force is thus, a sum of the thermodynamic forces. Close to an equilibrium, the Taylor series expansion of the Gibbs free energy yield:

$$G(\mathbf{h}) \approx G(\mathbf{h}^0) + \frac{1}{2}(\mathbf{h} - \mathbf{h}^0)^T \mathbf{A} (\mathbf{h} - \mathbf{h}^0) , \tag{1.68}$$

where $\mathbf{A} = A_{ij} = \left|\frac{\partial^2 G(\mathbf{h})}{\partial h_i \partial h_j}\right|_{\mathbf{h}^0}$ is the Hessian matrix, describing the local curvature of the free-energy surface. The metadynamics method requires no prior knowledge of the landscape because it explore the low free-energy regions first. Furthermore, it allows exploring new reaction pathways as the system evolves through the lowest free-energy pathway and a reconstructive phase transition can be uncovered [91,92]. The metadynamics simulations reported in this thesis were performed using metadynamics code introduced by Martoňák *et al* [92] interfaced with VASP [93].

1.4 Molecular dynamics post processing methods

There are several dynamical properties that can be obtained from the trajectories of MD simulations. Some of these properties, as used in the analyses of this thesis are the velocity autocorrelation function, vibrational density of states and the mean squared displacement. Other properties (not covered by the scope and objective of this thesis) such as diffusion coefficient and coefficient of viscosity derived from the mean square displacement and the velocity autocorrelation functions, respectively, can be further computed.

1.4.1 Velocity auto-correlation function

In a solid material, atoms vibrate around an equilibrium position. This vibration is described by the dynamical matrix, derived from a second order derivative of the system's energy surface with respect to the atomic positions, scaled by the atomic nuclei masses, $\frac{1}{\sqrt{M_I M_J}} \frac{\partial^2 E(\boldsymbol{R})}{\partial \boldsymbol{R}_I \partial \boldsymbol{R}_J}$. Therefore, atomic trajectories can be represented as a superposition of the eigenmodes of the dynamical matrix and as such the velocity autocorrelation function $V(t)$ holds information about the eigenfrequencies of the system.

For a system of N atoms, the velocity autocorrelation function is defined as [74]:

$$V(t) = \langle \boldsymbol{v}_i(t + t_0) \cdot \boldsymbol{v}_i(t_0) \rangle = \frac{1}{N} \sum_{t_0} \sum_{i=0}^{N-1} \boldsymbol{v}_i(t + t_0) \cdot \boldsymbol{v}_i(t_0) \ , \tag{1.69}$$

where $\boldsymbol{v}_i(t)$ is the velocity of the i-th atom at time t. The averaging is done over atom i at time origin t_0. The $V(t)$ is maximum at time $t = 0$ and at sufficiently large t, there will be no correlation between velocities. Hence,

$$\lim_{t\to\infty} V(t) \to \langle \boldsymbol{v}_i(t + t_0)\rangle \cdot \langle \boldsymbol{v}_i(t_0)\rangle = 0\,, \tag{1.70}$$

1.4.2 Vibrational Density of States

Phonon is a quantized lattice vibration in which a lattice of atoms uniformly oscillates at a single frequency. The phonon density of states thus describes the distribution of the number of vibrational modes per unit frequency per real space volume. Essentially, it is a measure of the probability of finding a mode vibrating at a particular frequency. At finite temperature, lattice vibrations begin to lose their quantization properties and as such, the density of states (which for distinction will be called vibrational density of states) will be embedded in the velocity autocorrelation function $V(t)$. To decompose $V(t)$ into a sum of sinusoidal curves, we perform Fourier transform on $V(t)$ sampled for a finite time interval, $[0, t_{max}]$. The Fourier transform is calculated based on (a) the theory of time invariance and (b) commutative property of the inner product. The two theories ensure the validity of the equality $V(t) = V(-t)$. Hence, the Fourier transform is calculated as:

$$\tilde{V}(\omega) \equiv \int_{-\infty}^{\infty} V(t)e^{i\omega t}dt = 2\int_{0}^{\infty} V(t)\cos\omega t\, dt\,. \tag{1.71}$$

Since we only sample $V(t)$ for a finite time interval during an MD simulation, then we can calculate the vibrational density of states spectral from the MD trajectory according to

$$\tilde{V}(\omega) = 2\int_{0}^{t_{max}} V(t)e^{-\left(\frac{t}{\tau}\right)^2}\cos(\omega t)\, dt\,. \tag{1.72}$$

Truncating the integration in Eq. (1.71) at a finite time introduces numerical noise and a damping time τ is introduced through Eq. (1.72) to smoothen out the numerical noise [88].

1.4.3 Mean-squared Displacement

Given an MD trajectory, it is possible to obtain information on how far an individual particle moves from its equilibrium (starting) position by calculating the mean squared displacement (MSD). MSD is defined as the square of the distance a particle has moved from its starting point within a time interval, t. Mathematically,

$$MSD = \langle |\boldsymbol{r}(t) - \boldsymbol{r}(0)|^2 \rangle \,. \tag{1.73}$$

For a liquid system, the plot of MSD against time is linear with a finite slope. From this slope, it is possible to get the diffusion coefficient, *D*. The MSD is related to the diffusion coefficient of an *N*-dimensional system as follows [88]:

$$D = \frac{1}{2N}\frac{d}{dt}\langle |\boldsymbol{r}(t) - \boldsymbol{r}(0)|^2 \rangle \,, \tag{1.74}$$

where N is an integer (1,2,3).

1.5 Mechanical properties and elastic constants

It is possible to establish the mechanical stability of a materials using the Born elastic stability criterion [94] for the crystal system. Elastic constants describe the behavior of crystals as a function of elastic deformations. A mathematical description of the elastic behaviors of a crystal lattice is characterized by its second-order elastic constant matrix:

$$C_{ij} = \frac{1}{V_0}\left(\frac{\partial^2 E}{\partial \varepsilon_i \partial \varepsilon_j}\right), \tag{1.75}$$

where V_0 is the equilibrium volume, ε is the strain and E is the total energy of the strained cell. Elastic stability requires that the matrix $\boldsymbol{C}$ in Eq. (1.75) be definite positive and that all eigenvalues of $\boldsymbol{C}$ are positive. Each of the crystal systems have different numbers of independent elastic constant C_{ij}. Details can be found in ref. [95]. For the purpose of this thesis, I will exemplify the Born elastic stability criteria for the cubic system. The cubic system has the simplest form of elastic matrix with three independent constants, C_{11}, C_{12} and C_{44}. The necessary and sufficient stability condition also called Born stability criteria for the system are:

$$C_{11} - C_{12} > 0\,, \qquad C_{11} + 2\,C_{12} > 0\,, \qquad C_{44} > 0\,, \tag{1.76}$$

The results from elastic constants calculation using stress-strain relationship can be used to determine the theoretical polycrystalline bulk modulus, shear modulus and some other derivative mechanical properties based on Voigt, Reuss, and Hill approximations [96]. The Voigt method predict the upper bounds and Reuss method, the lower bounds of the isotropic elastic modulus. Hill method predicts the average of the two extreme bounds.

1.5.1 Vickers Hardness

The resistance of a material to deformation is a measure of how hard it is. The theoretical description of this important mechanical property of a solid material poses a great challenge because of the inherent mechanical complexities. The fact that the hardness of a material connects both its elastic and plastic properties has made finding a unifying model a daunting task, leading to the loophole in the Teter's empirical correlation model [97]. For a wide variety of crystalline materials as well as bulk metallic glasses (BMGs), which by the way, are intrinsically brittle, the correlation between elasticity and hardness can correctly predict Vickers' hardness H_v; a metric that indicate how hard a material is.

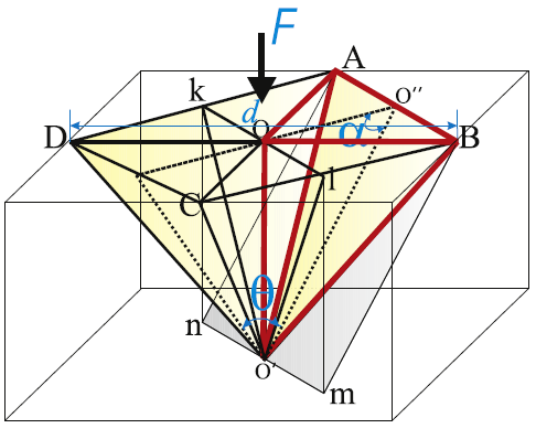

Figure 1.10. Illustration of indentation in terms of the squared diamond pyramid indenter. The red lines highlight one of four triangular based pyramid indenters. Adapted from Ref. [98].

According to Vickers, generally speaking, the hardness of a material is the ratio between the load force applied to an indenter, F, and the indentation surface area on the indenter (see Fig. 1.10). Mathematically,

$$H_v = \frac{2F\sin(\theta/2)}{d^2}\,, \tag{1.77}$$

where d and θ are the mean indentation diagonal and the angle between opposite faces of the diamond squared pyramid indenter, respectively.

For intrinsically brittle materials, the Vickers' hardness linearly correlates with the shear modulus according to $H_v = 0.151G$, proposed by Teter. However, the H_v of polycrystalline and covalent materials, as proposed by Chen *et al.* [98], correlates with the product of the squared Pugh's modulus ratio and the shear modulus G according to

$$H_v = 2(K^2G)^{0.585} - 3\,, \tag{1.78}$$

where $K = {}^{G}/_{B}$ is the Pugh's modulus ratio and B is the bulk modulus of the material. The model in Eq. (1.78), also shown in Fig. 1.10, was derived based on two assumptions: (a) the diamond squared pyramid indenter can be divided into four triangular based pyramid indenters with each indenter having a shear modulus of $G = F/4A\tan(\alpha)$, A being the shear area and (b) the H_v is measured within the elastic scale.

1.6 Description of the Thesis

The aim of this thesis work is to use first principles computational methods to predict phases and properties of selected Earth's interior-, High energy density- and technology-relevant materials. To also, where available, use the theoretical results to understand experimental data on these materials. All the materials that have been discussed in this thesis were subjected to high pressure and high temperature to discover new phases (if any) and the characteristics that such phase(s) exhibit. We have primarily studied crystal structure prediction, structural phase transitions of crystalline materials at some pressures and temperature regime relevant to the Earth's interior and some, at not so high thermodynamic conditions. Subsequent change in thermodynamic, electronic, and mechanical properties of these materials due to applied external stimuli were also

studied. The structural relaxations, molecular dynamics and electronic properties calculations were carried out using the Vienna *ab initio* Simulation Package (VASP) [93] and wien2k [82]. Phonon dispersion calculations were post processed using PHONOPY [99] code. These programs are briefly described below followed by the description of the chapters of this thesis.

1.6.1 VASP

VASP is an acronym for *Vienna Ab-initio Simulation Package*. It is an *ab initio* simulation package suitable for electronic structure calculation. The VASP code self consistently uses an iterative matrix diagonalization scheme to calculate ground state energy from Kohn-Sham equation. The Hatree-Fock approximation, LDA, GGA and hybrid functionals can be implemented with VASP. It employs plane wave basis sets in the determination of various materials properties such as electronic charge density, ground state energy from which other properties such as force, stress tensor, optical properties and magnetic properties can be determined. Iterations in VASP code run over electronic step and ionic step, thereby enabling two tiers of optimization – electronic optimization and ionic optimization. Within VASP, the interactions between electrons and ions are described using a frozen-core electronic method called the projector augmented waves [77] (PAW) method [93].

1.6.2 WIEN2K

The WIEN2k code was originally developed by Peter Blaha and Karlheinz Schwarz. The code performs electronic structure calculations based on the full potential linearized augmented plane-wave (FP-LAPW) [81] method within the density functional theory. The wien2k code is an all-electron scheme. The implementation of LAPW within wien2k captures relativistic effect with the capability to implement LDA, GGA, meta-GGA, LDA+U and hybrid-DFT. When wien2k is interfaced with Phonopy [99] program, it can perform phonon dispersion calculations [82]. The wien2k code is written in FORTRAN90 with capability for fine grain parallelization for multi-core machines or on a cluster of computers. The wien2k is also equipped with web user interface (W2web) which makes material modeling, input generation and adaptation seamless. The self-

consistent field (scf)-cycle in wien2k can be implemented with or without simultaneous optimization of atomic positions.

1.6.3 CALYPSO

CALYPSO (Crystal structure AnaLYsis by Particle Swarm Optimization) [100,101] is a global optimization code interfaced with VASP (or other compatible *ab initio* codes) to achieve best possible performance. The CALYPSO simulation algorithm scans the potential energy surface of a given chemical specie(s) for both local and global minimum potential energy using the particle swarm-intelligence algorithm (PSO). Finite pressure search can also be achieved in CALYPSO through unit cell volume scaling or direct application of Pulay stress. The CALYPSO code through the PSO algorithm makes few or no initial assumptions about the solutions of the given potential function. Furthermore, it can search very large space for candidate solutions by moving them in the search space over the particles' positions and velocities with fast convergence and without being trapped in a local potential energy minimum. In addition to symmetry constraints and bond characterization matrix implemented in the code, it also intermittently introduces random structures per generation as the search evolves. The CALYPSO can reduce the number of local optimizations and speed up the global minimization convergence by eliminating similar structures and reduces the search space by using symmetry. The simulation is halted when the stopping criterion is reached [55].

1.6.4 PHONOPY

PHONOPY [99,102] is an open-source software for post-processing gamma-point phonon calculation from *ab initio* programs into a full phonon dispersion across the BZ. PHONOPY perform its calculation in a supercell and was developed by Atsushi Togo. The accuracy of the phonon dispersion increases with increasing supercell size. The PHONOPY code can be interfaced with *ab initio* programs such as VASP and Wien2k for force calculations, which serves as input to PHONOPY. Both harmonic and quasi-harmonic approximations can be implemented within PHONOPY. Forces on atoms are used for the construction of interatomic force constant (IFC) using displacement method or force constant (FC) using density functional perturbation theory

(DFPT). Phonon frequencies are then calculated from either IFC or FC through the construction of dynamical matrix whose eigenvalues correspond to the phonon frequencies at a given phonon wave vector $\boldsymbol{q}$. The construction and symmetrization of IFCs and FCs are implemented using singular-value decomposition. In VASP, the calculation of the gamma-point phonon frequencies for the supercell is first carried out using finite difference method (when displacement method is implemented in PHONOPY) or the DFPT method (when DFPT is implemented in PHONOPY). The full phonon dispersion is then calculated by interpolating the gamma-point phonon frequencies through the various high-symmetry *k*-points in the BZ [55, 99].

1.6.5 Description of study

Chapter 2 of this thesis presents the results of structural phase transition in two elements: carbon (C) and nitrogen (N). The first part presents the results of structural phase transition in a two-dimensional polymeric C_{60} after being subjected to uniaxial compression at high temperature in a metadynamics simulation. The new structure is made up of 240 carbon atoms in an orthorhombic unit cell, termed as *o*-C_{240} with mixed sp^2/sp^3 hybridization. *o*-C_{240} is stable at ambient condition and exhibits superior mechanical performance including optimum Vickers hardness and fracture toughness, that outperform most of widely used hard ceramics. The second part presents theoretical results on identification, and characterization of single bonded nitrogen in crystal structure isostructural to black phosphorus (BP-N) at 146 GPa and 2200 K. The crystal structure exhibits a unique puckered two-dimensional layer with exciting physical and chemical phenomena including prospect for high energy density (HED) applications. First-principles methods were employed in the theoretical characterization of the new allotrope.

Chapter 3 presents the results of an extensive theoretical studies of transition metal (TM) - TM alloys/compounds. The first part of the chapter investigates structural phase transition leading to shape memory loss in the shape memory alloy, NiTi. The second part investigates the formation of Au-Fe compounds at high pressure. A detailed analysis of the transition kinetics and dynamical pathway in NiTi using the metadynamics method reveals the possibility of the B19′ phase of NiTi losing its shape memory when subjected to high stress conditions and heated above a critical temperature (T_c) of 700 K. Furthermore, using the particle swarm-intelligence optimization

algorithm interfaced with first principles methods, we predicted the formation of bulk intermetallic compounds of two bulk-immiscible components, Fe and Au. We found that the systems are stabilized by pressure and notable electron transfer. Electronic properties, mechanical properties, and transition pathways were also investigated and reported.

Chapter 4 presents the results of theoretical identification and studies of the formation of noble gas element-transition metal compound. In this chapter, we report the identification and theoretical characterization of a thermodynamically stable compound of Argon (Ar) and nickel (Ni) under thermodynamic conditions representative of the Earth's core, using density functional calculations. This study presents evidence of the reactability of Ar with one of the core's main constituents, Ni. The compound of Ar and Ni was identified as ArNi with a $L1_1$ Laves structure with space group *R-3m*. It was found that the *R-3m*-ArNi compound is stabilized by notable electron transfer from Ni to Ar. Electronic and lattice dynamical properties were also predicted.

Chapter 5 presents the result of an extensive theoretical studies of the formation of alkali metal-transition metal intermetallic compounds at high pressure and temperature relevant to the upper mantle and the core of the Earth. These studies were carried out using particle swarm-intelligence optimization and genetic algorithms interfaced with first principles methods. We exemplified this reaction using potassium (part of which are missing in the mantle) and the Earth's core's main constituents: Fe and Ni. The first part investigates the formation of K-Fe compounds at thermodynamics conditions relevant to the Earth's interior while the second part investigates the formation of K-Ni compounds in the Earth's interior. It was found that K and Fe can form intermetallic compounds that are stabilized by high pressure and energy reordering of atomic orbital. Phase transitions were also reported and the instabilities that induce them were also investigated. Furthermore, the study on K-Ni systems identify the crystal structure of the long-sought structure of the only experimentally known K-Ni compound. Although both constituent elements are metallic, the identified polymorph of K_2Ni exhibits a semiconducting ground state with an indirect bandgap. The mechanism of its stability was also identified. The results of both studies indicate that the chemical properties of elements can change dramatically under extreme conditions and have significant implications for the postulation that potassium is incorporated in Earth's core. Dynamic stability, mechanical stability, thermal stability, and electronic properties were also investigated.

Chapter 6 is an overall summary of the work I carried out for my doctoral studies. It also highlights areas of the work that may be exciting for future explorations.

All the works presented in this thesis have now been published in peer-reviewed journals or being drafted for publication. I only present my contributions in this thesis. The references are as follows:

1. **Adeleke, A. A.**, and Yao, Y. High-temperature shape memory loss in nitinol: a first principles study. *Phys. Chem. Chem. Phys.*, *21*, **2019** 7508-7517.
2. **Adeleke A. A.**, Kunz M., Greenberg E., Prakapenka V. B., Yao Y. and Stavrou E., High-pressure compound of argon and nickel: noble gas in the Earth's core? *ACS Earth Space Chem.,* 3, **2019** 2517-2524.
3. **Adeleke A. A.**, Adeniyi O. A., Tang H., Gou H., and Yao Y., *o*-C_{240}: A new sp^3-dominated allotrope of Carbon, *J. Phys.: Condens. Matter*. 32, **2020** 395401.
4. **Adeleke A. A.** and Yao Y. Formation of Stable Compounds of Potassium and Iron under Pressure. *J. Phys. Chem. A 124*, **2020** 4752-4763.
5. Ji, C.[*], **Adeleke, A. A.**[*], Yang, L.[*], Wan, B., Gou, H., Yao, Y., Li, B., Meng, Y., Smith, J. S., Prakapenka, V. B. *et. al*. Nitrogen in black phosphorus structure. *Sci. Adv., 6*, **2020** eaba9206. (* authors contributed equally).
6. **Adeleke A. A.**, Stavrou E., Adeniyi O. A., Wan B., Gou H., and Yao Y. Two good metals make a semiconductor: A potassium-nickel compound under pressure. *Phys. Rev. B. 102* **2020** 134120.
7. **Adeleke A. A.**, Bonev S. A., Wu C. J., Jossou E. E. and Yao Y., Aurum reservoir deep down: stable compounds of two bulk-immiscible metals under pressure (in preparation).

Couple more other studies have been performed and published. These studies, although have not been added as chapters in this thesis for reason of continuity, their references are listed below for completeness and to give an essence to readers about the scope of my PhD research.

1. Weber C. P., Masten M. G., Ogloza T. C., Berggren B. S., Man M. K. L., Dani K. M., Liu J., Mao Z., Klug D. D., **Adeleke A. A.**, and Yao Y., Using coherent phonons for ultrafast control of the Dirac node of $SrMnSb_2$, *Phys. Rev. B*, 98 **2018** 155115.

2. Zhang J., Wang X., **Adeleke A. A.**, Gao B., Wang H., Wu M., Liu H., and Yao Y., Oxysulfide Li_2BeSO: a potential new material for solid electrolyte predicted from first principles, *J. Alloy Compd.* 818, **2020** 152844.
3. Tong Q., Luo X., **Adeleke A. A.**, Xie Y., Liu H., Wang Y., Lv J., Yao Y. and Ma Y., Machine learning metadynamics simulation of reconstructive phase transition, *Phys. Rev. B*, 103 **2021** 054107.
4. Magad-Weiss L. K., **Adeleke A. A.**, Greenberg E., Prakapenka V. B., Yao, and Stavrou E., High-pressure structural study of α-Mn: Experiments and Calculations, *Phys. Rev. B*, 103 **2021** 014101.
5. Adeniyi A. O., **Adeleke A. A.**, Li X., Liu H., and Yao Y., Stable Helium-Hydrogen Compound (under review in Phys. Rev. B, revision submitted).

CHAPTER 2

STRUCTURAL CHANGES IN ELEMENTAL SOLIDS: A CASE STUDY OF CARBON AND NITROGEN

A similar version of this chapter has been published as a research article in the Journal of Physics: Condensed matter and the Science Advances. The references are as follows.

1. Adeleke A. A., Adeniyi O. A., Tang H., Gou H., and Yao Y., *o*-C_{240}: A new sp^3-dominated allotrope of Carbon, *J. Phys.: Condens. Matter*. 32, **2020** 395401.
2. Ji C.*, Adeleke, A. A.*, Yang L.*, Wan B., Gou H., Yao Y., Li B., Meng Y., Smith J. S., Prakapenka V. B. *et. al*. Nitrogen in black phosphorus structure. *Sci. Adv., 6,* **2020** eaba9206. (* authors contributed equally)

2.1 *o*-C_{240}: A New sp^3-dominated allotrope of carbon

We report a new, stable crystalline allotrope of carbon (that we named *o*-C_{240}) made up of 240 carbon atoms in an orthorhombic unit cell with sp^3 dominated framework from first principles calculations. The *o*-C_{240} is formed by subjecting two-dimensional polymeric C_{60} to isotropic then directional (uniaxial) pressure at 1500 K temperature. Detailed theoretical analyses reveal that the new phase is less dense compared to diamond and is semi conducting with indirect band gap of 1.72 eV. With a Vickers hardness of 44.75 GPa and fracture toughness of 4.10 MPa $m^{1/3}$, we are proposing *o*-C_{240} as a superhard material that could outperform many widely used hard ceramics. The *o*-C_{240} could also find applications in adsorption, photocatalysis, hydrogen storage and high frequency electronic devices.

2.1.1 Introduction

Over time, carbon has been found in various forms such as graphite, lonsdaleite, cubic diamond (*c*-diamond), fullerenes and amorphous carbon because of its ability to form sp^2- and sp^3-hybridized bonds. The sp^2-, sp^3- or blend of the two hybridizations give carbon a wide range of structural, electronic, and mechanical properties. Based on these interesting properties, search for new allotropes of carbon has remain at the fore-front of present-day research [35-38]. At room temperature, the *c*-diamond is the hardest known naturally occurring solid. The free energies of graphite are comparable with that of *c*-diamond, however, forming the later from the former requires a pressure significantly higher than those at which both of them coexists because of the large distortions that is associated with the formation of diamond nuclei which is not permitted at low pressures [103,104]. Furthermore, graphite has very strong sp^2 bonds making it extremely stable and more compressible than *c*-diamond at ambient conditions. Theoretical calculations suggests that phase transitions from graphite to *c*-diamond at high pressures require bonding change from sp^2 to sp^3 which starts to form between adjacent layers of graphite after fractional reduction in its interlayer distance. It is worthy of note that the interlayer distance in graphite promotes weak interactions between the layers: property that is exploited in its exfoliation into graphene. Three-dimensional network with high stiffness and insulating properties are consequence of sp^3 hybridization framework as commonly observed in lonsdaleite and *c*-diamond [105]. A (10,10) carbon nanotube (CNT) lattice was theoretically compressed to 20 GPa and was shown, through tight-binding molecular dynamics, to produce new distinct phase made up of only C4 square rings and has only sp^3 carbons [106]. Although, very intriguing, however, it is still at the level of theory because up to now, crystalline solid CNTs with uniform chirality (that are experimental precursor) are yet to make their real-world appearance. Besides ultrasoft compressibility, the sp^2 hybridization is responsible for narrow band gap up to completely closed gap (metallicity) as observed in graphite and graphene [107].

Intermediate hybridization open door for the design of materials with novel electronic and structural properties such as optimum combination of weight, strength, hardness, elasticity, and tunable electronic properties that make them candidate for direct applications in device fabrication. There has been series of work by various experimental groups to synthesize mixed sp^2/sp^3 forms of carbon using controlled compression of pure sp^2 carbons. For example, intermediate hybridizations have been reported in fullerenes [108], CNTs [109] and amorphous carbon [110].

Speaking of fullerenes, experiment combined with theory has realized the polymerized forms of solid C_{60} under pressure, reported to contain large numbers of both sp^2 and sp^3 carbons [111]. Collapsed fullerene has also being studied [112] and was found to yield a fine blend of sp^2-hybridized graphite-like and sp^3-hybridized diamond-like amorphous carbon with low compressive strength. The new property is due to restructuring heterogeneity developed when sp^2 carbons mix with sp^3 carbons as pressure is being quenched. Despite the low compressive strength which becloud their wide applicability in devices, such collapsed phase still exhibits high hardness and remarkable elastic strength. While at that, exploration was not limited to carbon-only, 3-dimentional sp^2/sp^3 materials. In fact, carbon-based clathrates composed of host cages and trapped guest atoms have also been extensively explored. Although, they showed prospect in that they could exhibit strength while being light-weighted and could also offer tunable mechanical and electronic properties by carefully choosing the guest atoms within the cage, but they could be quite challenging to synthesize. There are theoretical evidence suggesting that carbon-clathrate synthesis may need to proceed through a non-equilibrium pathway (which is only feasible in principle) because they are energetically unfavorable; a reason for its challenging synthesis [113].

Experimental discovery of metastable carbon with mixed sp^2/sp^3 is very time-consuming, expensive, and challenging, requiring specific (sometime high) pressure-temperature (*P*-*T*) conditions. Therefore, theoretical search for such allotropes of carbon could benefit immensely in the recent development of *ab initio* methods [114,115] and rise in computer power. Computer experiments at extreme thermodynamic conditions are cheaper than laboratory experiments, making it an alternative as against series of trial-and-error explorations in the laboratory. Once the new allotrope has been found computationally, follow-up experiments can be done at the computed *P*-*T* condition.

Here, we report a new superhard orthorhombic, mixed sp^2/sp^3 carbon allotrope that is semi conducting and light weighted, formed by subjecting two-dimensional polymeric C_{60} to isotropic then directional (uniaxial) pressure at 1500 K temperature. The new allotrope is composed of about 83.33% sp^3 hybridized carbon, making it a sp^3-dominated allotrope. The structural, dynamic, electronic, and elastic properties of the newly predicted phase were also studied. The newly predicted allotrope of carbon could find applications in adsorption, photocatalysis, hydrogen storage and high frequency electronic devices.

2.1.2 Computational Method

All calculations were performed using the Vienna Ab-initio Simulation Package (VASP) [93] with a cut-off energy of 500 eV and a projector augmented wave (PAW) potential [116], with the Perdew-Burke-Ernzerhof (PBE) functional [61]. The self-consistent field (SCF) and electronic structure calculations were performed using a dense *k*-point grid with a spacing of $2\pi \times 0.02$ Å^{-1}. The electron localization function (ELF) [117] and charge density were calculated with an 80 × 80 × 80 FFT grid. The dynamic stability calculation was carried out within the density functional perturbation theory (DFPT) [118] as implemented within the VASP with a *q*-point mesh of size 3×3×3. The conversion of polymeric C_{60} under high temperature and high-pressure conditions was simulated using the density functional-based metadynamics method [92]. Each metastep consists of a first-principles molecular dynamics simulation in a canonical (NVT) ensemble for a simulation time of 0.8 ps. The history-dependent potential well was constructed in the simulations using Gaussians with a width δs = 15 (kbar ·A^3)$^{1/2}$ and height W = 225 kbar ·A^3. To accelerate the conversion, the system was pressurized non-hydrostatically, with additional 10% anisotropic stress loaded on the *c*-axis. A recent modification of the metadynamics method [119] was used to load the uniaxial stresses to the simulation cell. The molecular dynamics components were carried out using a dense *k*-point grid with a spacing of $2\pi \times 0.08$ Å^{-1}.

2.1.3 Results and Discussion

2.1.3. 1. Transition pathway

Polymerization is a chemical reaction where monomer molecules react together to form polymer chains or three-dimensional (3D) networks. High pressure and high temperature (HPHT) could be used to speed up such reactions. For example, C_{60} molecules polymerize faster under HPHT through [2+2] cycloaddition of adjacent molecules [120]. Orthorhombic two-dimensional (*o*-2D), and rhombohedral two-dimensional (R-2D) C_{60} polymers have been reported to form below and above 3GPa, respectively [121]. The *o*-2D belong to the space group *Immm*. Interestingly, the dimensionality was also found to increase under pressure. A three-dimensional orthorhombic and rhombohedra (3D) C_{60} polymer was synthesized from their respective 2D C_{60}

polymer precursor through a topotactic conversion at 15 GPa and 600^{o}C [122]. The topotactic conversion ensures that orientation of (3D) C_{60} polymer is determined by the orientation of the precursor 2D C_{60} polymer. The orthorhombic 3D C_{60} polymer is made up of deformed units in the form of rectangular parallelopiped; where each parallelopiped, through [3+3] cycloaddition, is linked to 8 neighboring parallelopiped in a body centered arrangement. At high pressure and temperature, one would expect a different phase than the 3D C_{60} that were synthesized. Therefore, computational simulation was performed at a higher temperature and pressure that the one used for the experimental conversion.

Metadynamics is a computational method that can reconstruct low-energy pathway of a phase transition at a given *P*-*T* condition. Since we expect the higher pressure phase, just like the *o*-3D C_{60}) to be related to the precursor *o*-2D C_{60}. The metadynamics simulation is expected to reveal stable and metastable phase(s) as the o-2D C_{60} polymer is compressed and heated beyond the stability field of the synthesized *o*-3D C_{60} phase.

In the present study, the *o*-2D C_{60} was compressed to 40 GPa and 1500 K using metadynamics simulation (see Fig. 2.1a). Additional 10% uniaxial stress was loaded along the z-direction to reduce the space between the planes of adjacent *o*-2D C_{60} molecule. The uniaxial compression improves the rate of conversion [119]. More details on the thermal conversion pathway of the precursor, *o*-2D C_{60}, can be found in ref. [41]. Readers can find further and general discussions on polymerization of C_{60} molecules in ref. [41,120-122].

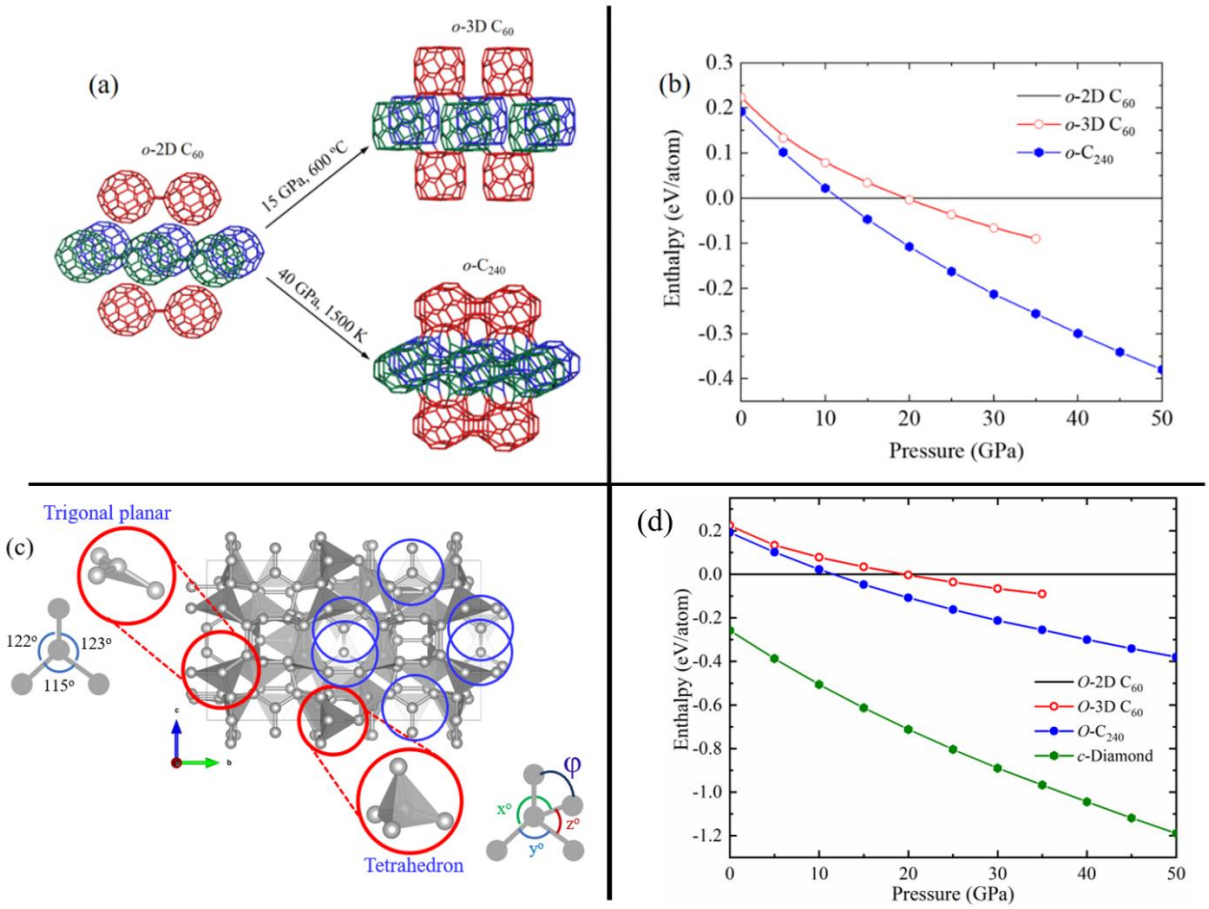

Figure 2.1. (a) Thermal conversion pathways for precursor o-2D C60 to o-3D C60 [122] and to *o*-C_{240}. C60 units are colored to highlights the stacking patterns. Figure is adapted from Ref. [41]. (b) Enthalpy evolution under pressure for *o*-C_{240}, *o*-3D C_{60} and *o*-2D C_{60}. The enthalpy of the precursor *o*-2D C_{60} is used as the reference enthalpy. (c) crystal structure of *o*-C_{240}, revealing how various carbon rings are connected in a tetrahedral and trigonal planar network. The blue circles are to guide the eye through the distribution of trigonal planar geometry in the structure. (d) Enthalpy evolution under pressure for *o*-C_{240}, *o*-3D C_{60}, *o*-2D C_{60} and *c*-Diamond. The enthalpy of the precursor *o*-2D C_{60} is used as the reference enthalpy.

2.1.3.2. Crystal Structure and dynamical stability of the *o*-C_{240} structure

The *o*-C_{240} structure crystallizes into an orthorhombic cell with space group *Pmmm* (see Fig 2.2a-b). The optimized structural parameters at 0 GPa are as shown in Table 2.1. The *o*-C_{240} structure contain 240 carbon atoms connected in a 3D framework. The *o*-C_{240} has a density of 2.86

g/cm^3 (lower than diamond with density 3.55 g/cm^3 but higher than the density of *o*-3D C_{60}: 2.55 g/cm^3 [122]). The *o*-C_{240} structure features five types of carbon rings: C3, C4, C5, C6 and C8 (Fig. 2.2c) fused together in a distorted tetrahedral and trigonal planar sp^2/sp^3 geometric network (see Fig. 2.1c). Specifically, the C4 and C8 are connected through a distorted tetrahedral network in which x^o, y^o and z^o ranges between 113^o and 123^o and φ ranges between 107^o and 110^o (see Fig. 2.1c). The C3, C5 and C6 rings are connected through a mixture of distorted tetrahedral and trigonal planar network. An undistorted trigonal planar geometry has angle of 120^o while undistorted tetrahedra has an angle of 109.5^o. The *o*-C_{240} structure has a distribution of single bonds (bond between two sp^3 carbon atoms) with bond length ranging between 1.55 Å and 1.66 Å, double bonds (bond between two sp^2 carbon atoms) with bond lengths ranging between 1.31 Å and 1.35 Å and mixed bonds (bond between one sp^3 and one sp^2 carbon atom) with bond lengths between 1.41 Å and 1.51 Å. The sp^3 and sp^2 bond lengths in diamond and graphite are typically 1.54 Å and 1.42 Å, respectively. In the *o*-C_{240} structure, 16.67% of the total carbon atoms are sp^2 hybridized while 83.33% are sp^3 hybridized giving rise to a mixed sp^2/sp^3 material. Therefore, the formation of this structure is considered a consequence of the competition between sp^2 and sp^3 bonding and as such, an intermediate phase between graphite and *c*-diamond. The domination of sp^3 hybridization therefore improves the bonding and bonding-dependent properties of the *o*-C_{240} structure (towards diamond), making it superior compared to graphite.

The enthalpies of the o-2D C_{60}, o-3D C_{60} and the *o*-C_{240} are computed and are compared relative to the low-pressure o-2D C_{60} phase in Fig. 2.1b. For perspective, the equation of state of *c*-diamond was also compared (see Fig. 2.1d). The result of the calculation reveals that the o-2D C_{60} is the lowest enthalpy phase from ambient pressure up to 11.5 GPa before transforming to the *o*-C_{240}. It was observed that above 20 GPa, the o-3D C_{60} is more stable than the precursor (o-2D C_{60}) but still less stable than the *o*-C_{240} up to at least 50 GPa considered in this study. We therefore conclude that the *o*-C_{240} is the energetically favorable high-pressure phase of the o-2D C_{60} and could guide future experiment. However, throughout the pressure range considered in this study (0 – 50 GPa), the *c*-diamond allotrope of carbon is the thermodynamic ground state relative to the o-2D C_{60}, o-3D C_{60} and the *o*-C_{240} phases.

SG	*a* (Å)	*b* (Å)	*c* (Å)	Site	Fractional atomic coordinates		
					x	*y*	*z*
Pmmm	13.25	14.74	8.581	8*a*	0.184	0.805	0.337
				8*a*	0.183	0.306	0.336
				8*a*	0.090	0.854	0.406
				8*a*	0.090	0.355	0.406
				8*a*	0.061	0.943	0.299
				8*a*	0.062	0.444	0.301
				8*a*	0.173	0.829	0.166
				8*a*	0.170	0.330	0.164
				8*a*	0.280	0.840	0.411
				8*a*	0.278	0.340	0.410
				8*a*	0.109	0.912	0.144
				8*a*	0.110	0.416	0.145
				8*a*	0.684	0.055	0.835
				8*a*	0.683	0.555	0.836
				8*a*	0.590	0.104	0.906
				8*a*	0.590	0.604	0.906
				8*a*	0.562	0.194	0.802
				8*a*	0.562	0.694	0.802
				8*a*	0.669	0.080	0.664
				8*a*	0.668	0.580	0.664
				8*a*	0.779	0.090	0.910
				8*a*	0.778	0.590	0.910
				8*a*	0.610	0.166	0.645
				8*a*	0.610	0.666	0.646
				8*a*	0.157	0.750	0.077
				4*w*	0.654	0.000	0.576
				4*x*	0.652	0.500	0.576
				4*u*	0.000	0.795	0.634
				4*u*	0.000	0.296	0.633
				4*v*	0.500	0.046	0.133
				4*v*	0.500	0.546	0.133
				4*y*	0.050	0.911	0.000
				4*y*	0.057	0.445	0.000
				4*z*	0.557	0.195	0.500
				4*z*	0.557	0.695	0.500

Table 2.1: Optimized Structural parameters of *o*-C_{240} phase at 0 GPa.

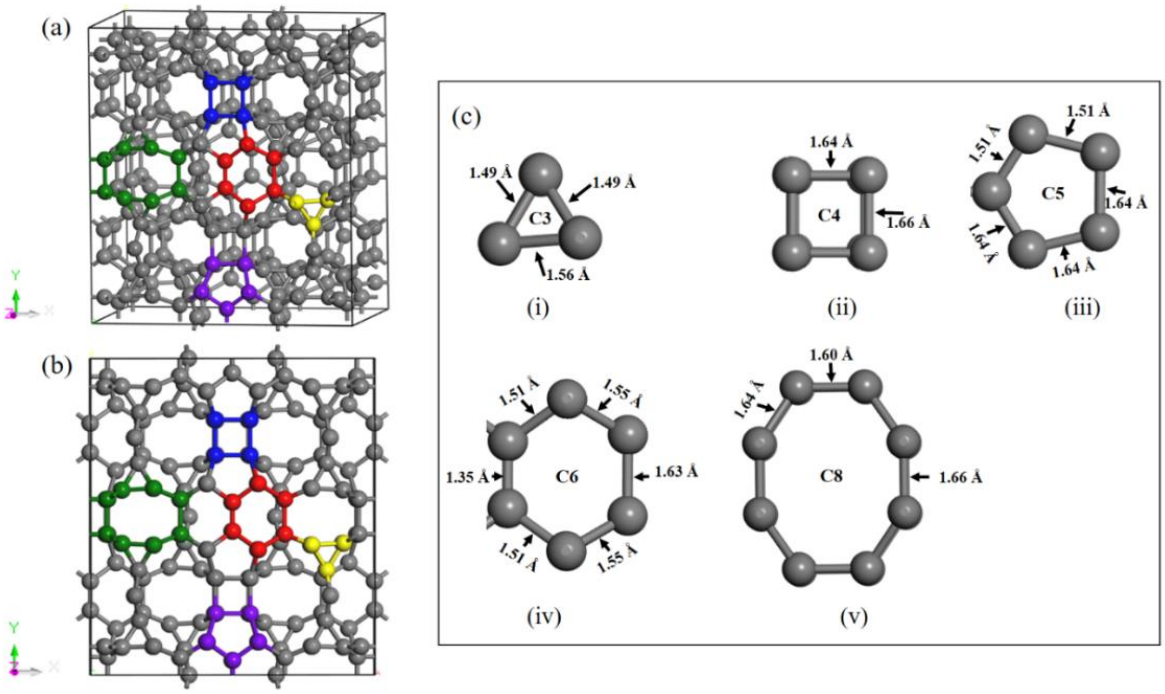

Figure 2.2. (a) Three-dimensional and (b) two-dimensional views of the crystal structure of the *o*-C_{240} phase at ambient conditions. Structure is shown in one unit cell. Colors are used to highlight various carbon rings in the structure. (c) Dimensions of unique carbon rings featured in the *o*-C_{240} structure.

The dynamic stability of the *o*-C_{240} structure was investigated at 0 GPa through phonon calculation. The absence of imaginary frequencies throughout the entire Brillouin zone (BZ) as shown in Fig. 2.3 indicate that the *o*-C_{240} structure is dynamically stable and quench recoverable in an event of HPHT synthesis. Beyond information about the dynamic stability of the *o*-C_{240} structure, the phonon band structure exhibits band gaps (in the optical phonon branch) in the range between 40 THz and 56 THz. Analysis of the gamma point phonon reveals that bands in this region are triply degenerate. As such, these modes could be a signature for the *o*-C_{240} structure and could be used in its identification during synthesis through Raman or Infrared spectroscopy. The modes vibrating at 40 THz (1334 cm^{-1}) and 42 THz (1401 cm^{-1}) are in the range of the signature frequency of sp^3 bonded carbon otherwise known as the diamond peak [123] that made up about 83.33% of the *o*-C_{240} structure at ambient conditions. The modes above 42 THz (1401 cm^{-1}), therefore, could be the signature modes of the *o*-C_{240} structure.

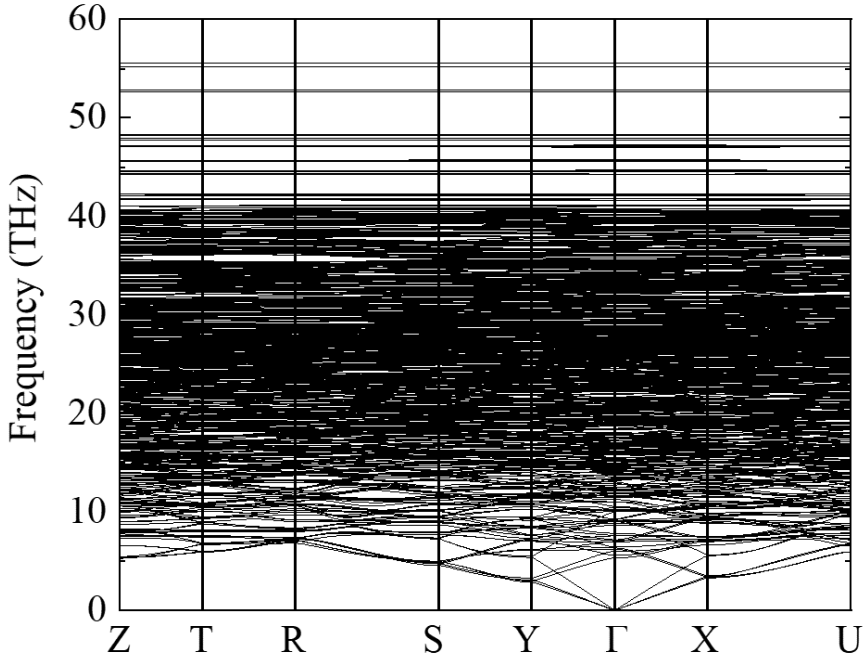

Figure 2.3. Calculated phonon dispersion relations of the *o*-C_{240} structure at 0 GPa. Figure is adapted from Ref. [41].

2.1.3.3 Electronic properties of the o-C_{240} structure

The calculated electronic band structure at 0 GPa shows that *o*-C_{240} is semi conducting in nature (Fig. 2.4a) with an indirect band gap of 1.72 eV. The band gap of *o*-C_{240} is small compared to other semi conducting, high pressure allotropes of carbon such as S-carbon, F-carbon [124], Protomene [125], H-carbon [126], D-carbon [127] and *o*C20 [128] previously predicted. The calculated bands are quite flat, which can be interpreted as a strong localization around the sp^2 rings. The projected electronic density of states reveals that, in the *o*-C_{240} structure, the C *p*-states predominantly lies at the valence band maximum (VBM) and the conduction band minimum (CBM). This suggests that when the *o*-C_{240} is excited into a conduction state, conduction electrons may be coming from the C *p*-state. The nature of bonding in each of the rings that made up the *o*-C_{240} structure was analyzed using the electron localization function (ELF). The ELF can help identify places in a structure where localization of electron (corresponding to covalent bonds or lone pairs) is located.

The C3 ring is made up of two distinct C-C bond lengths: 1.49 Å (mixed bonds) and 1.56 Å (single bond). The C3 ring features two sides of equal bond lengths, 1.49 Å and the third side is a single bond. It has a trigonal planar (sp^2) molecular geometry (like cyclopropane, C_3H_3) with an angle strain that causes an orbital overlap resulting in a σ-π-hybrid (that is neither end-to-end nor side long, often referred to as banana bond) between carbon atoms. Bonds in the C3 ring are localized but with predominantly π-bond character. The C3 rings connects two C5 rings, two C6 rings or a C5 to a C6 ring which further explains why it exhibit σ-π-hybrid.

The C6 ring (with geometry like benzene) is made up of four distinct C-C bond lengths: 1.35 Å, 1.51 Å, 1.55 Å and 1.63 Å resulting in 3 single bonds, 1 double bond and 2 mixed bonds. The C6 ring also shows interesting electron localization in that it exhibits lone pairs (lobes outside the carbon atoms) as shown in Fig. 2.4d. The lone pair plays an important role in balancing the electrostatic interactions within the C6 ring by reducing its potential energy while causing the C6 plane to be puckered. This configuration in turn contribute to the general stability of the *o*-C_{240} structure. In particular, the lone pairs are aligned on the short side (bond length of 1.35 Å) shared between two C6 rings which provides a screening of the carbon cores within the ring.

The rest of the rings (C4, C5 and C8) exhibits unpolarized σ-bonds with electrons highly localized mid-way between each C-C bond in a distorted tetrahedral sp^3 framework. The C4 ring is such that connects two C6 rings throughout the *o*-C_{240} structure. The C4 and C8 rings are both made of single bonds, consistent with their tetrahedral geometry. Overall, the charge density (Fig. 2.4c) and electron localization analyses (Fig 2.4d) reveals localization of electron density in favor of inter tetrahedron bonds thereby making them relatively strong, with shorter bond length, compared to the intra tetrahedron bonds with longer bond lengths. The framework thus balances the strain of the carbon tetrahedron assisting the *o*-C_{240} structure achieve stability. In graphite, metallicity is attributed to interlayer interactions with delocalized π-electrons and the dominance of sp^2 bonding. However, in the *o*-C_{240}, we have observed dominance of sp^3 bonding which means that majority of the delocalized π- electrons become localized and are converted to σ-bonds, inducing opening of an electronic band gap, making the *o*-C_{240} structure attain a semi conducting state. The band gap in the *o*-C_{240} structure (1.72 eV) is larger than was reported for graphite (40 meV) [129], due to the mixing of the sp^2/sp^3 bonding that the former exhibits. Thus, its halfway between narrow-gap-semiconducting and insulating state (strictly judging by the size of the band

gap) but could, in principle, be doped or biased towards an extrinsic semiconductor or metallic state when applied in the fabrication of devices.

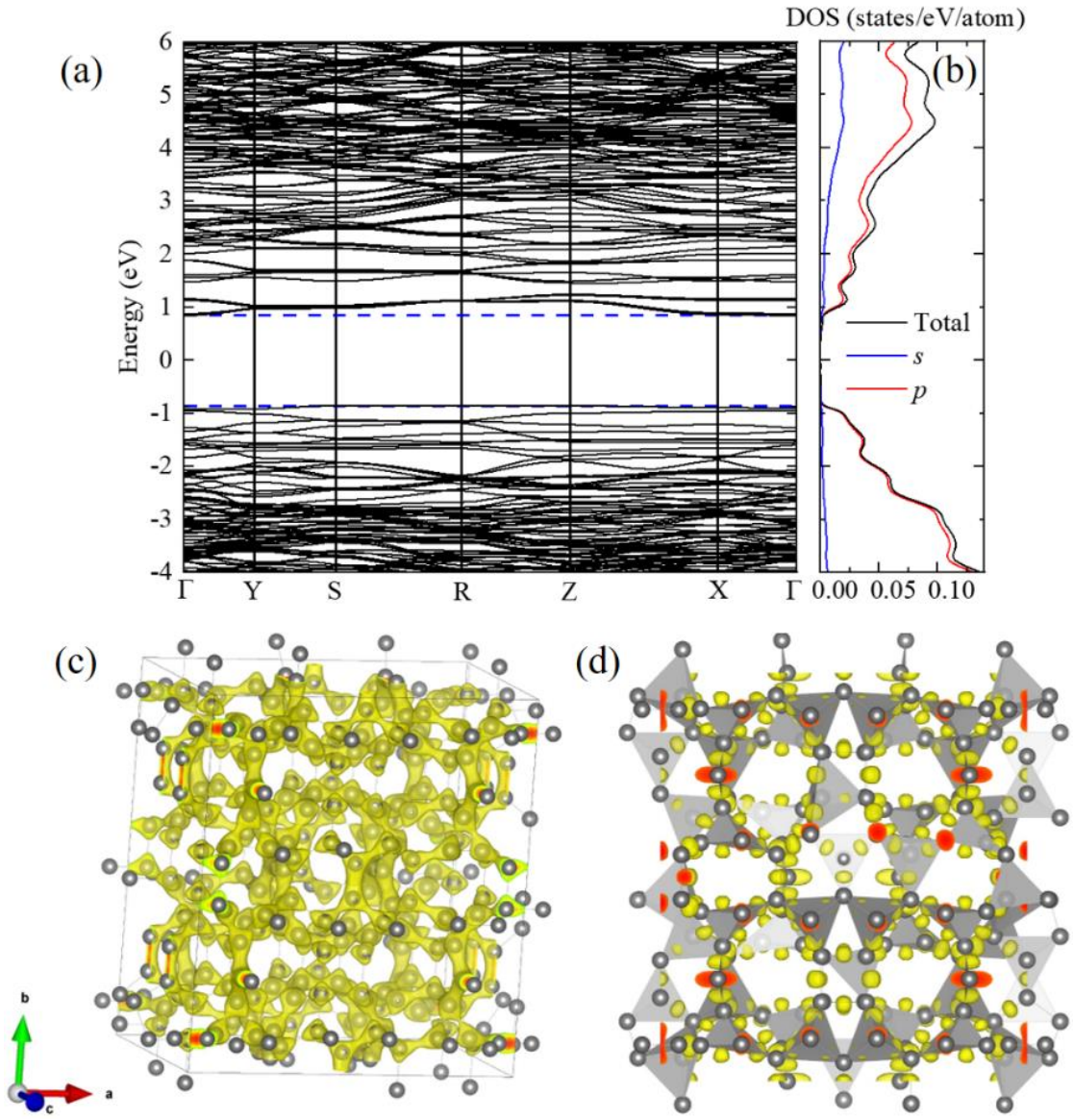

Figure 2.4. (a) Electronic band structure of *o*-C_{240}. (b) Total and electronic density of states projected to atomic orbitals for the *o*-C_{240}. (c) Charge density distribution for *o*-C_{240}. (d) Electron localization function (ELF) for *o*-C_{240}. The ELF isosurface is drawn with an isovalue of 0.85 to reveal all bonding and lone pairs.

2.1.3.4 Elastic properties and Hardness of o-C_{240}

In this section, we evaluate the mechanical properties of *o*-C_{240} with the aim of assessing its performance relative to other superhard materials and hard ceramics [130-136]. Mechanical and elastic stability of a material is assessed through its elastic constants. The *o*-C_{240} belong to the orthorhombic crystal class and as such requires nine independent elastic constants [95] (in the unit of GPa) summarized and compared with those from other superhard materials in Table 2.2 below. The results are found to satisfy the mechanical stability criteria for an orthorhombic crystal class. Furthermore, the C_{ij} matrix for the *o*-C_{240} is symmetric and has all-positive eigenvalues: necessary and sufficient conditions for elastic stability.

The bulk (*B*), shear (*G*) and young modulus (*E*) are measure of a material's intrinsic response to deformation of various kinds. Specifically, *B* is a measure of materials volumetric elasticity and its response to isotropic compression, *G* represents a material's tendency to shear under the influence of an opposing force while *E* is a measure of the stiffness of a material in the linear elasticity regime of a uniaxial deformation. The Poisson ratio (*v*), on the other hand, is a measure of the expansion of a material in directions perpendicular to the direction of compression. All these properties are indicator of how difficult (or easy) it is to compress a material [94,95]. The *B* and *G* were calculated for the *o*-C_{240} structure. The results compared with *c*-diamond and C_{64} and B_6O (shown in Table 2.3) indicate that the *o*-C_{240} structure is more compressible than *c*-diamond but less compressible than C_{64} and B_6O. We calculated *E* and *v* within the Voigt-Reuss-Hill (VRH) approximation [96], using the relation $E = [9BG/(3B+G)]$ and $v = [(3B-2G)/2(3B+G)]$. Since 'The larger, the stiffer' motif holds true for the calculated *E*, then, *o*-C_{240} structure is stiffer than C_{64} and B_6O but less stiff compared to *c*-diamond. The calculated *v* shown in Table 2.3 reveals that while the *c*-diamond is more covalent than the *o*-C_{240}, the *o*-C_{240} structure is more covalent than the C_{64} and B_6O.

	C_{11}	C_{22}	C_{33}	C_{44}	C_{55}	C_{66}	C_{12}	C_{13}	C_{23}
***o*-C_{240}**	728	787	817	258	249	227	103	67	74
***c*-diamond**[a]	1076			577			125		
C_{64}[b]	598		677	254		107	43	108	
***o*C20**[c]	794	760	979	405	251	261	112	61	75

Table 2.2: Calculated elastic constants C_{ij} (in GPa) for the *o*-C_{240} compared with other carbon allotropes. a is taken from Ref [135], b is taken from Ref [132], c is taken from Ref [136].

Properties	**Material**			
	***c*-diamond**	***o*-C_{240}**	**C_{64}**	**B_6O**
B (GPa)	457 (443[a])	313	264[c]	222[d]
G (GPa)	536 (535[a])	281	217[c]	204[d]
E (GPa)	1156 (1144[a'])	649	510[c]	468[d']
Poisson ratio (v)	0.079 (0.069[a'])	0.154	0.18[c]	0.15[d']
H_v (GPa)	92 (92[b])	45	34[c']	38[d'] 45[e]

Table 2.3: Calculated mechanical properties of *o*-C_{240} compared with *c*-diamond and other superhard materials. Numbers without superscripts are present results. Numbers with superscripts are previously reported in literature. Numbers with primed superscripts are estimations using VRH model using data reported in literature. a is taken from Ref [130], b is taken from Ref [131], c is taken from Ref [132], d is taken from Ref [133], e is taken from Ref [134].

Hardness is the extent to which a solid resist both elastic and plastic deformations. Vickers and Knoop [137] hardness metrics are often used to quantify the hardness of solids. Vickers hardness (H_v) is developed on the premise that the hardness of a crystal is proportional to the bond strengths and to the number of bonds in a unit cell volume of the crystal. Therefore, a hard material will have H_v value up to 40 GPa and superhard materials will have H_v value greater than 40 GPa. Another point to note about hardness is that it depends strongly on the creation and motion of dislocations which is an effect of plastic deformation. Using the Chen *et al*. empirical model for covalent solids [138], we reproduced the H_v of *c*-diamond, thereby validating the suitability of the model in predicting the H_v of sp^3-dominated carbon material. We calculated the H_v of the *o*-C_{240} structure using the Chen *et al*. model to be 45 GPa indicating that the *o*-C_{240} structure is a superhard material. We have also compared the H_v of *o*-C_{240} with that of other known and experimentally synthesized superhard materials such as B_4C (38 GPa) [139], WB_5 (45 GPa) [140], B_6O [134] and *c*-diamond [130,131]. These H_v are summarized in Table 2.3. The H_v of *o*-C_{240} is higher than that of graphite but less than *c*-diamond's. This is due to the coexistence of the sp^2 and sp^3 bonding inherent in the *o*-C_{240} structure and the dominance of sp^3 bonding. There is a strong correlation between a material's hardness and its ionicity: which is the degree to which each pair of atoms shares the electrons between bonds. The blend of sp^2 and sp^3 hybridized carbon in *o*-C240 makes it superhard while maintaining a semiconducting state. The Pugh's ratio (*B*/*G*) of the *o*-C_{240} structure indicates that it is brittle.

Fracture toughness (K_{IC}) is another important mechanical property of a material that shows how resistive it is to a propagating crack. Materials with an optimum combination of hardness and fracture toughness are continually being sought in technological applications. *c*-diamond has a very high H_v and K_{IC} while tungsten carbide (WC) has very low H_v and high K_{IC}. The *o*-C_{240} structure possess H_v and K_{IC} that are between *c*-diamond and WC's. We calculated the K_{IC} of the *o*-C_{240} structure using the Niu *et. al.* [141] empirical model to be 4.10 MPa $m^{1/2}$, similar to the value reported for *c*-BC_2N (K_{IC} = 4.5 MPa $m^{1/2}$) [139]. Such a K_{IC} value suggests that the *o*-C_{240} is ductile. The relatively high K_{IC} of *o*-C_{240} exceeds the widely used hard ceramics such as, γ-B, B_6O and B_4C [141]. Such K_{IC} performance of the *o*-C_{240} improves its potential for technological applications.

2.1.4 Conclusion

We have reported a new, stable allotrope of carbon that is made up of 240 carbon atoms in its unit cell, predicted from first principles calculations. The new carbon allotrope crystalizes into an orthorhombic cell with *Pmmm* space group. The carbon atoms are linked together by a network of C3, C4, C5, C6 and C8 carbon rings. *o*-C_{240} is predicted to be semi conducting (with an indirect band gap of 1.72 eV), superhard (with H_v of 45 GPa) and brittle. The *o*-C_{240} also possess fracture toughness of 4.10 MPa $m^{1/3}$, making it superior to other hard ceramics. The combination of these properties makes the *o*-C_{240} a suitable candidate for application in adsorption, photocatalysis, hydrogen storage and high frequency electronic devices. The mixing of the sp^2/sp^3 bonding in favor of sp^3 gives the o-C_{240} superior mechanical and electronic properties compared to other competitive allotropes previously predicted.

2.2 Nitrogen in Black Phosphorus Structure

Nitrogen, a material traditionally studied because of its high energy density applications, is now been searched in the black phosphorous (BP) structure: to complete the structure motif of the group V elements and for novel technological applications. The BP structure is generally puckered with hinge-like bonding configurations and unique anisotropic properties which if explored could lead to a nitrogen-based two-dimensional (2D) semiconductor with superior performance compared to conventional bulk semiconductors and other 2D materials like molybdenum disulfide (MoS_2). This work reports the theoretical identification of synthesized nitrogen at 146 GPa and 2200 K in BP structure likely coexisting with the cubic *gauche* (Cg) structure by comparing the theoretical XRD patterns of candidate nitrogen structures with experimental XRD patterns. The identification was further supported through Raman spectra matching. Theoretical characterizations of the identified BP-structured nitrogen are also reported. The results of the Raman spectroscopy exhibit huge Raman intensities that could be interpreted as coming from the anisotropic nature of the BP structures. At 150 GPa, the BP nitrogen is predicted to be a large band gap semiconductor with a direct energy band gap of 1.75 eV. The real-world appearance of BP nitrogen is therefore expected to lead to a rational design of pure nitrogen or nitrogen based, high-performance semiconductors that is environmentally clean.

2.2.1 Introduction

Nitrogen, as a group V (or group 15) element has found tremendous application as a high energy density material (HEDM). When nitrogen is compressed, it departs from van der Waals solid composed of N_2 molecules (that exhibits the strongest bond: triple bond) to single-bonded form of solid nitrogen. A huge amount of energy (954 kJ/mol) is therefore stored in the single bond of nitrogen during compression [39,142]. The high pressure causes delocalization of electron density which consequently weakens the triple bonds in nitrogen. Progressively compressing nitrogen therefore causes it to exhibit different polymorphs with few of the phases already identified through experiments [40, 143-145]. At pressure as high as 110 GPa and temperature above 2000 K, The N_2 molecule polymerizes to form network of single-bonded nitrogen. So far, at temperature up to 3300 K, polymeric nitrogen has been found in the cubic *gauche* (Cg-), layered polymeric (LP-) and hexagonal layered polymeric (HLP-) form, at 110-180, 125-180 and 244 GPa,

respectively [40, 146, 147]. The Cg-N is the high-pressure thermodynamic ground state of the nonmolecular nitrogen synthesized by Eremets *et al*. in 2004. The Cg-N was synthesized at pressure of 110 GPa and temperature of 2000 K [40]. So far, the crystal structure of the HLP-N and the Cg-N are well established. However, the unambiguous structure of the LP-N is yet to be established [147,148]. There are studies [146] that have proposed the layered *Pba*2 structure predicted by Ma *et al*. [149], as the structure that could explain the LP-N experimentally synthesized. Other studies have also proposed the coexistence of the *Pba*2 and the *Pccn* phase in the LP-N [148]. Still, LP-N structure remains open to discussions and scientists keep pushing both experimental and theoretical boundaries to establish its structure.

Based on structural behavior, nitrogen is like the phosphorus (P), arsenic (As), antimony (Sb) and bismuth (Bi). They are referred to as the pnictogens [150]. A generally accepted pattern is that elements of the same group on the periodic table are structurally connected: at high pressure, elements up in the group should adopt the structure of the elements below them. Since phosphorus is directly below nitrogen on the periodic table, at high pressure, one would expect nitrogen to take on the structure of phosphorus. Phosphorus exists as white- (least stable and most reactive), red-, violet-, scarlet- and black- (least reactive) phosphorus. The black phosphorous (BP) is formed by heating white phosphorus under high pressure (>1 GPa) [151]. At elevated pressure and temperature, different phases of BP exist (see Fig. 2.5): rhombohedral, incommensurate (IM) simple hexagonal (sh) simple cubic (sc), and orthorhombic, however, the orthorhombic structure of BP is the most stable phase [152]. The paradigm in structural behavior of the pnictogens has been observed up to phosphorus. Intuitively, one would expect that compressing nitrogen to high pressures, it should adopt the low-pressure phase of phosphorus – the 2D BP crystalline structure (see Fig. 2.5). However, up to now, nitrogen has not been found in the BP structure. If found, BP-N will not only complete the search for all pnictogens in the BP structure motif but could also birth the exploration of N in the design of 2D materials for electronic applications. Precedent with regard to 2D exploration of pnictogens has been set; phosphorene for phosphorus [153], arsenene for As, and antimonene for Sb [154]. It is important to note, however, that such exploration for nitrogen will require a significant scientific and experimental breakthrough, as polymeric nitrogen are mainly formed at high pressures and high temperatures. Recently, mono- and multi- layered nitrogen (nitrogene) were studied computationally at ambient pressure for potential applications in HED and electronics. The main observations were that the decomposition temperature into N_2

for the single-bonded multilayered nitrogen decreases with increasing number of layers. Furthermore, the energy band gap monotonically reduces with increasing number of layers. However, increasing the number of layers increases instability in the material. The material is capable of releasing energy between 6 to 12.3 kJ/gm [155]. The challenge, experimentally (with no success, yet) would be to recover them to ambient pressure (where they can be applied in electronic applications) without reverting to the N_2.

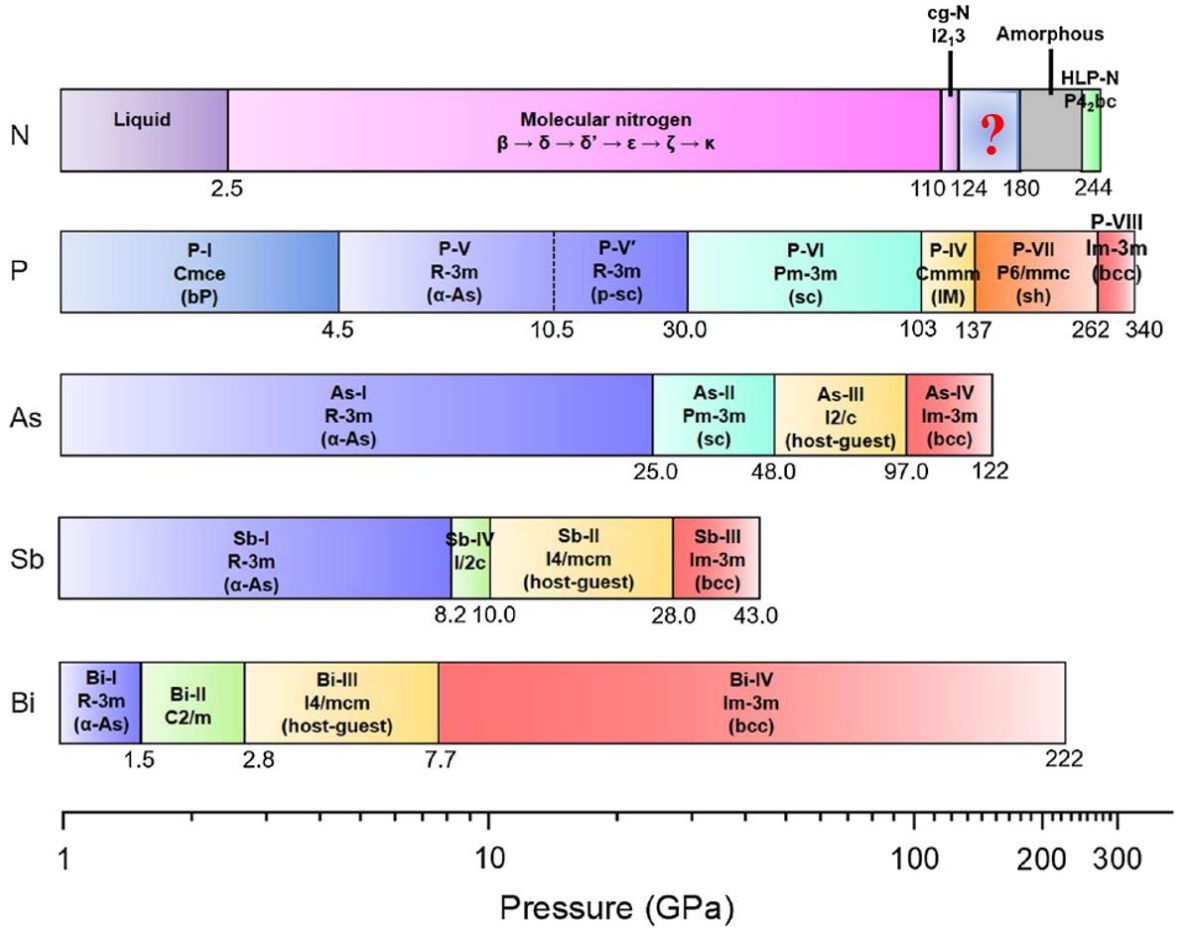

Figure 2.5. Pictorial illustration of the motivation for this study. The figure shows the various phases in which group V elements have been observed up to the high-pressure regime. In this figure, p-sc means pseudosimple cubic. Adapted from Ref. [152]. The red "?" in the figure is the region of interest for the present study. The Cg-N was predicted as the thermodynamic ground state of nonmolecular nitrogen up to 188 GPa [149]. Therefore, observing BP-N in the pressure field of 124 to 180 GPa may require specific *P-T* condition: carefully and simultaneously varying

the pressure and the temperature of exploration. Figure was adapted with permission from American Physical Society.

In the present study using complementary DFT techniques, we identified the long-sought nitrogen in the BP structure. This work reports the theoretical identification of synthesized nitrogen at 146 GPa and 2200 K in BP structure by comparing the theoretical XRD patterns of candidate nitrogen structures with experimental XRD patterns [42]. The identification was further supported through Raman spectra matching. Theoretical characterizations of the identified BP structured nitrogen were carried out. The results of the Raman spectroscopy exhibit huge Raman intensities that could be interpreted as coming from the anisotropic nature of the BP structure. The crystal structure of BP-N was also discussed relative to the Cg-N. The role of temperature in lowering the internal energy difference between the thermodynamic ground state Cg-N and the identified BP-N was also explored, thereby elucidating the need for laser heating in the actual experiment.

2.2.2 Computational Methods

First principles calculations were carried out within the framework of DFT discussed in chapter 1 of this thesis. Energy, phonon, and Raman spectra calculations were performed using the Vienna ab Initio Simulation Package (VASP) [93]. The simulated XRD patterns were calculated using Mercury software [156]. Energetic calculation was performed using Perdew-Burke-Ernzerhof (PBE) functional [61]. The electron–ion interaction was considered in the form of a 5-electron projector augmented wave (PAW) potential [116]. A kinetic energy cutoff of 900 eV was used for planewave expansion. A *k*-spacing of $2\pi \times 0.02$ Å^{-1} was used for Brillouin zone (BZ) sampling. Raman spectra were calculated with VASP using a $12 \times 12 \times 14$ *k*-point mesh. The small displacement of atomic position for the evaluation of normal modes were done around ± 0.01Å. Raman activities were then evaluated from the change in polarizability with respect to displacement in the normal modes activated by incident electric field (linear response to external electric field). Electronic band dispersion was calculated using Heyd–Scuseria–Ernzerhof exchange correlation functional [70] with a mixing parameter of 0.25 and long-range exchange

contribution parameter (ω) of 0.2. Details of the experimental methods and experimental results can be found in Ref. [42].

2.2.3 Results and Discussion

2.2.3.1 Identification of BP nitrogen by XRD

The *Pba*2 [149], *Pccn* [148] and Cg [40] structures were adopted as the starting structures in an attempt to identify the phase(s) of the synthesized high pressure layered polymeric nitrogen (experimental data from Ref. [42]). The experimental XRD was collected at 132 GPa. The choice of these structures was informed by the thermodynamic stability of the Cg-N from 110 GPa up to 188 GPa, the *Pba*2 from 188 GPa up to 320 GPa [40,149]. Furthermore, the *Pccn* structure was also included because it was predicted to have comparable energy with the Cg-N at 140 GPa and 2500 K [148]. The XRD pattern of these three structures were calculated with $\lambda = 0.4066$ Å. The simulated XRD pattern (see Fig. 2.6a) reveals the Cg-N could explain part of the experimental XRD pattern. Specifically, the peak at 2θ=9.3^o, can be uniquely indexed to the Cg-N structure. Furthermore, the weak peaks at 2θ =19.2^o, 21.5^o and 23.6^o can be uniquely indexed to the Cg-N. The peak at 2θ =13.5^o in the simulated XRD of the Cg-N may be a "shoulder peak" that was not obvious due to noise or broadening of experimental data. The *Pba*2 and the *Pccn* structures are off and as such were discarded. The BP-N was then considered in the fitting of the experimental XRD pattern. The XRD pattern of the BP-N was calculated with $\lambda = 0.4066$ Å. The simulated XRD pattern (see Fig. 2.6b) reveals the BP-N could explain the remaining part of the experimental XRD pattern. Specifically, the peaks at 2θ=7.1^o, 10.9^o, 14.1^o, and 22.6^o can be uniquely indexed to the BP-N structure. Furthermore, the weak peaks at 2θ =17.4^o, 20.2^o, 21.9^o and 23.0^o and 24.5^o can be uniquely indexed to the BP-N. The two peaks at 2θ =16.4^o and 21.4^o appear to be an overlap of peaks from both Cg-N and BP-N. overall, most of the Bragg peaks occupying the various 2θ positions in the experimental XRD were successfully indexed to the Cg-N and BP-N. The disparities between the observed and calculated peaks could be due to weak scattering of x-ray by nitrogen, background subtraction error or preferred orientation in the sample since the experimental data were collected from a polycrystalline sample using a single crystal XRD method (see Ref. [42] for details of the experimental results). Note that the Mercury software [156] used

in the simulation of theoretical XRD assumes a single crystal, hence the intensity is reported in arbitrary unit. The agreement between the experimental and simulated XRD patterns support the interpretation of the synthesized phase as the BP-N with some Cg-N phase.

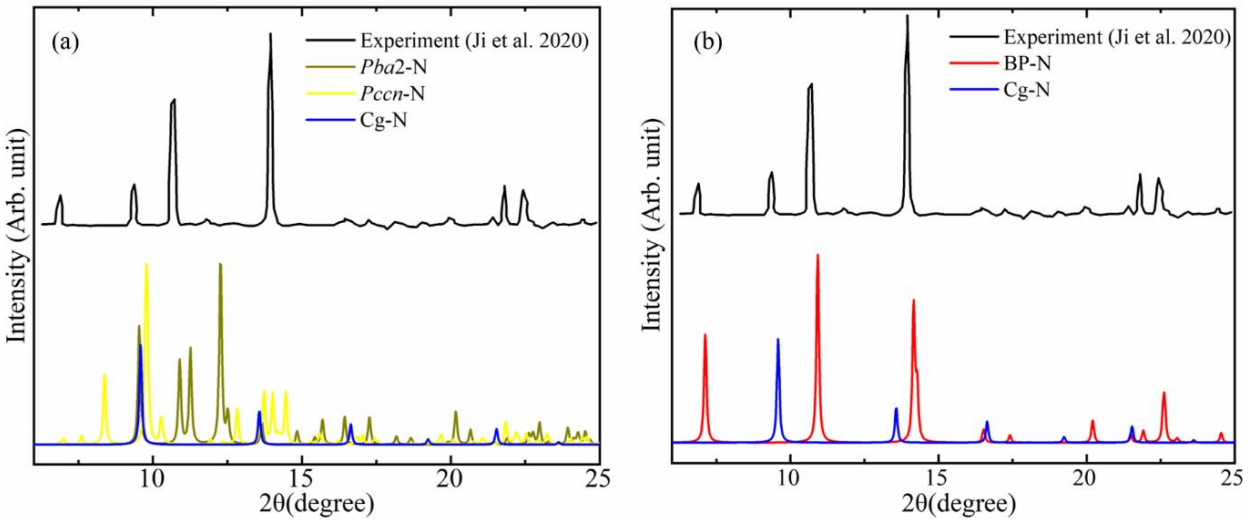

Figure 2.6. Calculated XRD pattern for the (a) *Pba*2 N, *Pccn* N, and Cg-N at 132 GPa compared with the experimental pattern from Ref. [42] at the same pressure (b) BP N and Cg-N at 132 GPa compared with the experimental pattern from Ref. [42] at the same pressure. An x-ray wavelength of 0.4066 Å (as reported in Ref. [42]) was used. The XRD pattern was calculated using Mercury software [156].

2.2.3.2 Identification of BP nitrogen by Raman spectroscopy

BP- and Cg- nitrogen were also clearly identified from the measured Raman spectrum. Raw Raman spectra data at different positions in the sample were supplied by Dr. Cheng Ji. The Raman spectra measurement was done at 138 GPa. The *Pba*2-N, *Pccn*-N and Cg-N structures were adopted as the starting structures to identify the phase(s) of the synthesized high pressure layered polymeric nitrogen. Simulated Raman spectra for the *Pba*2-N, *Pccn*-N and Cg-N structures were calculated using the method of Porezag and Pederson based on the double harmonic approximation [157] as implemented in ref. [158]. Within this formalism, higher order changes of the energy, dipole moment and polarizability with respect to the normal modes are ignored. Brief formalism of this method can be found in appendix A2.1. The experimental and simulated Raman

spectra (Fig. 2.7a) reveals that a Raman peak/activity at Raman frequency 860 cm^{-1} from experiment can be assigned to the calculated Raman peak/activity at Raman frequency 872 cm^{-1}, of the Cg-N. It is worthy of note that Cg-N sample was prepared at 120 GPa (where Cg-N is clearly the thermodynamic ground state without having to worry about coexistence of phases. This aids the identification of the Cg-N peak; details of the experimental procedure can be found in ref. [42]. No Raman activity from the experiment could be assigned to both the *Pba*2 N and the *Pccn* N structures, consistent with the observation and conclusion from the XRD pattern analyses in section 2.2.3.1. We therefore rule out the possibility of the synthesized phase being either the *Pba*2 N or the *Pccn* N structure. Table 2.4 shows the various Raman active modes of Cg-N according to our calculation and the relative activities of each mode to the mode vibrating at the highest frequency.

The simulated Raman spectra for the BP-N structure was also calculated and the data is summarized in table 2.5. The experimental and simulated Raman spectra (Fig. 2.7b) reveals that Raman peaks/activities at Raman frequencies: 796 cm^{-1}, 830 cm^{-1}, 993 cm^{-1}, 1296 cm^{-1} from experiment can be assigned to the calculated Raman peaks/activities at Raman frequencies: 797 cm^{-1}, * cm^{-1}, 977 cm^{-1}, 1270 cm^{-1}, of the BP-N, respectively. The calculated Raman activities agree very well with the experimental values. The * cm^{-1} indicate a missing peak according to our calculation. This could be due to insufficiency in the method used or numerical artifact. The simulated Raman peak/activity at Raman frequency: 1408 cm^{-1} was not observed in the experiment because this frequency is in the region of vibrating/stretching diamond (first order Raman mode of diamond) of the diamond anvil cell used in the experiment. From table 2.5, modes 2, 3 and 9 are theoretically insignificant because their activities are well below 1% of the activity of the mode with the maximum frequency. This then implies that there are six Raman active modes for the BP-N. The agreement between the experimental and simulated Raman spectra supports the interpretation of the synthesized phase as the BP-N with some Cg-N phase.

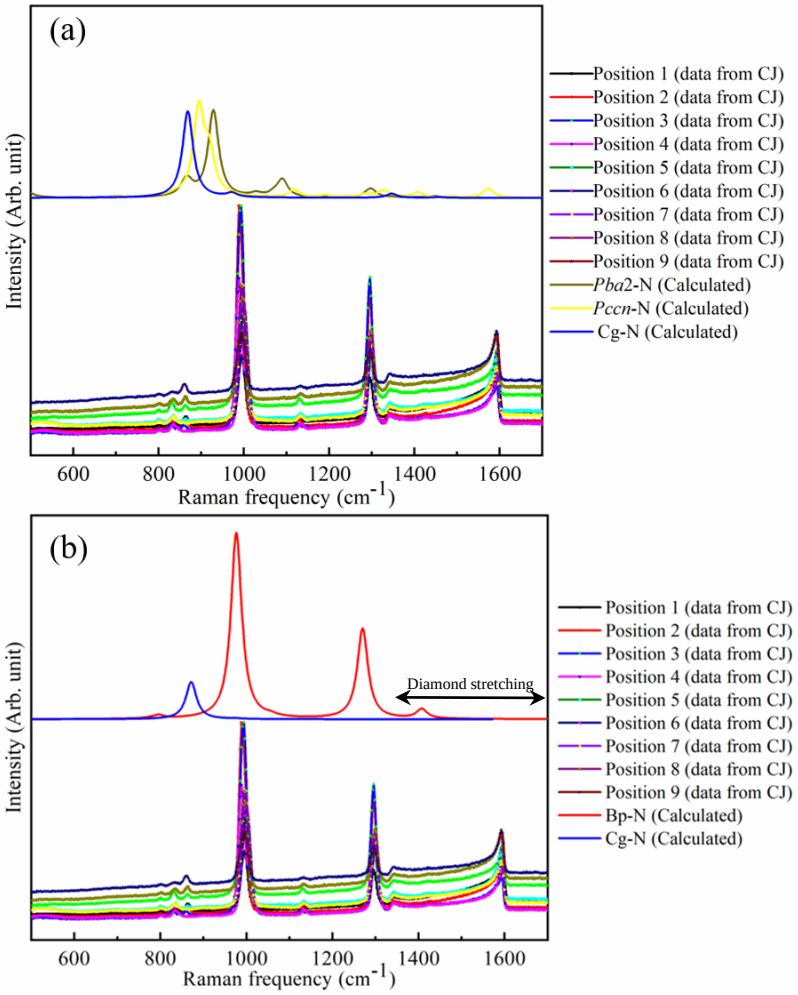

Figure 2.7. Calculated Raman spectra for the (a) *Pba*2 N, *Pccn* N, and Cg N at 138 GPa compared with the experimental spectra received from Dr. Cheng Ji [referred as CJ] (b) BP N and Cg N at 138 GPa compared with the experimental spectra received from Dr. Cheng Ji at the same pressure.

Mode #	Frequency (cm^{-1})	α	β'^2	Raman Activity	Percent of highest Activity
8	974	0.00	0.35	2.44	1.57
9	872	1.86	0.00	155.30	100.00

Table 2.4: Raman modes for the Cg nitrogen at 138 GPa. The table shows the mode number, the frequency, the derivative of the mean polarizability (α), anisotropy of the derivative of the

polarizability tensor (β'^2), the Raman scattering activity and the relative Raman scattering activity of each mode to the mode vibrating at the highest frequency.

Mode #	Frequency (cm^{-1})	α	β'^2	Raman Activity	Percent of highest Activity
1	1408	0.00	68.85	481.94	5.10
2	1393	0.00	0.01	0.04	0.00
3	1362	0.00	0.00	0.00	0.00
4	1270	7.11	328.72	4576.00	48.42
5	1056	0.02	12.96	90.70	0.96
6	977	11.74	464.59	9450.78	100.00
7	797	0.00	22.89	160.21	1.70
8	777	0.01	5.31	37.19	0.39
9	776	0.01	0.01	0.04	0.00

Table 2.5: Raman modes for the BP nitrogen at 138 GPa. The table shows the mode number, the frequency, the derivative of the mean polarizability (α), anisotropy of the derivative of the polarizability tensor (β'^2), the Raman scattering activity and the relative Raman scattering activity of each mode to the mode vibrating at the highest frequency.

The bulk BP crystal belong to the point group D_{2h}, the face centered group and the primitive cell is orthorhombic with space group *Cmce* and has four atoms per cell with six irreducible representation of Raman active modes, which, depending on the axis convention, could be ($2A_g$, B_{1g}, B_{2g}, $2B_{3g}$) or ($2A_g$, B_{3g}, B_{1g}, $2B_{2g}$) [159]. The assignment of these modes in term of the six irreducible representation of Raman active modes is available in ref. [42]. The huge value of the anisotropy of the polarizability tensor derivative in the mode # 6 (see table 2.5) is responsible for the high Raman scattering activity of the mode (see Fig. 2.7b) and in turn, a huge Raman cross section. This means that polarizability changes so much along mode #6 and about half that rate of change along mode #4.

2.2.3.3 The BP nitrogen and Cg nitrogen structure

The optimized lattice parameter of the BP-N crystal structure at 140 GPa (Fig. 2.8a) is $a = 2.133$ Å, $b = 6.534$ Å and $c = 2.860$ Å with N atoms located at 8*f*: 0.500, 0.100, 0.390. The BP-N possesses a layered structure (Fig. 2.8c) and arrangement of singly bonded nitrogen atoms (hinge-like bonding) such that all three crystallographic directions of the crystal structure are distinct. The structure of the BP-N can be thought of as follows: BP-N is formed from stacking of BP-N layers. The nitrogen atoms in a BP-N layer are arranged as follows: nitrogen atoms are arranged zigzag along *a* direction (viewed in *ac* plane, Fig. 2.8d) and armchair along *c* direction (viewed in *bc* plane, Fig. 2.8c). These layers are then stacked along *b* direction to form the bulk BP-N structure. The nitrogen atoms in the zigzag chains (bond lengths=1.3292) can be thought of as forming a network of honeycomb arrangement that are puckered by the nitrogen atoms in the armchair (bond lengths=1.4464 Å) configuration leading to a distorted hexagon. The nitrogen atoms arranged in the armchair configuration have bond lengths between 1.3292 Å and 1.4464 Å (bondlength difference of 8.1%) and N-N-N angle of 104.772^{o}. This difference in bondlength of the armchair configured nitrogen atoms of BP-N is greater than the 1.7% [160] and 0.3% [161] reported for P-P and As-As in black phosphorous and black arsenic, respectively. The consequence of a high bondlength difference in BP-N, compared to black phosphorus and black arsenic, is seen in its pronounced structural anisotropy. The BP-N layers are stacked along *b* direction with an interlayer distance of 2.3193 Å. Such interlayer distance would disallow the formation of covalent bonding between the terminal nitrogen atoms of each layers, thereby inducing weaker out-of-plane interactions (in-plane directions are *a* and *c*, and out-of-plane direction is *b* with respect to Fig. 2.8).

Geometrically, the BP-N structure can also be explained as three nitrogen atoms in the zigzag configuration connecting with one of the armchair nitrogen atoms to form a [distorted] tetrahedral network as shown in Fig. 2.8b. The structure of BP-N also suggests that it should exhibit anisotropy in its compressibility. For example, in the bulk BP-N, the in-plane compressibility should be low but with high bulk modulus and the out-of-plane compressibility should be high with low bulk modulus. Furthermore, in the BP-N layer, with emphasis on the in-plane directions (*a* and *c*), one would expect the armchair nitrogen network to respond differently

to deformation strain relative to the zigzag nitrogen network. Since the interaction between the layers are weaker than the in-plane bonds (see discussion on electronic properties of BP-N in section 2.2.3.5), then, in principle, fewer layers of BP-N could be exfoliated to produce monolayer crystals that are 2D in nature, like in graphene from graphite.

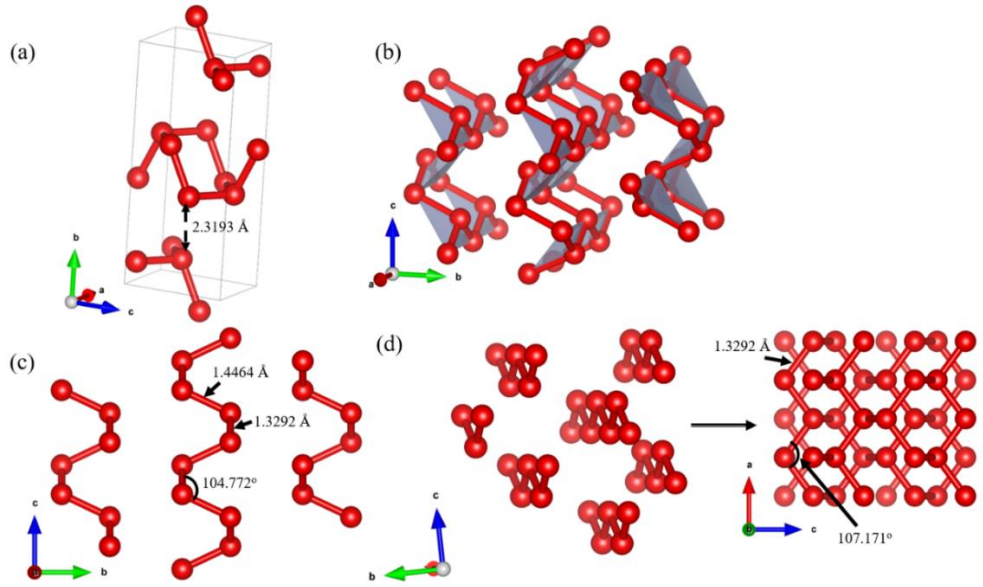

Figure 2.8. Crystal structure and structural analysis of the BP-N. (a) The BP-N structure (b) The BP-N structure revealing the tetrahedral network of nitrogen atoms in the in-plane directions. (c) layers of armchair arrangement of nitrogen atoms in the BP-N (d) the zigzag arrangement of nitrogen atoms and the derived puckered honeycomb arrangement of the nitrogen atoms in the BP-N structure.

Since the Cg-N was also detected (indexed) in the experiment, then I will briefly explain the Cg-N structure. The optimized lattice parameter of the Cg-N crystal structure at 140 GPa (Fig. 2.9a) is $a = 3.418$ Å with N atoms located at 8*a*: 0.180, 0.680, 0.819. The Cg-N belong to the $I2_13$ space group. In contrast to the BP-N that is layered, the Cg-N is characterized with connected N_{10} rings (shown in Fig. 2.9b and c) with each pair of nitrogen atom in the ring having the same bond length: 1.3227 Å. Generally, the Cg-N structure is well studied, and I suggest that readers see refs. [40,148] for more general discussions. For the purpose of this thesis, specific properties of Cg-N

that contributed to its identification along with the BP-N will be the subject of subsequent discussions.

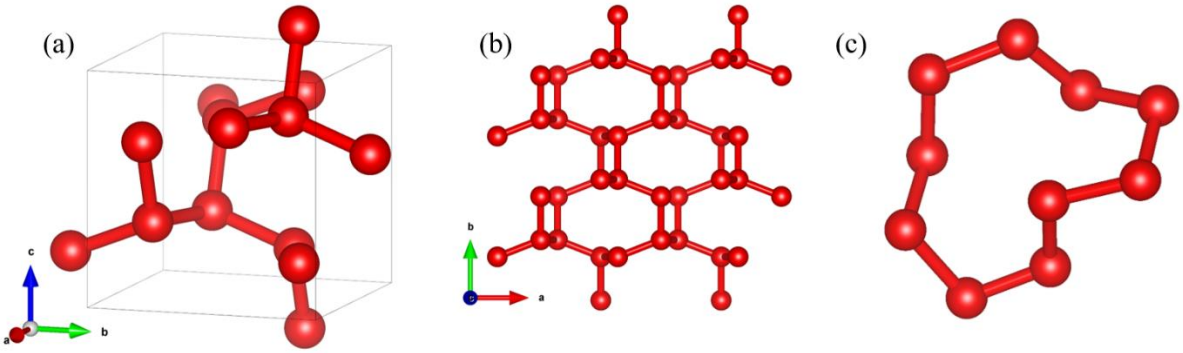

Figure 2.9. Crystal structure and structural analysis of the Cg-N. (a) The unit cell of Cg-N structure (b) The Cg-N structure revealing nitrogen rings fused together in the *ab* plane and (c) isolated N_{10} ring featured in the Cg-N.

2.2.3.4 Energetic stability and Dynamic stability of BP nitrogen

The calculated volume per atom for the Cg-N and BP-N are shown in Fig. 2.10a. The figure also compares various reported experimental data of Cg-N, BP-N and HLP-N as well as the experimental data on Cg-N and BP-N used for this thesis (marked as Ji et al. 2020 [42] in Fig. 2.10a). This calculation reveals that phase transformation (from Cg-N to BP-N) is accompanied by volume shrink per nitrogen. Furthermore, in the region of interest, clearly marked in Fig. 2.10a, Experimental volume per nitrogen atom in the Cg-N and the BP-N structure are close and align within the limits of theoretically calculated values. The HLP-N continue to have lowest volume per atom up to at least 150 GPa, which suggests that should BP-N transforms to HLP-N, it will be accompanied by a decrease in volume.

At temperature of 0 K, The Cg-N is the thermodynamic ground state of high pressure nitrogen up to 190 GPa (Fig. 2.10 b). The Cg-N transforms to the *Pba2*-N above 190 GPa and remain preferable up to at least 210 GPa considered in this study. According to this calculation, the BP-N and the *Pccn*-N are only metastable and remain so, throughout the pressure range studied. In the search for BP-N, experiment [42] was done between 132 and 140 GPa; a pressure range for

which only Cg-N is energetically stable. Therefore, pressure and temperature must be carefully tunned to observe the BP-N. Theoretically, temperature effects must be captured so that the effect of the free energy of the, in this case, two competing phases may be understood. The vibrational free energy contribution to Helmholtz free energy within the harmonic approximation [162] is one way to capture temperature effects into the energetics and also modify Fig. 2.10b. The vibrational free energy, F_{vib} is the phonon contribution to Helmholtz free energy at finite temperature, T, defined as:

$$F_{vib} = \frac{1}{2}\sum_{\omega} g(\omega)\hbar\omega + k_B T \sum_{\omega} g(\omega) \ln\left[1 - \exp\left(-\frac{\hbar\omega}{k_B T}\right)\right] , \qquad (2.1)$$

where $g(\omega)$ is the normalized density of states (DOS) for the phonon branch ω and k_B is the Boltzmann's constant.

Although, there is another method beyond the harmonic approximation for determining vibrational free energy. The quasi-harmonic approximation [163] captures volume dependence of the phonon frequencies and by extension vibrational free energy; this volume dependence is considered part of anharmonic effect. Within quasi-harmonic approximation, the vibrational free energy, F_{vib}^{Q} can be written from Eq. (2.1) as

$$F_{vib}^{Q}(T,V) = \frac{1}{2}\sum_{\omega} g(\omega)\hbar\omega\,(V) + k_B T \sum_{\omega} g(\omega) \ln\left[1 - \exp\left(-\frac{\hbar\omega(V)}{k_B T}\right)\right] . \qquad (2.2)$$

The equilibrium volume $V(T)$ at a given temperature is obtained through minimization of set of F_{vib}^{Q} for changing volume. The negative of differentiating Eq. (2.2) with respect to the volume thus yield the thermal pressure, otherwise known as the phonon pressure:

$$P(V;T) = -\frac{\partial F_{vib}^{Q}(V;T)}{\partial V} . \qquad (2.3)$$

The quasi-harmonic approximation is good for evaluation of thermal properties of materials such as the heat capacity, Grüneisen parameter e.t.c. However, since we are interested only in the phonon contribution to free energy, the F_{vib} from harmonic approximation (Eq. 2.1) is then added to the 0 K enthalpy, $H(0)$, so that effective temperature-dependent enthalpy $H_{eff} = H(0) + F_{vib}$. From Eq. (2.1), it become obvious that the harmonic approximation requires that the crystal structure be dynamically stable. Therefore, we investigated the dynamical stability of

the BP-N. Note that the Cg-N is known to be dynamically stable in the pressure range of interest [40,148].

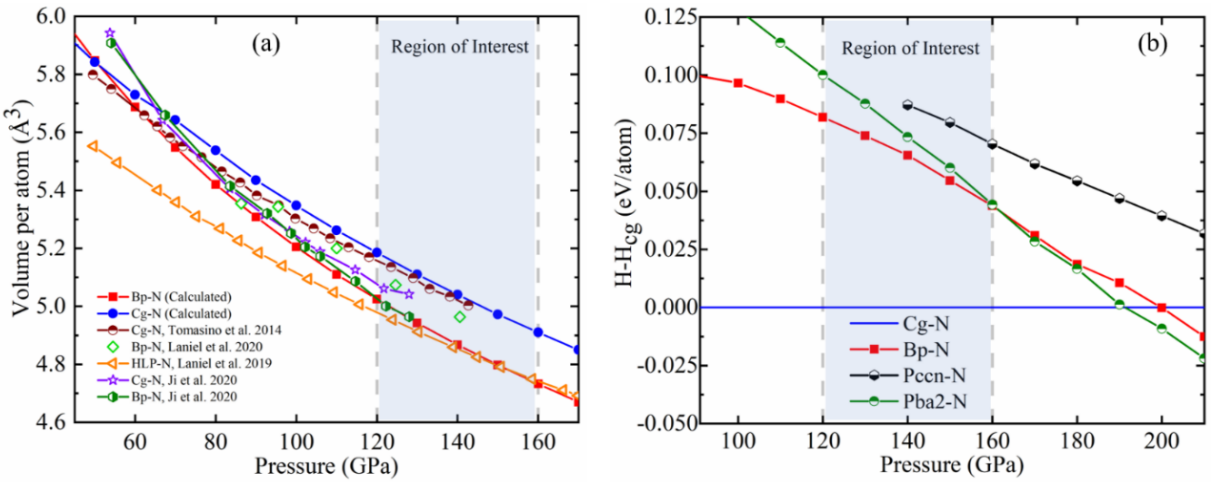

Figure 2.10. (a) Evolution of experimental and calculated volume per nitrogen atom under pressure for the Cg-N and BP-N calculated in this work and experimental data on Cg-N [42,146], BP-N [42,152] and HLP-N [147]. (b) Enthalpy curves (relative to Cg-N structure) of BP-N, *Pccn*-N, and *Pba*2-N structures. The grey area is to guide the eye and mark out the pressure range within which experimental XRD and Raman spectra data were collected.

The lattice dynamic stability of the BP-N was examined at 150 GPa by calculating the phonon dispersion within the density functional perturbation theory (see Fig. 2.11). The absence of imaginary frequencies throughout the Brillouin zone indicates that the BP-N is dynamically stable. As shown in Fig. 2.11, the optical phonons split into two distinct groups: the low energy phonons and the high energy phonons. This type of phonon gap is induced in diatomic or poly atomic systems when the mass ratio between constituent elements' species are high [164]. However, in monatomic system like the BP-N, the gap is a consequence of the anisotropy in the structure and the type of motion exhibited by the bond during vibration. The Kleinman parameter [165,166] ($\zeta = C_{11} + 8C_{12}/7C_{11} + 2C_{12}$), calculated from the elastic constants of BP-N at 150 GPa is 0.61. The calculated elastic constants of BP-N at 150 GPa can be found in Table A2.1 in the appendix. The value of ζ approaches 1, indicating that the optical phonons will be predominantly bond-stretching type in character while few (likely the low energy phonons) will

be bond-bending type in character. The linearly dispersed acoustic branches near the zone center (in Fig. 2.11) indicate a relatively strong covalent bonds between nitrogen atoms in the BP-N structure.

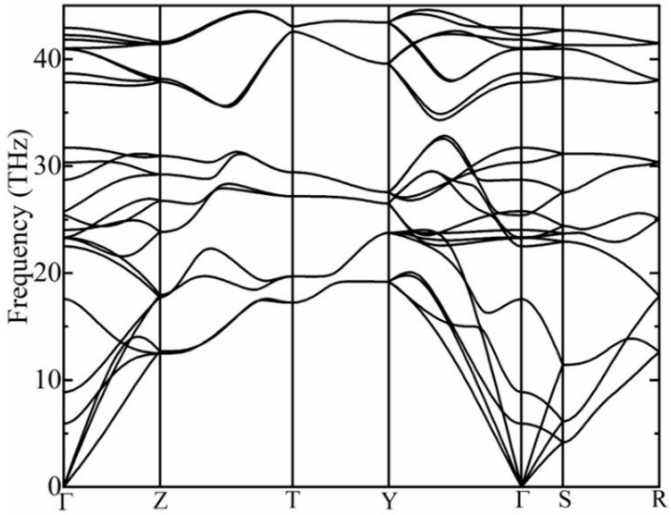

Figure 2.11. Calculated phonon dispersions for the BP-N at 150 GPa.

At 120 GPa, 0 K and 190 GPa, 0 K, there exits an enthalpy difference of 81.81 meV/atom and 10.67 meV/atom between the Cg-N and the BP-N, respectively. This energy difference precludes observing the BP-N at 0K within this pressure range and as such, energy must be added to the system to remove the difference. There are different ways to achieve this; one of which is changing thermodynamic variables: pressure and/or temperature. For instance, increasing the pressure from 120 GPa to 190 GPa reduces the enthalpy difference to 10.67 meV/atom. Now, our constraint is on the pressure, which means that we cannot continue to increase the pressure due to the specific pressure region we are interested in. Thus, we begin to tune the temperature. This process is schematically represented in Fig. 2.12a. Theoretically, while a material is still a solid, temperature effects can be included to the energetic of the material through the lattice contribution to free energy, consequently influencing the relative stability of different phases of the same material. Using the harmonic approximation, the calculated $H(0)+F_{vib}$ at 150 GPa, 170 GPa, and 190 GPa are shown in Fig. 2.12b, Fig. 2.12c and Fig. 2.12d, respectively. The pressures and temperatures choice were informed by the experimental *P-T* condition (132-150 GPa, 2200 K [42]). We observe that at 150 GPa, 0 K, the Cg-N is 44.65 meV/atom more stable than the BP-N

(This already included the zero-point energy) and at 150 GPa, 2500 K, the Cg-N is 25.88 meV/atom more stable than the BP-N. At 170 GPa, 0 K, the Cg-N is 20.27 meV/atom more stable than the BP-N and at 170 GPa, 2500 K, The Cg-N is 0.9 meV/atom more stable than the BP-N. At 170 GPa, 2500 K, the internal energy difference between the Cg-N and the BP-N is so small that both structures could be indistinguishable based solely on their energies with possibility of the Cg-N and Bp-N coexisting. At 190 GPa, 0 K, the Cg-N is 0.69 meV/atom more stable than the BP-N and at 190 GPa, 2500 K, The BP-N is 15.88 meV/atom more stable than the Cg-N. Therefore, this shows that between 170 GPa and 190 GPa, the BP-N is more stable at higher temperature than the Cg-N. This further explains the experimental identification of BP-N at pressure between 132 GPa and 150 GPa after laser heating to above 2000 K. The difference between the predicted stability pressure field and the experimental synthesis pressure could be due to uncertainties in the experimental and/or theoretical methods used.

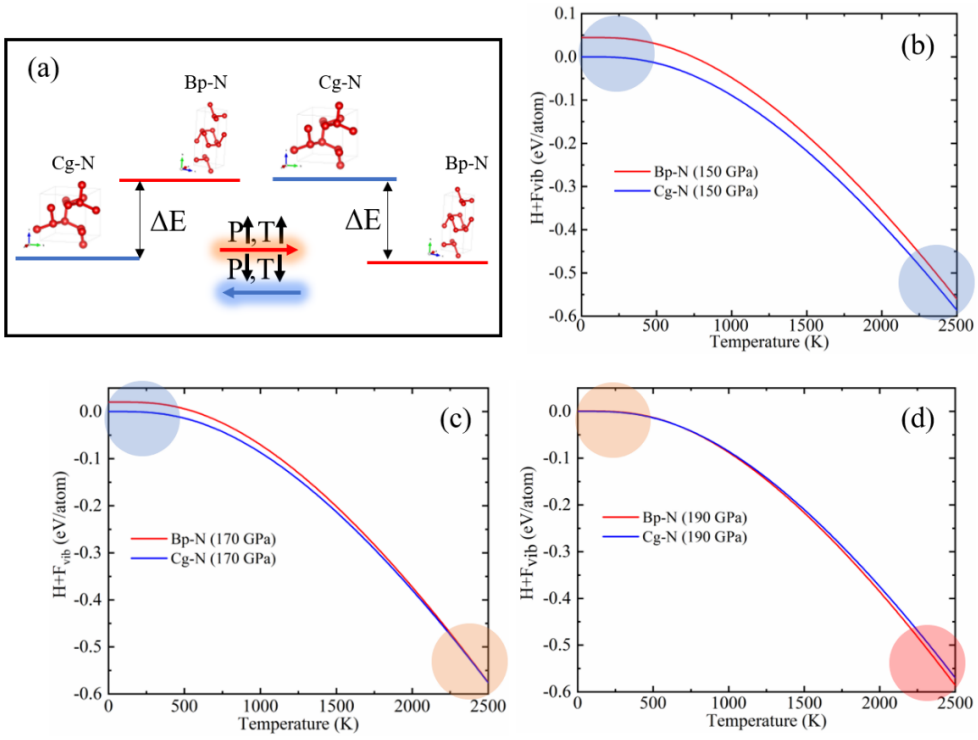

Figure 2.12. (a) Schematic diagram illustrating stability control between Cg-N and BP-N using pressure (P) and temperature (T). ΔE represents the enthalpy difference. The structure above ΔE is having higher enthalpy relative to the one below and hence energetically unstable relative to the one below. The temperature dependent H + F_{vib} (H is the enthalpy and F_{vib} is the vibrational free

energy) for the Cg-N and the BP-N structures at (b) 150 GPa (c) 170 GPa (d) 190 GPa. The enthalpy of the Cg-N structure at 0 K was used as the zero-energy origin. The Blue and red circles indicate the structure that is preferred at various P-T condition. The almost yellow circle shows that in the region, both structures are not distinguishable solely on their energy.

2.2.3.5 Electronic properties of BP nitrogen

Applications in electronics and device fabrications is one of the motivations for searching for nitrogen in BP structure. The black phosphorus and black arsenic are narrow band gap semiconductor with energy band gap of 0.3 eV (infrared) [161,167]. We therefore investigated the electronic properties of the newly identified BP-N. The emergence of Raman scattering activities suggests that BP-N is either semi conducting or insulating. To nail this down, we calculated the electronic band structure of the BP-N between 50 GPa and 200 GPa using hybrid functional (HSE06) which is known to give better prediction of energy band gap [70]. The electronic band structure of BP-N at 150 GPa is shown in Fig. 2.13. The electronic band structures of BP-N at 50, 100 and 200 GPa are shown in Fig. A2.1 of the appendix. Clearly, throughout the pressure studied, the BP-N is semi conducting with direct energy band gap ranging between 1.22 eV and 2.02 eV.

The direct energy band gap, unlike the indirect energy band gap predicted in the *o*-C_{240} [41], is when the valence band maximum (VBM) and the conduction band minimum (CBM) are situated on the same momentum direction in the Brillouin zone. Thus, the amount of energy required to bias the semiconductor into a conducting state equals the energy band gap i.e., no phonon assisted transition is required. The evolution of electronic energy band gap under compression (Fig. 2.14a) reveals that the energy band gap of BP-N increases linearly with increasing pressure; similar trend was observed in the evolution of direct energy band gap of some semiconductors such as GaP and AlP [168]. To have the energy band gap decreases with decompression is good for application of BP-N in device fabrication, especially with controlling of band gap, provided that the BP-N is successfully quenched to a very low pressure and eventually to ambient pressure. Doping BP-N with some suitable dopants could help reduce the pressure needed to keep the nitrogen atoms in BP-N singly bonded and in layered form. It could also help

in biasing it towards a conducting state. This hypothesis will require several experimental, theoretical development and investigations; however, it is good to note such possibility.

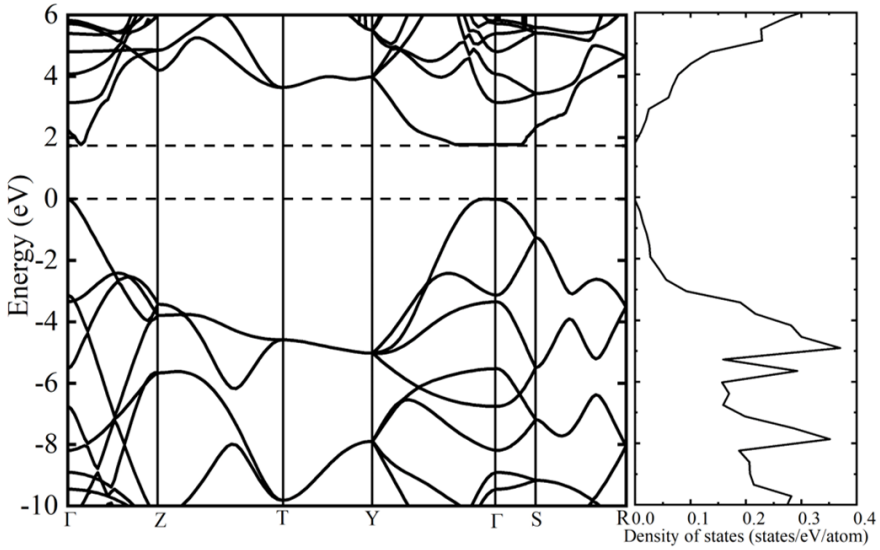

Figure 2.13. Electronic band structure and electron density of states of BP-N at 150 GPa.

Electron localization function (ELF) is the probability of finding electron pair at a given point and with opposite spin state. The ELF of BP-N (Fig. 2.14b and c) shows different localization depending on the direction being considered. This is not surprising owing to the anisotropic nature of the BP-N structure. The ELF reveals that electrons accumulate half-way between pair of nitrogen atoms in a zigzag network (Fig. 12.14b) indicating a covalent bonding between the participating nitrogen atom pairs. This is also consistent with the inference drawn [earlier] from the linear dispersion of the acoustic phonons of the BP-N near the zone center. The lone pair electrons are pushed to the interlayer gap (Fig. 12.14c) and they adopt a configuration in space that reduces the potential energy of the system but weakens the out-of-plane interactions between different layers in the BP-N. The weak interlayer interaction thus has its merit in device engineering. Weak interlayer interaction facilitates exfoliation of monolayers from a bulk, layered material [169]. Thus, The BP-N has the propensity to be used as a 2D material, the prospect that its affinity for high pressure and temperature currently precludes.

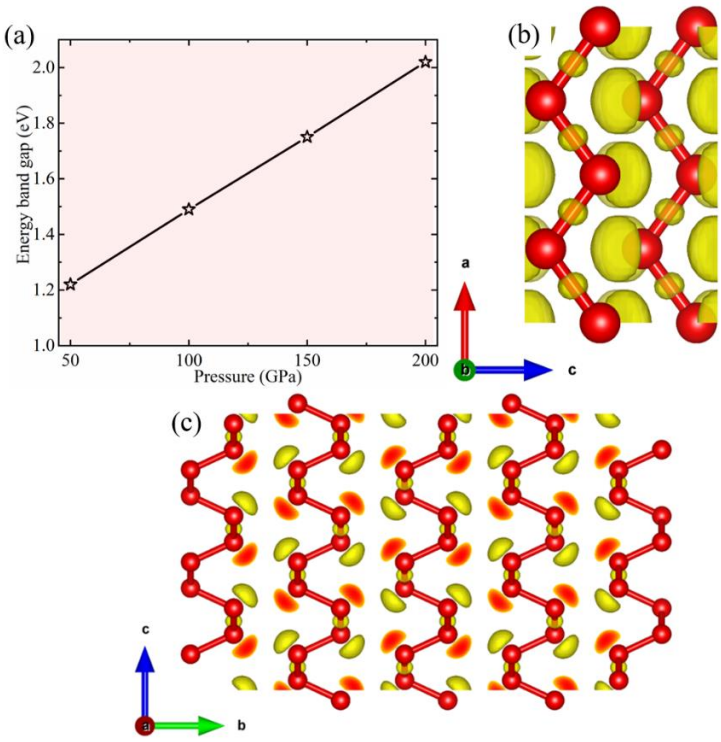

Figure 2.14. (a) Evolution of energy band gap of BP-N under pressure. Electron localization function (ELF) of BP-N along the (b) zigzag arrangement (c) armchair arrangement. An isovalue of 0.7 was used in the ELF.

2.2.4 Conclusion

In conclusion, we report the theorical characterization of experimentally synthesized nitrogen at high pressure of 146 GPa and high temperature of 2200 K. The synthesized phase, through XRD pattern and Raman scattering activities, is identified as the long-sought BP phase. The crystal structure of the new BP-N exhibits structural anisotropy. At 150 GPa, the BP nitrogen is predicted to be a large band gap semiconductor with a direct energy band gap of 1.75 eV. The ELF reveals that electrons accumulate half-way between pair of nitrogen atoms in a zigzag network. Furthermore, lone pair electrons are pushed to the interlayer gap thereby inducing a weak interlayer (out-of-plane) interaction. This property positions the BP-N for exfoliation and possible use in semiconductor devices. The current study, therefore, completes the search for all pnictogens in the BP structure motif and give a glimpse into the exploration of BP-N in the design of 2D materials for electronic applications.

CHAPTER 3

FORMATION AND STRUCTURAL CHANGES IN TRANSITION METAL – TRANSITION METAL COMPOUNDS: A CASE STUDY OF Ni-Ti AND Fe-Au

A similar version of this chapter has been published as a research article in the Physical Chemistry Chemical Physics journal and the second part is being drafted. The references are as follows.

1. Adeleke, A. A., and Yao, Y. High-temperature shape memory loss in nitinol: a first principles study. *Phys. Chem. Chem. Phys.*, *21*, **2019** 7508-7517.
2. Adeleke A. A., Bonev S. A., Wu C. J., Jossou E. E. and Yao Y., Aurum reservoir deep down: stable compounds of two bulk-immiscible metals under pressure (in preparation).

3.1 High temperature shape memory loss in nitinol: A first principles study

First-principles calculations were employed to investigate shape memory loss in a member of the titanium-based binary smart alloys – NiTi. Analysis of the transition pathway reveals that the $B19'$ phase of NiTi loses its shape memory under a high pressure condition when heated above a critical temperature, T_c. The $B19'$ phase is shown to transform to the *P*-1-NiTi which is also predicted to be dynamically stable and temperature-quench recoverable. It is found that the $B2(B33) \rightarrow B19'$ transition is dominated by the β shearing mode. Furthermore, the $B19' \rightarrow P$-1 transition is predominantly driven by the γ shearing mode. Aggregation of both processes activates the lowering and eventual break of symmetry in the precursor phases, leading to permanent deformation and eventual shape memory loss. We further show that *P*-1-NiTi structure is stabilized (over $B19'$ structure, the martensite) by kinetics. The findings of this study could guide the exploration and design of smart alloys used in the fabrication of devices operated beyond ambient conditions.

3.1.1 Introduction

Metal alloys with novel ability to 'remember' their shape after deformation has been the subject of many research in recent years [170-172]. This property is colloquially known as shape-memory and alloys with such properties are called shape memory alloys. The interest in this class of material is due to their application in automotive, aerospace, and in the fabrication of medical devices. 'Shape memory' is the effect of restoring the original shape of a plastically deformed sample by heating. Titanium alloys belong to the shape memory alloy. Titanium alloys are employed in the manufacture of orthopedic joint replacements [173-176], making titanium alloys one of the actively studied materials both experimentally and theoretically. Therefore, understanding the effect of extreme thermodynamic variables such as pressure and temperature on these materials could assist in their exploration. In a study by Duerig *et al*. [177], it was found that the erasable strains of 3 - 8%, significant internal damping and high yield stresses are desirable mechanical properties and should be considered when developing or growing smart alloys such as NiTi, CuZnAl, CuAlNi and AuCd. Interestingly, NiTi (titanium alloy) is favored in most applications that requires smart alloys due to its superior memory and structural properties. 'Smart' property in the form of structural memory was predicted in α-berlinite ($AlPO_4$) [178] during compression and decompression. The study shows a single crystal of α-berlinite transforms into an amorphous solid and back to the original crystalline structure upon compression and release of pressure, respectively.

Experimental [179-181] and theoretical [170,172,182] studies have been carried out on NiTi. One of such experimental studies was done on thermally induced martensite (M) structure, with monoclinic cell and its parent (P) structure, with CsCl-type cell between 255 K and 363 K using neutron time of flight diffraction [179]. The temperature range of study covers a closed cycle of the M→ P→ M transformations. Martensitic transformation including specimen texture changes were reported in the sample used for the experiment. Furthermore, the behavior of nitinol under directional pressure and temperature were investigated. The experiment was performed in the same temperature and pressure regime for which nitinol exhibits shape memory effect and pseudo elasticity (the process is illustrated in Fig. 3.1). The study indicates the possibility of memory loss at some pressure and/or temperature regime. However, shape memory effect was reportedly observed up to 373 K [180]. Another study investigated the role of $B19'$ martensitic deformation in stabilizing the two-way shape memory effect in NiTi using combined *ex situ* mechanical

experimentation and *in situ* neutron diffraction measurement at finite stress and temperature condition. It was observed that the $B19'$ martensite is deformed by reorientation, detwinning and dislocation activity [181].

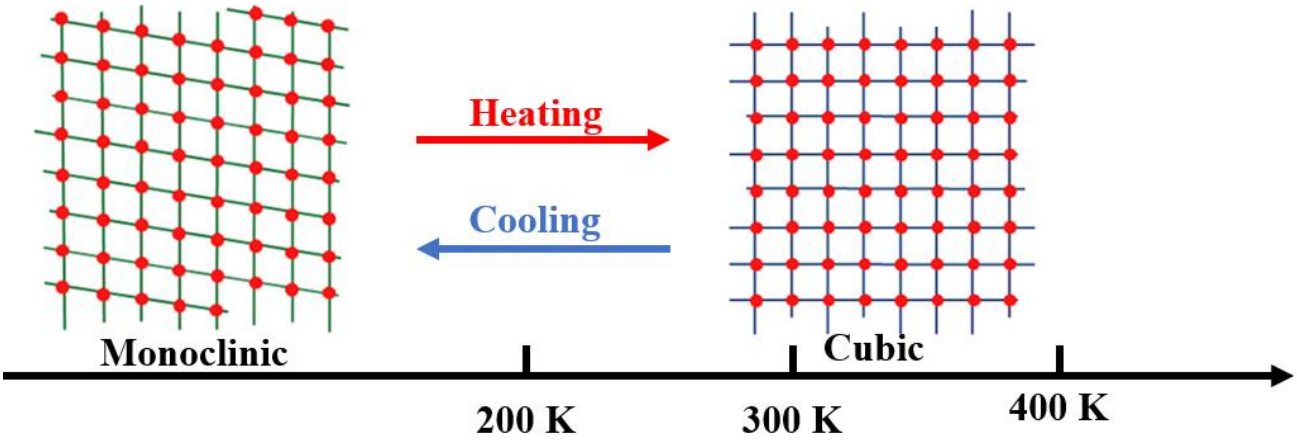

Figure 3.1. Illustration of martensitic transformation in the lattice of NiTi below 400 K. The figure covers a closed cycle of the Monoclinic structure (Martensite) → Cubic (Parent) → Monoclinic (M) transformations. Adapted for illustration from Ref. [182].

From theory standpoint, the energetic stability of nickel-rich, titanium-rich, and equiatomic Ni-Ti alloys relative to elemental Ni and Ti atoms were investigated using the full potential linear-muffin-tin-orbital method [170]. The ambient pressure composition-temperature phase diagram of the Ni-Ti system was established. The study established NiTi as the most preferred stoichiometric configuration for Ni-Ti alloy at temperatures below 373 K. Later, Huang *et al.* [172] performed a first-principles study of the structural energetics of NiTi. The study found the body centered orthorhombic structure with space group *Pbcm* (which lacks shape memory) to be energetically more stable than the known and experimentally observed $B19'$ structure. The $B19'$ structure has space group $P2_1/m$ and shape memory ability. The dynamic stability of the $B19'$ structure, however, is attributed to the presence of residual internal stresses. It is thus proposed that shape memory is primarily stored at the microstructural level. Recently, Liu *et. al*, [183] predicted a semiconducting, high pressure phase of NiTi without shape memory ability. The semiconducting behavior of the predicted phase was associated with the special topological transition and the characteristic *3d* electrons.

Heat-treating titanium alloys such as nitinol suggests improvement in their strength. This observation was made through experimental [179,180] and theoretical studies [170,172] on the materials. However, the threshold beyond which there is a trade-off between improving the strength and the shape memory effect has been scarce in literature. Specifically, structural, and thermodynamic changes that could disrupt martensitic transformation thereby resulting in the loss of shape memory abilities of this material have not been unambiguously established. It is therefore interesting to show that temperature used for the activation of shape memory effects in a mechanically deformed nitinol could also be used to drive it in to a shape-memory-loss regime otherwise known as the permanent deformation phase. Motivated by this gap in knowledge, we perform first principles simulations on the known ambient phase of NiTi (with shape memory) at experimentally achievable thermodynamic conditions. This study sets a precedent for theoretical studies on temperature-induced shape memory loss in nitinol and other titanium alloys with shape memory.

3.1.2 Computational Method

All calculations were performed within the framework of density functional theory (DFT) [184]. Phase transformation and new structure formation under high-pressure, high-temperature (HPHT) conditions were simulated using the metadynamics method [92,185] combined with the projector-augmented plane wave (PAW) method [116] as implemented in the Vienna *ab initio* simulation package (VASP) [93] program. Kinetic energy cut-off of 400 eV was employed for plane wave basis set expansion. Structural optimization, total energies, and electronic band structure of NiTi were calculated using the VASP program, employing the Perdew-Burke-Ernzerhof (PBE) exchange-correlation functional. The Ni and Ti potentials adopt $3d^8 4s^2$ and $3d^2 3s^2$ respectively, as valence states. Bader charge analysis was done using VASP and post processed using Henkelman code [186]. The dynamical stability of known and newly predicted phases of NiTi were investigated using the density functional perturbation theory (DFPT) [118] method. The linear response hessian matrix was computed through the DFPT as implemented in VASP program and post processed using the PHONOPY [102] program. The phonon frequency calculations were performed with a supercell of size 3 × 4 × 6 on a k-point mesh of 2 × 2 × 2 for the $B19'$ phase and supercell of size 3 × 2 × 2 on a k-point mesh of 2 × 2 × 2 for the *P*-1 phase. A Monkhorst–Pack k-point sampling of 12 × 12 × 12 was specifically used to sample the Brillouin

zone (BZ) to ensure that the total forces converge to within 1 meV/atom. Energy convergence was reached when the difference between two iterations is less than 1×10^{-6} eV. Metadynamics [92,185] simulations were carried out in supercells with 24 NiTi formula units (f. u.) and 8 × 8 × 8 *k*-point mesh was used for BZ sampling. Molecular dynamics (MD) [92] for metadynamics simulation was implemented in VASP using a canonical NVT ensemble with a 2 fs time step. The temperature in the simulation was controlled through the Nose-Hoover (NH) [187] thermostat with negligible fluctuation in temperature for metals. Gaussian width (W) and height (δs), related by $W \approx \delta s^2$ were chosen to be 15 (kbarÅ^3)$^{1/2}$ and 225 kbarÅ^3, respectively with the h-space sampled at a step-length of 0.03Å. Ab initio molecular dynamics was performed using VASP in isothermal-isobaric (*NpT*) ensemble. AIMD trajectories were obtained from a 40 ps long simulations sampled with 2 *fs* timestep equilibrated after 2 ps.

3.1.3 Results and Discussion

We began the study by ensuring that the metadynamics method is suitable for this type of study. Thus, we employed metadynamics method in the simulation of martensitic transformation by reproducing the previously observed M→ P→ M transformation cycle [179] in the experimental pressure-temperature (*P-T*) region. Thereafter, we applied the method to simulate structural transformation in NiTi at higher *P-T* region above the field reported in experiment [179]. We also investigate the dynamic stability of NiTi at T=0 K and the vibrations that characterize the high temperature regime. We further study the equation of states and electronic properties of NiTi after the shape memory loss has occurred.

3.1.3.1 Metadynamics simulation of martensite → austenite (parent) → martensite transformation cycle

Metadynamics method was validated through the successful simulation of the experimentally observed martensitic transformation in the $B19'$. This implies that such process can be studied (with confidence) using metadynamics method. An experimental study of thermally induced transformation between martensite (M) and its parent (P) structure in NiTi was studied between 255 K and 363 K using neutron time of flight diffraction [179]. The temperature range of study covers a closed cycle of the M→ P→ M transformations. The Metadynamics method used is

capable of simulating phase transformation at finite pressure-temperature (*PT*) conditions, therefore, we approximate the ambient pressure with ~1 GPa pressure. Test metadynamics simulation was performed at 300 K; a temperature that falls within the 255 K and 363 K used in previous experimental study [179]. The x-ray diffraction (XRD) pattern of the $B19'$ (martensite) structure was calculated before the simulation begins. The simulation was allowed to proceed, until the system attain a temperature of 300 K. The XRD pattern of the configurational average of the 'warm' system (at 300 K) was calculated. All configurations were quenched to 0 K and the XRD patterns were also calculated as shown in Fig 3.2a.

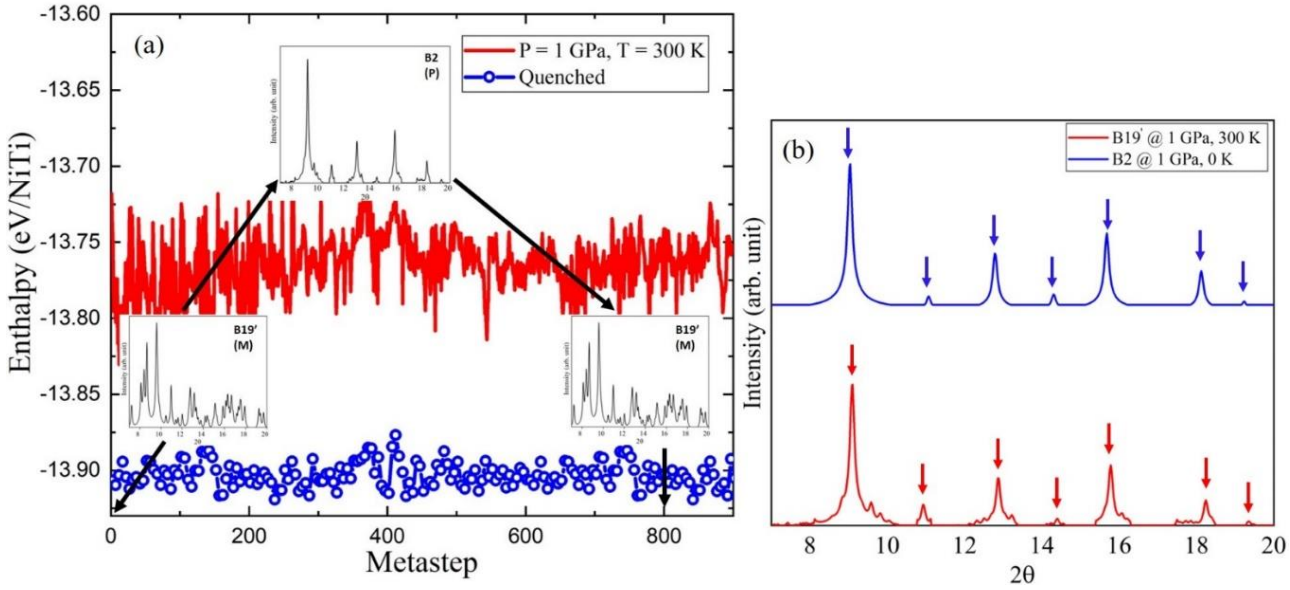

Figure 3.2. (a) Enthalpy evolution during metadynamics simulation of martensitic transition from $B19'$ (M) to B2 (P) and back to $B19'$(M) structure at ~1 GPa, 0 K to ~1 GPa, 300 K and ~1 GPa, 0 K, respectively. Inset is the calculated XRD pattern for the Martensite $B19'$ structure before the simulation, configurational average of the 'warm' system at the end of the simulation time and the quenched configuration (b) Comparison of the calculated XRD pattern for the B2 structure at ~1 GPa, 0 K and the $B19'$ at ~1 GPa, 300 K ($\lambda = 0.3344$ Å). The XRD pattern was calculated using Mercury software [156].

Analysis of the quenched configuration shows that it has an identical XRD pattern with the $B19'$ structure before the start of the simulation. However, the XRD pattern of the 'warm' configuration is completely different from the $B19'$s'. Interestingly, all of the distinct peaks from the 'warm' configuration were successfully indexed to the B2 structure at 0 K (see Fig 3.2b), which shows that the 'warm' $B19'$ structure transforms to the B2 structure for temperature within the martensitic transformation temperature field and back to the $B19'$ when temperature-quenched to 0 K. The evolution of the six collective variables (CV), shown in Fig. 3.3, reveals that the $B19' \rightarrow B2$ transition occurs around 350 metastep. Table 3.1 shows the eigenvalues and the corresponding eigenvectors of the Hessian matrix for the $B19'$ at ~1 GPa indicating that the structure is well within its stability field and reconstructive phase transition can be studied.

Eigenvalue	s_1	s_2	s_3	s_4	s_5	s_6
	1638.51	6167.38	6733.64	8247.67	10598.95	42500.10
Eigenvectors						
h_{11}	0.246	0.208	0.019	0.001	0.805	-0.498
h_{22}	-0.175	0.473	0.026	-0.001	-0.503	-0.701
h_{33}	0.055	-0.851	-0.040	0.000	-0.112	-0.509
h_{12}	0.000	-0.015	0.283	-0.960	-0.001	0.002
h_{13}	-0.952	-0.083	0.004	0.001	0.294	-0.029
h_{23}	0.006	-0.048	0.960	0.284	-0.007	0.007

Table 3.1: Eigenvalues (in unit of kbar Å) and the corresponding eigenvectors of the Hessian matrix for the starting $2 \times 2 \times 3$ $B19'$ supercell calculated at ~1 GPa.

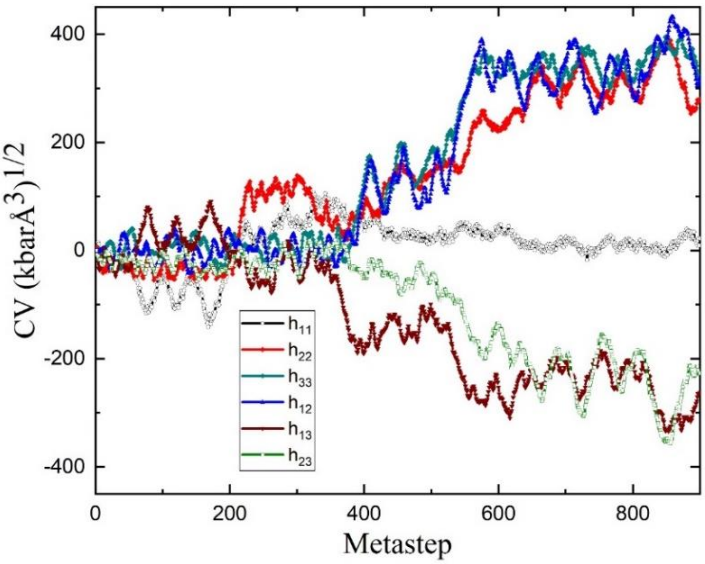

Figure 3.3. Evolution of the six collective variables during metadynamics simulation of transition from $B19'$ to B2 structure at ~1 GPa, 300 K.

3.1.3.2. Crystal Structure and Phase Stability

Metadynamics algorithm has been successfully applied in the study of reconstructive phase transitions in different materials [148,188]. Metadynamics simulations in this study were performed at T = 273 K, 700 K, and 1200 K and at a deformation pressure of 10 GPa, starting from the ambient-pressure B33 (with space group *Cmcm*) structure. The B33 structure was over pressured to push the system to the edge of its stability field in order to accelerate the transformation process. We explored the highest pressure point (10 GPa) for which the eigenvalues of the Hessian matrix are all positive (Tables 3.2 and 3.3), which established the B33 structure as a stable minimum in the potential energy surface. The transformation from austenite to martensite (or vice versa) is instantaneous, hence we simulate this instantaneous effect by temperature-quenching the metadynamics trajectory to 0 K, while maintaining the deformation from external pressure. The simulation reveals a B33→ $B19'$ transformation (see later).

The shape-memory effect in Ni-Ti alloys near equiatomic stoichiometry is related to a reversible martensitic transformation which occurs near room temperature. At ambient pressure and low temperatures, the NiTi is known to crystallize in a monoclinic structure (B19') while the high-temperature P (parent) phase has the simple cubic B2 (with space group *Pm*-3*m*) structure

characterized with lattice instability throughout the Brillouin zone at 0 K [189]. On cooling the B2 structure below the martensitic transformation temperature, the system undergoes a displacive structural transformation into a metastable intermediate phase and then undergoes a martensitic transformation to the monoclinic B19' structure [189]. The high temperature, ambient pressure deformation above preserves martensitic transformation in the material and we successfully reproduced these experimental observations using the metadynamics method employed in this study. Moreover, we observe that the process changes if deformation is first applied in the form of internal stress (or external pressure) to the material before heating it up.

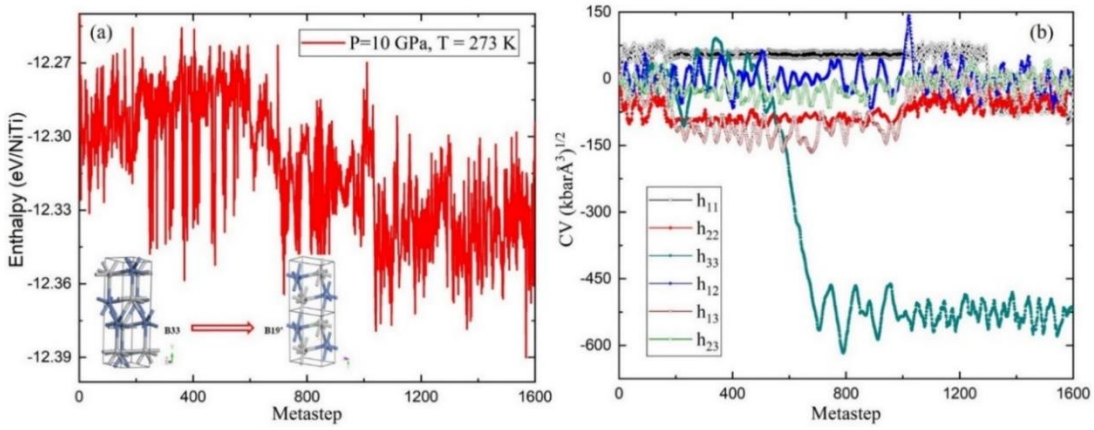

Figure 3.4. (a) Enthalpy evolution during metadynamics simulation of transition from *B33* to $B19'$ structure at 10 GPa, 273 K, (b) Evolution of the six collective variables during metadynamics simulation of transition from *B33* to $B19'$ structure at 10 GPa, 273 K.

The martensitic transformation and shape memory were observed until a T_c [190] of ~700 K was reached. At and beyond 700 K, the B19' NiTi has completely lost correlation with the B2 (the parent) and the B33 (the precursor) phase (see Fig. 3.4a and Fig. 3.5a). This can be linked to the change in coordination number of Ni from 5 to 3 during the initial severe distortion that led to a displacive structural transformation with characteristics lowering and eventual break of symmetry.

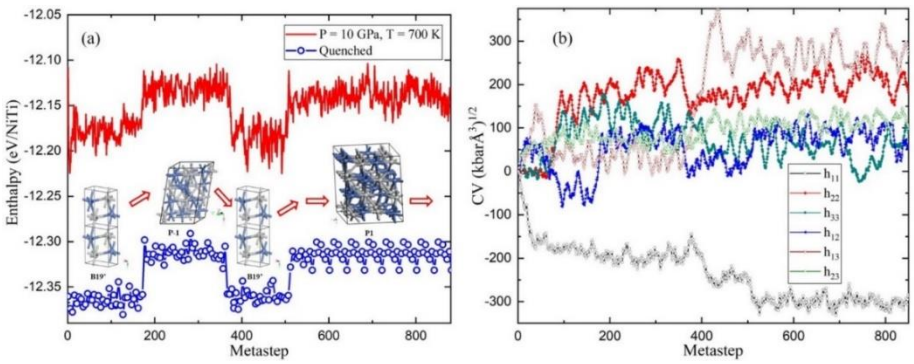

Figure 3.5. (a) Enthalpy evolution during metadynamics simulation of transition from $B19'$ to $P1$ structure at 10 GPa, 700 K, (b) Evolution of the six collective variables during metadynamics simulation of transition from $B19'$ to $P1$ structure at 10 GPa, 700 K.

The metadynamics simulation reveals the occurrence of several metastable phases. The structural information of the metastable phase *P*-1-NiTi is shown in Table 3.4 and *P*1-NiTi in Table A3.1 (in the appendix). We analyze the mechanisms (at the atomic level) that induce the B33→ $B19'$ transformation using the collective variables (CV) extracted from the trajectory of the metadynamics simulation (see Figs. 3.4b and 3.5b). The CVs are linear combinations of the six vectors of the simulation cell (elements in upper triangular matrix of the simulation cell $\vec{h}$) under isotropic deformation supplied to the system in the form of an external pressure.

Eigenvalue	s_1	s_2	s_3	s_4	s_5	s_6
	415.73	7539.16	10361.39	10755.77	12974.95	54150.91
Eigenvectors						
h_{11}	0.002	0.816	0.001	-0.001	-0.242	-0.524
h_{22}	0.001	-0.080	-0.000	0.002	0.851	-0.519
h_{33}	0.000	-0.572	-0.001	0.002	-0.465	-0.676
h_{12}	1.000	-0.001	0.000	0.000	0.000	0.002
h_{13}	0.000	0.001	-1.000	0.000	0.000	0.000
h_{23}	0.000	0.002	-0.000	1.000	-0.001	0.002

Table 3.2: Eigenvalues (in unit of kbar Å) and the corresponding eigenvectors of the Hessian matrix for the starting 3 × 1 × 2 B33 supercell calculated at 10 GPa.

Eigenvalue	s_1	s_2	s_3	s_4	s_5	s_6
	2875.45	6110.08	8251.63	10441.59	13633.92	54323.77
Eigenvectors						
h_{11}	0.204	0.003	0.002	0.100	0.827	0.515
h_{22}	-0.205	0.003	0.002	-0.707	-0.254	0.627
h_{33}	0.113	0.004	0.003	0.653	-0.470	0.583
h_{12}	-0.001	-0.800	0.600	0.001	-0.000	0.002
h_{13}	-0.951	0.003	0.002	0.252	0.176	0.045
h_{23}	-0.002	-0.600	-0.800	0.002	0.000	0.007

Table 3.3: Eigenvalues (in unit of kbar Å) and the corresponding eigenvectors of the Hessian matrix for the starting $2 \times 2 \times 3$ $B19'$ supercell calculated at 10 GPa.

Space group	*a* (Å)	*b* (Å)	*c* (Å)	*α*	*β*	*γ*	*Fractional atomic Coordinates*			
							Atom	x	y	z	Site
P-1	5.18	7.12	8.96	105.51	74.63	90.22	Ti	0.02	0.30	0.14	2i
							Ti	0.09	0.11	0.63	2i
							Ti	0.31	0.96	0.12	2i
							Ti	0.40	0.76	0.61	2i
							Ti	0.59	0.63	0.12	2i
							Ti	0.80	0.45	0.62	2i
							Ni	0.19	0.03	0.87	2i
							Ni	0.43	0.90	0.37	2i
							Ni	0.47	0.71	0.85	2i
							Ni	0.71	0.57	0.35	2i
							Ni	0.91	0.36	0.90	2i
							Ni	0.14	0.21	0.38	2i

Table 3.4: Predicted structural parameters for the NiTi-*P*-1 at a pressure of 10 GPa and 0 K temperature.

As the simulation proceeds, the h_{11} mode remains inactive for a very long time while the other five modes ($h_{22}, h_{33}, h_{12}, h_{13}, h_{23}$) were instantly activated (see Fig. 3.4b and Table 3.3). If we define the edges of the simulation box that contains the B33 (or the $B19'$) structure as $\vec{h}(\vec{a}, \vec{b}, \vec{c})$, it then follows that the volume $V = \det \vec{h}(\vec{a}, \vec{b}, \vec{c})$. Thus, the transformation of B33 to $B19'$ drives the eigenvalues of all the excited modes into negative suggesting that the $B19'$ phase has a reduced volume compared to the precursor B33 phase.

A look at the eigenvalues (Table 3.2) suggests that $B33 \rightarrow B19'$ is dominated by the h_{12} shearing mode with pronounced distortion in the (001) planes and slight volume reduction due to the shortening of the h_{22} and h_{33} mode. The structural change corresponds to pressure on the (011) plane. Significant volume reduction follows the activation of the h_{33} mode causing the cell to adopt the monoclinic face plane. A similar analysis on Table 3.3 suggests a different dynamic. $B19' \rightarrow P$-1-NiTi is dominated by the h_{13} shearing mode with pronounced distortion in the (010) planes and slight volume expansion due to the elongation of the h_{11} and h_{33} mode and reduction of h_{22}. The next change activates the h_{12} and h_{23} shearing mode in the same direction with almost no change in length to compensate for the 'squeezing'. The change does induces lowering of symmetry on the internal coordinates because the cell expands slowly relative to the rate of perturbation of the internal coordinates, causing the cell to eventually adopt a triclinic face plane.

The two major shape memory loss routes identified during the dynamics are discussed below:

3.1.3.2.1 B19' to *P*-1-NiTi

We observe that the lowering and partial breaking of symmetry drives The B19' →*P*-1 transition. The Ti atoms align themselves toward each other (although, no Ti-Ti bonding was observed as the shortest Ti-Ti distance = 2.84 Å) which if formed should be weaker than the Ni-Ti bonding (bond length = 2.10 Å). The *P*-1 can be thought of as the 'pseudo-thermoset' phase of NiTi (thermally distorted form of B19'). This suggests that the *P*-1 phase can only form in the presence of high temperature at high pressure (10 GPa) and then recovered by rapid temperature-quench to 0 K (below martensitic transformation temperature). It further indicates that the free energy surface (FES) of NiTi is significantly modified by temperature which we identified as the

main driver of the observed shape memory loss. Although, we cannot rule out the possibility of a potential energy surface (PES) and FES modification due to the number of NiTi formula units per simulation box.

3.1.3.2.2 B19' to *P*1-NiTi

When the simulation run longer, the system experiences complete symmetry break-down thereby inducing the B19' →*P*1 transition through the *P*-1 phase with negligible energy change. The small energy difference suggests that, in principle, the *P*-1 and *P*1 phase could coexist under this condition. Thus, the *P*1 phase can be thought of as a slightly distorted form of the *P*-1-NiTi. In addition to being structurally different, the *P*-1-NiTi and *P*1-NiTi phases are also topologically slightly different as shown in Figs. 3.6a and 3.6b. with Ni-Ti bond lengths ranging between 2.42 Å and 2.49 Å (still longer and weaker than the typical Ni-Ti bond). As the simulation progresses, hexagonal Ni-Ti rings are formed after the *P*-1-NiTi transformed into the *P*1-NiTi.

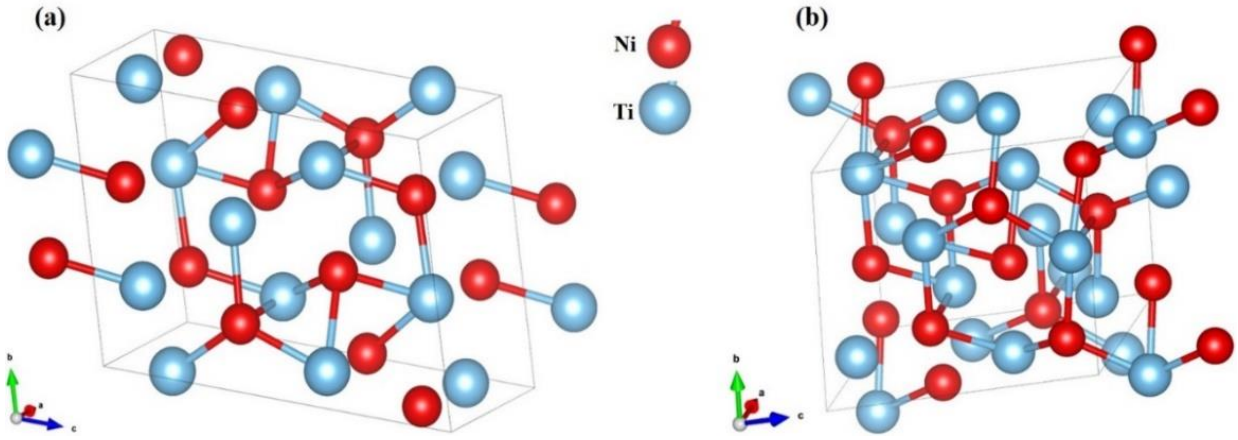

Figure 3.6. Crystal structure of the (a) *P-1*-NiTi (b) *P1*-NiTi at 10 GPa.

The compressibility and the strength of the bonds between atoms in a given structure can be characterized using the bulk modulus (*B*). The *B* is also known to be approximately correlated with the hardness of a material [171,172]. The *B* for the *P*-1-NiTi was obtained by fitting the pressure-volume data to the second order-Birch-Murnaghan equation of states (EOS). The bulk modulus for the *P*-1-NiTi is 211.75 GPa. The *B* of *P*-1-NiTi is about triple of the precursor $B19'$

phase (B = 72.49 GPa) and significantly higher than that of the B33 phase (B = 154.22 GPa). At 10 GPa, the *P*-1-NiTi structure experienced 1.51% expansion in volume relative to the $B19'$. This volume expansion corresponds to a partial weakening of the Ni-Ti bonds and short-range structural changes.

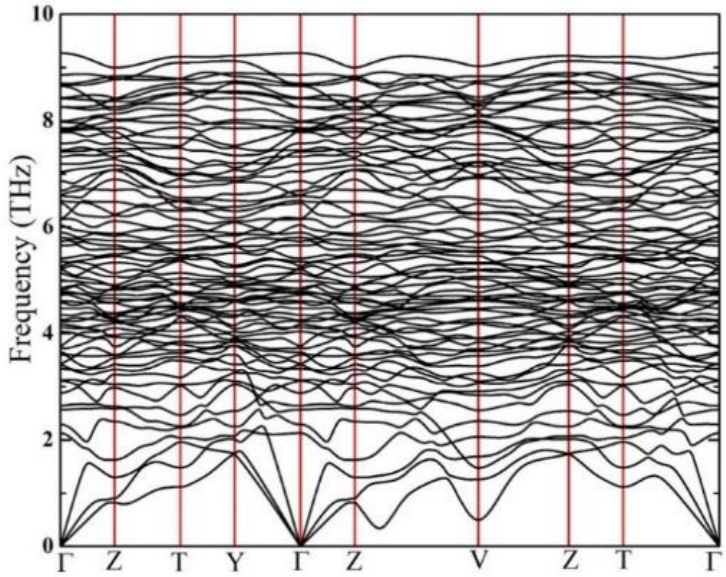

Figure 3.7. Calculated phonon dispersion curve for the *P-1*-NiTi structure at 10 GPa.

3.1.3.3 Lattice dynamics in NiTi at ambient and elevated temperatures

The dynamic stability of the *P*-1-NiTi structure was assessed at 10 GPa, 0 K through phonon calculations (Fig. 3.7). The absence of imaginary frequencies in the phonon dispersion relations establishes its lattice dynamic stability. It also shows that the *P*-1-NiTi structure is temperature quench-recoverable to ambient temperature. Furthermore, the optic branches are nearly flat, revealing collective and nondispersive Ni-Ti vibrons. There is presence of significant soft modes at high symmetry point V and close to Z along $Z \rightarrow V$ direction in the BZ (see Fig. 3.7) suggesting the possibility of the *P*-1-NiTi becoming unstable and possibly transform to another phase, should it be compressed further. The projected phonon density of states (Fig. 3.9b) shows atomic species' contribution to the phonon modes. As expected, because of the smaller atomic mass of Ti compared to Ni, Ti vibration is more probable at high frequency regime than the low frequency regime.

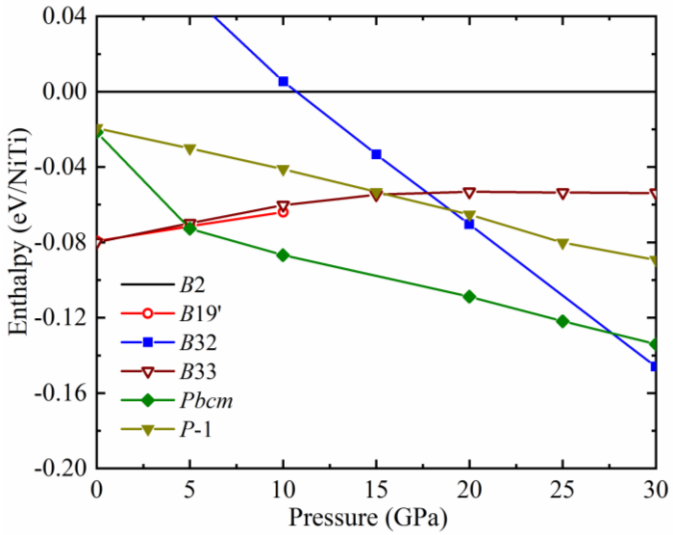

Figure 3.8. Calculated equation of states for NiTi structures in the pressure range 0 – 30 GPa. The B2 structure's enthalpies are taken as reference.

The permanently deformed *P*-1-NiTi is not a thermodynamic ground state (see Fig. 3.8): *P*-1-NiTi is ~0.03 eV/NiTi enthalpically less stable relative to the (experimentally observed) $B19'$ at 10 GPa. Thus, we would expect the $B19'$ phase and the NiTi-*P*-1 phase to have different vibrational free energy that could compensate for the enthalpy difference and possibly stabilize the *P*-1-NiTi structure and make it preferable at high temperature where we have predicted permanent deformation. We therefore estimated the Helmholtz free energy for the *P*-1-NiTi and the $B19'$ structures at 10 GPa using the harmonic approximation [162]. The Helmholtz free energy at temperature *T* is calculated using the relation [191]:

$$F(T) = E_0 + F_{el}(T) + F_{vib}(T)\,, \tag{3.1}$$

Where E_0 is the static crystal energy (which in this case is interpreted as the enthalpy *H*, taken from static calculation at 10 GPa, temperature T = 0 K), $F_{el}(T)$ is the contributions of electronic excitation to the free energy and $F_{vib}(T)$ is the phonon contribution to Helmholtz free energy at finite temperature, defined as:

$$F_{vib}(T) = \frac{1}{2}\sum_{\omega} g(\omega)\hbar\omega + k_B T \sum_{\omega} g(\omega) \ln\left[1 - \exp\left(-\frac{\hbar\omega}{k_B T}\right)\right]\,. \tag{3.2}$$

The $g(\omega)$ is the normalized density of states (DOS) for the phonon branch ω and k_B is the Boltzmann's constant. Considering the effect of the zero-point energy contribution to enthalpy At T = 0 K, the $B19'$ structure remain more stable than the *P*1-NiTi structure by 0.023 eV/NiTi.

For metallic alloys like NiTi, contributions of electronic excitation to the free energy near room temperature are negligible [191,192]. Hence, for the systems under study, at finite temperature and pressure, equation (3.1) reduces to

$$F(T) = H + F_{vib}(T)\,. \tag{3.3}$$

The result of the Helmholtz free energy calculation (Fig. 3.9c) shows that indeed, the *P*-1-NiTi structure is stabilized by temperature. Above temperature of 750 K, the NiTi-*P*-1 structure becomes preferable than the precursor $B19'$ phase. Interestingly, this temperature is near the predicted critical temperature (700 K) for shape-memory loss in the $B19'$ phase.

The vibrational density of states (*v*DOS) was calculated at three different temperatures (273 K, 700 K and 1200 K) below the melting point (1583.15 K) of nitinol using the velocity autocorrelation function obtained from the thermal trajectory of an *NpT* molecular dynamics which in principle, captures the harmonic and anharmonic vibrations [193]. We would like to note that the B33 [194] → $B19'$ transformation proposed in ref. [195] were also verified by this work.

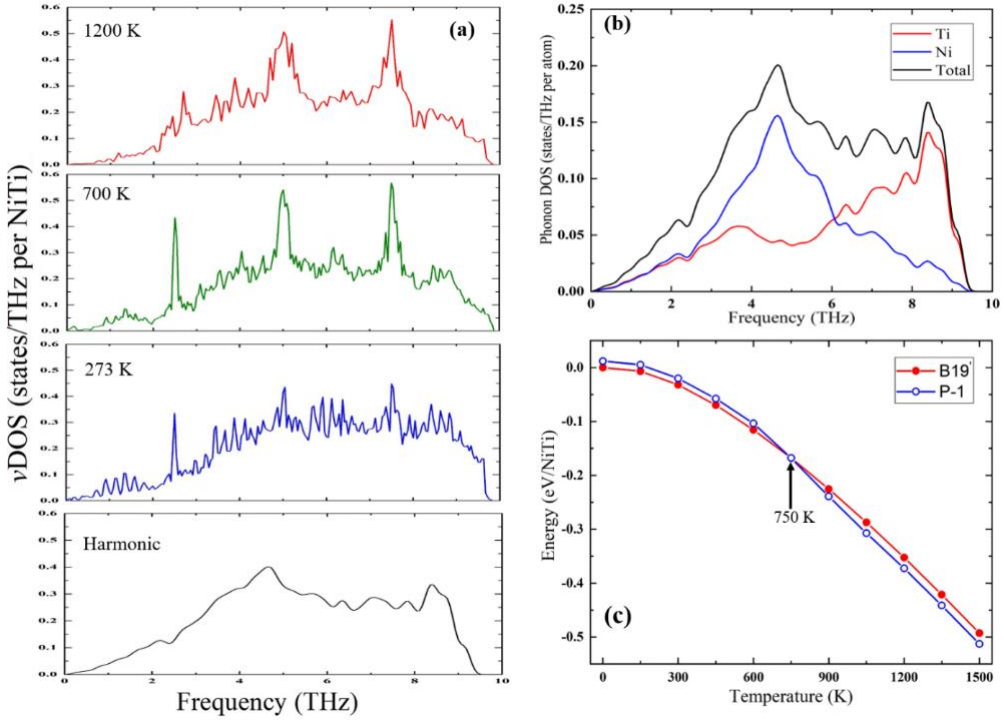

Figure 3.9. (a) Phonon DOS and temperature-dependent *v*DOS for the *P*-1-NiTi structure at 10 GPa (b) The projected DOS for the *P*-1-NiTi structure at 10 GPa. The *v*DOS at finite temperatures were calculated from the trajectories of the molecular dynamics (MD) simulation (c) The

temperature dependent $H+F_{vib}$ (H is the enthalpy and F_{vib} is the vibrational free energy) for the precursor $B19'$ and the *P*-1-NiTi structures at 10 GPa. The energy of the $B19'$ structure at 0 K was used as the zero-energy origin.

From the result of our phonon density of states (phonon DOS) at 0 K and *v*DOS calculations (Fig. 3.9a) at finite temperatures, we observe that the overall profile of the *v*DOS up to about 700 K was retained. A parallel comparison with the phonon DOS reveals that the *v*DOS at finite temperatures (up to about 700 K) have proportionately broadened peaks due to greater degrees of freedom as the temperature of the system is raised. We expected a slightly lowered frequencies due to the unit cell expansion, however we did not observe that (rather, we observed a slightly raised frequencies), probably because the $B19'$ structure is already close to the edge of the stability field (due to over pressuring) before the heating begins. Another possibility is that the *P*-1-NiTi become slightly denser compared to the precursor $B19'$ structure, which, again is expected to raise the frequencies of its vibrational modes. The trend is similar even at 1200 K but characterized by the broadening of several peaks which were not significant in the structure at 0 K and close to room temperature of 273 K. The lattice vibration around 700 K and above become vigorous. The vibrational energy eventually overcome the internal energy that maintain the symmetry of the crystal structure, thereby internally deforming the *P*-1-NiTi structure. This development is partially responsible for the permanent deformation and eventual loss of shape memory in the *P*-1-NiTi and the *P*1-NiTi structures.

3.1.3.4 Electronic structure

The calculated electronic band structure of the *P*-1-NiTi is as shown in Fig. 3.10. The calculated electronic band structure features bands crossing from states below the Fermi energy level to states above it. In most metallic alloys, a large band expansion causes the states slightly below and above the Fermi energy level to overlap, thereby forming a metallic state [196]. It is therefore not unexpected that the band structure of the system under study possesses similar trend. The band structure calculation in the present work reveals that the *P*-1-NiTi structure is metallic.

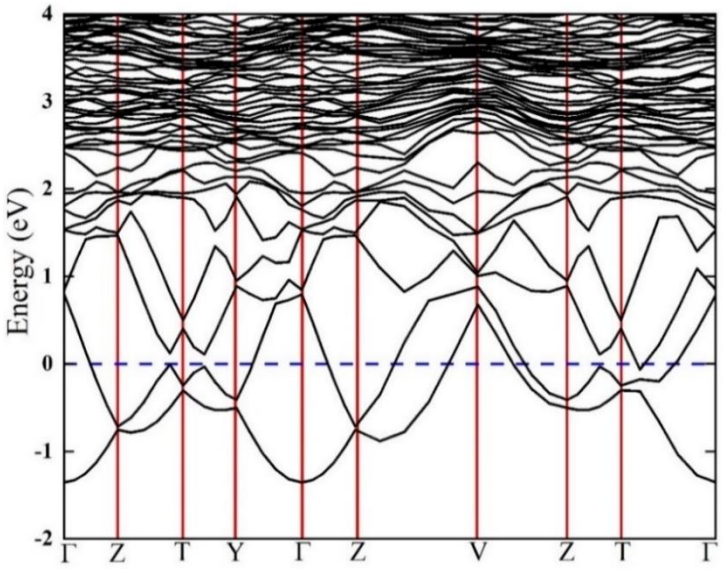

Figure 3.10. Calculated electronic band structure of *P*-1-NiTi structure at 10 GPa along the high-symmetry path. The blue dash line is the Fermi energy level.

3.1.4 Conclusion

We report shape memory loss in NiTi when subject to a pressure of 10 GPa and heated above 700 K. Under high pressure and temperature, the B33 phase transforms to the martensite ($B19'$) phase with shape memory. At and above the critical temperature of 700 K, the $B19'$ structure undergo a permanent deformation during which its losses its shape memory capability and transform to the *P*-1-NiTi and *P*1-NiTi structures. The *P*-1-NiTi structure is predicted by phonon calculations to be dynamically stable at 0 K. The result of the Helmholtz free energy calculation shows that the *P*-1-NiTi structure becomes lower in energy than the $B19'$ structure at 10 GPa and in the temperature range between ~750 K and 1500 K considered in this study, suggesting that the structure is stabilized by kinetics. The study elucidates, at the atomic level, the process that drives such permanent deformation. This study will stimulate both experimental and theoretical studies on property stability of smart structures and Ti alloys such as nitinol in order to prevent property failure when used in fabrication of devices intended to be operated at extreme conditions.

3.2 Stable compounds of two bulk-immiscible metals, Fe-Au under high pressure

The earth crust is known to be depleted of gold (Au) among other slightly heavy noble metals transported by magma from the mantle to the crust. The bulk silicate earth (BSE) model also suggests significant depletion of Au in the silicate mantle which cannot be explained by the amount of Au in the mantle's magma. The partitioning of depleted Au from the mantle farther into the Earth's interior could be possible but this conjecture needed to be computationally tested to understand the behavior of Au around Fe at high pressure especially since magnetic Fe do not form bulk alloy or compounds with heavier metals such as Au. Here, using first principles methods, we predicted the formation of bulk intermetallic compounds of two bulk-immiscible components, Fe and Au. We found that the systems are stabilized by pressure and notable electron transfer. The results also point towards chemical properties' change under pressure for Au as we have found that Au that would exist as cation could gain electrons to become anions under pressure.

3.2.1 Introduction

The collision followed by aggregation of planetesimals resulted in the formation of the Earth [197]. Geological and seismological models for various regions of the earth are constrained by comparing the composition of meteorites, which are similar to the planetesimals that make up the region of interest [32]. These direct comparisons have led to the conclusion that the earth crust was depleted of some siderophile elements such as platinum (Pt), nickel (Ni) and gold (Au). Furthermore, one cannot rule out the possibility that other lithophiles, with propensity to become siderophiles under pressure, such as vanadium (V), chromium (Cr), manganese (Mn) and cesium (Cs) may have also percolated deep down into the core [32-33,197]. The big challenge one must deal with is the fate of these elements in the presence of core dominant materials such as Fe/Ni at high pressures up to the pressure of the inner core [198,199]. Possible answer to the question of where these depleted elements went, was proposed by Wood *et al*. [33], where it was suggested that these elements were pulled into the Earth's iron-rich core while maintaining a molten magma-decorated surface. Meanwhile, some seismological studies [200] have suggested 2-5% density deficit for the solid Earth's inner core, proposing that the Earth's core is not a 'bank' of pure Fe,

after all. The Earth core, therefore, must as well be home to light siderophile elements such as Si, S, H, and C [30,201]. Recent high temperature-high pressure experiments combined with theoretical studies have proposed the reactivity of noble gases such as Xe [22] and Ar [44] with Ni and Fe through the formation of intermetallic compounds.

Au, being one of the precious noble metals and one of the least reactive chemical elements is of great interest, partly because of its economic values, inertness and remarkable stability of its crystal structure over a wide range of pressures [202-204]. We know that the Earth's core is a bank of Fe and Ni, but predominantly Fe. However, Au is heavier than Fe suggesting that if they successfully form compound, it may or may not have direct implication for the Earth's core. Therefore, as a first step, it will be interesting to demonstrate that a chemical reaction could occur between Au and Fe. Meanwhile, that many pairs of metals do not mix, at least under ambient conditions pose some challenges for such a reaction and preclude our understanding of how Fe-Au alloy maybe remotely or directly related to the Earth's interior. For example, many magnetic metals such as Ni, Fe and Co do not form bulk alloy or compounds with many other heavier metals (e.g. Au) primarily because of the mismatch between the sizes of the constituent atoms involved [205,206]. Therefore, the effect of pressure in creating a perfect configuration for both Fe and Au to mix will be worth investigating.

Interesting physics plays out under pressure and as such ushers in new chemistry. One of such chemistry is demonstrated in the formation of intermetallic compound of Fe and Au under pressure, being reported here. Notably, we uncovered several interesting results. As it will be shown in the subsequent sections, Fe-Au compounds can form at a pressure of at least 123 GPa and the crystal structures adopted when formed were predicted. Analysis of the electron density topology and Bader charges [207] revealed an unusual charge transfer between Au and Fe. This work contributes to our understanding of the chemistry of Au.

3.2.2 Computational method

Crystal structure search was carried out using the particle swarm-intelligence optimization (PSO) [100,101] algorithm. All predicted crystal structures were processed through density functional theory [184] calculations. The structure search was done at ~0 GPa, 50 GPa, 100 GPa, 140 GPa and 200 GPa with simulation cells containing 1, 2, 3, 4, Fe_xAu_y formula unit (f.u).

Correlation effect on the 3*d* electrons of Fe were treated within the GGA+U framework with an on-site coulomb interaction U_{eff} ($U_{eff} = U\text{-}J$) of 8.6 eV [208,209]. Since such treatment of Fe yields good agreement with experimental results especially in the pressure field of interest (see Fig. A3.2 in the appendix), pressure dependence of U was ignored. Structural optimization and electronic structure calculations were performed with in the density functional theory (DFT) [184] and dynamic stability calculations within the density functional perturbation theory (DFPT) [79,118] as implemented in the Vienna ab initio simulation package (VASP) [93] code. The projector-augmented wave (PAW) [116] potentials with Perdew-Burke-Ernzerhof (PBE) [61] functional was used in which the valence state of Au and Fe are treated as $5d^{10}6s^1$ and $3p^63d^74s^1$, respectively, with an energy cut-off of 450 eV. To ensure that force on all atoms converge to within 1 meV/Å, the entire Brillouin zone (BZ) was sampled with a k-point grid of $2\pi \times 0.02$ Å^{-1}. We performed first-principles electronic structure calculations within DFT, using the VASP [93]. Bader charge analysis was done using VASP and post processed using Henkelman code [186].

3.2.3 Results and discussion

3.2.3.1 Phase Stability and Stable Crystal structures of Fe-Au

We systematically searched for stable structures of the binary Fe_xAu_y ($x, y \in \{1, \ldots, 4\}$) with cells containing 1 to 4 Fe_xAu_y formula unit (f.u.) at pressures (P) between 0 and 200 GPa and 0 K temperature. The convex hull calculated at various search pressure points shows that Au and Fe do not form a compound at ambient conditions up to at least 140 GPa (Fig. 3.11). At 140 GPa, an orthorhombic $AuFe_4$ (with space group *Cmcm*) becomes thermodynamically stable relative to elemental decomposition into *fcc*-Au and *hcp*-Fe as it lies on the convex hull and as such should be synthesizable (Fig. 3.11a). Furthermore, at 200 GPa, The $AuFe_4$ crystalizes into a tetragonal cell with space group *I*4/*m*. An orthorhombic metastable phase with respect to the tetragonal *I*4/*m*-$AuFe_4$ was also uncovered (Fig. 3.11b) with stoichiometry $AuFe_3$ (*Pmmn*).

The inclusion of the contribution of lattice vibration at 0 K (zero-point energy) to free energy did not change the formation pressure nor destabilize stable phases, however, the magnitude of the formation enthalpy for stable phases were slightly changed (Fig. 3.12). The calculated equation of states (EOS) for the predicted structures reveals that *Cmcm*-$AuFe_4$ has a stability pressure field of 120 to 160 GPa (Fig. 3.11c) and as such will decompose below 120 GPa

and above 160 GPa. This explains why our structure search at 100 GPa and 200 GPa could not identify this structure. On the other hand, however, the *Pmmn*-$AuFe_3$ and *I4/m*-$AuFe_4$ phases are thermodynamically stable from 184 GPa up to at least 210 GPa considered in this study (see Fig. 3.11d). The crystal structures of *Cmcm*-$AuFe_4$, *Pmmn*-$AuFe_3$ and *I4/m*-$AuFe_4$ phases are shown in Fig. 3.13. The optimized structural parameters of *Cmcm*-$AuFe_4$ at 140 GPa are a = 12.12 Å, b = 4.00 Å, c = 3.69 Å with Au atoms located at 4c: 0.000, 0.796, 0.750 and Fe atoms at 8g: 0.883, 0.325, 0.750; 8g: 0.705, 0.333, 0.750. At 200 GPa, the optimized structural parameters of the thermodynamic ground state *I4/m*-$AuFe_4$ are a = 10.00 Å, c = 10.01 Å with Au atoms located at 2b: 0.000, 0.000, 0.500 and Fe atoms at 8h: 0.091, 0.690, 0.000. For completeness, the optimized structural parameters of the metastable *Pmmn*-$AuFe_3$ at 200 GPa are a = 2.35 Å, b = 2.95 Å, c = 9.86 Å with Au atoms located at 2b: 0.000, 0.500, 0.585 and Fe atoms at 2b: 0.000, 0.500, 0.833; 2b: 0.500, 0.000, 0.947; 2b: 0.500, 0.000, 0.729.

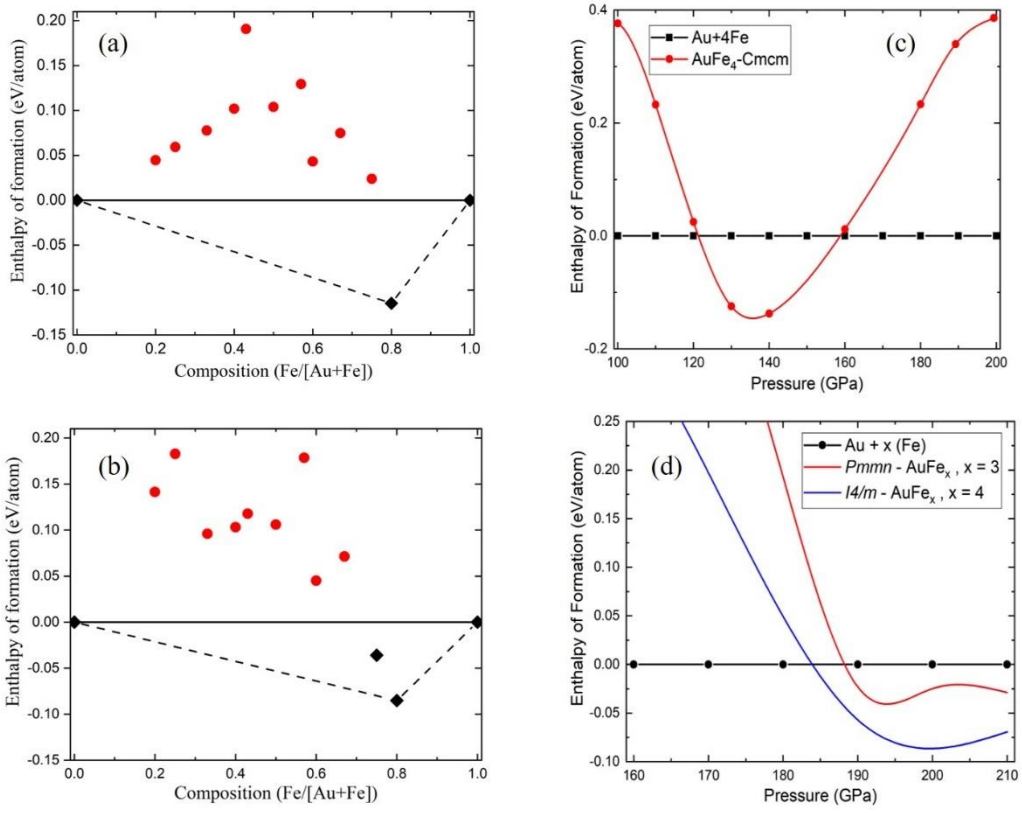

Figure 3.11. Enthalpy of formation of various Fe-Au compounds with respect to constituent elemental decomposition (a) at 140 GPa (b) at 200 GPa. Calculated enthalpies per atom for (c) *Cmcm*-$AuFe_4$ structure with respect to the mixture of elemental Fe and Au (d) *Pmmn*-$AuFe_3$ and *I4/m*-$AuFe_4$ structures with respect to the mixture of elemental Fe and Au.

We performed spin polarized quantum energetic calculations on the *Cmcm*-$AuFe_4$ phase at 140 GPa, and 2×2×1 supercell of *Pmmn*-$AuFe_3$ and *I4/m*-$AuFe_4$ phases at 200 GPa. The results of the energetic calculation reveal that the preferred magnetic states of each structure are as follows: (a) The ferromagnetic configuration of the *Cmcm*-$AuFe_4$ at 140 GPa is 0.4 meV/atom lower than the nonmagnetic configuration and is ~0.17 eV/atom lower than the paramagnetic, antiferromagnetic and ferrimagnetic configurations, indicating that the ferromagnetic configuration is preferred with a magnetic moment of $2.15\mu_B$, although elemental Au exists as a diamagnet in its bulk form [210]. (b) for the *Pmmn*-$AuFe_3$ and the *I4/m*-$AuFe_4$ at 200 GPa, we obtained that the nonmagnetic configuration is preferred, which is ~1.2 meV/atom lower than the ferromagnetic configuration and ~0.2 eV/atom lower than the paramagnetic, antiferromagnetic and ferrimagnetic configurations. This is not entirely surprising since 200 GPa already exceeded magnetic transition pressure for most transition metals [211]. We would like to note that spin polarized quantum calculations were carried out on the lowest enthalpy structures for all stoichiometries explored.

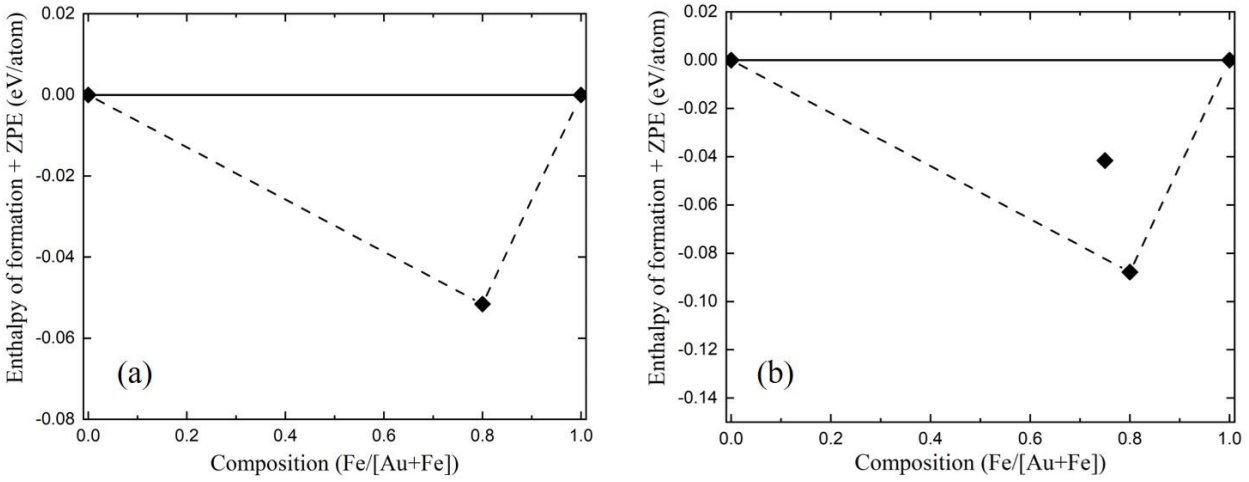

Figure 3.12. Enthalpy of formation + zero-point energy of various Fe-Au compounds with respect to constituent elemental decomposition (a) at 140 GPa (b) at 200 GPa.

The crystal structure of the *Cmcm*-$AuFe_4$ phase at 140 GPa and the *I4/m*-$AuFe_4$ and *Pmmn*-$AuFe_3$ phases at 200 GPa is shown in Fig. 3.13 (a, c, d). The *Cmcm*-$AuFe_4$ at 140 GPa is

characterized by two layers of distorted hexagonal close packed Fe atoms connected by four-coordinated Au atoms (Fig 3.13b). The bond length of metal-metal Fe-Au bond is 2.34 Å and Fe-Fe bond is between 2.16 Å and 2.22 Å (which is well within the Fe-Fe bond length of 2.21 Å for *hcp*-Fe at 140 GPa) with Au-Au having interatomic distance of the order of 2.45 Å suggesting that the Au-Au interaction is rather weak. The formation of Fe-Au bonding at 140 GPa is thus favorable as an average of Fe-Fe and Au-Au bonding. In the *I*4*/m*-$AuFe_4$ at 200 GPa, Au atoms adopt a body centered cubic position while Fe atoms are interspersed within the cell (Fig. 3.13d). In the primitive cell of the *I*4*/m*-$AuFe_4$ phase, the metal-metal Fe-Au bond is 2.29 Å (which is shorter and stronger than is observed in the *Cmcm*-$AuFe_4$ at 140 GPa if we follow 'shorter'='stronger' maxim for chemical bonds) and Fe-Fe is 2.32 Å. The Au-Au have interatomic distance of the order of 3.94 Å which indicate a very weak (or close to none) Au-Au interaction compared to what was observed at 140 GPa.

We observe however, that the metastable *Pmmn*-$AuFe_3$ at the same pressure may be phase segregated with Fe atoms coming together to form two distinct 3D hexagonal caged structures with four-coordinated Au atom occupying one of the cage terminals but packed in the same unit cell (see Fig. 3.13e). The 3D hexagonal caged structures are arranged such that the cage above is shifted about halfway between the Au-Au interatomic distance below it, while Au atoms form a puckered but non-bonding interface in space. This unique configuration increases coulombic interactions between the Au-decorated interface between the 3D hexagonal caged structures along the *c* direction thereby increasing the energy of the structure and inducing phase segregation in the same direction. This suggests that the *Pmmn*-$AuFe_3$ phase may require high temperature to stabilize over the *I*4*/m*-$AuFe_4$ phase in an event of laboratory synthesis. In general, the external stimuli, pressure, thus stabilize the formation of Fe-Au intermetallic compounds through the formation of stronger Fe-Au bonding.

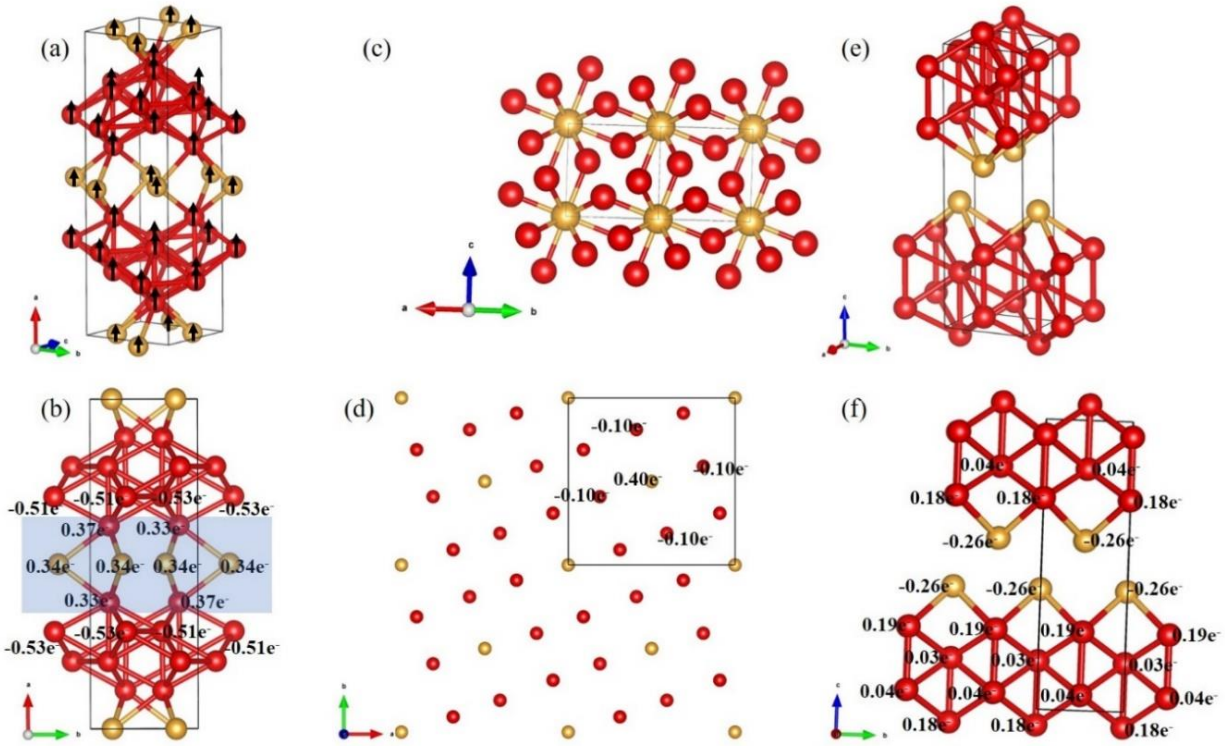

Figure 3.13. Crystal structure of (a) *Cmcm*-$AuFe_4$ at 140 GPa. The arrows, not drawn to scale, indicate spins aligned parallel to each other – ferromagnetic ground state (b) *Cmcm*-$AuFe_4$ at 140 GPa in 2D with Bader charge distribution. The blue shaded region indicates the Au/pseudo-Au charge transfer region (c) *I*4/*m*-$AuFe_4$ at 200 GPa (d) *I*4/*m*-$AuFe_4$ at 200 GPa in 2D with Bader charge distribution (e) *Pmmn*-$AuFe_3$ at 200 GPa (f) *Pmmn*-$AuFe_3$ at 200 GPa in 2D with Bader charge distribution. Red spheres are the Fe atoms.

3.2.3.2 Dynamic stability and Mechanical properties of Fe-Au

We established the dynamic stability of the various predicted phases of Fe-Au through the calculation of phonon dispersion relations (Fig. 3.14). All of them show no imaginary frequencies throughout the BZ indicating dynamic stability within the harmonic approximation [162]. The phonon density of states projected to each atomic species show that the vibration of both Fe and Au are correlated in the acoustic region while optic vibrations are due (predominantly) to Fe atoms.

At 200 GPa, two structures are predicted to be synthesizable (see Fig. 3.11b) with the *I*4/*m*-$AuFe_4$ being the thermodynamic ground state and the *Pmmn*-$AuFe_3$ being metastable.

We further investigate the response of all predicted phases to an external strain, which in principle, is a measure of their elastic and mechanical stability (Table A3.2 in the appendix). The results indicate that all the predicted phases are elastically and mechanically stable and their Pugh's ratio also indicates that they are ductile.

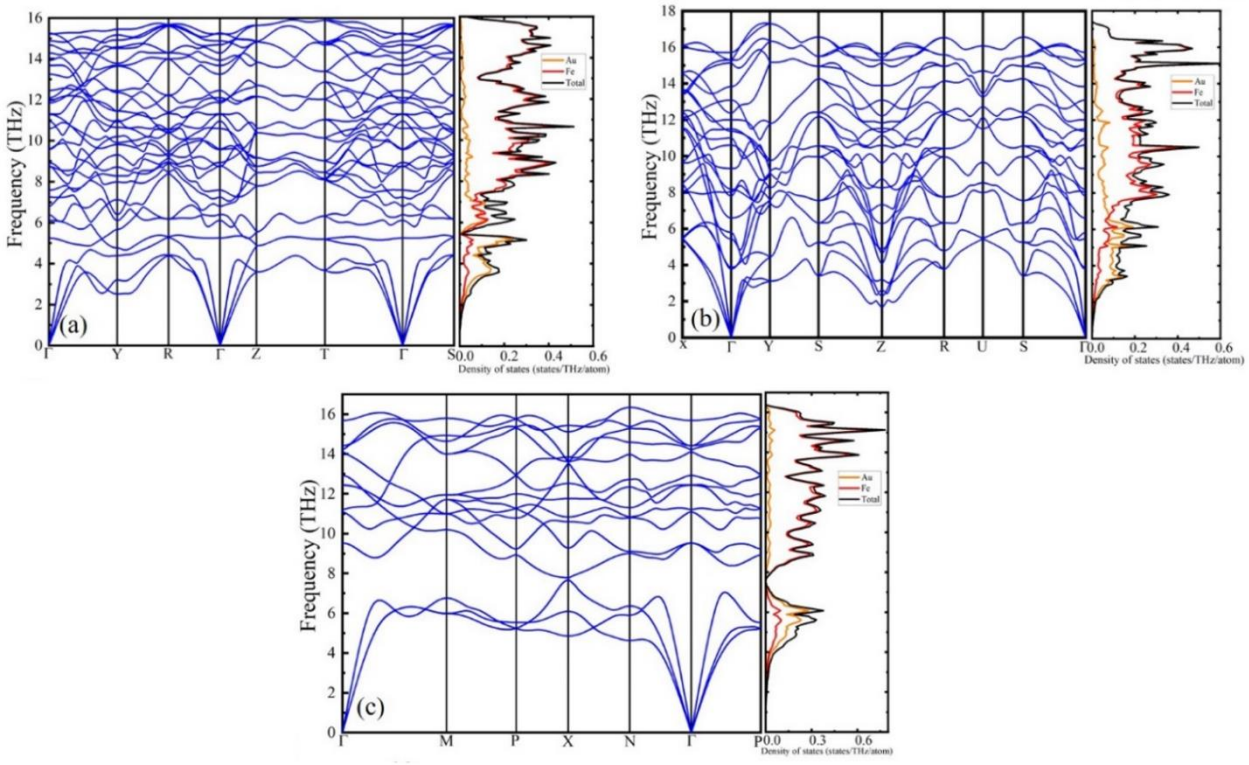

Figure 3.14. Phonon dispersion relations and phonon density of states projected to atomic species for (a) *Cmcm*-$AuFe_4$ at 140 GPa (b) *Pmmn*-$AuFe_3$ at 200 GPa (c) *I*4/*m*-$AuFe_4$ at 200 GPa.

3.2.3.3 Electronic structure of Fe-Au

The calculated electronic band structure (Figs. A3.1a-c, in the appendix) shows that all the three Fe-Au systems reported in this work are metallic in nature. The electronic density of states (DOS) projected to orbitals (Figs. 3.15) reveal that the states around the Fermi level are primarily Fe 3*d* states with some contribution from Au 5*d* states, thus, Fe 3*d* and Au 5*d* states are responsible

for their metallicity. The electronic structure of Au is very similar to the alkali metals with one electron in an *s*-state, but different from the alkali metals in that conduction electrons in Au are influenced by the overlap of the *d*-electrons (from *d*-band that lies below the Fermi surface) of the atomic core with the bottom of the *s*-band. This induces a raise in the density of states (DOS) contributed by Au *d*-electrons in the Fe-Au systems relative to the elemental DOS, while the *s*-band contributes no *s*-electrons around the Fermi energy level signifying an $s \rightarrow d$ transition in Au electronic structure as it forms intermetallic compound with Fe under pressure (with exception observed in the metastable *Pmmn*-$AuFe_3$ at 200 GPa).

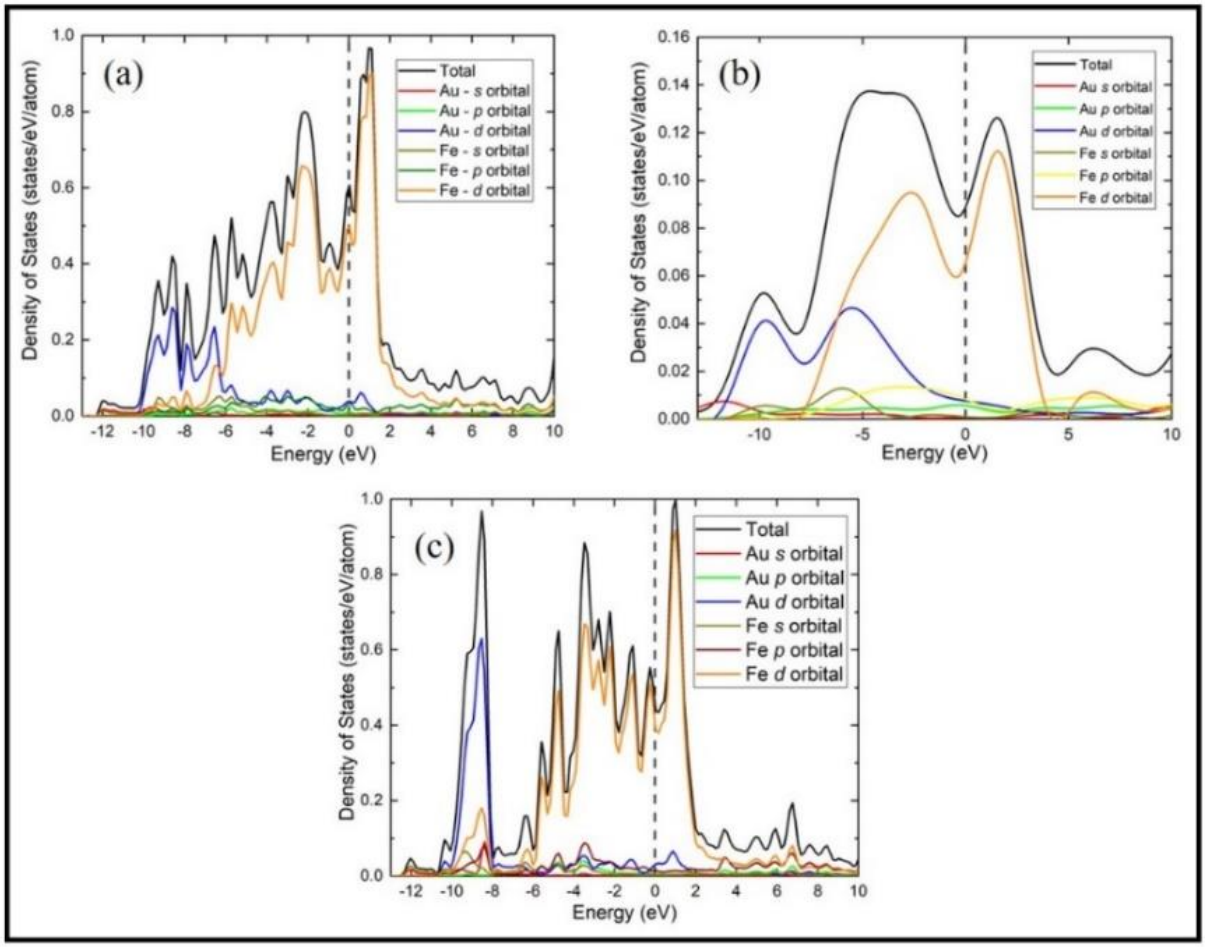

Figure 3.15. Calculated, non-magnetic, electronic density of states projected to orbitals for the (a) *Cmcm*-$AuFe_4$ at 140 GPa (b) *Pmmn*-$AuFe_3$ at 200 GPa (c) *I*4/*m*-$AuFe_4$ at 200 GPa. The black dashed line represents the Fermi energy level.

The result of Bader charge analysis (Figs. 3.13b, 3.13d, and 3.13f) reveals that one type of charge transfer motif dominates this class of material. During charge transfer, atoms of the same chemical elements can behave as though they are different, depending on their neighboring atom which is dictated by their atomic site. This is particularly observed in Fe atoms for all the systems studied. Interestingly, in the metastable *Pmmn*-$AuFe_3$ at 200 GPa, Au functions as anion with each Au atom gaining $0.26e^-$ and each Fe atom losing between $0.04e^-$ and $0.19e^-$. Although, it is odd for electron to be transferred to Au; in fact, only the most electropositive elements are able to fully transfer an electron to Au thereby making it achieve a negative oxidation state as observed in Cesium auride (CsAu) [212,213]. This means that in the metastable *Pmmn*-$AuFe_3$, the 6*s* orbital of Au atom is energetically stabilized and its electron affinity increased thereby resulting in a negatively polarized valence state with a negative charge number.

At 140 GPa, Au atoms in the *Cmcm*-$AuFe_4$ each lose $0.34e^-$ making them cationic in nature, although the mechanism is different for Fe atoms. The Fe atoms at the first 8g sites also lose between $0.33e^-$ and $0.34e^-$ there by making them cations and as such behave like Au (for the purpose of charge transfer discussion, we will refer to them as pseudo-Au). The region occupied by the Au and the pseudo-Au atoms in the unit cell is marked with a blue background in Fig. 3.13b. Fe atoms at the second 8g sites, are second nearest neighbor to Au and therefore gain between $0.51e^-$ and $0.53e^-$ each to become anions. Thus, the *Cmcm*-$AuFe_4$ is stabilized through electron transfer from Au and pseudo-Au atoms to Fe atoms.

It can be summarized that the role of Fe atom in charge transfer (for the *Cmcm*-$AuFe_4$) depends on the atomic site it belongs in the crystal which greatly influence their electron affinity. Similar charge transfer mechanism to *Cmcm*-$AuFe_4$ is also observed in the *I*4*/m*-$AuFe_4$ at 200 GPa although with no pseudo-Au behavior because Fe atoms become highly electronegative at such high density. Au atom in the *I*4*/m*-$AuFe_4$ loses $0.40e^-$ making it a cation while each Fe atom gain $0.10e^-$ there by making them anions. Similar charge transfer mechanism has been reported for Fe and Ni in Xe-Fe/Ni system [22] where Fe functions as electron acceptor.

3.2.4 Conclusion

We investigated the reactivity of Au and Fe using first principles methods. It was found that at a threshold pressure of 123 GPa, Au could form stable compound with Fe. The Fe-Au intermetallic compounds are predicted to be stabilized by high pressure and electron transfer. Au exists as anion in the $AuFe_3$ configuration and as cation in the $AuFe_4$ configuration, providing further evidence to support the striking chemistry of Au being able to adopt variable oxidation state spanning both negative and positive numbers. At 140 GPa, a ferromagnetic *Cmcm*-$AuFe_4$ was uncovered. The present work also set the stage for further studies to completely elucidate the elastic properties of the predicted Fe-Au solid phases at finite temperatures and higher pressure above 300 GPa.

CHAPTER 4

FORMATION OF NOBLE GAS ELEMENT – TRANSITION METAL COMPOUND: A CASE STUDY OF Ar-Ni

A similar version of this chapter has been published as a research article in the ACS Earth and Space Chemistry. The references are as follows.

1. Adeleke A. A., Kunz M., Greenberg E., Prakapenka V. B., Yao Y. and Stavrou E., High-pressure compound of argon and nickel: noble gas in the Earth's core? *ACS Earth Space Chem.,* 3, **2019** 2517-2524.

4.1 High-pressure compound of Argon and Nickel: noble gas in the Earth's core?

Ar is the most abundant noble gas element in the atmosphere with an octet state configuration. However, studies of the earth's atmosphere have shown about 50% of the degassed Ar are unaccounted for by various proposed geophysical models. Furthermore, Ar produced from natural decay of ^{40}K remains in the Earth's core. This suggests that sizable amount of Ar may have found their way into the Earth's core and chemically react with the core's nickel or iron. Here we report the theoretical identification of a synthesized stable Ar-Ni compound under a condition representative of the Earth's core thermodynamic condition. First principles calculations reveal that Ar is anionized and the Ar-Ni is an intermetallic compound. This finding shows that the Earth's core is a viable reservoir for Ar storage. The synthesis of a Ar-Ni compound has significant implications for understanding the natural decay of ^{40}K and the heat balance for continuous running of the Earth's geodynamo.

4.1.1 Introduction

The heat powering the dynamics of the Earth is produced by the cooling of the inner core's solid iron. The various heat sources identified to be powering the Earth's geodynamo are latent heat, primordial heat, heat from chemical differentiation, heat from natural decay of ^{40}K and heat from natural decay of heavy radionuclides such as ^{238}U and ^{232}Th [214]. Heating from natural decay of mantle domicile radionuclides is believed to come from ^{40}K. This is because during the Earth's differentiation, lithophilic U and Th are believed to have moved to the silicate mantle and their abundance in the mantle are consistent with the composition of undifferentiated protoplanetary materials [32,214]. The concentration of ^{40}K on the other hand is believed to be depleted: its abundance in the mantle is about 50% less than in undifferentiated protoplanetary materials [34]. Therefore, the missing ^{40}K could have escaped into the space or percolated into the Earth's core. So far, no isotope of K has been reported to have exceeded their expected concentration in various solar system bodies in space [215]. This suggests that the missing ^{40}K could not have escaped into space. Potassium exhibits interesting properties under pressure. The lithophilic K progressively becomes siderophile under high pressure [32,33,197,214]. This creates a perfect condition for K to segregate into the Earth's core at high pressure relevant to the core. If the missing ^{40}K (50%) has indeed percolated into the core, it means that the Earth's core contains a lot of radioactive ^{40}K, that generate heats as it decays.

Argon (Ar), a member of the noble gas (NG) elements is produced in the Earth's core mainly through natural decay of potassium (^{40}K) and its concentration is directly and linearly related to the concentration of ^{40}K in the Earth's core [216,217]. Ar is produced from ^{40}K through electron capture. The ^{40}K has a half-life of 1.25 billion years, which means that the radioactive process is slow enough for ^{40}K to generate heat for a very long time. The Ar produced during this process must either remain in the Earth's core or escape into the mantle. Early in Earth's history, volcanic degassing resulted in mass fractionation of the abundance Ar, resulting in about 50% deficit in the abundance of Ar. This means that the mass of Ar in the bulk silicate earth (BSE) does not balance with the sum of the mass of atmospheric Ar, continental crust Ar and the depleted mantle Ar [34,216-218]. This observation is the 'missing argon' paradox which is one of the long-standing problems in geophysical sciences. Since Ar cannot escape to the space owing to its heavy atomic mass (mass number 36-40), then it is not unreasonable to opine that the Ar produced within

the Earth's core through natural decay of ^{40}K is retained within the Earth. While retained in the Earth's core, Ar must somehow chemically react with main Earth's core materials – Fe/Ni.

Ar do not form compound at ambient conditions because of its octet state configuration. So far, experimentalists have not been able to show reaction between Ar and the Earth's core main constituents – Fe/Ni, even at extreme conditions. Previous theoretical explorations shows that Ar could react with Mg at 300 GPa [219] and Li in a $1{:}\,x;\ x \in \{1,3,5\}$ for Li:Ar stoichiometry at 109 GPa [220]. However, up to 400 GPa explored, there was no show of reactivity between Ar and Ni [221]. The report of no show of reaction between Ar and Ni by previous theoretical study is unexpected but could be due to insufficiency in the computational methods (see later). Over the years, the chemistry and physics of NG elements has evolved [22,221] and the state of NG elements such as Xe, He, Ne and Kr [219, 222-224] at high pressures have been extensively studied and they show propensity to form stable compounds.

While conclusive solution to the "missing argon" paradox within the mantle remains elusive, various theoretical and experimental efforts have also not been successful in realizing stable Ar containing compound(s) in the pressure-temperature (*PT*) field of the Earth's core. In the present study, we address the question of 'where the Ar produced from ^{40}K goes within the Earth's core. The possibility of a chemical reaction between Ar and Ni at *PT* conditions representative of the Earth's core was explored. High pressure experiment was performed by compressing a mixture of Ar and Ni in a laser-heated (LH) diamond anvil cell (DAC). Following the experimental realization (corroborated by density functional theory, DFT, calculations) of a stable Ar – Ni compound, we propose that the earth core has a great propensity to function as a reservoir for the Ar produced during radioactive decay of ^{40}K, in the form of an intermetallic compound, ArNi. The result of this study will motivate further study into geological verification of the existence of ArNi compound(s) in the Earth's core and contribute, broadly, to the understanding of the physics and chemistry of NG elements at high pressure and temperature. Details of experimental methods and other experimental results can be found in Ref. [44].

4.1.2Theoretical methods

Total energy calculations were performed using the full-potential linearized augmented plane-wave (FP-LAPW) method [81] via the WIEN2K package [82] employing the Perdew-

Burke-Ernzerhof (PBE) exchange-correlation functional [61]. Ten thousand *k* points were employed in the sampling of the first Brillouin zone for a *k*-mesh size of 21 × 21 × 12 with an RK_{max} of 10.50. Phonon dispersion relations and DOS were calculated using the small displacement method via WIEN 2K and post processed using the PHONOPY program [102]. Vibrational free energy (F_{vib}) of the crystal structure was estimated using harmonic approximation [162]. Bader charge analysis was done based on the theory of atom in molecule using Henkelman code [186]. Details of experimental methods and results can be found in Ref. [44].

4.1.3 Results and discussion

4.1.3.1 Core electron effect

The chemistry at ambient conditions predicts that Ar should not form stable compounds owing to its filled (3*s* and 3*p*) shell configurations. For a neutral Ar atom, the 3*d* orbital have higher energies than the 4*s* orbital and hence (3*d*) is not accessible for bonding. Thus, it is required that, when for example, halogen (such as fluorine, F) interact with Ar, the energy barrier between the Ar 3*p* and 3*d* reduces, creating for each orbital, half-filled states for making covalent bonds [225]. However, we observe that the mechanism changes completely for Ar interacting with transition metals for which the *d* orbitals are partially filled. When such interactions happen at high pressure, the ionization energy of Ar reduces drastically, and requires that the [Ne]-like core's 2*p* orbital become accessible for oxidation or 4*s* orbital for reduction.

For this to happen, the Ar 2*p* along with the 3*s*, 3*p* and 4*s* must be treated as valence orbital (and as such, make the core smaller). The Ar potential supplied with the standard potential library treated only the 3*s* and 3*p* orbital as the valence states thereby rendering the 2*p* and 4*s* orbitals inaccessible. The consequence is a strong core-core electrostatic repulsion between Ar and Ni which will therefore require a large $p\Delta V$ work for stabilization (see Fig. A4.1). We postulate, therefore, that the no-show of Ar-Ni compound in the previous study could be an indication of insufficiency of Ar potential from the standard potential library at extreme pressures. This emphasizes the need for a decreased cutoff radius for Ar pseudo-core, to make more valence states accessible for chemical reaction and bonding. To circumvent this problem, we used the full-potential linearized augmented plane-wave (FP-LAPW) method [81].

4.1.3.2 Structure identification and thermodynamic stability

The first order of business was to find out the favorable stoichiometry for the synthesized Ar-Ni compound using experimental equation of states (EOS) data. For details of how the unit cell volumes of the Ar-Ni compound, FCC-Ni and FCC-Ar (solid symbols, Fig. 4.1) were experimentally obtained at different pressures, readers should see ref. [44]. As shown in Fig. 4.1, the volume of Ar-Ni compound is smaller than the calculated volume sum of different physical mixture of Ar and Ni in which the atomic percent of Ar is equal or larger than the atomic percent of Ni. Also, the volume of Ar-Ni compound is larger than the calculated volume sum of different physical mixture of Ar and Ni in which the atomic percent of Ar less than the atomic percent of Ni. It is required that the atomic volume of Ar_xNi_y compound should be less than the superposition of (xAr+yNi)/(x+y). In line with this maxim, the equi-composition and Ar-rich Ar-Ni compounds such as ArNi and Ar_3Ni are thermodynamically allowed while Ni-rich compounds such as $ArNi_3$ are forbidden. Therefore, the experimental EOS (corroborated by theoretical EOS) shows that the synthesized Ar-Ni compound may have equal compositions of Ar and Ni (e.g. ArNi) or be Ar-rich (Ar_xNi, x > 1).

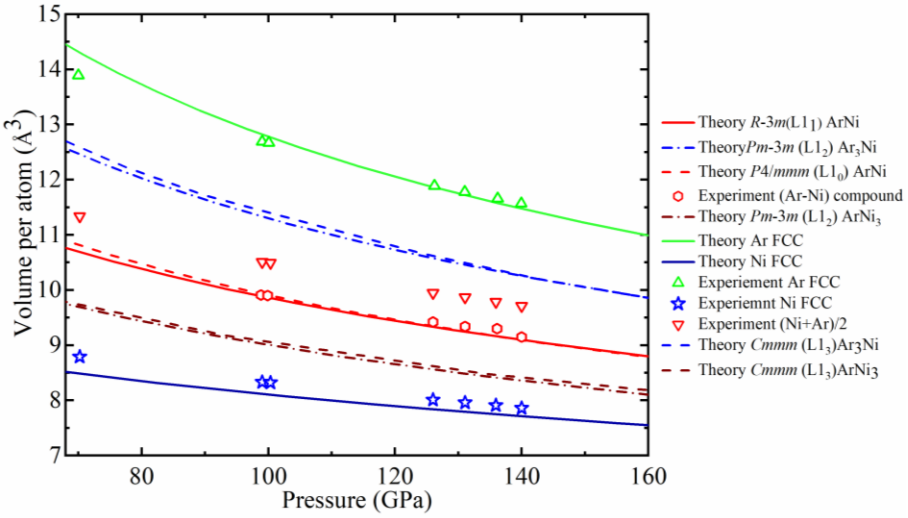

Figure 4.1. Comparison of equation of states determined in diamond anvil cell (DAC) experiment and DFT calculation. Experimental EOSs for Ar, Ni, and Ar-Ni compound are shown in solid symbols. Theoretical EOSs for other considered structures are shown in dashed and dash-dot curves. Experimental data used for this figure were produced by Dr. Stavrou.

Now, we know that the Ar-Ni crystalizes into equi-composition or Ar-rich stoichiometry. Thus, the next point of call is establishing the right stoichiometry and eventually the crystal structure. Since the Ar-Ni compound is similar to an intermetallic phase, we considered Laves phases for alloys of the form AB and AB_3. Details of all the Laves phases considered in this work can be found in Ref. [44]. Based on the experimental volume-pressure data, we narrow down the candidate structures to the $L1_1$ (*R*-3*m*) and $L1_0$ (*P*4/*mmm*) structures of ArNi due to remarkable agreement in their calculated EOS and experimental EOS (see Fig. 4.1). Since the candidate structures have identical atomic volume at the pressure of synthesis, 140 GPa, then, we calculated the formation enthalpy (EOS) of the ArNi compounds over a pressure range of 100 and 300 GPa relative to decomposition into elemental Ar and Ni (Fig. 4.2). The *R-3m* ArNi is predicted to become most stable around 183 GPa and the *P*4/*mmm* ArNi is predicted to form above 226 GPa (Fig. 4.2). The Calculated formation pressures for the two candidate structures are higher than what is observed in the LH-DAC experiment. We remark that the volume per atom of Ar-Ni compound is selective of stoichiometry rather than the actual crystal structure.

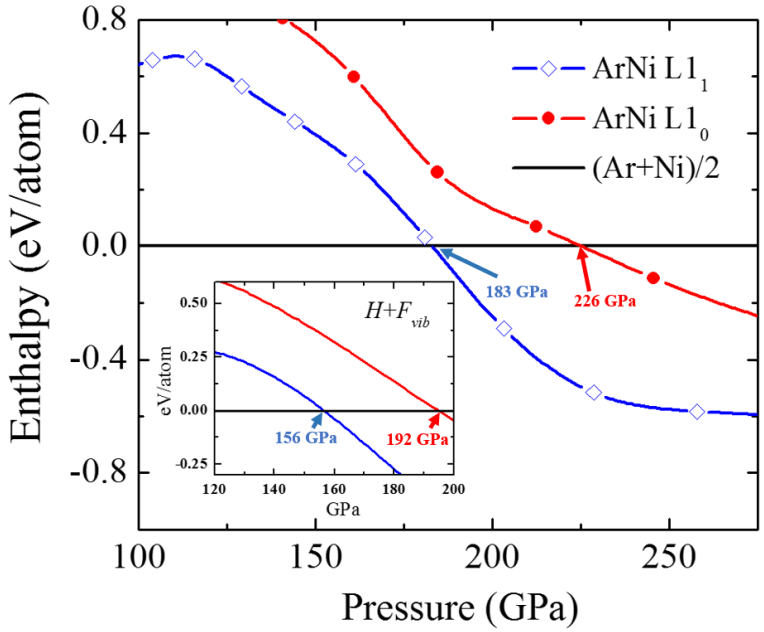

Figure 4.2. Calculated enthalpies for the *R*-3*m* ArNi (ArNi $L1_1$) and the *P*4/*mmm* ArNi (ArNi $L1_0$) structures with respect to the mixture of elemental Ar and Ni. Inset shows the evolution of finite temperature energy under pressure at 2000 K i.e. $H + F_{vib}(2000\ K)$.

We still have the ~43 GPa difference between the theoretically predicted and experimentally observed formation pressure for the *R*-3*m* ArNi. To solve this problem, we investigated temperature effects on the formation pressure of the *R*-3*m* ArNi and the *P*4/*mmm* ArNi. We expect that, increasing the temperature of the system (as high as the experimental temperature of synthesis, 2000 K) should increases the entropic contribution ($T\Delta S$) to its free energy, consequently reducing the internal energy difference between the reactants (Ar + Ni) and the product (ArNi). The Ar – Ni compounds and the mixture of the elemental Ar and Ni have different vibrational free energy that could compensate for the enthalpy difference (at reduced pressures) and possibly stabilize the Ar - Ni compounds faster, making it preferable at high temperature and reduced pressure. To this end, we estimated the Helmholtz free energy for the *R*-3*m* and *P*4/*mmm* structures at several pressure points between 100 and 300 GPa using the harmonic approximation [162] according to Eq. (3.2). Indeed, with increasing temperature, the ArNi compound become more stable than the mixture Ar+Ni at a slightly lower pressure than the 0 K calculation. This suggests that laser heating the mixture is critical for the chemical reaction between Ar and Ni. The inclusion of temperature effects also compensates for the over estimation of the formation pressure, putting it at 160 GPa for the *R*-3*m* (as oppose 183 GPa) and 192 GPa (as oppose 226 GPa) for the *P*4/*mmm* structure (see inset in Fig. 4.2). We therefore conclude that the synthesized phase is the *R*-3*m* ArNi. The ~ 23 GPa discrepancy (between experiment and theory) in the estimation of critical pressure can be explained by the uncertainties inherent in the LH-DAC method used for the experiment and in various approximations of the theoretical (DFT) method used for the study.

We examine the consistency of the *R*-3*m* ArNi structure with the XRD pattern obtained after laser heating Ar – Ni mixture to 2000 K at 140 GPa (Fig. 4.3a) and the agreement is remarkable – all the major peaks were successfully indexed to the *R*-3*m* ArNi and unreacted FCC Ni. This confirms that indeed, a chemical reaction occurs after the laser heating and that the crystal structure of the compound formed can be explained using the *R*-3*m* ArNi structure. Raman spectroscopy was carried out on the laser heated (2000 K) sample at 140 GPa but no signal was detected suggesting that the compound formed is metallic or semi metallic [226,227] (see later)

with a constant polarizability for all eigen displacements of vibration modes activated by the incident electric field.

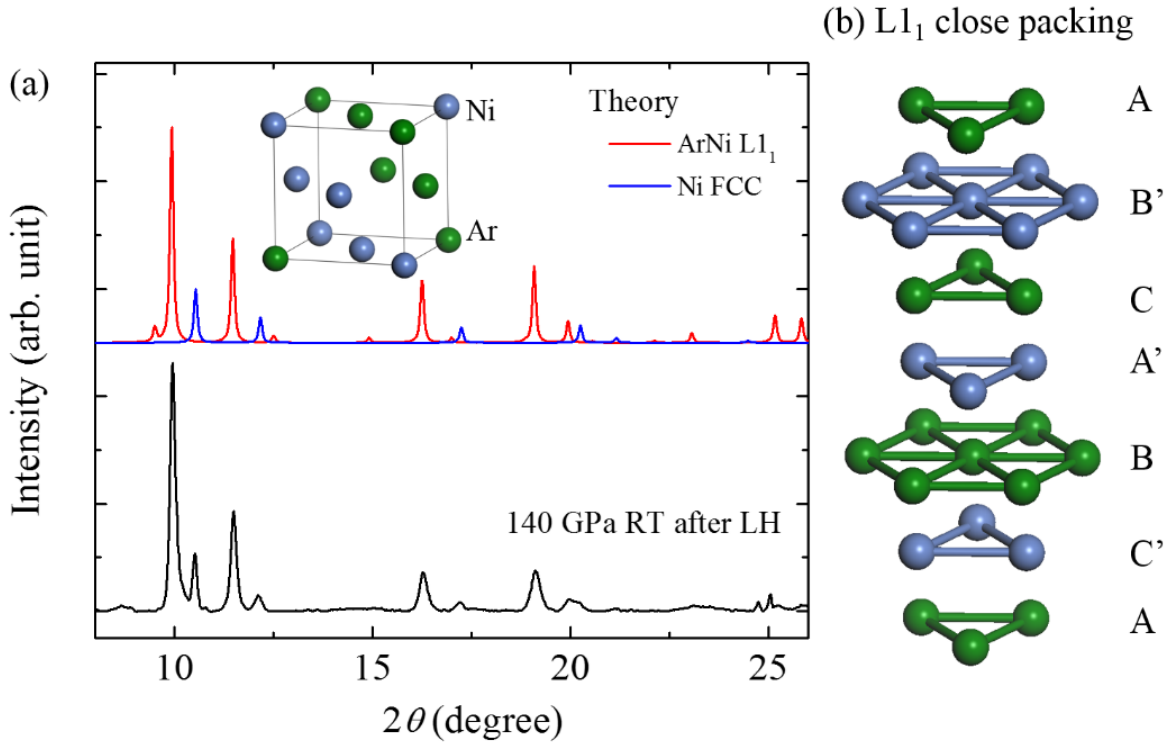

Figure 4.3. (a) Comparison of experimental XRD pattern for quenched sample at 140 GPa to calculated pattern for *R*-3*m* ArNi (ArNi $L1_1$) and FCC Ni at the same pressure. Inset: crystal structure of ArNi showing the distribution of Ar and Ni atoms in *R*-3*m* ArNi structure illustrated in a 4-atom segment. (b) Stacking of closed packed planes (100) in *R*-3*m* ArNi. A, B, and C represents the orientation of the three planes and prime indicates a different atom type. Adapted from Ref. [44].

The structural parameters of the predicted *R-3m* ArNi structure (optimized at 140 GPa) are Ni 1*a*: 0.000, 0.000, 0.000; Ar 1*b*: 0.500, 0.500, 0.500, with a = 6.69 Å , $\alpha = 33.56^o$. It belongs to the trigonal crystal class and the unit cell is a rhombohedron. The *R*-3*m* ArNi structure (in triple hexagonal cell) exhibits a cubic close packing of Ar and Ni atom thereby producing an ordered structure with stacking order ABC. Since the cell contains two types of atom, then the stacking changes according to the atom type as shown in Fig. 4.3b. Details of the conversion of the trigonal

cell to the cubic cell can be found in ref. [44]. We investigated the dynamic stability of the *R*-3*m* ArNi and *P*4*/mmm* ArNi at 0 K using phonon calculation within the harmonic approximations. The phonon dispersion relations for the *R*-3*m* ArNi (Fig. 4.4a) and the *P*4*/mmm* ArNi (Fig. 4.4b) structure at 160 GPa were calculated. There are no imaginary frequencies in the entire BZ, establishing that these structures are indeed dynamically stable at such pressure representative of the Earth's core. The phonon density of states projected to the atomic species for both the *R*-3*m* ArNi and the *P*4*/mmm* ArNi shows that the low-frequency vibrational modes are predominantly due to Ni atoms while the high-frequency modes are predominantly due to Ar atoms.

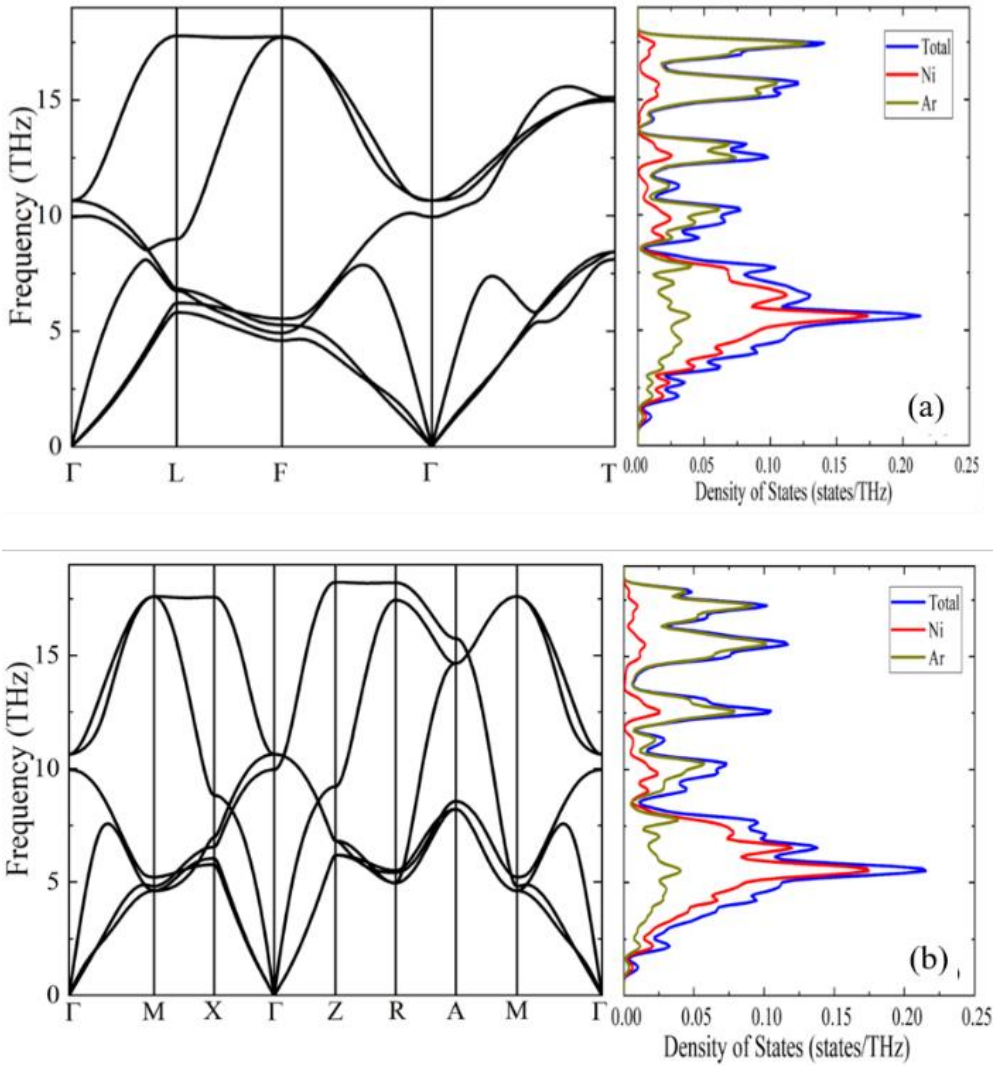

Figure 4.4. Phonon dispersion curve and projected phonon density of states for the (a) *R*-3*m* ArNi (b) *P*4*/mmm* ArNi at 160 GPa.

Pressure is known to modify the properties of materials [22]. we calculated the charge transferred within the system using Bader's charge partitioning model for electron charge density. In this formalism, electronic charges on individual atoms in molecules or crystals are calculated based on partitioning of electron density according to its zero-flux surfaces [207]. The analysis reveals that fractional charge transfer occurred between Ar and Ni atoms in the *R*-3*m* ArNi compound. Ar atoms are anionized, gaining ~0.2 e^-/atom. The formation of ArNi compound can thus be attributed to the extreme pressure applied to the mixture of Ar and Ni, while charge transfer stabilizes the system. Under pressure, the inert Ar becomes electronegative and can accept fraction of electron (~0.2 e^-) into its 4*s* orbital from its neighboring Ni atom's 3*d* orbital.

4.1.3.3 Electronic properties of ArNi

We study the electronic structures of the newly formed Ar-Ni compounds by calculating their electronic band dispersions. The dispersions show that both the *R*-3*m* ArNi (Fig. 4.5a) and the *P*4/*mmm* ArNi (Fig. 4.5b) structures are metallic due to bands crossing the Fermi energy level. The electronic DOS projected to orbitals reveal that the states around the Fermi level are primarily Ni 3*d* states. Spin-polarized energetics calculation indicates that antiferromagnetic configuration has slightly lower energy (~0.1 meV/atom) than non-magnetic and ferromagnetic configurations. The delocalized nature of Ni 3*d* electrons induced a very small magnetic moment on Ni. The spin polarized density of states for the ArNi compounds (Fig. 4.5c and d) show equal and symmetric contribution of both (up and down) spin states to metallization thereby corroborating the results of the electronic band structure calculation that ArNi compounds are metallic. Furthermore, the symmetric nature of the up and down spin states shows that the total magnetic moment is zero which further support the observation that the antiferromagnetic configuration of ArNi is the most energetically stable phase. The metallic state calculated for the ArNi compound is consistent with the 'no show of Raman signal' during laser heating of sample at 140 GPa, further supporting the successful synthesis of the ArNi compound.

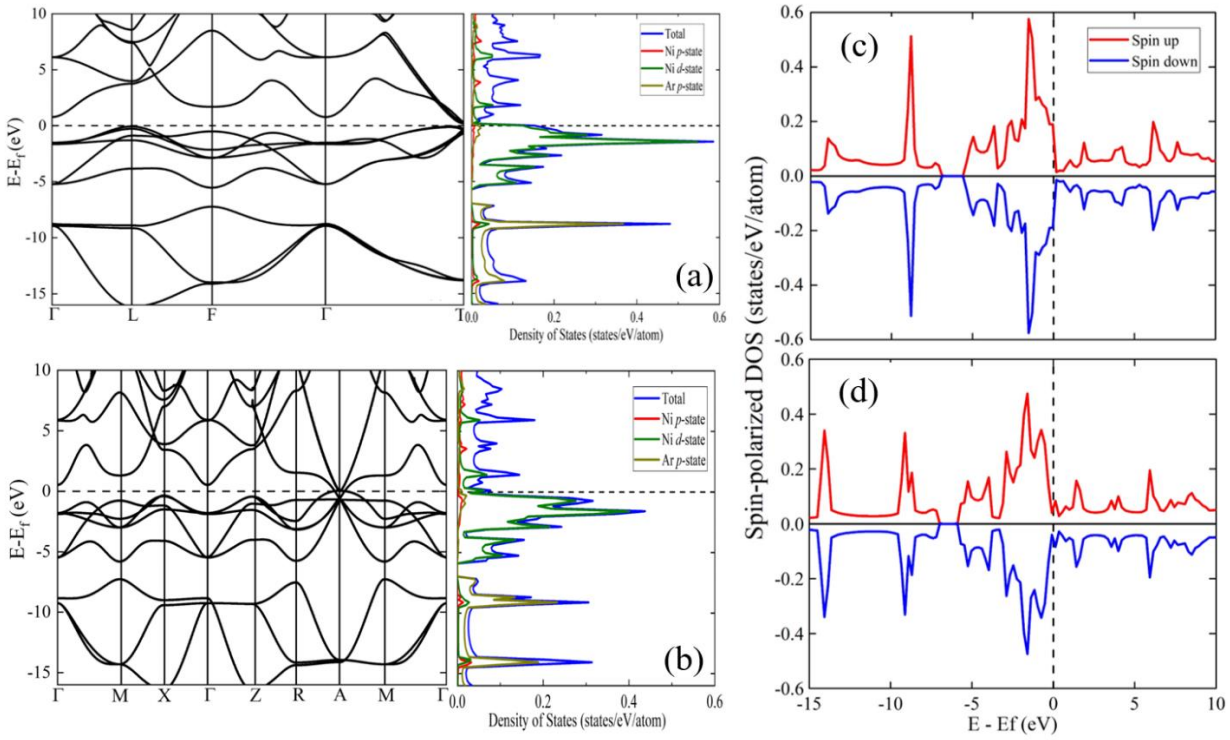

Figure 4.5. Calculated electronic band structure and projected density of states for the (a) *R*-3*m* ArNi (b) *P*4/*mmm* ArNi at 160 GPa. Spin-polarized total density of states for the (c) *R*-3*m* ArNi (d) *P*4/*mmm* ArNi at 160 GPa.

The synthesis of ArNi compound has similar motivation to the Xe-Ni compound. However, their science of charge transfer is fundamentally different. For example, we found that under pressure, the inert Ar becomes electronegative and can accept fraction of electron into its 4*s* orbital from its neighboring Ni atom's 3*d* orbital. Meanwhile, Ni acts as oxidant in $XeNi_3$ accepting electron from Xe [22]. Further studies would be required to completely understand Ar in the Earth's core. For instance, exploring the reactivity of Ar-Fe at higher pressures, since the abundance of Fe (by mass) is about 80% in the Earth's core. Furthermore, the reactability of Ar with Fe should not be limited to the hexagonal close-packed phase of Fe. The possibility of a body-centered cubic Fe should not be ruled out especially at the pressure of the inner Earth's core. The formation of ternary compound of Ar with Fe-Ni alloy is also interesting and all these could help to resolve outstanding scientific question such as the "missing Ar" in a Fe-Ni dominated Earth's core.

4.1.4 Conclusion

In this study, first principles methods were used in the identification and characterization of experimentally synthesized Ar-Ni compound under Earth's core condition. We showed that indeed, formation of stable NG-Ni compound is possible under the Earth's core conditions (140 GPa, 2000 K). The compound formed is predicted to be dynamically stable. If the valence orbital's configuration is right for Ar, at pressures and temperature within the *PT* field of the Earth's core, Ar will react with Ni to form intermetallic compound and electrons will be transferred from the Ni 3*d* orbital to the Ar's 4*s* orbital. This work suggests that the formation of ArNi in the Earth's core is a likely explanation for the fate of Ar produced during natural decay of ^{40}K.

CHAPTER 5

ALKALI METAL – TRANSITION METAL COMPOUNDS AT HIGH PRESSURE: A CASE STUDY OF K-Fe AND K-Ni

A similar version of this chapter has been published as a research article in the Journal of Physical Chemistry A and the Physical Review B. The references are as follows.

1. Adeleke A. A., and Yao Y. Formation of Stable Compounds of Potassium and Iron under Pressure. *J. Phys. Chem. A 124*, **2020** 4752-4763.
2. Adeleke A. A., Stavrou E., Adeniyi O. A., Wan B., Gou H., and Yao Y. Two good metals make a semiconductor: A potassium-nickel compound under pressure. *Phys. Rev. B. 102* **2020** 134120.

5.1 Formation of stable compounds of Potassium and Iron under pressure

Using first principles methods, we predict stable stoichiometric potassium-iron (K-Fe) intermetallic compounds at high pressures. We investigated and established the thermodynamic stability, crystal structures and bonding properties of the predicted compounds. Dynamic stability of the predicted structures was established through phonon calculations. We found that the intermetallic compounds of potassium and iron are stabilized by high pressure and energy reordering of atomic orbitals through electron transfer. Above 120 GPa, K-Fe transforms from K-rich, featuring clustering of phase-segregated K atoms, to Fe-rich compound. The predicted K-Fe compounds may further explain a potassium-containing Earth's core.

5.1.1 Introduction

The Earth's core is composed of Fe and small amount of elements whose atomic numbers are less than Fe's (light elements) such as silicon (Si), sulfur (S), oxygen (O), and carbon (C). Understanding the structure of the Earth's interior, particularly the core, is key to fulfilling its energy budget. The inner dynamics of the Earth is maintained by the heat produced from gravitational potential energy and the radioactive decay of radionuclides such as uranium (U), thorium (Th) and potassium (^{40}K) [32,214]. The radiogenic heat from ^{40}K accounts for less than 3% of all heat generated in the Earth's core, rendering it a minor source of heating, however, such contribution is significant enough and should be understood [228]. Potassium is lithophile (rock loving) but progressively become siderophile (iron loving) under pressure. Compared with chondrites, K is depleted in the Earth's mantle, suggesting its percolation into the Fe-rich core during the Earth's accretion and under increasing pressure and in the presence of a combination of other light elements [34,228].

Computer simulations has shown that the density jump across the core-mantle boundary (CMB) cannot be sufficiently explained by the partitioning of S, Si and O between the mantle and core [229]. Therefore, the slightly siderophile K may as well be present in the Earth's core, most like in a dissolved form. The presence of O and C in the Earth's core has been extensively studied. For example, formation of stable FeO and Fe_2O_3 have been predicted at 350 GPa and 500 GPa, respectively, using first principles methods [31]. Furthermore, stable iron carbide (Fe_3C) solution was synthesized and studied using both shock wave experiments and thermodynamic calculations up to 330 GPa and 2500 K. Carbon solubility in Fe was found to increase with pressure. Thus, with the Earth's core having a concentration of 0.3% C at 330 GPa, Fe_3C may form in the inner core but cannot plausibly be the sole light element in the core [230]. Pressure induced affinity for Fe in K has been reported, but do not unambiguously establish the formation of stable K-Fe compounds. In one of those studies, through molecular orbital calculations on KFe_{14} cluster, it was reported that K cannot alloy with metallic iron at high pressure although the affinity of K for metallic Fe is enhanced [231]. It was shown that neutral K atoms are not stable in metallic iron, thereby inducing instability throughout the cluster.

The partitioning of K at the CMB condition was experimentally studied and it was found that the distribution coefficient of K is dependent on the composition of the silicate melt at the

CMB condition, making its direct extrapolation into the inner core condition difficult [232]. In the absence of sulfur or oxygen, high pressure experiment has shown that K can mix with Fe through substitution at deep magma-ocean conditions (above 26 GPa and 2500 K). This result can serve as an upper bound estimation to the amount of K present in the core by using a hypothetical structure model of K-Fe [233,234]. The presence of K (in small amount) in the Earth's core is possible if we assume that it has segregated into the Earth's core in the presence of oxygen and Sulphur-rich iron sulphide liquid. This will create a suitable condition for dissolution of significant amount of K in the Fe alloy of the core [228]. Experimentally, K has been shown to form compound with Ni at 37 GPa and 2500 K through a *s* to *d* transition that usually occur in alkali metals at high pressures – Miedema's rule [235]. The study produced the only K-Ni compound known to date [236]. Since the Earth's core is predominantly Fe (88.8%) compared to Ni (5.8%) [237], it will be interesting to show that stable K-Fe compounds, like K-Ni compound, can form at high pressures. Although, educated guesses can be made based on electronic structure and equation of states calculations on K metals [238], however, a definitive and systematic study is required in order to understand the reactivity of K in Fe or in iron sulphide (with 4.5% core abundance in the Earth's core) at the Earth's interior conditions; from the mantle deep down. Finding stable structures of K-Fe compounds is therefore key to this understanding, which motivates the present study.

In the present study, we report results from a theoretical investigation of the binary K-Fe structures under high pressure. The present simulation using particle swarm optimization algorithm revealed several stoichiometric K-Fe compounds and their crystal structures. The result uncovered several K-rich and Fe-rich compounds predicted to be stable relative to decomposition to elemental Fe and K. We demonstrate that when K reacts with Fe under pressure, stable intermetallic compounds with different compositions are formed and stabilized through electron transfer. The formation of stable compounds between K and Fe at high pressure do not only shed light on the hypothesis that depleted K could move deep into the Earth and chemically bond to Fe but also expand our understanding of the chemistry of K under pressure.

5.1.2 Computational Method

The crystal structure search was carried out using the particle swarm-intelligence optimization (PSO) [100,101] algorithm. The underlying geometrical optimization and energetic

calculations were performed using the Vienna ab initio simulation package (VASP) code [93] within which the density functional theory was implemented. A 9-electron (for K) and 14-electron (for Fe) projector-augmented wave (PAW) [116] potential with Perdew-Burke-Ernzerhof (PBE) functional [61] and a 450 eV kinetic cutoff energy was used. A *k* spacing of $2\pi \times 0.02$ $Å^{-1}$ for Brillouin zone (BZ) sampling was employed for structural optimization. The structure search was done at 0 GPa, 30 GPa, 60 GPa, 90 GPa, 120 GPa, 150 GPa and 200 GPa with simulation cells containing 1, 2, and 4, K_xFe_y formula units. Correlation effect on 3*d* electrons were treated within the generalized gradient approximation (GGA)+U framework using the Dudarev approach [239] with an on-site coulomb interaction U_{eff} ($U_{eff} = U - J$) of 8.6 eV [208,209]. Bader charge analysis was done using VASP and post processed using Henkelman code [186]. Electron localization function [117] calculation was performed using a 120 ×120 × 120 mesh via the VASP code with PBE functional. The stability of various phases with respect to decomposition was assessed by constructing their convex hull. The dynamic stability of predicted structures was established using the density functional perturbation theory [103] as implemented in the VASP code with a *q*-point mesh of size 5 × 5 × 5. The elastic and the mechanical stability of the predicted structures were also investigated using the Born-Huang criteria for mechanical stability [94,95]. A*b initio* molecular dynamics (AIMD) [92] simulations were performed employing an isothermal-isobaric (*NpT*) ensemble in a supercell with 240 atoms at 30 GPa, a supercell with 180 atoms at 60 GPa, and supercells with 180, 360 and 288 atoms at 90, 120 and 150 GPa, respectively using the VASP code. AIMD trajectories were obtained from at least 10 ps long MD simulations sampled with a 2 fs time step. The Langevin dynamics was used and the system temperature was controlled using the Langevin thermostat. The high temperature anharmonic vibrational density of states (*v*DOS) was obtained from the velocity autocorrelation function (VACF) of the MD trajectories.

5.1.3 Results and Discussion

5.1.3.1 Phase Stability and Stable Crystalline structures

5.1.3.1.1 Phase stability of K-Fe

The crystal structure of binary K_xFe_y with variable compositions was searched at 0, 30, 60, 90, 120, 150 and 200 GPa pressures and temperature of 0 K. Crystal structure search was

performed without spin polarization because magnetic order is expected to collapse in Fe under the Earth's core condition. The enthalpy of formation (ΔH_f) per atom of K_xFe_y was computed using the relation:

$$\Delta H_f = \frac{H(K_xFe_y) - xH(K) - yH(Fe)}{x+y}, \quad (5.1)$$

where *x* and y are the number of K atoms and the number of Fe atoms, respectively. The K-bcc is stable in the pressure range of 0 - 11.6 GPa, K-fcc in the pressure range of 11.6 - 25 GPa, K-*h*P4 in the pressure range of 25 - 35 GPa, K-*o*P8 in the pressure range of 54 - 90 GPa, K-*t*I4 in the pressure range of 90 - 96 GPa and K-*o*C16 above 96 GPa [240]. We have used the hexagonal *h*P4 structure of K to represent the K-III phase throughout this work. The *hcp*-Fe is the known stable phase of Fe in the pressure range of 14 GPa up to at least 200 GPa [29,241]. The bcc-Fe was used for ΔH_f calculation at 0 GPa, since it is the stable phase of Fe up to 14 GPa [241]. The convex hull [242] was constructed using the minimum of the calculated ΔH_f of the most stable structures for each composition. In principle, structures whose ΔH_f lies on the convex hull are considered energetically stable while structures whose ΔH_f are slightly above the convex hull but below the enthalpies of the elemental decompositions are energetically metastable [242]. Metastable structures are sometimes experimentally synthesizable structures that require high temperatures (or other reaction catalysts) for their synthesis. The convex hull for K_xFe_y at various search pressures are shown in Fig. 5.1.

The result of our structure search shows no thermodynamically stable compound is formed between K and Fe at ambient pressure. At 30 GPa, respectively, K-rich and Fe-rich K-Fe compounds in the K_4Fe and KFe_3 stoichiometries are formed. Other stoichiometries, K_3Fe, K_2Fe and KFe_4, are predicted to be metastable. At 60 GPa, K_4Fe and KFe_2 are the most energetically stable stoichiometries with several other metastable structures in the K_3Fe, K_2Fe, K_3Fe_2, K_4Fe_3, KFe_3 and KFe_4 stoichiometries. At 90 GPa and 120 GPa, the K_4Fe stoichiometry continue to be energetically stable but crystalizes into different structures as shown in Fig. 5.2a. In addition to the K_4Fe stoichiometry, KFe_4 becomes thermodynamically stable up to 150 GPa where KFe_3 stoichiometry become thermodynamically stable again. Under further compression, KFe_4 eventually become stable. All the predicted structures with negative enthalpy of formation were examined and screened using their dynamic stability (see later). After dynamic stability screening

of the predicted structures, four K rich structures and one Fe rich, *C*2/*m*-KFe_3 structure were studied further.

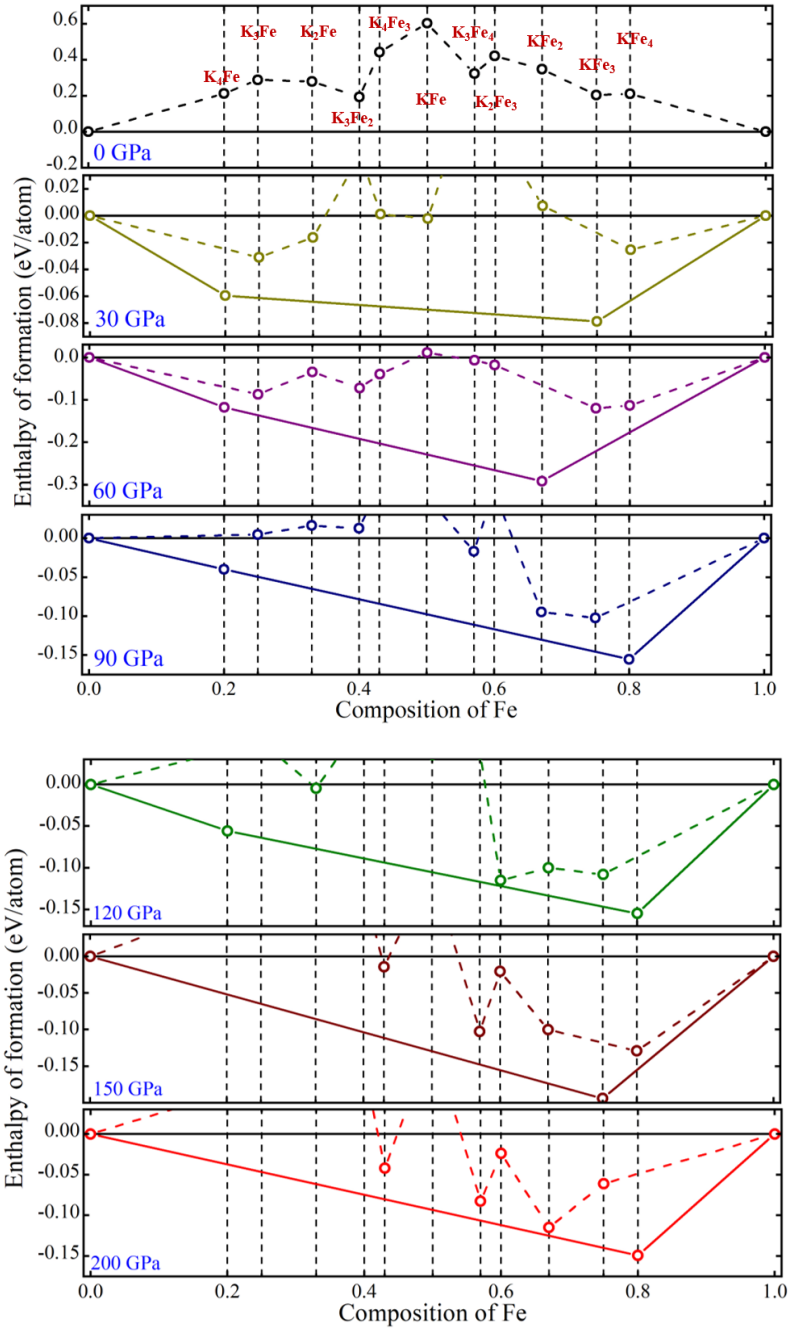

Figure 5.1. Enthalpy of formation of various K-Fe compounds with respect to constituent elemental decomposition (convex hull) at 0, 30, 60, 90, 120, 150 and 200 GPa. The energetically stable phases are connected using solid lines on the convex hull.

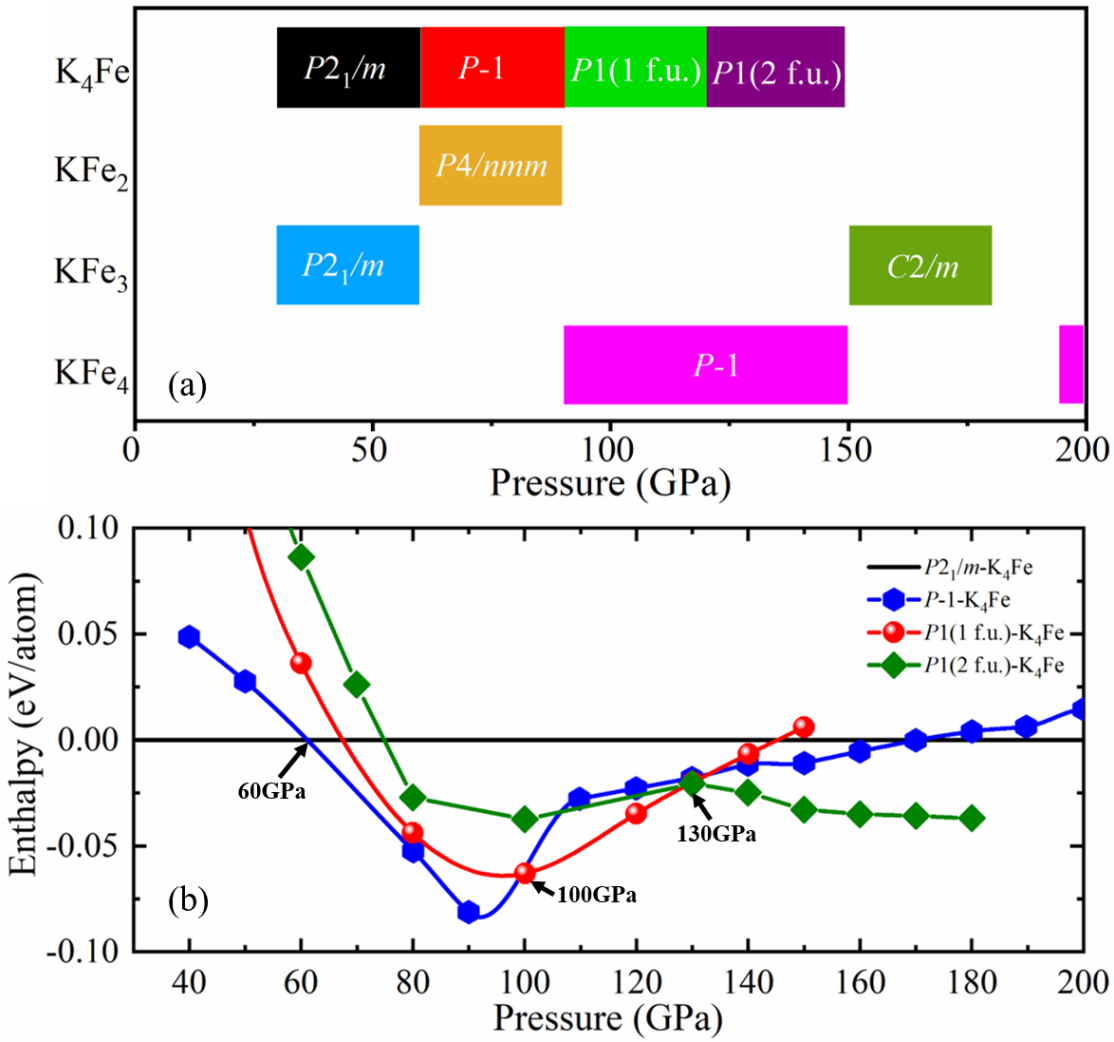

Figure 5.2. (a) Pressure ranges in which predicted phases of stoichiometric K-Fe compounds are thermodynamically stable. (b) Calculated enthalpies as functions of pressure for dynamically stable structures of K-Fe system. The enthalpy of the low-pressure phase, $P2_1/m$-K_4Fe is used as the zero-energy reference.

5.1.3.1.2 Stable crystalline structures of K-Fe

The optimized structural parameters of the candidate structures and their corresponding pressure are shown in Table 5.1 and a complete list of structural parameters for all other structures with negative formation enthalpy (not considered further) are shown in Table A5.1. The crystal structures of the K-Fe are shown in Fig. 5.3.

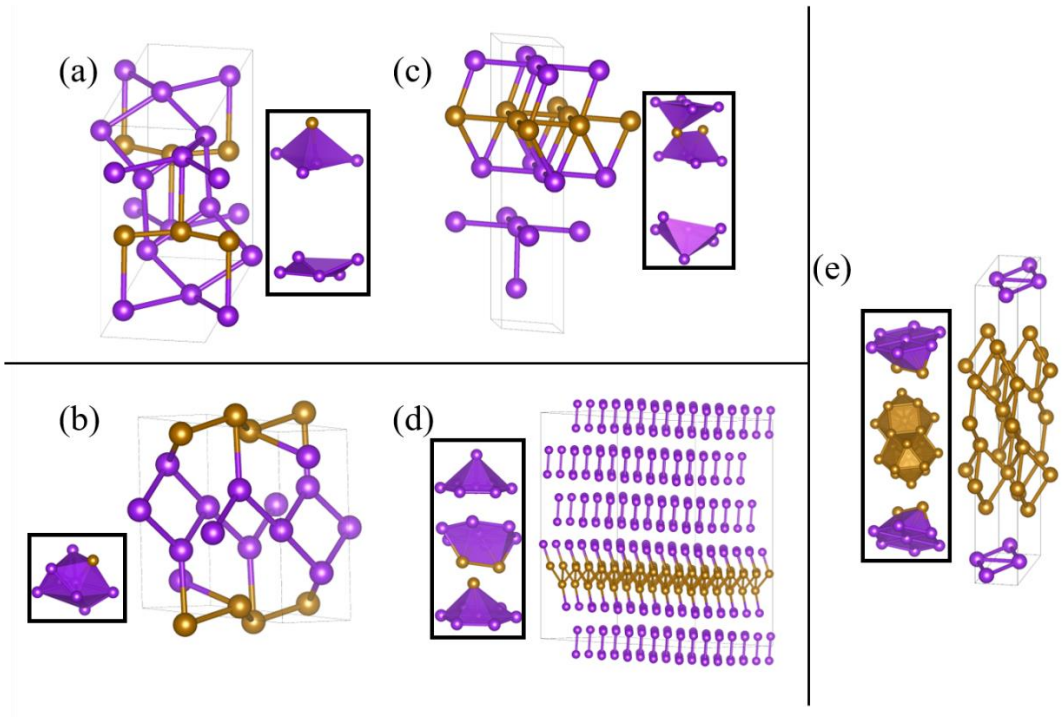

Figure 5.3. Crystal structure of candidate K-Fe phases (a) K_4Fe in $P2_1/m$ structure at 30 GPa (b) K_4Fe in P-1 structure at 60 GPa (c) K_4Fe (1 f.u.) in $P1$ structure at 90 GPa (d) a 6×6×1 supercell of K_4Fe (2 f.u.) in $P1$ structure at 120 GPa (e) KFe_3 in $C2/m$ structure at 150 GPa. Distinct polyhedron(s) within the cell are shown in the box and Fe atoms are shown by the golden balls.

P (GPa)	SG	*a* (Å)	*b* (Å)	*c* (Å)	α	β	γ	Atom	Fractional atomic coordinates			
									x	*y*	*z*	Site
30	$P2_1/m$	5.93	4.06	7.93		111.26		K	0.258	0.250	0.879	2*e*
								K	0.069	0.250	0.157	2*e*
								K	0.566	0.250	0.250	2*e*
								K	0.351	0.750	0.383	2*e*
								Fe	0.955	0.750	0.499	2*e*
60	*P*-1	4.19	5.12	6.53	90.14	77.82	97.56	K	0.637	0.102	0.146	2*i*

								K	0.055	0.825	0.235	2*i*
								K	0.521	0.250	0.541	2*i*
								K	0.898	0.664	0.670	2*i*
								Fe	0.722	0.560	0.049	2*i*
90	*P*1	2.45	2.46	10.88	91.27	88.89	61.97	K	0.378	0.371	0.342	1*a*
								K	0.407	0.341	0.127	1*a*
								K	0.656	0.740	0.546	1*a*
								K	0.790	0.610	0.922	1*a*
								Fe	0.171	0.226	0.735	1*a*
120	*P*1	2.41	2.41	21.08	93.45	90.63	119.68	K	0.673	0.157	0.834	1*a*
								K	0.102	0.982	0.043	1*a*
								K	0.194	0.246	0.517	1*a*
								K	0.506	0.859	0.416	1*a*
								K	0.051	0.897	0.935	1*a*
								K	0.462	0.727	0.145	1*a*
								K	0.242	0.330	0.625	1*a*
								K	0.623	0.073	0.726	1*a*
								Fe	0.081	0.379	0.241	1*a*
								Fe	0.459	0.105	0.321	1*a*
150	*C*2/*m*	3.92	2.29	15.47		104.15		K	0.918	0.000	0.072	4*i*
								Fe	0.223	0.000	0.559	4*i*
								Fe	0.546	0.000	0.208	4*i*
								Fe	0.003	0.000	0.676	4*i*

Table 5.1: Optimized Structural parameters of candidate K-Fe phases.

5.1.3.1.2.1 The potassium rich K_4Fe compound

The stoichiometric K_4Fe compounds are found to be stable over a wide range of pressures above 30 GPa (see Figs. 5.2a) with various crystal structures as shown in Fig. 5.3. The enthalpies per atom (H = [E + pV] / *n*, *n* is the number of atom in the unit cell) of candidate K_4Fe structures between 30 and 200 GPa were calculated and shown in Fig. 5.2b. Below 60 GPa, the $P2_1/m$-K_4Fe structure is the most energetically stable phase and transforms to the P-1-K_4Fe phase at 60 GPa. The P-1-K_4Fe structure remain stable between 60 and 100 GPa and the $P1$-K_4Fe (with 1 f.u.) become most stable between 100 and 130 GPa. The $P1$-K_4Fe (with 1 f.u.) transforms into the $P1$-K_4Fe (with 2 f.u.) when pressure is increased above 130 GPa.

The K_4Fe compound crystalizes into a monoclinic unit cell with space group $P2_1/m$ at 30 GPa. The crystal structure features K and Fe arranged in a tetrahedral geometry with edge-sharing K atoms with Fe atom sitting on one (top) of the vertices. The $P2_1/m$-K_4Fe structure also features isolated K atomic sublattice arranged in a two face-sharing tetrahedral geometry. The Fe-Fe bondlength is 2.10 Å while the K-K bond distance ranges between 2.65 Å and 2.75 Å. The K-Fe bond distance is 2.78 Å: the longest found in the crystal structure.

As the pressure increases to 60 GPa, the $P2_1/m$ structure transforms into a triclinic P-1 structure in which the K and Fe atoms are arranged in a triaugmented triangular prism geometry with Fe atom occupying one of the vertices. As expected, the K-Fe and K-K bondlength become shorter than in the $P2_1/m$ phase. The K-Fe bondlength ranges between 2.34 Å and 2.47 Å while the K-K bondlength ranges between 2.51 Å and 2.59 Å. This suggests that K-Fe and K-K bonding become more favorable under pressure. The Fe-Fe bondlength ranges between 2.11 Å and 2.44Å which notably deviate from Fe-Fe bondlength in the $P2_1/m$ phase.

Under further compression to between 100 GPa and 130 GPa, the P-1-K_4Fe transforms into another triclinic cell with $P1$ symmetry containing only one K_4Fe formula unit. The crystal structure features K and Fe atoms arranged in a tetrahedral geometry with edge-sharing K atoms. The Fe atom sits on one (top) of the vertices in an edge-sharing configuration with another Fe atom in a triangular prism geometry. Like the $P2_1/m$-K_4Fe structure, the $P1$-K_4Fe is also characterized by isolated K atomic sublattice arranged in a two face-sharing tetrahedral geometry.

Above 130 GPa, the *P*1-K_4Fe structure transforms into another phase with the same space group. The difference is that the new phase contains two K_4Fe units per cell. For discussion purposes, we will call this phase the *P*1(2 f.u.)-K_4Fe. This phase features some K atoms clustered into K-K units with bondlength of 2.27 Å. Such clustering leads to phase segregation between K and Fe. The remaining K atoms, that are not involved in cluster formation, adopt a hexagonal antiprism geometry with Fe atoms occupying one of the vertices. This phase precedes the transformation from K-rich K-Fe compounds into Fe-rich K-Fe compounds.

5.1.3.1.2.2 The iron rich KFe_3 compound

At 150 GPa, stoichiometric, iron-rich K-Fe compounds are formed. They crystalize into a triclinic unit cell with space group *P*-1 and a monoclinic cell with space group *C*2/*m*. Although the *P*-1-KFe_4 phase is the most energetically favorable phase, it was not considered further because of its dynamic instability (see later). Therefore, the energetically metastable but dynamically stable *C*2/*m* phase is the candidate structure for the iron rich K-Fe system. In contrast to the $P2_1/m$-K_4Fe and the *P*1-K_4Fe structures, the *C*2/*m*-KFe_3 structure features some Fe atoms that form atomic sublattice, adopting a cuboctahedron geometry linked through their triangular faces. The Fe sublattice is trapped between two layers of K atoms. The structure features K-Fe bond length of 2.35 Å and Fe-Fe bond length of 2.20 Å. The strong Fe-Fe interaction exhibited by the *C*2/*m*-KFe_3 structure can be explained by the abundance of Fe atoms in the system, which lead to the availability of more Fe atoms in close proximity to form bonds with each other as soon as the energy barrier is tuned down through the application of pressure. In general, the evolution of bond distances (K-K, K-Fe and Fe-Fe) under pressure for all candidate structures considered in this work is shown in Fig. A5.1. The figure suggests that application of pressure favors orbital interaction between abundant chemical specie in a material.

5.1.3.2 Dynamic, Mechanical, and thermal stability of K_xFe_y

5.1.3.2.1 Dynamic stability of K_xFe_y

The dynamic stability of all candidate structures was assessed at 0 K within the harmonic approximation through phonons. The phonon dispersion of the structures examined are shown in Fig. 5.4.

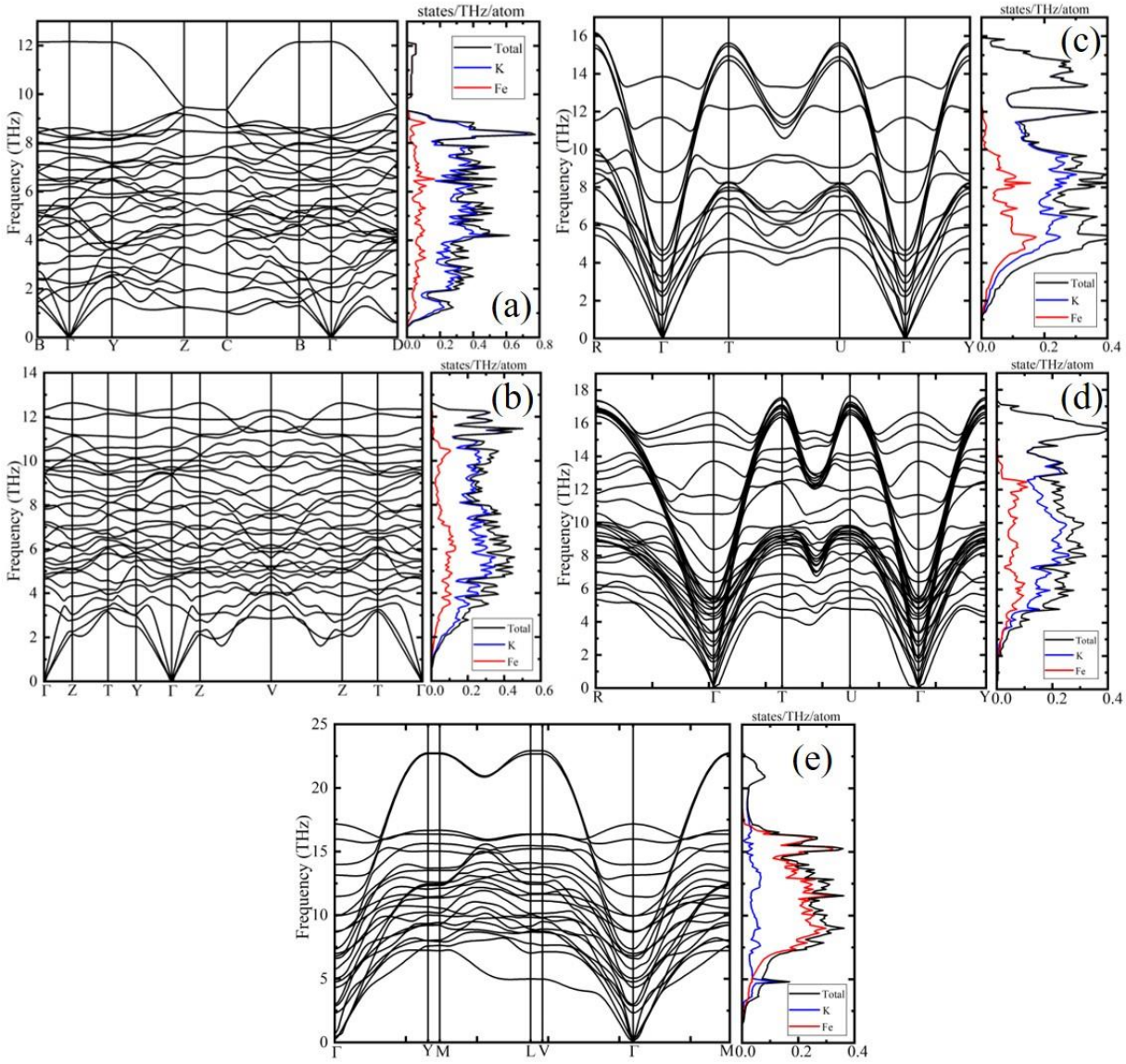

Figure 5.4. Phonon dispersion relations and density of states for the (a) K_4Fe in $P2_1/m$ structure at 30 GPa (b) K_4Fe in P-1 structure at 60 GPa (c) K_4Fe (1 f.u.) in $P1$ structure at 90 GPa (d) K_4Fe (2 f.u.) in $P1$ structure at 120 GPa (e) KFe_3 in $C2/m$ structure at 150 GPa.

All structures are dynamically stable as their phonon dispersions do not show negative frequencies. The projected phonon density of states (DOS) of all candidate structures are also shown in Fig. 5.4. The phonon DOS of the $P2_1/m$-K_4Fe structure at 30 GPa, suggests that frequencies up to ~9.5 THz are dominated by vibrations of K atoms through K-K and/or K-Fe bonds, while above 9.5 THz, are predominantly due to Fe atoms through Fe-Fe bonds. The *P*-1-K_4Fe at 60 GPa shows similar trend as the $P2_1/m$-K_4Fe without the signature high frequency Fe-Fe vibration. The *P*1-K_4Fe phases at 90 GPa and 120 GPa exhibits similar trends: vibrations of K and Fe are coupled strongly in the low-frequency region, while the high frequency vibrational modes are predominantly due to K atoms. Above ~12 THz at 90 GPa and above ~14 THz at 120 GPa, vibrations are purely due to K atoms through the K-K bonds. The clustering of K atoms through phase segregation in the *P*1(2.f.u)-K_4Fe at 120 GPa can also explain the large phonon DOS observed above *~14* THz at 120 GPa. In the Fe-rich KFe_3 at 150 GPa, vibrations of the two atomic species are coupled strongly in the low-frequency region, while the high frequency vibrational modes are predominantly due to Fe atoms. Above ~18 THz, vibrations are purely due to K atoms through the K-K bonds.

5.1.3.2.2 Mechanical stability of K_xFe_y

A material is considered mechanically stable if it satisfies the Born-Huang mechanical stability criteria [94,95] under elastic strain perturbations for its crystal system. The stability criteria require that elastic stiffness matrix C_{ij} have all-positive eigenvalues. The results of mechanical and elastic stability calculations indicate that all candidate structures considered are mechanically and elastically stable. Table 5.2 shows calculated elastic properties of the candidate K-Fe phases. The calculated bulk modulus *B* is observed to consistently increase with increasing pressure stability field of the candidate structures. The calculated shear modulus *G* is found to also increase with increasing pressure stability field of the candidate structures. These results suggest that the low-pressure phases of K-Fe system are more compressible than the high pressure phases. Furthermore, the Young's modulus *E* was calculated within the Voigt-Reuss-Hill's approximation [96]. Similar trends to the calculated *B* and *G* were also observed in *E*, indicating that the *C*2/*m*-KFe_3 is the stiffest; the $P2_1/m$-K_4Fe is the least stiff while other phases fall in between. The Poisson's ratio (ν), which is the ratio of the transverse contraction to the longitudinal extension of

a material during the stretching process was also calculated for all candidate structures. Materials with small v values (typically 0.1) usually exhibit covalent properties, while those with v value about 0.25 and whose G/B ~0.6 are ionic materials. In the same vein, materials whose v is about 0.33 and whose G/B ~ 0.4 are usually metallic materials. The calculated v for all candidate structures reveal that they all have metallic properties, except the P1-K_4Fe with 2 f.u. The P1(2 f.u.)-K_4Fe could have a blend of both metallic and ionic properties. The calculated Pugh ratio, B/G, indicate that the P1-K_4Fe (with 2 f.u.) is brittle with $B/G < 1.7$ and other candidate structures are ductile ($B/G > 1.7$).

System	Pressure (GPa)	B (GPa)	G (GPa)	E (GPa)	Poisson's ratio	G/B	Pugh's ratio B/G
K_4Fe ($P2_1/m$)	30	69.67	30.82	80.46	0.31	0.44	2.26
K_4Fe (P-1)	60	128.62	45.22	121.27	0.34	0.35	2.84
K_4Fe (P1)	90	259.87	117.93	298.32	0.31	0.45	2.20
K_4Fe (P1, 2 f.u.)	120	285.85	204.55	484.65	0.21	0.71	1.40
KFe_3 ($C2/m$)	150	559.41	236.57	608.45	0.32	0.42	2.37

Table 5.2: Calculated elastic properties of candidate K-Fe phases.

Elastic waves are very useful in the evaluation of mechanical characteristics of materials. The elastic properties of a material determine the properties of the elastic waves that propagate through it. Such properties include number of different modes which can propagate and their respective velocities. Elastic waves are generated in a material through different means such as mechanical, acoustic, piezoelectric and ultrasound. The speed of elastic wave for a uniform medium is determined by its elastic moduli and one of its intrinsic properties such as density [243]. The speed of elastic wave propagating through a material, like density, is a property of material that can be easily matched with seismic or experimental data when modeling the Earth's interior.

Thus, we calculated the longitudinal (v_l), transverse (v_t), and average (v_m) elastic wave speeds (Table 5.3) using the Navier's relations [244,245],

$$v_l = \sqrt{\frac{3B + 4G}{3\rho}} \tag{5.2}$$

$$v_t = \sqrt{\frac{G}{\rho}} \tag{5.3}$$

$$\frac{1}{v_m} = \left[\frac{1}{3} \left(\frac{2}{v_t^3} + \frac{1}{v_l^3} \right) \right]^{-\frac{1}{3}} \tag{5.4}$$

where ρ is the density of the material. The results indicate that longitudinal elastic waves propagate between 1.65 to 2.04 times faster than transverse elastic waves in all of the candidate structures. This suggests the presence of small elastic anisotropy in the materials. The v_m consistently increases with pressure up to 6.14 km/s at 120 GPa and decreases beyond 120 GPa. We observe a huge density jump between 120 GPa and 150 GPa (see Table 5.3). The density jump corresponds to a change in slope (on the density-pressure curve, see Fig. A5.5) of 0.030 g/cm^3/GPa between 30 and 120 GPa to 1.18 g/cm^3/GPa between 120 GPa and 150 GPa. This is consequence of the change in compositional stoichiometry of the K-Fe system from K-rich to Fe-rich under pressure.

To have a rough estimate of the phase boundary between the solidus and the liquidous phases in the candidate structures, we estimated their melting temperature (T_m) using the empirical relation [246],

$$T_m = 607 + 9.3B \pm 555 \tag{5.5}$$

The estimated T_m (Table 5.3) gives a rough but educated guess of the range of temperatures below which the candidate structures are solid. Such knowledge assists in choosing the temperature range in which molecular dynamic simulations are performed. We observe a monotonic increase in the T_m with increasing pressure as shown in Fig. 5.5f.

System	Pressure (GPa)	ρ (g/cm^3)	v_l (km/s)	v_t (km/s)	v_m (km/s)	T_m (K) ± 555 K
K_4Fe (*P2$_1$/m*)	30	3.96	5.29	2.79	3.12	1254.94
K_4Fe (*P-1*)	60	5.20	6.03	2.95	3.31	1803.20
K_4Fe (*P1*)	90	6.09	8.27	4.40	4.92	3023.80
K_4Fe (*P1*, 2 f.u.)	120	6.63	9.18	5.55	6.14	3265.43
KFe_3 (*C2/m*)	150	10.16	9.28	4.83	5.40	5809.52

Table 5.3: Calculated density (g/cm^3), longitudinal (v_l), transverse (v_t), and average (v_m) elastic wave speeds and melting (T_m) temperatures of candidate K-Fe phases.

5.1.3.2.3 Thermal stability of K_xFe_y

Using molecular dynamics simulations, each candidate structure is heated to 300 K within their stability pressure. The configuration at 300 K was step-wisely heated to 2500 K in an *NpT* ensemble. The following observations were made: formation of K-Fe units become more favorable as the temperature is increased. This is a consequence of the decrease in the nearest neighbor (NN) distance between K and Fe atoms as temperature increases (see Figure A5.3). The decrease in NN distance is known to favor bond formation [247] and it is, therefore, reasonable to expect more bonding between K and Fe if the temperature is further increased (for the high-pressure phases). We establish thermal stability of all candidate structures at high temperatures by evaluating their vibrational density of states (*v*DOS) and the mean square displacement (MSD) of K and Fe atoms from their lattice site during an AIMD simulation (see Figs. 5.5 and 5.6).

The MSD reveals that atomic vibrations at low temperature (300 K) are collective and nondispersive. Atomic vibrations at temperatures close to the solid-liquid phase boundary of the system follows the rule of effective mass mixing: the K atoms (with a smaller mass) experience more displacement, suggesting that phase transition from solid to liquid is driven by rigorous vibration of K sublattice from its mean position. The vibration thus induces softening of

potassium's low frequency modes. At 30 GPa, the MSD shows that at 1000 K, the $P2_1/m$-K_4Fe is still solid but already melted at 2000 K, indicating a melting temperature between 1000 and 2000K (Figs. 5.5a and 5.6a). This is consistent with the prediction from the empirical relation in Eq. 5.5 that predicted the melting temperature as 1254.94 K ± 555 K. The results of the MSD are corroborated by the *v*DOS at 1000 K and 2000 K. While softening of mode is barely visible at 1000 K, instability has propagated throughout the system at 2000 K (finite vibrational states at $\omega^2 \leq 0$) with characteristic broadening of most peaks, indicating a high degree of freedom in the melt.

Similar analyses are applicable to other candidate structures at higher pressures which allow us to generalize that near the phase boundary where melting occurs, instability gradually builds up until the system attain a state similar to a superheated solid. Further increasing the temperature eventually melts the system and the liquid phase becomes preferable. The MSD also indicates that the candidate structures at 30 GPa and 60 GPa (up to at least 1000 K), 90 GPa (up to at least 2000 K), 120 GPa and 150 GPa (up to at least 2500 K) are solid and are thermally stable.

The newly identified K-Fe compounds have interesting implication for the Earth's interior especially in explaining the missing K in the Earth's mantle. We therefore estimate the pressure-temperature (*P*-*T*) phase diagram for the K-Fe as shown in Fig. 5.5f. The result shows that within the computational error of the empirical model used for the *P*-*T* calculation, the K-Fe compounds match very well with the profile of the earth's interior (geotherm) up to 60 GPa. Above 60 GPa up to 120 GPa, the K-Fe compounds' *P*-*T* curve deviates slightly from the geotherm but matches very well with the profile of the *hcp*-Fe, which is the phase of Fe in the Earth's core [29]. Under further compression beyond 120 GPa, the K-Fe compound's *P*-*T* curve deviates further from the geotherm as well as the *hcp*-Fe with higher melting temperature. If energetics is favorable at higher pressure (>300 GPa) as we extrapolate further into the inner core pressure, the K-Fe compounds are expected to be thermally stable beyond 6000 K. This conjecture will still require direct investigation of compound formation between K and Fe above 300 GPa to conclusively determine the extent of K implications for the Earth's inner core.

Generally, below 130 GPa, the K-rich K-Fe compounds were dynamically stable and above 130 GPa, the Fe-rich compound is dynamically stable. These results revealed that the missing K from the Earth's mantle could form compound with Fe in the form of Fe-rich K-Fe compound at

pressures above 130 GPa and those left behind in the mantle (pressures below 130 GPa) may remain there in the form of K-rich K-Fe compounds. Although, we must comment that the complete validity of this will depend on the behaviour of other light elements at the region being considered.

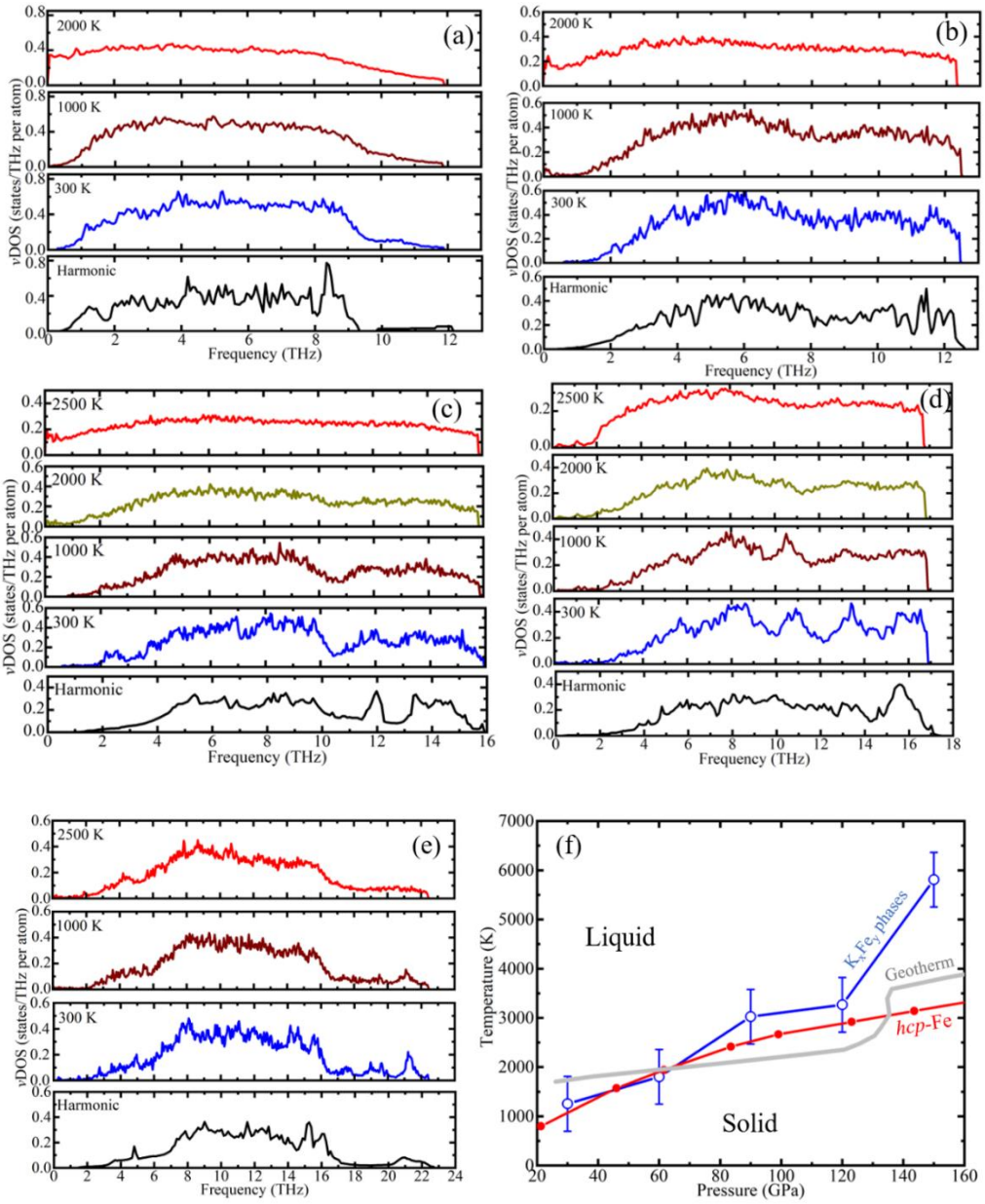

Figure 5.5. Total phonon DOS (harmonic) and temperature-dependent vibrational density of states (*v*DOS) calculated from the autocorrelation function of the MD simulation in an *NpT* ensemble at finite temperatures for the (a) K_4Fe in $P2_1/m$ structure at 30 GPa, (b) K_4Fe in $P\bar{1}$ structure at 60 GPa, (c) K_4Fe (1 f.u.) in $P1$ structure at 90 GPa, (d) K_4Fe (2 f.u.) in $P1$ structure at 120 GPa, and

(e) KFe_3 in *C*2/*m* structure at 150 GPa. (f) Pressure-temperature (*P*-*T*) phase diagram showing the phase stability field of the K-Fe phases (from empirical Eq. 5.5) compared with the *P*-*T* profile of the Earth's interior (geotherm) and the *hcp*-Fe from ref. [29].

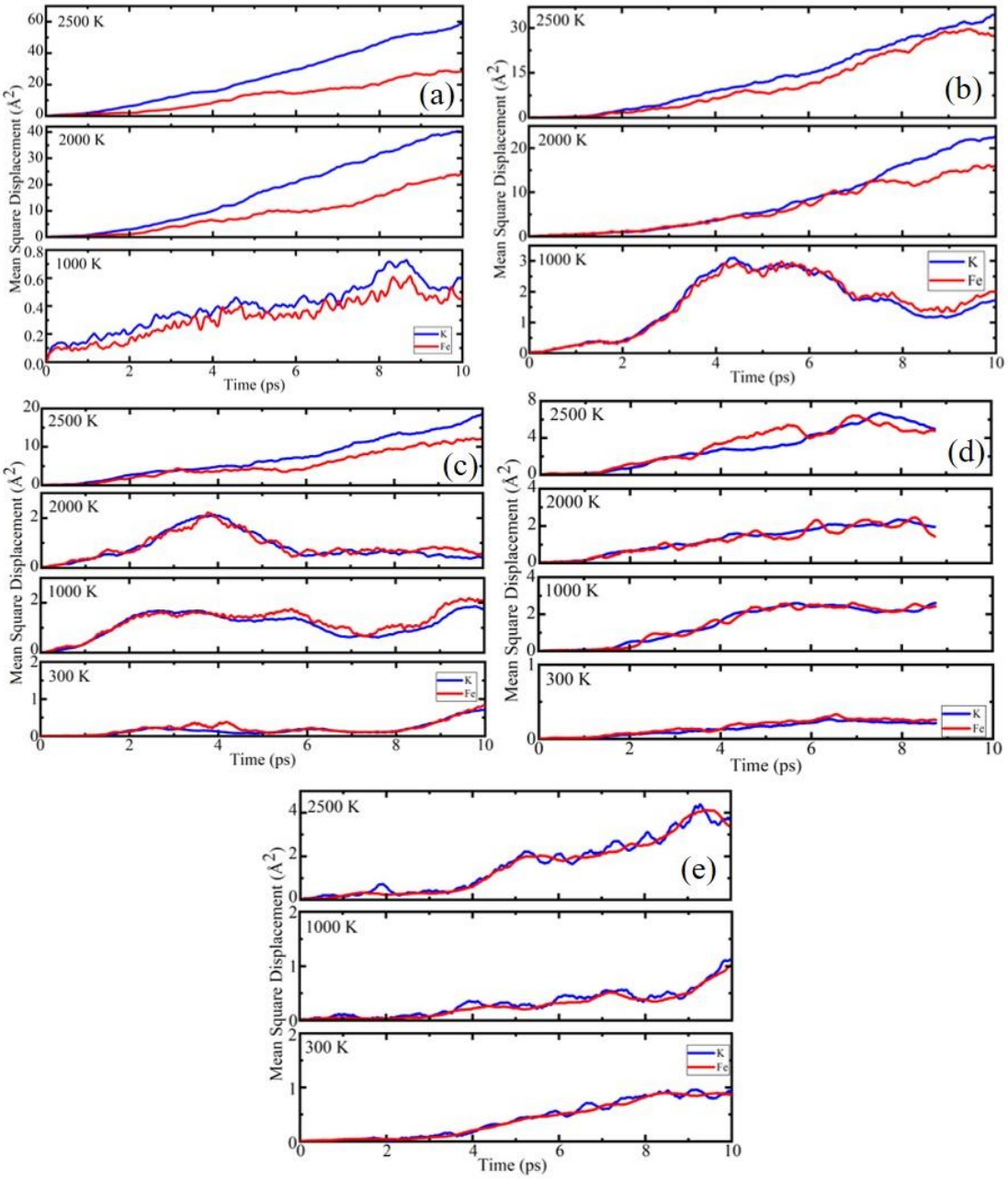

Figure 5.6. Temporal evolution of mean square displacement of the (a) K_4Fe in $P2_1/m$ structure at 30 GPa (b) K_4Fe in *P*-1 structure at 60 GPa (c) K_4Fe (1 f.u.) in *P*1 structure at 90 GPa (d) K_4Fe (2 f.u.) in *P*1 structure at 120 GPa (e) KFe_3 in *C*2/*m* structure at 150 GPa. The plots are shown for each atomic species at temperatures 300 K, 1000 K, 2000 K and 2500 K.

5.1.3.2 Electronic structures and electron localization in K_xFe_y

Chemical, electronic, and energetic change during compression [248] created a favorable condition for the formation of K-Fe compounds. At ambient pressure, alkali metals do not form compounds with transition metals due to large difference in size and electronic structure. Small difference in charge density at the Wigner-Seitz radius and large difference in electronegativity is necessary for compound formation between two metals [249,250]. The electronic band structure, electronic density of states (DOS) projected to atomic orbitals, electron charge transfer and electron localization function (ELF) were calculated for all the candidate structures. The calculated electronic band dispersions (Fig. A5.2) reveal that all the candidate structures are metallic, consistent with the Poisson's ratio discussed earlier.

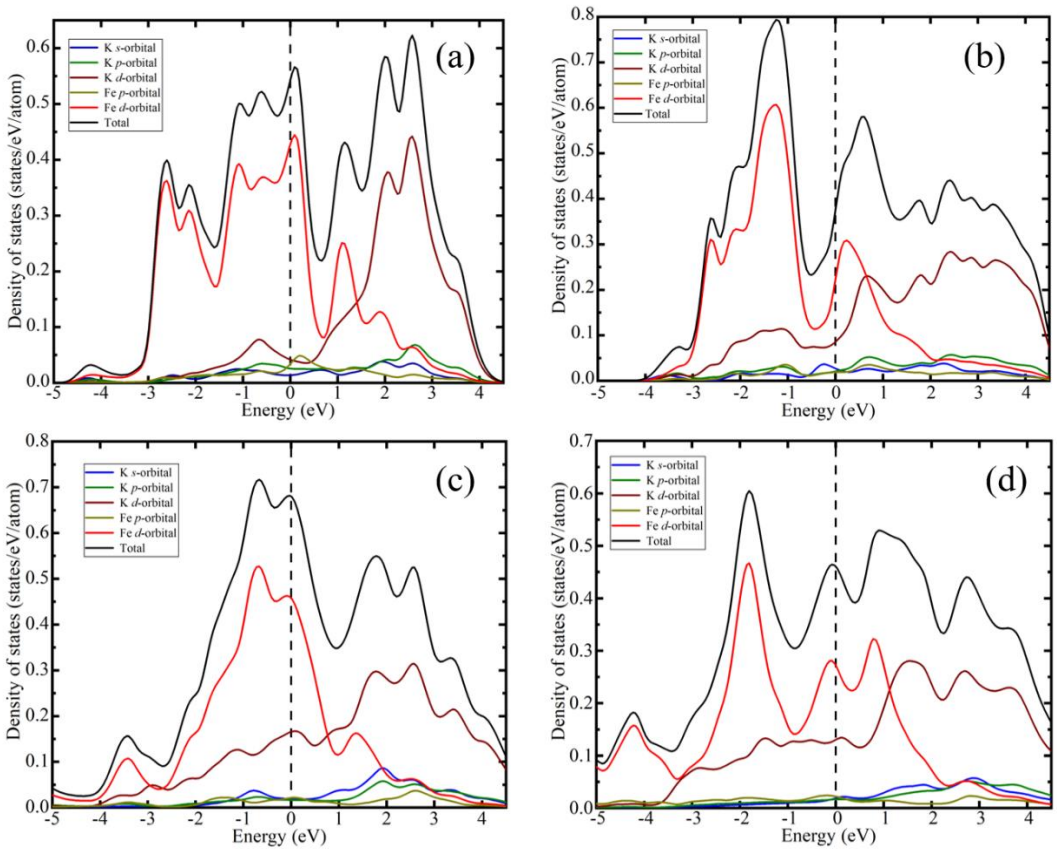

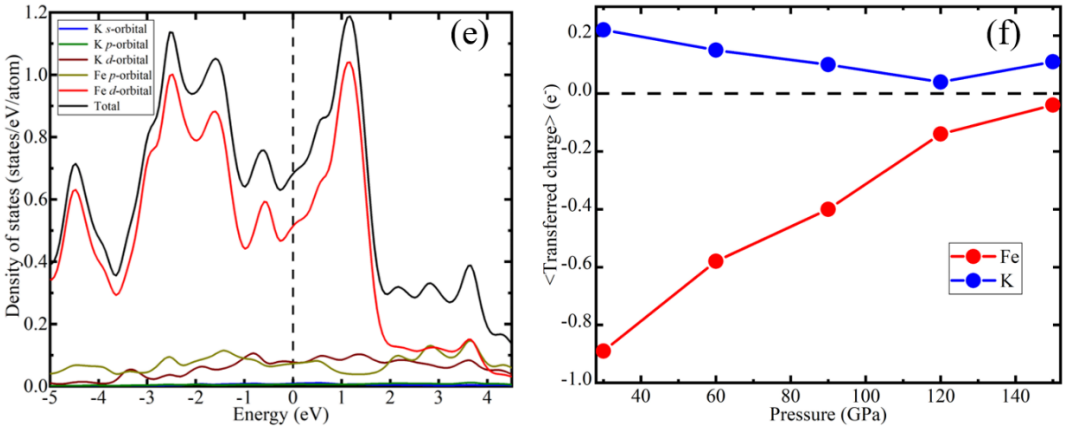

Figure 5.7. Electronic density of states projected to atomic orbitals for the (a) K_4Fe in $P2_1/m$ structure at 30 GPa (b) K_4Fe in P-1 structure at 60 GPa (c) K_4Fe (1 f.u.) in $P1$ structure at 90 GPa (d) K_4Fe (2 f.u.) in $P1$ structure at 120 GPa (e) KFe_3 in $C2/m$ structure at 150 GPa. Average charge transfer evolution under pressure for (f) candidate structures of the K-Fe binary systems. The $\langle ... \rangle$ on the y-axis label of (f) is the average transferred charge at a given pressure.

The calculated electronic DOS projected to atomic orbital (see Figs. 5.7a-e) reveals that the K's and the Fe's *d* electrons are primarily responsible for metallic character in K-Fe candidate structures. The delocalization of K *d* (Fe *d*) electrons slightly increases (decreases) under pressure up to 60 GPa beyond which it remains fairly constant up to 150 GPa considered in this study. Bader charge analysis (BCA) [207] was performed on K-Fe candidate structures. The results reveals that the K-Fe compounds are stabilized through notable electron transfer from K to Fe upon compound formation. The Fe atoms gain fraction of electron from K atoms. As shown in Fig. 5.7f, Fe atoms are anionized by striping the K atoms of averagely between 0.22 e^- at 30 GPa and 0.11 e^- at 150 GPa while Fe atoms gain averagely between 0.89 e^- at 30 GPa and 0.04 e^- at 150 GPa. Similar electron transfer mechanism was recently predicted in K-In systems [251] and PuH_2 [252]. Under pressure, the average charge transfer between K and Fe atoms reduces which suggest that under further compression to extremely high pressures (>> 150 GPa), K and Fe may switch their roles in the stabilization of K-Fe compounds with Fe atoms losing electrons (see Fig. 5.7f). This is a reasonable expectation since monotonic decrease in average K-Fe interatomic distance under pressure (Fig. A5.1) reduces the ability of K atoms to lose electron.

The result of ELF calculations (Fig. A5.4) reveals that while there are no signs of stripped electrons occupying the interstitial regions in all the candidate structures studied, they populate the Fe 3*d* orbital which is relatively lower in energy under pressure [22]. Furthermore, ELF of all candidate structures lack charge overlap along the K-Fe, Fe-Fe, and K-K bonds or contacts indicating the absence of covalency in these structures.

While the present study provides theoretical evidence for the formation of stable compounds of K and Fe under pressure, its actual composition in the core and the amount of heating due to such reactions remain open and requires further study. In fact, the formation of stable K-Fe compounds above 200 GPa up to pressures relevant to the solid Earth's core still require direct investigation. We have previously reported the formation of stable intermetallic compound between Ar and Ni at deep earth conditions [44]. Such consideration was hinged on the assumption that radioactive ^{40}K produces heat through electron capture, leaving Ar behind to react with the constituents of the earth's core. The present study therefore considers, in general, the reaction of the nonradioactive isotope of K without necessarily constraining its abundance as it is drawn into the Earth's core from the mantle - its main reservoir.

5.1.4 Conclusion

Using a combination of the particle swarm optimization and density functional theory calculations, we have identified and studied stable stochiometric structures of K-Fe intermetallic compounds. Potassium forms stable compounds with iron at 30 GPa and above. Five dynamically and thermodynamically stable structures were unearthed with interesting structural and mechanical properties. All the candidate structures reported are predicted to have metallic ground state contributed predominantly by the K's and the Fe's *d* electrons. The K-Fe compounds are stabilized by high pressure and notable electron transfer between K and Fe. Furthermore, K-rich K-Fe compound is predicted to undergo phase transformation under pressure and clustering of K atoms through phase segregation is observed to precede phase transformation to Fe-rich phase above 120 GPa. The current study has significant implication for understanding the Earth's core if energetics is favorable for a K-Fe compound above 300 GPa.

5.2 Two Good Metals Making a Semiconductor: a Potassium-Nickel Compound under Pressure

At high pressure, unconventional compounds with interesting properties can be uncovered with significant implication for geosciences. We report the formation of intermetallic potassium-nickel compounds at 37 GPa. A particularly interesting, stoichiometry - K_2Ni, was considered for which the ground state structure crystalizes into an orthorhombic cell with space group *Cmcm*. Interestingly, a metastable phase with the $P2_1/m$ space group is also predicted to form an unexpected, semi conducting ground state with an indirect band gap of 0.65 eV. We also report a remarkable agreement between the simulated x-ray diffraction (XRD) pattern of the K_2Ni-$P2_1/m$ phase and the experimentally synthesized K-Ni compound at 37 GPa. A high temperature compound formation pathway for the K_2Ni-$P2_1/m$ structure is also proposed. An interplay between Peierls distortion and symmetry breaking is found to drive the opening of a band gap. The prediction of a non-metallic K-Ni compound under pressure will stimulate further research into the fundamental high pressure and high temperature chemistry of potassium. Furthermore, such result could help to understand a potassium-containing Earth's core if energetics is favorable at the pressure of the inner core.

5.2.1 Introduction

The chemistry and reactivity of alkali metals with transition metals has been subject of extensive investigation, especially at elevated pressures and temperatures. At ambient conditions, heavy alkali metals possess much smaller charge densities relative to transition elements which is known to inhibit compound formation between them. However, high pressure, which can cause pressure-induced mixing between 4*s* and 3*p* and 3*d* electronic shell may be used to drive a *s*-to-*d* transition in alkali metals to become transition metal-like with comparable charge densities [236,253]. Overall, the occupation of the *d* band plays an important role in the formation of complex structures. In connection with this transition, Significant attention has been paid to potassium (K) because of its implication for the Earth's interior, where K is abundant, and pressure grows rapidly beyond moderate depth and extrapolation of ambient (low pressure) data breaks down [233,236].

For example, the formation of alkali metal (K) – transition metal (Ag) anisotropic compound was reported at room temperature upon compression of stoichiometric mixture of the elements at 6.1 GPa – a pressure less than the ~26 GPa required for the *s*-to-*d* transition for the alkali metals. Such system is stabilized through "chemical pressure" induced during compound formation where reduction in inter atomic distance between K atoms corresponds to what is observed in elemental K at 44 GPa. Since lithium (Li) is the only alkali metal that form compound with Ag at ambient pressure, then, under pressure, K exhibits comparable properties with ambient pressure Li [254]. A follow up study was done where mixture of K and Ag was compressed up to 40 GPa at room temperature. This study resulted in the formation of C14 AB_2 Laves phase of Ag rich (KAg_2) compound, quench recoverable down to 7 GPa. The KAg_2 is stabilized through the lowering of the electron density of K towards that of Ag as predicted by Miedema's rule [255]. With several other experimental studies [233,236] undertaken to understand the nature of compounds formed by alkali – transition metals under pressure, similar trends were observed.

Theoretically, possible chemical reaction between K and Fe was modelled using density functional calculations by incorporating K into the unit cell of *hcp*-Fe at 35 GPa. The result shows a high amount of K alloying with Fe [234]. Recently, phase stabilities of equiatomic K_xIn_y (x = y = 1,2,3,4) under pressure up to 100 GPa was studied through quantum calculations [256]. The study predicted the formation of compounds at as low a pressure as 5 GPa. The K_xIn_y compounds are said to be stabilized through significant electron transfer from K atom to In atom, consequently forming a metallic compound. The formation of semi conducting alkali metal (K) – transition metal compound is unconventional, counter intuitive and therefore, it will be interesting to understand why combining two metals under pressure could open a band gap.

The formation of stable K-Ni compound under pressure is also relevant in geosciences. Potassium is depleted in the bulk silicate earth (BSE). This conclusion is based largely on unbalanced abundance of K in the BSE relative to the CI chondrite [32,34]. Part of the depleted K was proposed to have escaped into space through evaporation [32] while bulk of it was proposed to have segregated into the Earth's core during its accretion [32,34. Following the successful synthesis of a K-Ni compound at 37 GPa by Parker *et al.* [236], its exact structure is yet to be identified, a problem that preclude a full characterization and unambiguous understanding of the material. Beyond solving the crystal structure of the synthesized K-Ni compound, the broader

impact of investigating the formation of stable K-Ni compound would be improving our understanding of the chemistry of alkali metals under pressure, all of which motivate the present study.

In this study, we systematically investigate the potential energy landscape of the K-Ni system at 37 GPa using a combination of both the particle swarm-intelligent optimization and the genetic algorithm. We found a monoclinic structure in the K_2Ni stoichiometry with space group $P2_1/m$ to sufficiently explain the structure of the K-Ni compound synthesized by Parker *et al* [236] when combined with FCC Ni. We therefore propose the $P2_1/m$-K_2Ni structure to be the structure of the synthesized K-Ni compound. We further elucidate the processes that stabilize the $P2_1/m$-K_2Ni structure at the *P-T* condition of synthesis. The formation of stable, quench recoverable and semiconducting K-Ni compound expand our understanding of alkali metal materials' property change under pressure.

5.2.2 Computational Methods

A search for stable structures was carried out using two global search methods: genetic algorithm (GA) [257] and particle swarm-intelligence optimization (PSO) [100,101]. The PSO search was done at 0 GPa and 37 GPa (*i.e.*, synthesis pressure for K-Ni compound [236]) with simulation cells containing up to four K_xNi_y formula units. Geometrical optimization, total energy calculation, and molecular dynamics (MD) simulation were performed using the Vienna *ab initio* simulation package (VASP) [93] and projector-augmented wave (PAW) potentials [116] with the Perdew-Burke-Ernzerhof (PBE) functional [61]. The K and Ni potentials with valence states of $3s^2 3p^6 4s^1$ and $3s^2 3p^6 3d^8 4s^2$, respectively, were employed and an energy cutoff of 450 eV was used. A *k* spacing of $2\pi \times 0.02$ Å^{-1} was used for Brillouin zone (BZ) sampling. Phonons were calculated using the density functional perturbation theory as implemented in the VASP code and the calculated force constants were post processed using the PHONOPY code [102]. *Ab initio* molecular dynamics (AIMD) simulations were performed employing an isothermal-isobaric (*NpT*) ensemble in a 3×3×3 supercell containing 162 atoms. AIMD trajectories were obtained from 10 ps long simulations sampled with a 2 fs time step. The system temperature was controlled using

the Langevin thermostat. The finite temperature vibrational density of states (*v*DOS) was obtained from the velocity autocorrelation function (VACF) of the MD trajectories [258].

Since hybrid functionals predict energy band gap more accurately than semilocal density functionals such as PBE, electronic band structure and electron localization function (ELF) calculations were done using Heyd-Scuseria-Ernzerhof (HSE) hybrid functional [70] with a mixing parameter of 0.25 and long-range exchange contribution parameter (ω) of 0.2 as implemented in the VASP code. Bader charge analysis was done using VASP and post processed using Henkelman code [186]. ELF calculation was performed using a 120×120×120 mesh. Magnetic (spin polarized quantum) energetics calculations were performed on a model built from a 2×2×2 supercell comprising of 48 atoms. The ferromagnetic, ferrimagnetic, antiferromagnetic, and paramagnetic configurations were constructed, and their ground state energies calculated within GGA+U approximation using the PBE functional. The correlation effect on 3*d* electrons were treated within the GGA+U using the Dudarev approach [239] with an on-site coulomb interaction U_{eff} (U_{eff} = U - J) of 5.0 eV, which is according to the U_{eff} value proposed for Ni [259] where linear response theory was used.

5.2.3 Results and Discussion

5.2.3.1 Phase Stability and Stable Crystalline structures

We systematically searched for stable structures of the binary K_xNi_y ($x, y \in \{1, \dots, 4\}$) with cells containing 1 to 4 K_xNi_y formula units (f.u.) at a pressure (P) of 37 GPa and temperature (T) of 0 K. The search pressure was informed by the pressure of synthesis reported by Parker *et al* [236]. The energy difference between different magnetic states for the energy minimum structure is expected to be small, therefore, structure search was done without spin polarization. We have used the hexagonal *h*P4 structure of K to approximate the incommensurate K-III phase throughout this work. The K-III is known to be stable in the pressure range of 23 GPa and 57 GPa [260] while the FCC Ni is known to be stable in the pressure range of 0 GPa up to at least 320 GPa [261]. The enthalpy of formation (ΔH_f) per atom of K_xNi_y relative to elemental K-III and FCC Ni solids was calculated according to Eq. (5.1). We established the fitness for synthesis and thermodynamic stability of each stoichiometry using the convex hull [262]. The convex hull was constructed using

the minimum of the calculated ΔH_f of the most stable structures for each composition. In principle, structures whose ΔH_f lies on the convex hull are deemed stable and could be realized experimentally.

The convex hull for K_xNi_y at 37 GPa, 0 K is shown in Fig. 5.9a. At 37 GPa and 0 K, Ni and K are predicted to form compounds in the K_4Ni, K_2Ni, K_3Ni_2, K_3Ni_4 and KNi_4 stoichiometries, all unknown before but accessible according to this calculation.

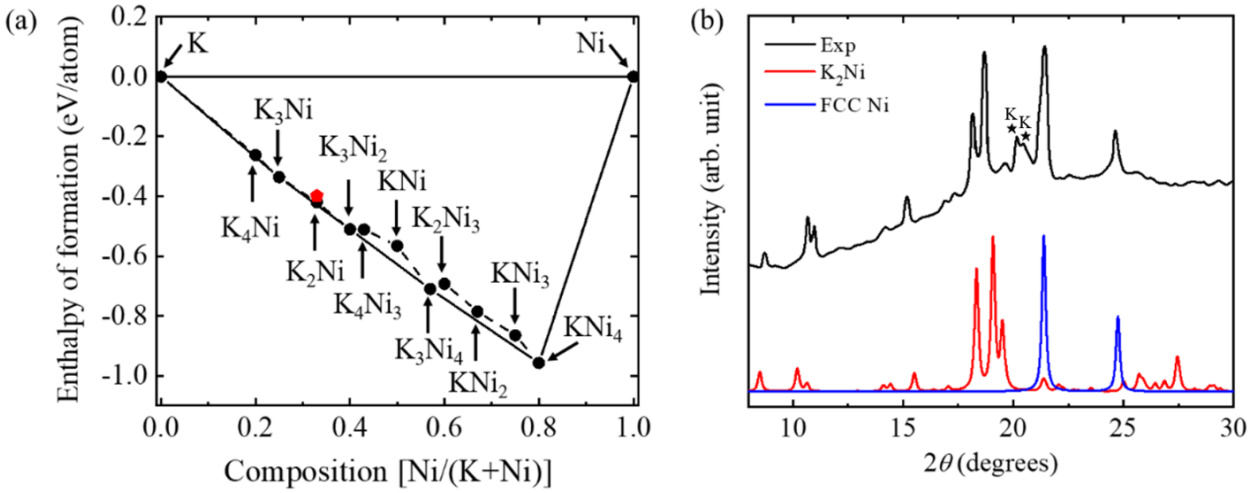

Figure 5.8. (a) Convex hull for K-Ni compounds at 37 GPa from PSO search. The red diamond is the *P*2$_1$/*m*-K2Ni from GA search. (b) Calculated XRD patterns for the *P*2$_1$/*m*-K_2Ni and the FCC Ni at 37 GPa, compared with the previously reported experimental XRD pattern [236] at the same pressure. The X-ray wavelength used is λ = 0.72 Å. Asterisks with K shows the positions of K-III peaks at 30 GPa (slightly shifted downward due to volume difference). Figure 5.9b was adapted from Ref. [46].

In this work, the K_2Ni stoichiometry is of interest as one of the predicted structures (marked as a red object in Fig. 5.8a) corresponds to the experimental observation in Ref. [236] where a reaction between elemental K and Ni was reported (see later). At 37 GPa, the monoclinic *P*2$_1$/*m*-K_2Ni have higher enthalpy (0.02 eV/atom) than the orthorhombic *Cmcm*-K_2Ni structure – thermodynamics ground state at 0 K. It is worthy of note that at the pressure of evaluation, both structures have similar zero-point energy (ZPE). The convex hull calculated at 0 GPa (Fig. 5.9a)

shows no thermodynamically stable K-Ni compounds form. Furthermore, the evolution of ΔH_f under pressure for K_2Ni (shown in Fig. 5.9b) predicts a formation pressure of ~17 GPa.

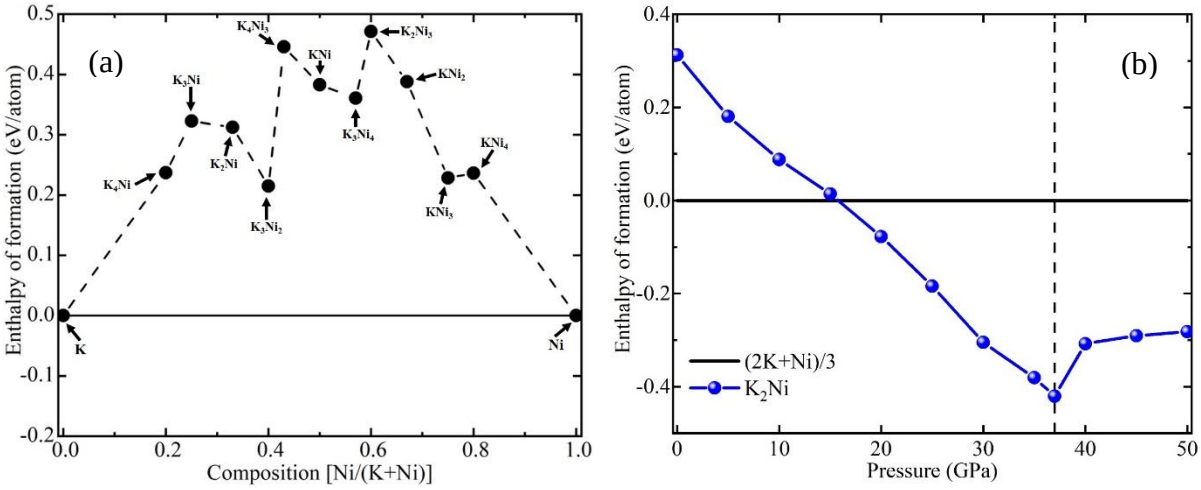

Figure 5.9. (a) Convex hull for K-Ni compounds at 0 GPa from PSO search. (b) Evolution of enthalpy of formation of K_2Ni relative to elemental mixture of K and Ni under pressure. The vertical dash line is the pressure of interest (37 GPa).

A chemical reaction was reported between elemental K and Ni powder after the mixture (molar ratio of 2:1 for K:Ni) was compressed up to 37 GPa and laser heated up to ~2500 K but with no knowledge of the crystal structure [236]. Here, we demonstrate that the XRD pattern can be explained by the $P2_1/m$-K_2Ni structure. The structural parameter of the $P2_1/m$-K_2Ni structure at 37 GPa are $a = 5.21$ Å , $b = 4.25$ Å, $c = 4.35$ Å and $\beta = 111.37^0$ with K atoms located at 2e: 0.669, 0.75, 0.087; 2e: 0.015, 0.75, 0.764 and Ni atoms at 2e: 0.622, 0.25, 0.573. For completeness, the structural parameter of the *Cmcm* (lowest energy) structure on the convex hull for the K_2Ni stoichiometry at 37 GPa are $a = 4.61$ Å , $b = 10.25$ Å and $c = 3.77$ Å with K atoms located at 4c: 0.0, 0.0885, 0.25; 4c: 0.5, 0.2355, 0.25, and Ni atoms at 4c: 0.0, 0.4563, 0.25. We found that the $P2_1/m$-K_2Ni structure alone was not sufficient to index all the peaks in the experimental XRD. We achieved remarkable agreements in the relative intensities and 2θ positions between the simulated and experimental XRD when the $P2_1/m$-K_2Ni structure was combined with unreacted FCC Ni (see Fig. 5.8b).

The peak at $2\theta = 24.8°$ can be uniquely indexed to the FCC Ni, while the peak at $2\theta = 21.4°$ appears to be an overlap of stronger peak from FCC Ni and weak peak from the $P2_1/m$-K_2Ni structure. The two peaks at $2\theta = 20.2°$ and $2\theta = 20.5°$ was previously interpreted as belonging to the starting K-III structure [236]. Most of the remaining Bragg peaks (of the 2θ positions) are signature peaks of the $P2_1/m$-K_2Ni structure and can be indexed to it. We also note that there are no Bragg peaks from the $P2_1/m$-K_2Ni structure occupying the 2θ position of the K-III structure. Deviations in intensities are likely due to uncertainties and both theory and experiment.

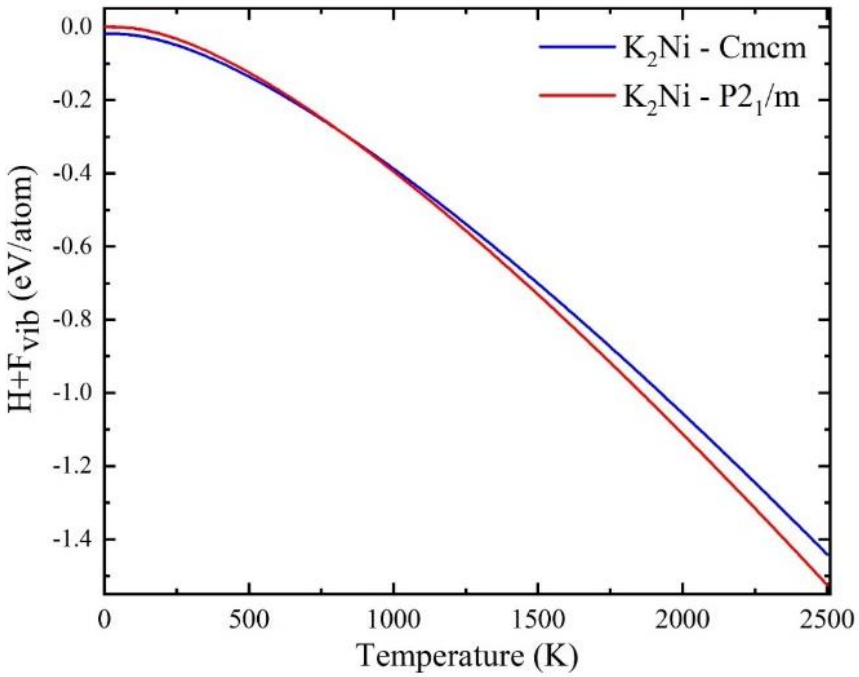

Figure 5.10. Temperature dependent enthalpy ($H+F_{vib}$) for the $P2_1/m$-K_2Ni and the *Cmcm*-K_2Ni structures at 37 GPa. The enthalpy (H) of the $P2_1/m$-K_2Ni at 0 K was used as the zero-enthalpy origin. F_{vib} is the vibrational free energy.

The synthesis of a stable K-Ni compound was achieved at high temperatures between 2000 K and 2500 K. This suggests that the compound could be metastable at 0 K and stabilize (possibly) through kinetics. To establish the validity of our conjecture, we consider the Helmholtz free energy $F_{vib}(\mathrm{T})$ at temperature T , with harmonic approximation, according to Eq. (3.2). The vibrational free energy $F_{vib}(T)$ of both the $P2_1/m$-K_2Ni and the *Cmcm*-K_2Ni structures were evaluated up to the temperature field representative of the experimental synthesis condition (2500 K). The result

of the Helmholtz free energy calculations (Fig. 5.10) establishes that at the temperature of synthesis reported by Parker *et al*, the $P2_1/m$-K_2Ni structure is stabilized by temperature. The $Cmcm$-K_2Ni structure is predicted to be preferred at 37 GPa and temperature of 0 K up to ~750 K as it consistently possess lower energy than the $P2_1/m$-K_2Ni structure. Between 750 K and ~1000 K, both structures cannot be differentiated purely by their energy as both structures are predicted to have similar energy. However, above 1000 K, up to at least 2500 K (considered in this study) the $P2_1/m$-K_2Ni structure become preferred, establishing the $P2_1/m$-K_2Ni as a high temperature phase. The drop in the energy of the $P2_1/m$-K_2Ni structure relative to the $Cmcm$-K_2Ni structure at temperature above 1000 K can therefore be pinned to the vibrational free energy contribution.

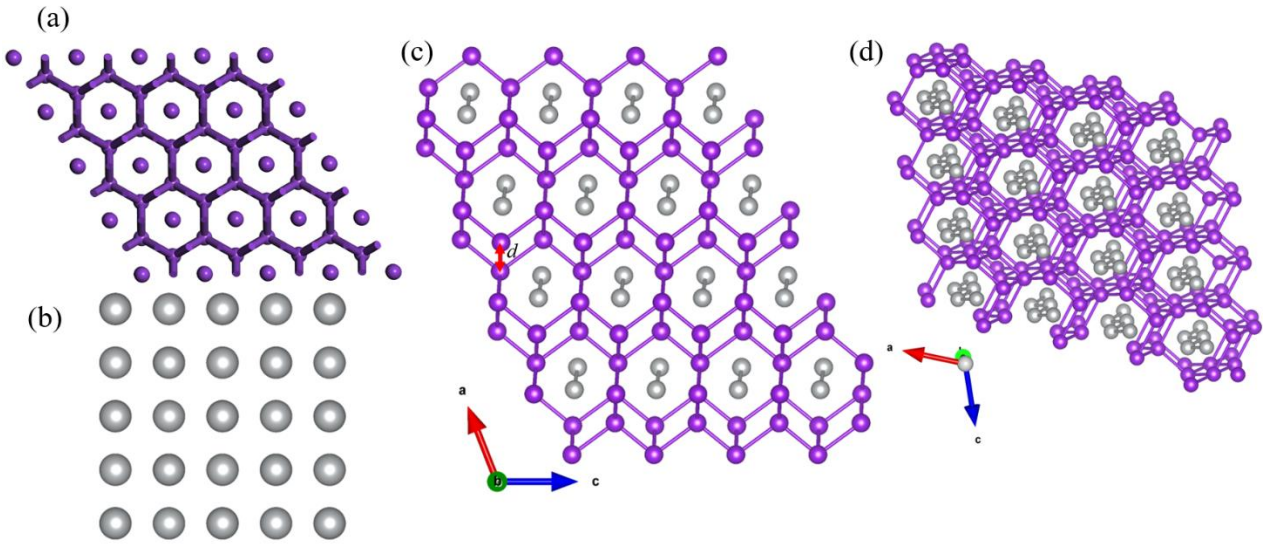

Figure 5.11. Two-dimensional (010) view of the crystal structure of (a) hexagonal $P6_3/mmc$ potassium (K-III) at 37 GPa (b) cubic Fm-3m nickel (FCC Ni) at 37 GPa. (c) $P2_1/m$-K_2Ni at 37 GPa. The red double-headed arrow shows the translation of stacked layers of honeycomb K network by a distance *d*. (d) Three-dimensional crystal structure of $P2_1/m$-K_2Ni at 37 GPa. K and Ni atoms are colored purple and grey, respectively.

The crystal structure of the $P2_1/m$-K_2Ni is shown in Figs. 5.11c and 5.11d. The mechanism of formation of the $P2_1/m$-K_2Ni compound under pressure can be thought of in terms of incorporation of Ni atoms from FCC lattice into base K-III (see Figure 5.11 a-c). In principle, when metals mix with one another under extreme conditions, alloy or compound can form through either atom exchange or through interstitial mechanism [263]. Atoms of relatively similar size

form alloys through atom exchange method. Under compression (to 37 GPa), K-I transforms to K-III though K-II, accompanied by electronic topological transition (ETT). The ETT makes K to become transition metal-like with similar electron density to Ni and by extension, Ni attain similar size with K [236]. Thus, at the pressure of interest (37 GPa), central atoms in the K-III lattice (see Fig. 5.11a) are replaced by group of Ni atoms from the fcc-Ni lattice (see Figure 5.11b) to form an intermetallic, $P2_1/m$-K_2Ni structure (see Fig. 5.11c). The successful exchange of the central K atom with the group of Ni atoms induces a distortion on the hexagonal network of the K-III lattice and a Peierls distortion in Ni lattice so that the perfect order in Ni atoms arrangement is broken. More details can be found in section 5.2.3.2 and ref. [46].

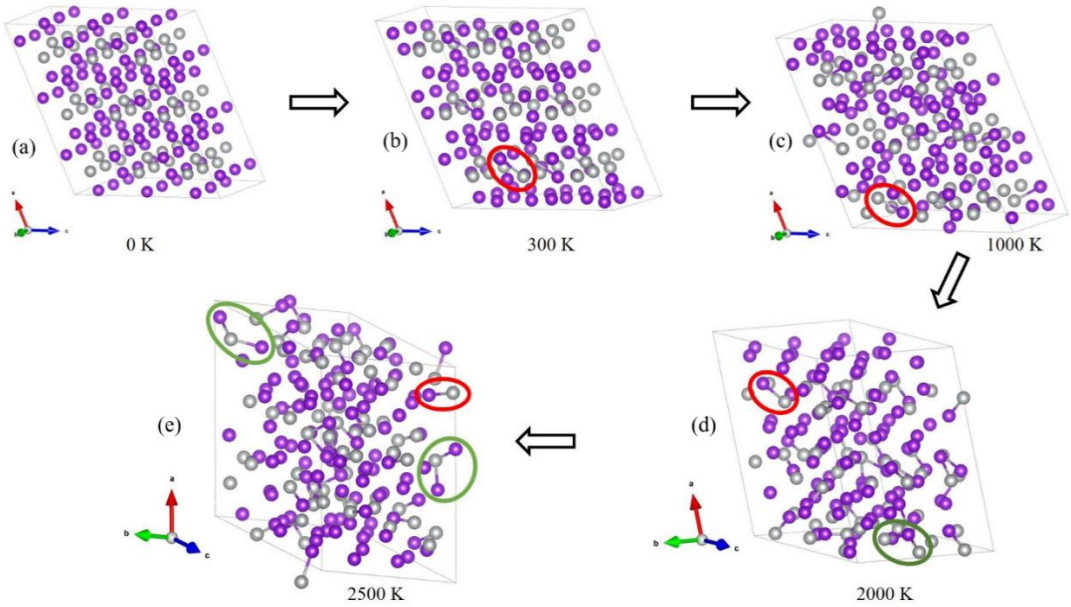

Figure 5.12. (a) Starting structure at P = 37 GPa and T = 0 K. Snapshot of average configuration from the *ab initio* MD simulation in an *NpT* ensemble at P = 37 GPa and (b) T = 300 K (c) T = 1000 K (d) T = 2000 K (e) T = 2500 K. The average configuration was calculated after the system has fully equilibrated between 8000 and 9000 time step in step of 100. To guide the eye, the red circle is used to identify the K-Ni unit and the green circle is used to identify the K-Ni-K unit. The simulation cells contain 162 atoms with the purple balls being the K atoms.

At a constant pressure, the dynamics of atoms in a chemical system changes as temperature is increased. We investigated the effect of temperature on $P2_1/m$-K_2Ni compound formation using

ab initio molecular dynamics (AIMD) simulation. The results of our AIMD simulation reveal that the system transforms from being a simple alloy of K and Ni to being a chemical compound (see Fig. 5.12). We slowly heat the system, initially at 37 GPa, 0 K (Fig. 5.12a), to 300 K and in steps up to 2500 K in an *NpT* ensemble. The AIMD simulation reveals that, at as low as 300 K up to 1000 K (Fig. 5.12b-c), there is tendency for the development of K-Ni units. There is increased tendency in for the formation of K-Ni units and formation of K-Ni-K units (Fig. 5.12d-e) as temperature increases to 2500 K. This can be explained by the decrease in the nearest neighbor (NN) distance between K and Ni atoms as temperature increases (see Fig. 5.13). The decrease in NN distance is known to favor bond formation [264] and as such it is reasonable to expect more bonding between K and Ni if temperature is further increased.

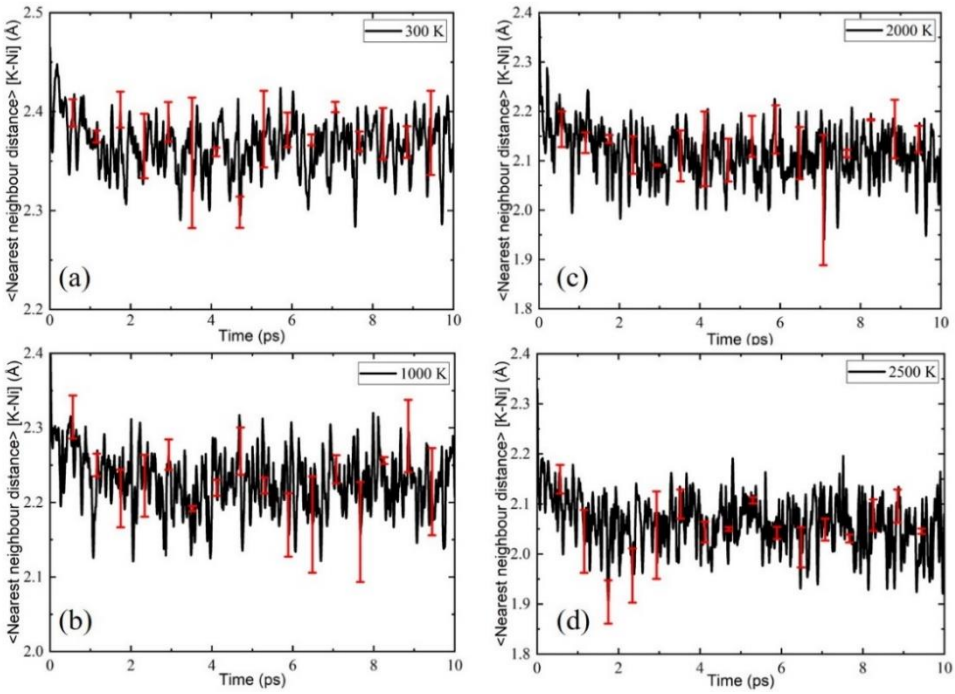

Figure 5.13. Temporal evolution of the average nearest neighbor (NN) distance with error band for the K-Ni unit of the $P2_1/m$-K_2Ni system at 37 GPa. The plot is shown for temperatures (a) 300 K, (b) 1000 K, (c) 2000 K, and (d) 2500 K. The red bands show time evolution of the standard error in the NN distance calculated from three (triplicate) separate *ab initio* molecular dynamics (AIMD) simulations. The ⟨...⟩ bracket in the *y*-axis label is the instantaneous average at a given time step in the AIMD simulations.

5.2.3.2 Electronic structure and electron localization in K_2Ni

Alkali metals do not form compound with transition metals at ambient pressure (with exception observed in Au) due to large difference in size and electronic structure. Miedema's rules [249] requires that there be small difference in charge density at the Wigner-Seitz radius and large electronegativity difference between two metals for successful compound formation which is not the case in alkali and transition metals at ambient condition. Bader charge analysis reveals that the $P2_1/m$-K_2Ni structure is stabilized through notable electron transfer from K to Ni upon its formation. The Ni atom behaves like an oxidant, gaining (fraction of) electron from K atoms. In the $P2_1/m$-K_2Ni structure, Ni atom is anionized by striping each of the two K atoms of $0.4\,e^-$ thereby gaining a total of $0.8\,e^-$ thereby inducing strong electrostatic interaction in the system. Similar electron transfer was recently predicted in K-In systems [256]. High pressure diamond anvil cell (DAC) experiments on noble gas elements and transition metals also reported intermetallic compounds of Xe-Ni/Fe [22] system at high pressures in which the Ni/Fe atoms behaves like an oxidant, gaining fraction of electron and a reverse mechanism in Ar-Ni [44] system where Ar behaves like an oxidant.

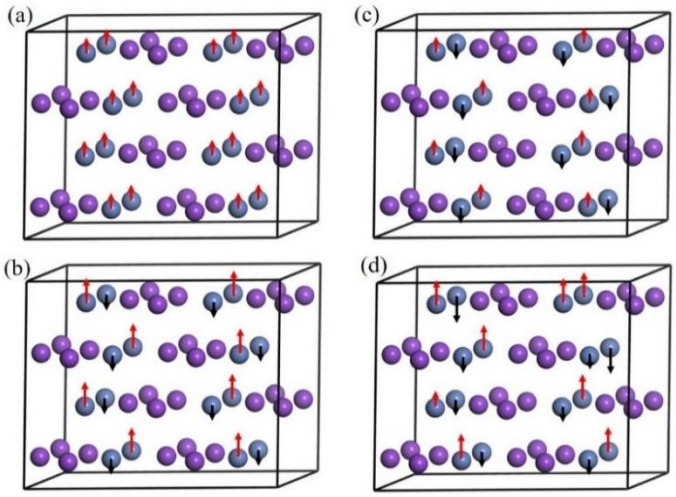

Figure 5.14. Constructed magnetic models of K_2Ni (a) The ferromagnetic (b) The ferrimagnetic (c) The antiferromagnetic and (d) The paramagnetic configurations. The red and black arrows indicate spin up and spin down, respectively. The length of the arrows (although not drawn to scale) qualitatively describes the magnitude of the spin states. The purple balls and the blue balls are the potassium and nickel atoms, respectively.

Spin polarized quantum calculations was done on a 2 × 2 × 2 cell comprising of 48 atoms. The result reveals that the $P2_1/m$-K_2Ni structure corresponds to the ferromagnetic ground state in which spins aligns parallel to each other on Ni atoms (Fig. 5.14a). The ferromagnetic configuration is 0.9 meV/atom lower than the ferrimagnetic configuration (in which spins of unequal magnitudes aligns in an anti-parallel configuration, see Fig.5.14b) and 2 meV/atom lower than the paramagnetic (Fig. 5.14d), antiferromagnetic (Fig. 5.14c) and nonmagnetic configurations.

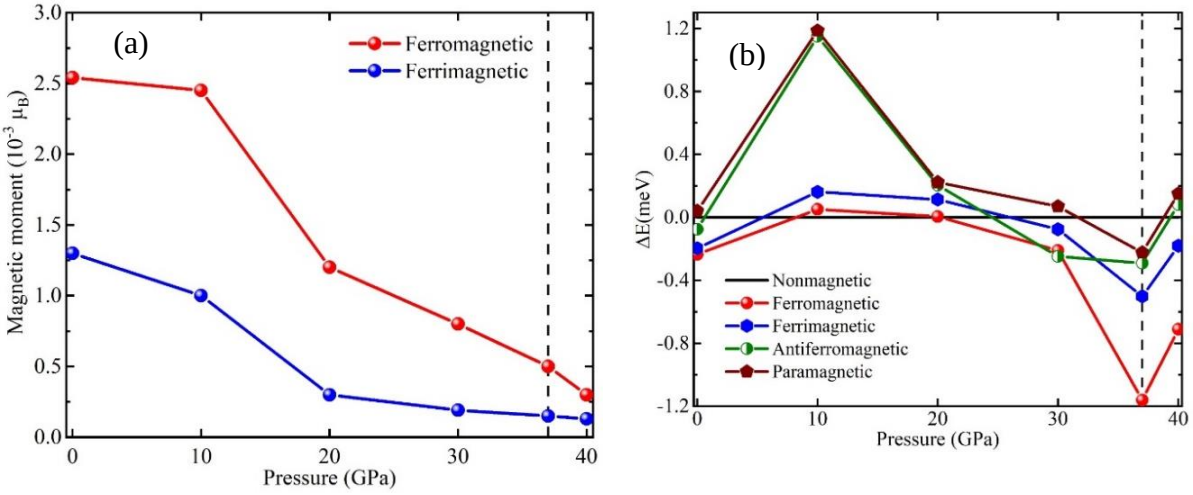

Figure 5.15. (a) Evolution of magnetic moment in ferromagnetic and ferrimagnetic models of K_2Ni under pressure. The vertical dash line is the pressure of interest (37 GPa) (b) Evolution of energetics of various magnetic models relative to the nonmagnetic model of K_2Ni under pressure. The vertical dash line is the pressure of interest (37 GPa).

The evolution of total magnetic moment (Fig. 5.15a), energetic stability (Fig. 5.15b) and structural parameters (Fig. 5.16) of various magnetic configurations of the $P2_1/m$-K_2Ni structure under pressure were investigated. The result shows that the ferromagnetic ground state of the $P2_1/m$-K_2Ni structure is energetically preferred at high pressure between 30 and 40 GPa. The total magnetic moment of ferromagnetic configuration is continually higher than that of ferrimagnetic configuration throughout the pressure field considered in this work. Furthermore, the magnetic moment approaches zero as the pressure is increased indicating that the $P2_1/m$-K_2Ni structure may

lose it magnetic properties to become nonmagnetic at extremely high pressure such as pressure relevant to the Earth core (>>120 GPa).

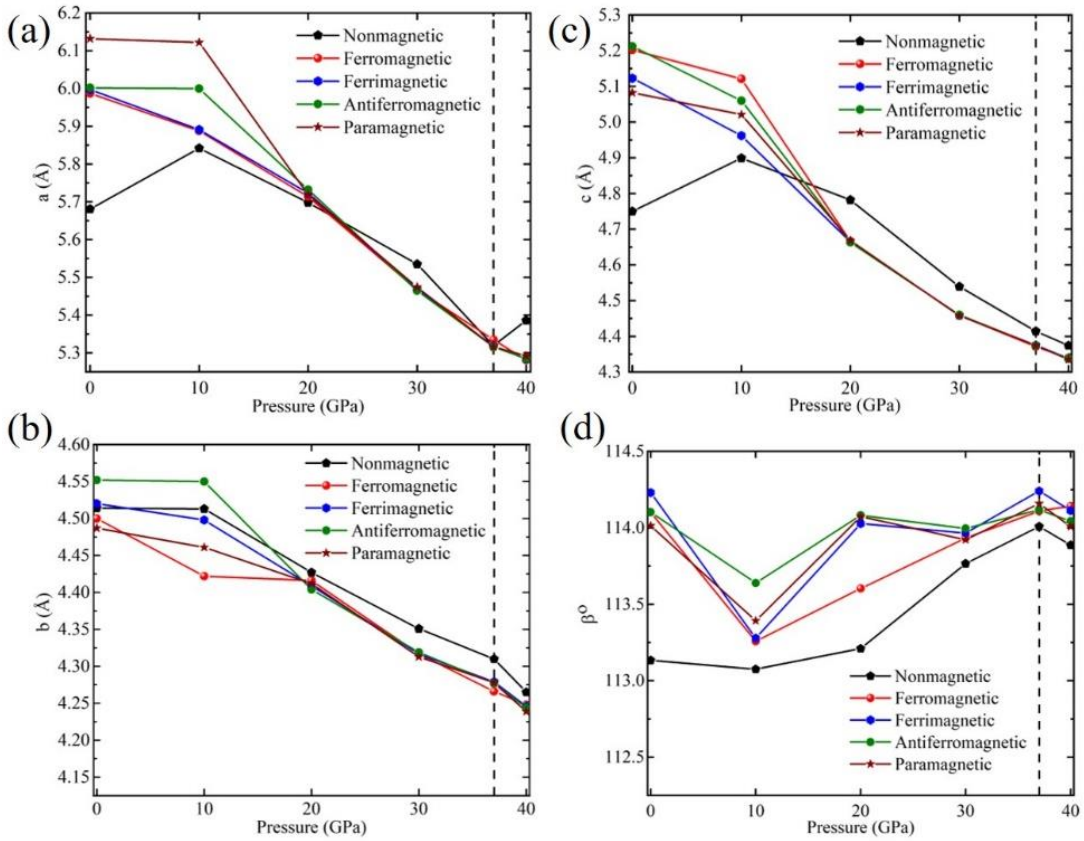

Figure 5.16. Evolution of structural parameters of various magnetic models and the nonmagnetic model of K_2Ni under pressure (a) – (c) are the lattice parameters, (d) is the angle β. The vertical dash line is the pressure of interest (37 GPa).

The calculated electronic band structure (see Fig. 5.17a) and electronic density of states (eDOS) (see Figure 5.18b) show that the $P2_1/m$-K_2Ni structure is semi conducting with an indirect band gap of 0.65 eV. The calculated eDOS of the model *Cmcm*-K_2Ni (see A5.1 in appendix for details) where the layers of K atoms are shifted such that they are exactly on top of each other (see Fig. 5.18a) and the *Cmcm*-K_2Ni (thermodynamic ground state structure, see Fig. 5.18c), are metallic. The $P2_1/m$-K_2Ni reaches semi conducting state through simultaneous translation and distortion of layers of K atoms honeycomb network, an effect known as symmetry-energy

lowering Peierls distortion (see Fig. 5.11a-c). We arrive at this conclusion after testing the conjecture that parallel layers of K honeycomb structure should be metallic, and a significant translation of these layers should induce a bandgap at the Fermi level (see detail in A5.1). The parent structure, with *Cmcm* space group features parallel, untranslated honeycomb layers of K atom with Ni atoms distributed in between, forming a linear chain. The formation of the $P2_1/m$-K_2Ni structure causes lowering of symmetry from orthorhombic system to monoclinic system (unit cell distortion) inducing distortion on the K honeycomb network within the cell. The unit cell distortion is followed by translation of the honeycomb layers of K by a distance *d* that is about half of K-K distance (see Fig. 5.11c). The Ni atoms responds to the distortion by forming a zig-zag network as shown in Fig. 5.11d. The $P2_1/m$-K_2Ni system also respond electronically to the structural distortion by adopting a ferromagnetic ground state.

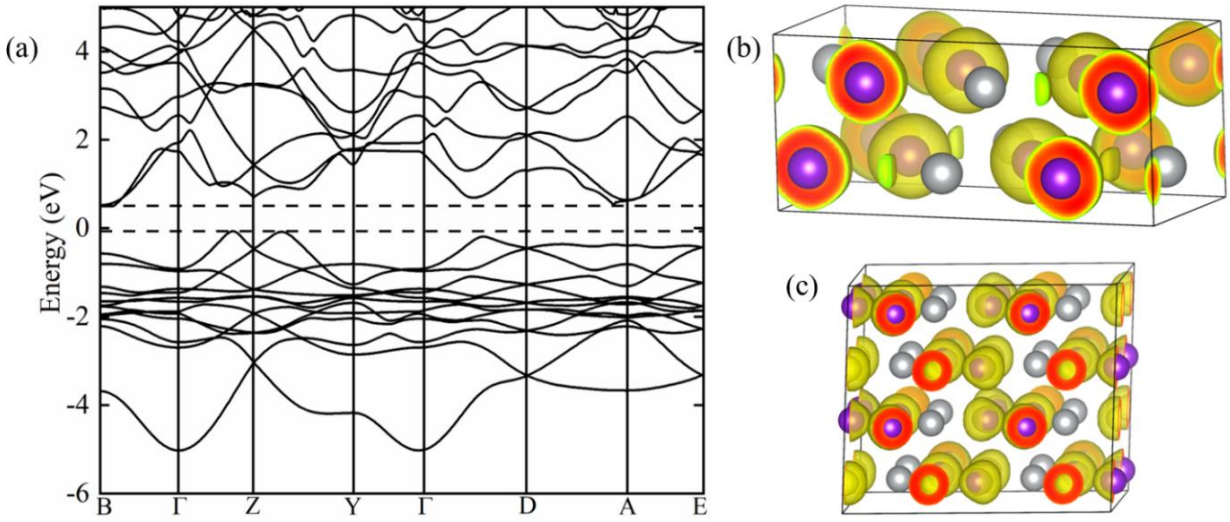

Figure 5.17. (a) Electronic band structure of $P2_1/m$ K_2Ni within the DFT+U framework. Electron localization function (drawn using an isovalue = 0.6) of (b) ideal *Cmcm* structure and (c) $P2_1/m$ structure of K_2Ni. K and Ni atoms are colored purple and grey, respectively. All calculations were carried out using HSE functional at 37 GPa.

Electron localization function (ELF) [117] was calculated for the parent *Cmcm*-K_2Ni structure (as shown in Fig. 5.17b) and for the *P*2_1/*m*-K_2Ni (as shown in Fig. 5.17c). The result of ELF calculation for the *Cmcm*-K_2Ni structure reveal that small fraction of electron from the K atoms form an electride state as they are pushed to the interstitial site. The virtual interstitial orbital become available in the system due to pressure effects. The distortion in the parent structure mitigates against the pushing of electron transferred from K to the interstitial site in the *P*2_1/*m*-K_2Ni structure. Instead, electrons are pushed to the Ni-3*d* orbital. The *P*2_1/*m*-K_2Ni also do not show electron localization that could be interpreted as covalent character.

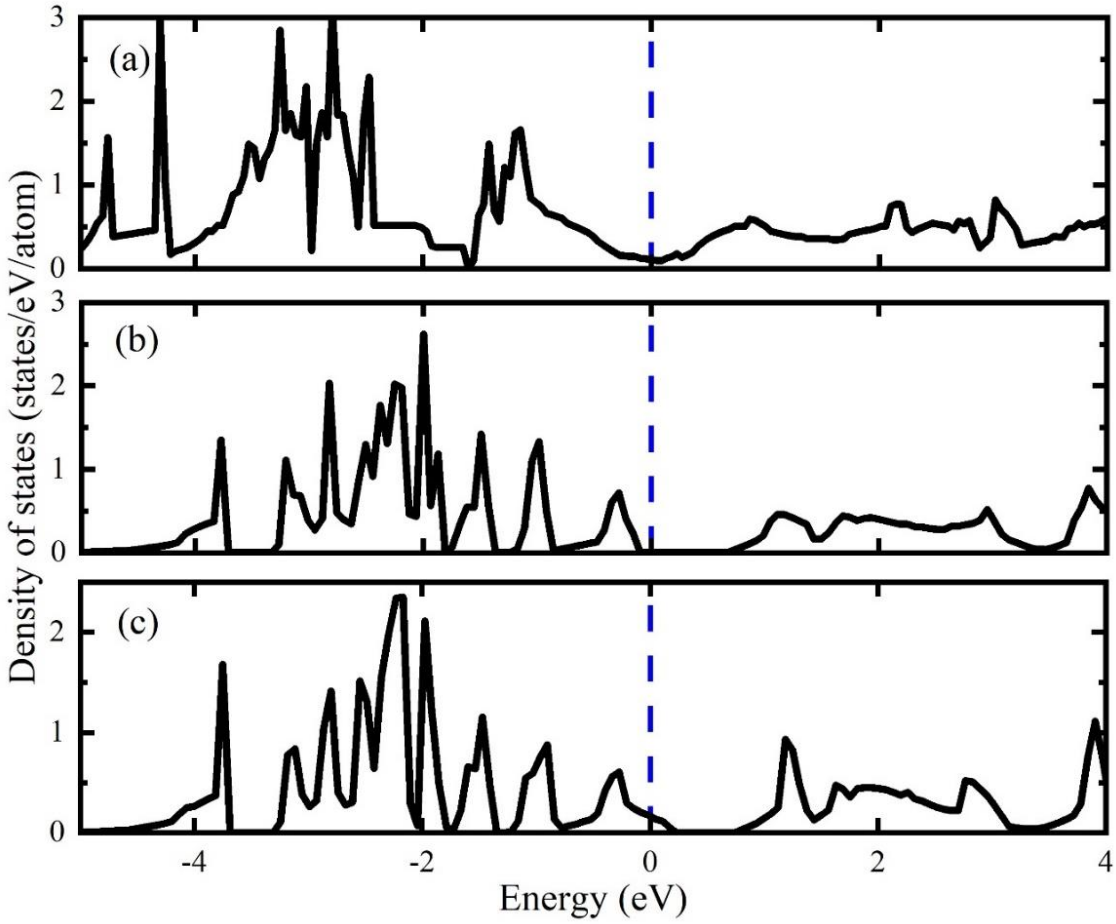

Figure 5.18. Calculated electronic density of states for (a) the model *Cmcm*-K_2Ni with the layers shifted such that they are parallel (exactly on top of each other) (b) the *P*2_1/*m*-K_2Ni structure (c) the *Cmcm*-K_2Ni (thermodynamic ground state structure). The blue dash line is the Fermi energy level.

5.2.3.3 Dynamic, Mechanical, and thermal stability of K_2Ni

The dynamic stability of the $P2_1/m$-K_2Ni structure (see Fig. 5.19) and the $Cmcm$-K_2Ni structure (see Fig. A5.6) at 37 GPa were established through the phonon calculations done at 0 K. The dispersion relation of both structures lacks negative frequencies showing that they are dynamically stable as well as temperature quench recoverable in an event of high temperature synthesis. The projected phonon DOS in Fig. 5.20 reveals that in the low frequency regime K and Ni have correlated vibrations. However, in the high frequency regime, vibrational modes are predominately due to K atoms.

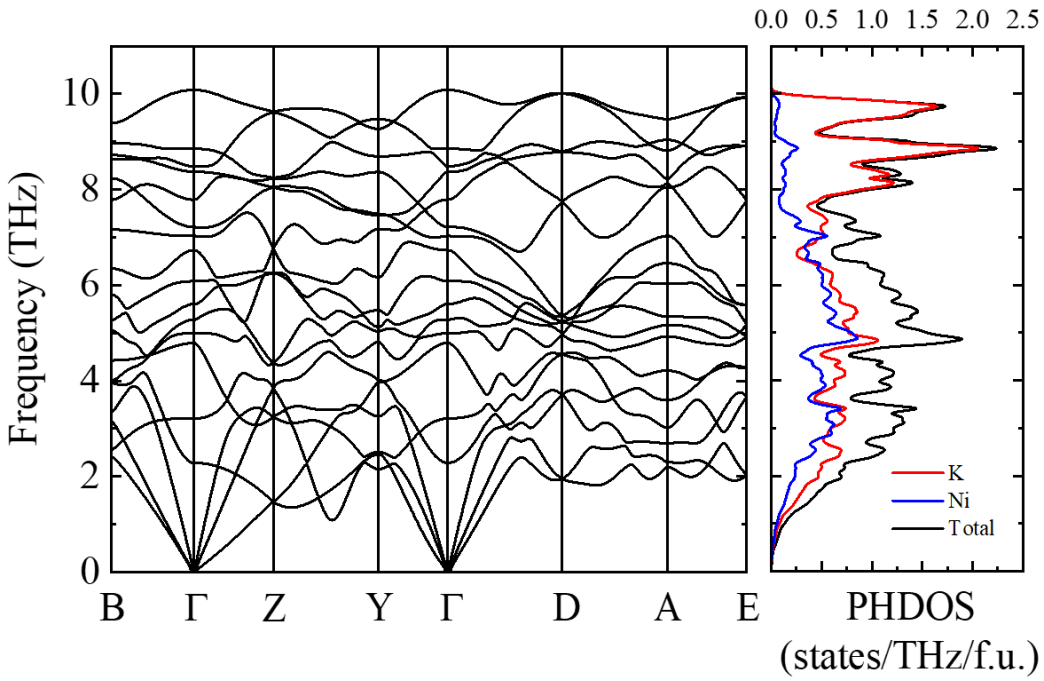

Figure 5.19. Phonon dispersion relations and projected phonon density of states for $P2_1/m$-K_2Ni calculated at 37 GPa.

Figure 5.20 shows a comparison between the harmonic and finite temperature lattice vibrations (vDOS) in the $P2_1/m$-K_2Ni structure. The vDOS are calculated at 300 K, 1000 K, 2000 K and 2500 K. The profile of the vDOS (relative to the harmonic) was maintained up to 2000 K. The vDOS shows that the $P2_1/m$-K_2Ni is stable at 300 K, 1000 K with tendency of melting when the temperature is raised above 2000 K. The observation of significant vibration mode softening

between 0 and 1THz (33.36 cm^{-1}) in the *v*DOS of the $P2_1/m$-K_2Ni at 2500 K, suggests that instability develops throughout this system at that temperature. Such development could cause a phase transition either into another solid phase or into a liquid.

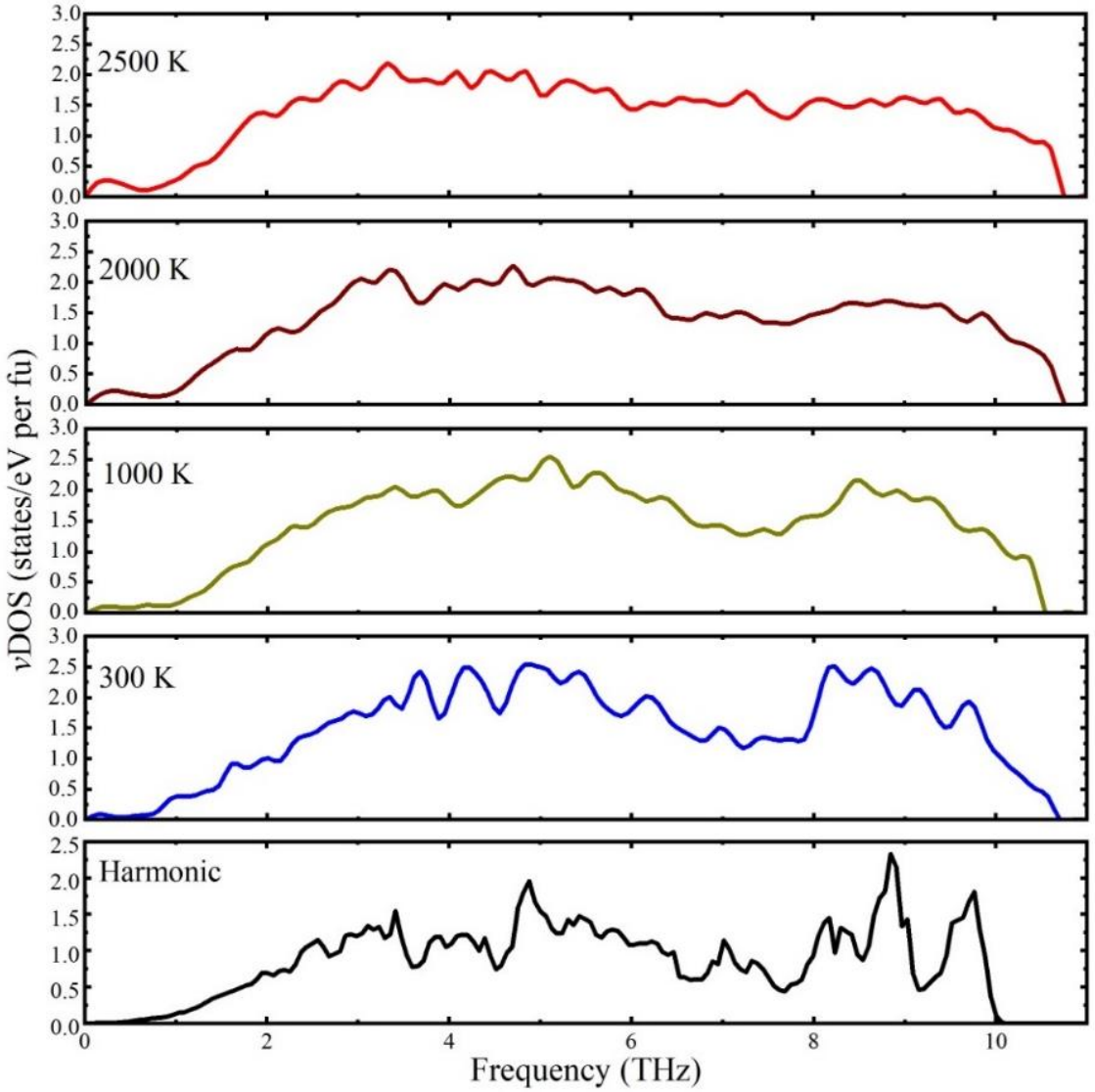

Figure 5.20. Total phonon DOS (harmonic) and temperature-dependent vibrational density of states (*v*DOS) for the $P2_1/m$-K_2Ni structure calculated from the autocorrelation function of the MD simulation in an *NpT* ensemble at P = 37 GPa and T = 300 K, 1000 K, 2000 K and 2500 K.

The response of a material to an external strain measures the extent of its mechanical stability and reliability of its lattice elastic constants [95]. Mechanical and elastic stability for non-cubic systems can be established through the Born-Huang elastic stability criteria [94,95]. The $P2_1/m$-K_2Ni structure (monoclinic crystal system) have 13 independent elastic constants shown in Table A5.2. The general elastic stability condition for any crystal system requires that the second-order elastic constants calculated using Eq. (1.75) satisfies the conditions highlighted in refs. [94, 95]. The $P2_1/m$ structure also satisfied all the mechanical stability criteria for monoclinic systems stated in ref. [95].

Using the Voigt-Reuss-Hill approximation [96], the $P2_1/m$-K_2Ni structure is calculated to have a bulk modulus of 98.6 GPa ± 1.17 GPa and shear modulus of 20.1 GPa ± 10.77 GPa. The bulk/shear ratio of 4.9 ± 0.11 indicates that the $P2_1/m$-K_2Ni is ductile in nature (details of the bounds are shown in Table 5.4).

Property	**Voigt**	**Reuss**	**Hill (Average)**	**V-R-H error**
Bulk modulus (GPa)	99.81	97.47	98.64	1.17
Shear modulus (GPa)	30.86	9.32	20.09	10.77
Young's modulus (GPa)	83.92	27.10	55.51	28.41
Pugh's ratio	3.23	10.46	4.91	0.11

Table 5.4: Calculated bounds for bulk modulus, shear modulus and other elastic properties of the $P2_1/m$-K_2Ni structure using Voigt-Reuss-Hill's approximation.

5.2.4 Conclusion

We report a stable, semi conducting K-Ni compound with K_2Ni stoichiometry at 37 GPa and temperature up to 2500 K. The K_2Ni structure (with $P2_1/m$ space group) could explain the XRD of the previously synthesized K-Ni compound. We establish that the $P2_1/m$-K_2Ni structure

adopts a ferromagnetic ground state in which spins aligns parallel to each other on Ni atoms. Although both K and Ni are metals, the $P2_1/m$-K_2Ni structure is semi conducting with an indirect bandgap of 0.65 eV. Peierls distortion was identified as the process responsible for the opening of small energy bandgap in the material. Dynamic stability of the $P2_1/m$-K_2Ni structure is established by phonon calculations for which there are no imaginary frequencies throughout the entire Brillouin zone. Vibrational free energy calculation shows that the synthesized $P2_1/m$-K_2Ni structure is stabilized over the thermodynamic ground state structure, $Cmcm$-K_2Ni, at high temperature (>1000 K) by kinetics. Mechanical stability of the K_2Ni-$P2_1/m$ structure is established through the Born-Huang stability criteria for monoclinic system and the result shows the $P2_1/m$-K_2Ni structure is mechanically and elastically stable. The present study establishes the phase that corresponds to the lab synthesized K-Ni compound and expands our understanding of the chemistry of alkali metal – transition metal compounds under pressure.

CHAPTER 6

CONCLUDING REMARKS

The general aim of this thesis is to theoretically investigate structural transitions, predict and characterize new materials at high pressure and temperature and use these results to understand experimental data, in cases where they are available. The theoretical calculations were performed using *ab initio* methods and crystal structure prediction algorithms such as genetic algorithm and particle swarm-intelligence optimization algorithm. The *ab initio* methods include density functional theory (DFT), molecular dynamics (MD) and metadynamics. These tools have been used to study structural phase transitions, thermodynamic, electronic, vibrational and transport properties of the selected materials.

In Chapter 1, the thesis subject was briefly introduced, setting the stage for the importance and the significance of the studies carried out. The theoretical methods were also discussed, establishing the fundamental theory behind the computational tools that were employed for all the calculations. An overview of the scope of the project(s) discussed in each chapter were also stated, highlighting the experimental and/or theoretical tools employed.

Chapter 2 reported the results of detailed study on two elemental solids: Carbon and nitrogen for technology and high energy density applications. It described the application of *ab initio* metadynamics method in the study of structural phase transition in the 2D-C_{60} allotrope of carbon at high temperature and pressure, which turns out to be the high-pressure ground state of 2D-C_{60} and 3D-C_{60}. The second part of the chapter described the theoretical identification and characterization of the black phosphorous (BP) structured nitrogen. The conclusion of the chapter is that *ab initio* metadynamics method is a powerful tool for scanning the potential energy surface and for searching locally (metastable) stable or globally (ground state) stable configurations. It was also concluded from this chapter that density functional theory can be applied in synergy with experiments to have deep understanding of new physics and chemistry of materials that emerge at extreme pressure and temperature regime.

Chapter 3 described the application of *ab initio* metadynamics method in the study of structural phase transition in shape memory alloy - NiTi at high temperature and pressure. The second part investigated the formation of Au-Fe intermetallic compounds under pressure using particle swarm-intelligence optimization algorithm coupled with *ab initio* density functional theory. The chapter, overall, studied phase transition in transition metal-transition metal alloy/compound using first principles techniques with technological and possibly, geophysical applications. Detailed characterization of various properties exhibited by the new phases were also reported. The conclusion of the chapter was that, above the critical temperature of 700 K, the $B19'$ NiTi structure undergo a permanent deformation during which it lost its shape memory capability and transform to the *P*-1-NiTi and *P*1-NiTi structures. Furthermore, it was found that at a threshold pressure of 123 GPa, Au could form stable compound with Fe stabilized through different charge transfer mechanisms. Further studies would be required to completely understand the predicted Au-Fe alloys under pressure. Molecular dynamics simulation of these systems could further elucidate intricate mechanism on the formation or dissociation of the system under high temperature and pressure that goes beyond simple charge transfer. Thermal properties of these alloys can also be studies which could inform their applications for technology or in understanding fundamental phenomena.

Chapter 4 reported the use of *ab initio* density functional theory to identify and characterize compound formed between noble gas element and Earth's core relevant transition metal – a very interesting topic with geophysical implications. A case study on Ar, a natural decay product of ^{40}K and Ni was carried out. Experimental data were generated using high pressure, in situ synchrotron X-ray diffraction techniques. The study presented evidence of the reactability of Ar with Ni. The compound of Ar and Ni was identified as *R*-3*m* ArNi with a $L1_1$ Laves structure, further strengthening the hypothesis that the Ar produced from natural decay of ^{40}K may have remain in the Earth's core. Also, that the Ar could have being stored in the core in the form of ArNi. Further studies would be required to completely understand Ar in the Earth's core especially at pressures that goes beyond the outer core. For instance, exploring the reactivity of Ar-Fe at higher pressures above 300 GPa, since the abundance of Fe (by mass) is about 80% in the Earth's core. The formation of ternary compound of Ar with Fe-Ni alloy is also interesting and all these could help to resolve outstanding scientific questions such as the "missing Ar" in a Fe-Ni denominated Earth's core.

Lastly, chapter 5 explored the possibility of compound formation between the nonradioactive isotope of light element, alkali metal, K and the two Earth's core dominant constituents, Fe and Ni. This is a very interesting geophysical topic, as the results from this chapter revealed that the missing K from the Earth's mantle may have percolated into the core and remain there in the form of Fe-rich K-Fe compound and those in the mantle may remain there in the form of K_2Ni or K-rich K-Fe, provided that equilibration conditions of the Earth are perfect. The potential energy surface of both the K-Fe and the K-Ni binary compounds were explored using the particle swarm-intelligence optimization and the genetic algorithm coupled with the *ab initio* density functional theory methods. Stable and metastable structures of interest were theoretically characterized using first principles methods. The Finite temperature dynamics were studied by employing *ab initio* molecular dynamics. The study on the K-Fe system showed transition from a K-rich to a Fe-rich stoichiometry as pressure grows above 120 GPa. Although, the exact application of this transition to the Earth's interior will rely heavily on knowing the Earth's actual composition. Also, the study on K-Ni systems identify the crystal structure for the long-sought structure of the only known K-Ni compound to date. The K_2Ni compound was predicted to exhibits a semiconducting ground state with an indirect bandgap even though both constituent elements are metallic. We should point out that further studies would be required to completely understand the presence and behavior of K in the Earth's core. For example, investigating a possible compound formation between K and Sulphur-rich iron sulphide or iron oxide at the outer core's pressure condition will be interesting. Above 300 GPa, investigation of the formation of iron-rich K-Fe compounds in a way that put constraint on the abundance of K could also be systematically investigated through accelerated crystal structure prediction (with machine learning capabilities). These studies could provide definitive premise upon which the K content in the core may be negligible or extremely significant. Furthermore, having a very accurate melting curve for K-Fe/Ni systems is also very interesting. This would, with high confidence, compare K-Fe/Ni phase diagram with the phase diagram of pure hexagonal close packed iron and that of the geotherm and reliable predictions about the composition of the Earth's interior can be made.

APPENDIX

Supplementary Material for Chapter 2

A2.1 Calculation of Raman spectrum

Simulated Raman spectra for the various structures were calculated using the method of Porezag and Pederson based on the double harmonic approximation [157] as implemented in VASP [93]. The double harmonic approximation ignores higher order derivative of energy, dipole moment and polarizability with respect to normal mode coordinates.

The stokes component of the *i*th eigenmode has a first order differential Raman cross section described by

$$\frac{d\sigma_i}{d\Omega} = \frac{(2\pi v_S)^4}{c^4}\left|\hat{e}_S \frac{\partial\tilde{\alpha}}{\partial Q_i}\hat{e}_L\right|^2 \frac{h\left(n_i^b+1\right)}{8\pi^2 v_i}, \qquad (A2.1)$$

where v_i is the frequency of the *i*th mode, Q_i is the coordinate of the *i*th normal mode, v_S is the frequency of the scattered light, $\hat{e}_L$ and $\hat{e}_S$ are the unit vectors of the electric-field polarization for the incident and the scattered light, respectively while $\tilde{\alpha}$ is the polarizability tensor. n_i^b is the Bose-Einstein statistical factor defined as

$$n_i^b = \frac{1}{\left[\exp\left(\frac{hv_i}{kT}\right)-1\right]}. \qquad (A2.2)$$

If we assume that the direction of the incident beam, direction of polarization of the beam and the direction of observation are orthogonal to each other, then Eq. (A2.1) becomes:

$$\frac{d\sigma_i}{d\Omega} = \frac{(2\pi v_S)^4}{c^4}\frac{h\left(n_i^b+1\right)}{8\pi^2 v_i}\frac{I^R}{45}, \qquad (A2.3)$$

Where the Raman scattering activity, I^R is defined as:

$$I^R = 45\left(\frac{d\alpha}{dQ}\right)^2 + 7\left(\frac{d\beta}{dQ}\right)^2 = 45\alpha'^2 + 7\beta'^2, \qquad (A2.4)$$

where α' and β'^2 are the derivative of the mean polarizability and the anisotropy of derivative of the polarizability tensor, respectively. The polarizability tensor has six independent variables. α' and β'^2 are defined as follows:

$$\alpha' = \frac{1}{3}\left(\tilde{\alpha}'_{xx} + \tilde{\alpha}'_{yy} + \tilde{\alpha}'_{zz}\right), \qquad (A2.5)$$

$$\beta'^2 = \frac{1}{2}\left[\left(\tilde{\alpha}'_{xx} - \tilde{\alpha}'_{yy}\right)^2 + (\tilde{\alpha}'_{xx} - \tilde{\alpha}'_{zz})^2 + \left(\tilde{\alpha}'_{yy} - \tilde{\alpha}'_{zz}\right)^2 + 6\left(\tilde{\alpha}'_{xy}{}^2 + \tilde{\alpha}'_{xz}{}^2 + \tilde{\alpha}'_{yz}{}^2\right)\right]. \qquad (A2.6)$$

Generally, in response to an external electric field, the derivative of polarizability with respect to atomic coordinates, R_k, can be calculated according to:

$$\frac{\partial \tilde{\alpha}_{ij}}{\partial R_k} = -\frac{\partial^3 E}{\partial G_i \partial G_j \partial R_k} = \frac{\partial^2 F_k}{\partial G_i \partial G_j}\ , F_k = -\frac{\partial E}{\partial R_k}\ . \qquad (A2.7)$$

In Eq. (A2.7), $i, j \in \{x, y, z\}$, F_k is the force acting on an atom, E is the total energy calculated from DFT. G_i and G_j are the *i*th and *j*th component of a uniform external electric field, respectively.

For more discussions on the formalism of double harmonic approximation, theoretical Raman and infrared spectroscopy, readers should see Refs. 157, 265 and 266.

Table A2.1: Elastic constants of the BP-N at 150 GPa.

The BP-N belong to the orthorhombic crystal class and as such requires 9 independent elastic constants (in the unit of GPa) summarized in the table below.

C_{ij}	C_{11}	C_{12}	C_{13}	C_{22}	C_{23}	C_{33}	C_{44}	C_{55}	C_{66}
	950.39	336.96	251.22	1772.86	350.65	768.62	646.36	242.98	435.68

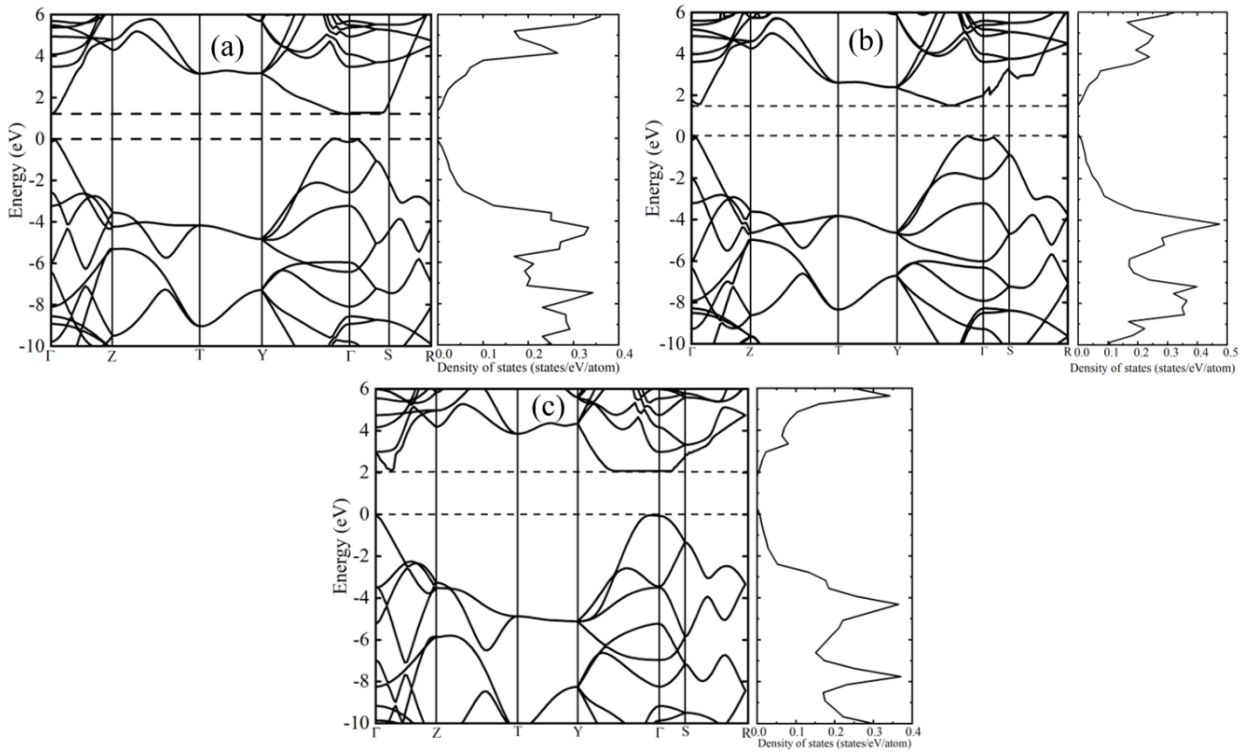

Figure A2.1. Calculated electronic band structure and electron density of states of BP-N at (a) 50 GPa (b) 100 GPa and (c) 200 GPa.

Supplementary Material for Chapter 3

A.3.1 Electronic free energy in NiTi at ambient and elevated temperatures

If we assume that the electronic DOS is temperature independent (fixed density-of-states approximation), and approximate the electronic free energy using the T=0 K electronic DOS, $D(\varepsilon) = D(\varepsilon)[\rho(\boldsymbol{r}, T = 0\ K)]$. The electronic free energy can be written as:

$$F_{el}(T) = E_{el}(T) - TS^{el}(T)\,, \qquad (A3.1)$$

where

$$E_{el}(T) = \int_{min.\ VB_{cutoff}}^{max.\ CB_{cutoff}} D(\varepsilon)\, f(\varepsilon_i, T)\varepsilon\, d\varepsilon - \int_{min.\ VB_{cutoff}}^{\varepsilon_F} D(\varepsilon)\, f(\varepsilon_i, T)\varepsilon\, d\varepsilon\,, \qquad (A3.2)$$

$$S^{el}(T) = \gamma k_B \int_{min.\ VB_{cutoff}}^{max.\ CB_{cutoff}} D(\varepsilon)\, S(\varepsilon, T) d\varepsilon\,. \qquad (A3.3)$$

$S(\varepsilon, T)$ is the temperature dependent entropic contribution to electronic free energy and is defined as:

$$S(\varepsilon, T) = -\big[f(\varepsilon_i, T)\ln f(\varepsilon_i, T) + \big(1 - f(\varepsilon_i, T)\big)\ln\big(1 - f(\varepsilon_i, T)\big)\big]\,, \qquad (A3.4)$$

and the Fermi-Dirac occupation, $f(\varepsilon_i, T)$ is defined as $f(\varepsilon_i, T) = \left[\exp\left(\frac{\varepsilon_i - \varepsilon_f}{k_B T}\right) + 1\right]^{-1}$. In our calculations, the vibrational entropy is 5.8 meV/atom which is less than 25.7 meV, the value of $k_B T$ at 298 K. For this reason, it suffices to ignore the entropic contribution ($S^{el}(T)$) to free energy so that electronic contribution to free energy is approximated by the vibrational internal energy of the electron, $E_{el}(T)$ only. If we assume energy equipartition for the system under study in the temperature regime below the melting point, then we expect the differences of the $E_{el}(T)$ between the *P*-1-NiTi and $B19'$ structure to be nearly constant, hence plays no significant role in stabilizing the structures at high temperatures and as such can be ignored.

Table A3.1: Predicted structural parameters for the *P*1-NiTi at a pressure of 10 GPa and 0 K temperature.

Space group	*a* (Å)	*b* (Å)	*c* (Å)	*α*	*β*	*γ*	*Fractional atomic Coordinates*			
							Atom	x	y	z	Site
*P*1	5.17	7.13	8.73	73.15	99.59	90.68	Ti	0.65	0.12	0.87	1a
							Ti	0.09	0.63	0.38	1a
							Ti	0.94	0.78	0.88	1a
							Ti	0.51	0.29	0.38	1a
							Ti	0.24	0.45	0.87	1a
							Ti	0.79	0.97	0.37	1a
							Ti	0.30	0.05	0.63	1a
							Ti	0.29	0.52	0.14	1a
							Ti	0.42	0.72	0.62	1a
							Ti	0.99	0.21	0.12	1a
							Ti	0.13	0.39	0.62	1a
							Ti	0.32	0.87	0.12	1a
							Ni	0.82	0.04	0.63	1a
							Ni	0.22	0.52	0.15	1a
							Ni	0.09	0.73	0.63	1a
							Ni	0.50	0.20	0.11	1a
							Ni	0.36	0.41	0.62	1a
							Ni	0.79	0.87	0.12	1a
							Ni	0.16	0.12	0.86	1a
							Ni	0.43	0.64	0.36	1a
							Ni	0.56	0.77	0.89	1a
							Ni	0.03	0.28	0.39	1a
							Ni	0.29	0.46	0.88	1a
							Ni	0.71	0.96	0.37	1a

A.3.2 Elastic properties of various Fe-Au system

Table A3.2: Elastic modulus of various Fe-Au systems.

Properties	System (pressure)		
	Cmcm-AuFe4 (140 GPa)	I4/m-AuFe4 (200 GPa)	Pmmn-AuFe3 (200 GPa)
Shear modulus (GPa)	251.54	393.06	323.97
Bulk modulus (GPa)	682.64	842.61	836.97
Young modulus (GPa)	671.98	1019.42	858.90
Bulk/Shear ratio	2.71	2.14	2.58

Table A3.3: Calculated sound velocity (v_s) and density at 200 GPa and 0 K for the *Pmmn*-$AuFe_3$ and the *I*4/*m*-$AuFe_4$ compared with simulation data of modeled inner core in [267] at 360 GPa.

	Pmmn-$AuFe_3$	*I*4/*m*-$AuFe_4$	*hcp*-Fe	$Fe_{62}C_2$	$Fe_{60}C_4$
v_s (Km/s)	4.28	4.82	6.80	6.38	6.00
Density (g/cm^3)	17.72	16.88	14.25	14.10	13.82

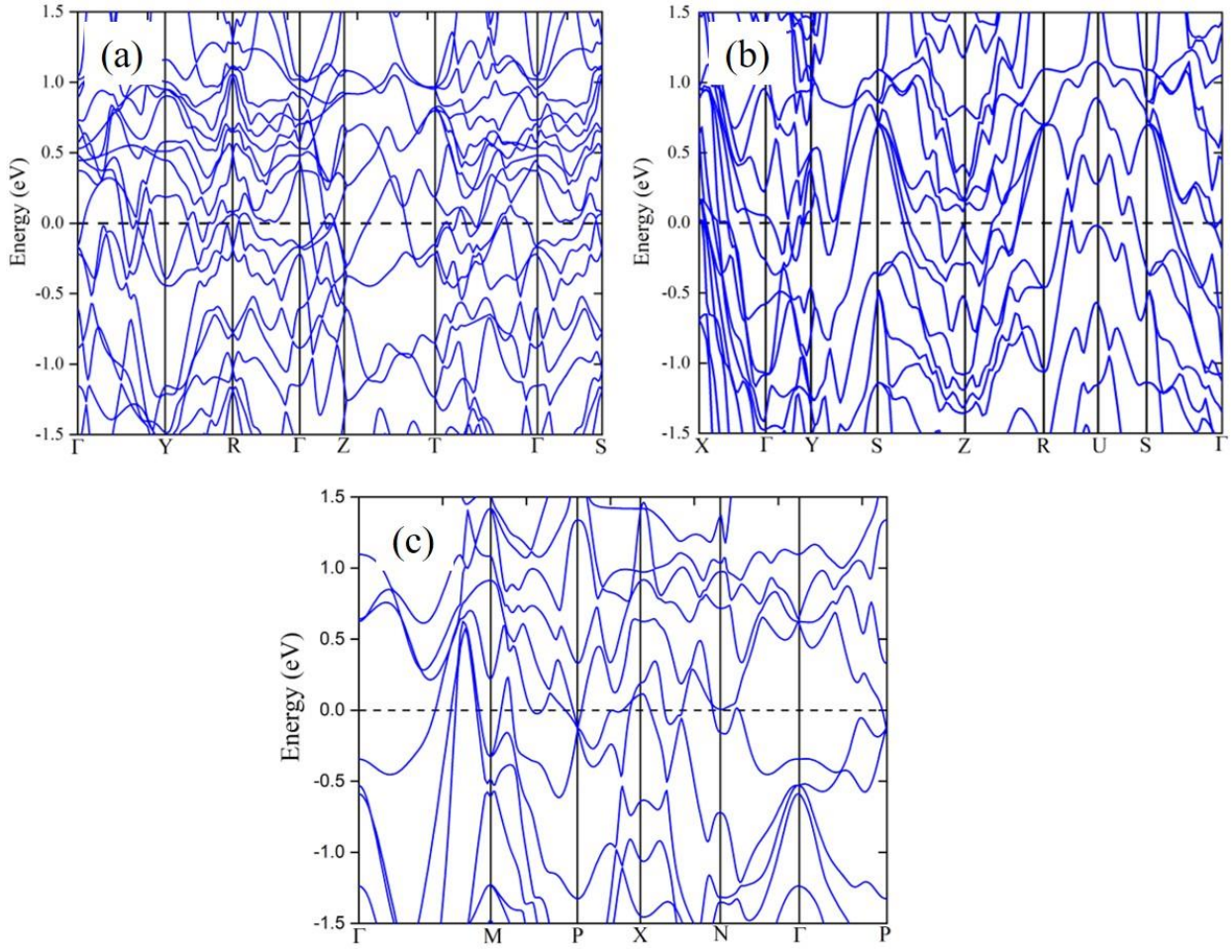

Figure A3.1. Calculated nonmagnetic electronic band structure for the (a) *Cmcm*-$AuFe_4$ at 140 GPa (b) *Pmmn*-$AuFe_3$ at 200 GPa (c) *I4/m*-$AuFe_4$ at 200 GPa. The black dashed line represents the Fermi energy level.

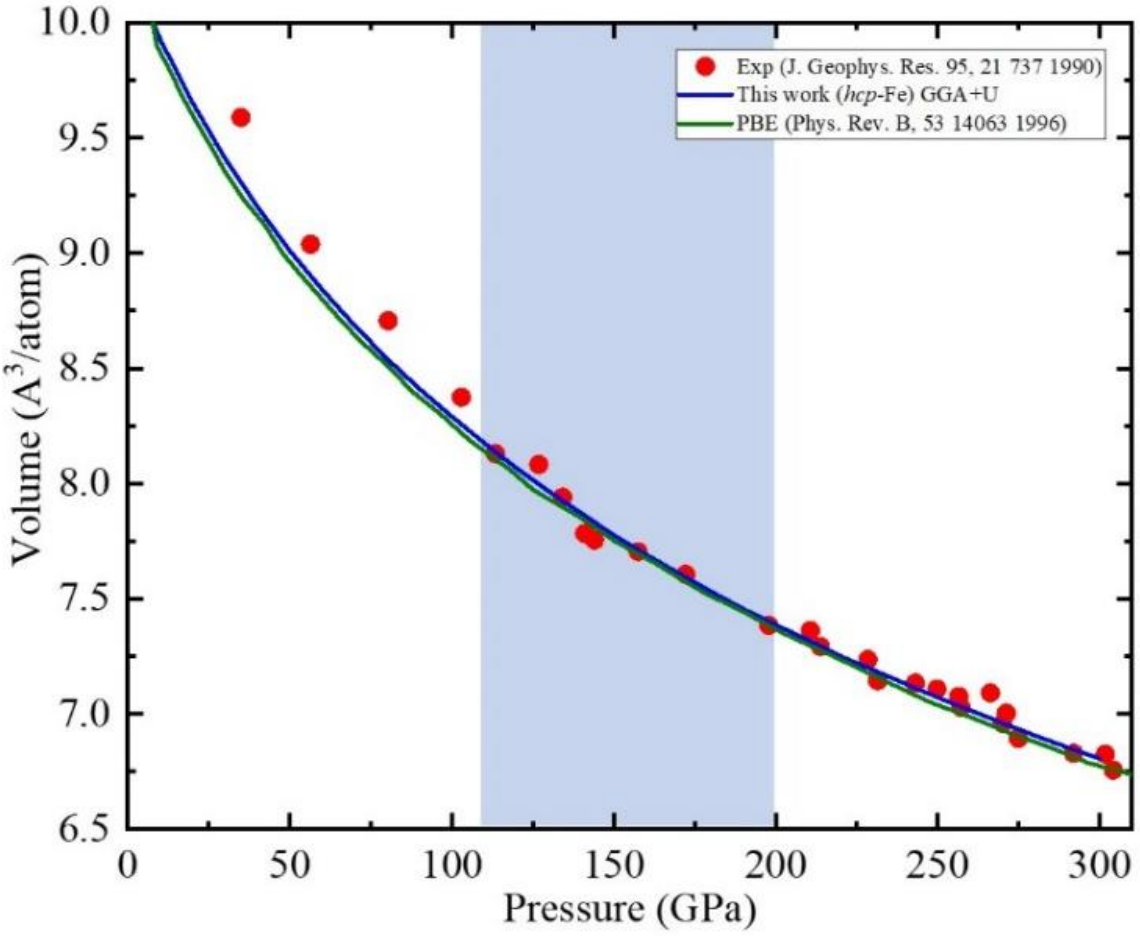

Figure A3.2. Calculated volume-pressure relation for hcp-Fe using GGA+U parameters of this study compared with calculated values using GGA XC functional in previous theoretical study and experimental room-temperature static compression data from previous experiment. The blue box shows pressure region of interest for this study.

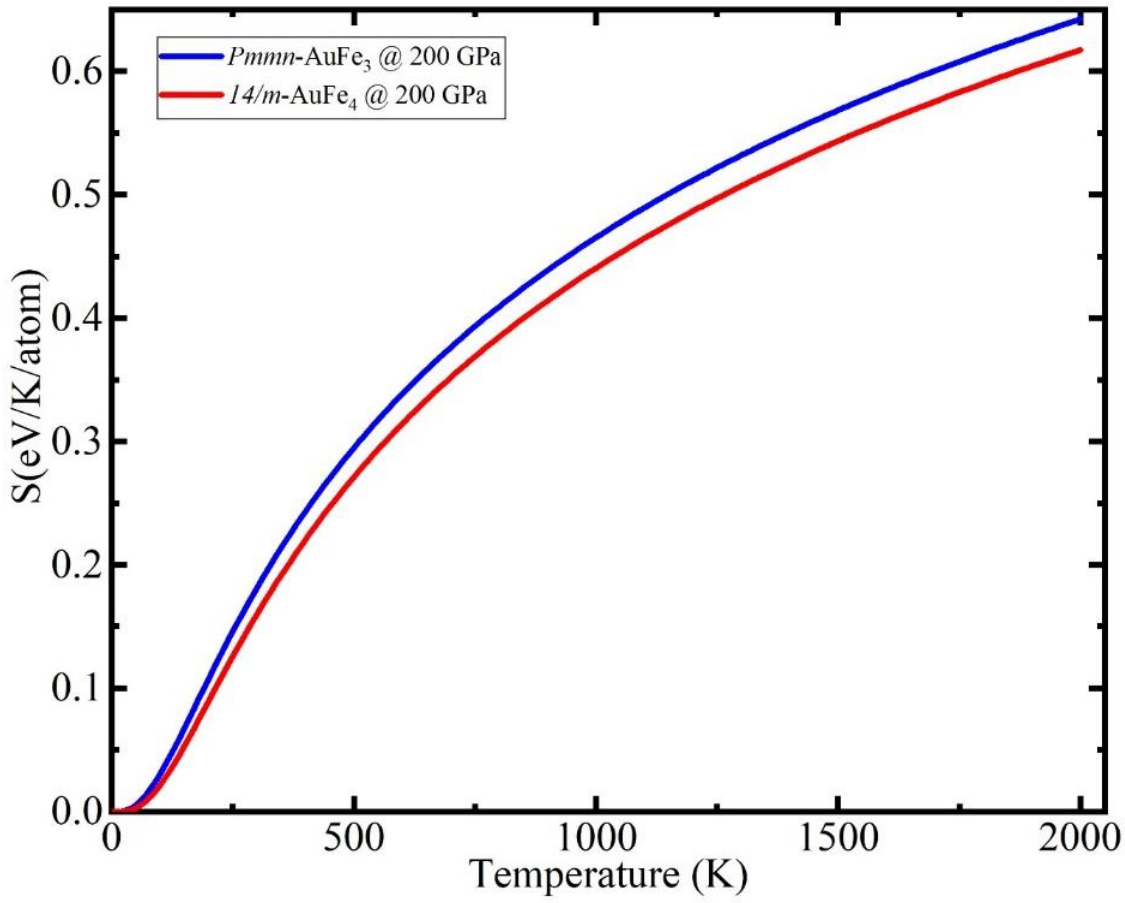

Figure A3.3. Calculated temperature dependence of the vibrational entropies of the *Pmmn*-$AuFe_3$ and *I*4/*m*-$AuFe_4$ phases at 200 GPa.

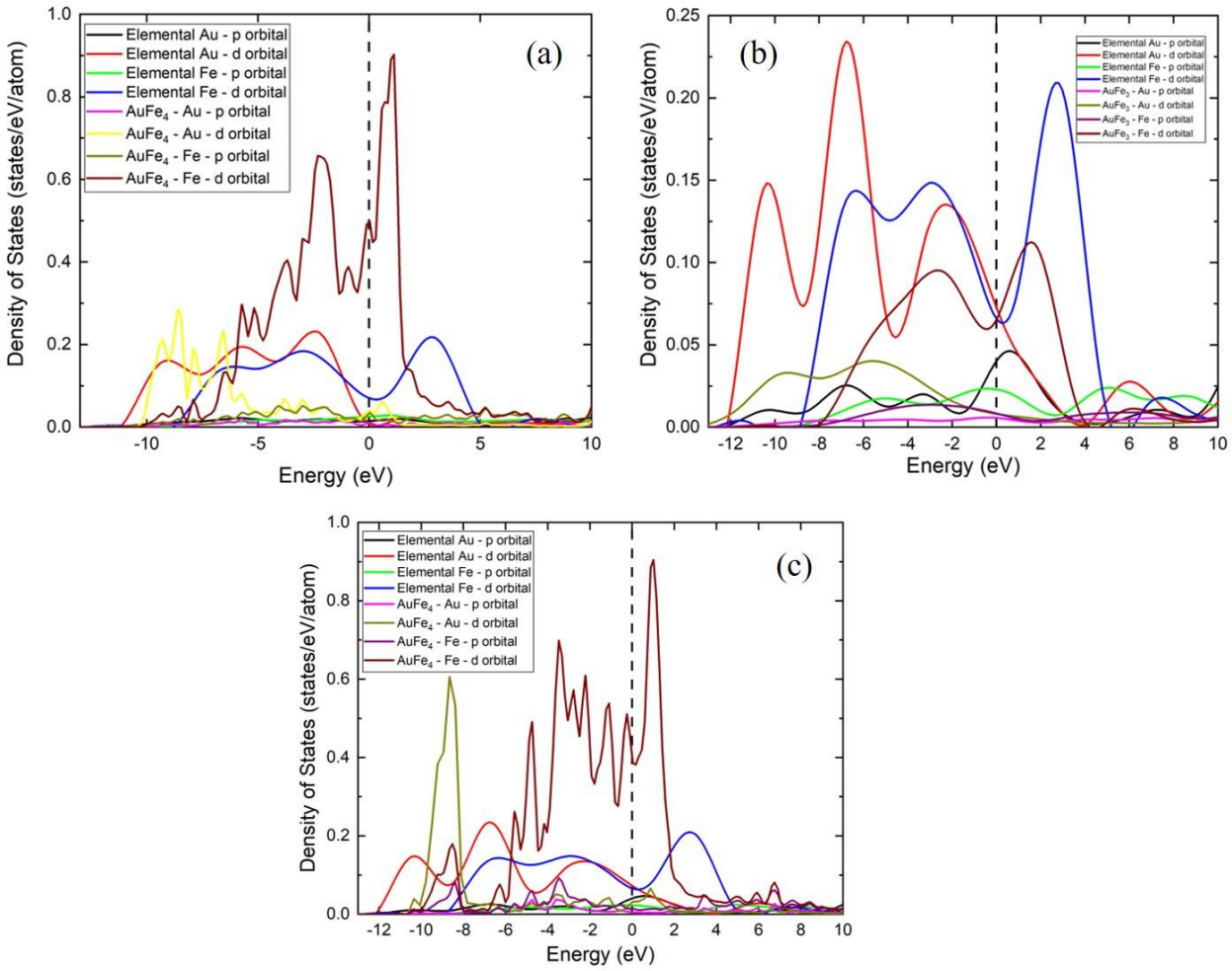

Figure A3.4. Calculated electronic density of states projected to orbitals of elemental Fe, Au and the (a) *Cmcm*-$AuFe_4$ at 140 GPa (b) *Pmmn*-$AuFe_3$ at 200 GPa (c) *I4/m*-$AuFe_4$ at 200 GPa. The black dashed line represents the Fermi energy level.

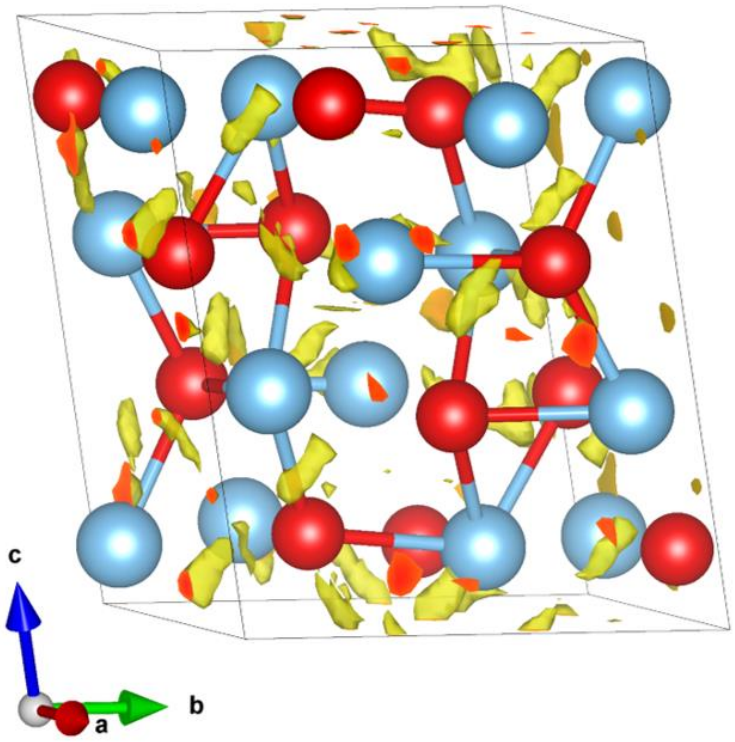

Figure A3.5. Calculated electron localization function (ELF) for the *P*-1-NiTi at 10 GPa. Nickel atoms are red and Titanium atoms are blue. An isovalue of 0.4 was used to reveal residual electron localization.

Supplementary Material for Chapter 4

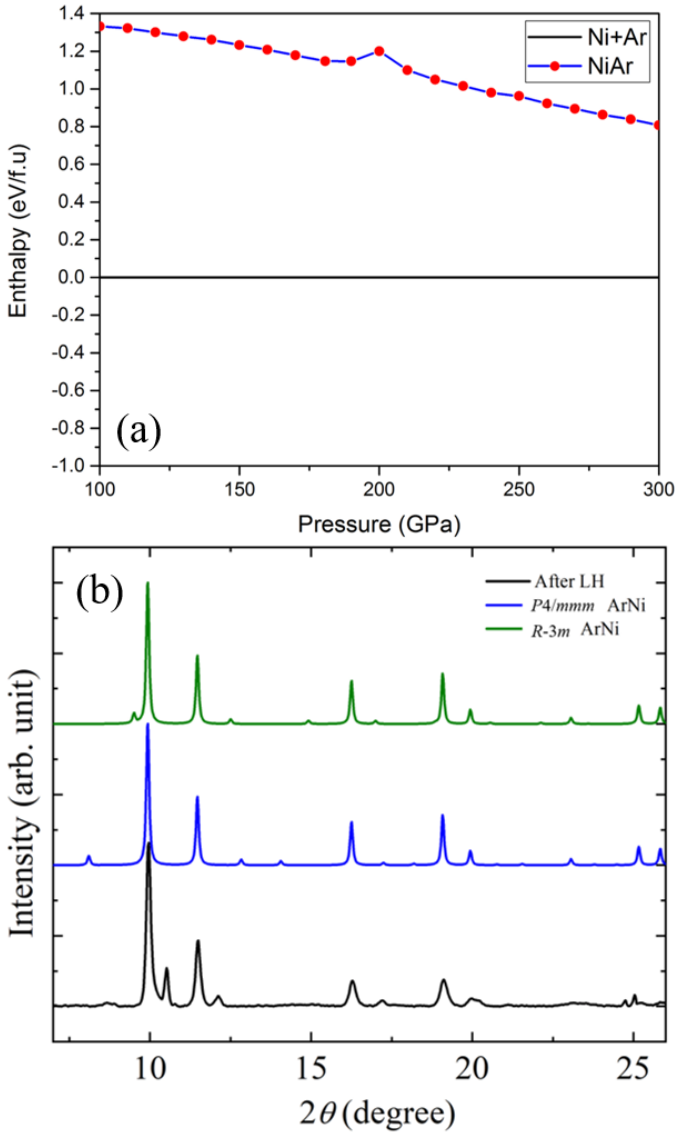

Figure A4.1. (a) Enthalpy of formation for ArNi compound using standard VASP library potential for Ar and Ni. The enthalpy of ArNi compound is continually higher than the enthalpy sum of elemental decomposition into Ar and Ni, indicating that the formation pressure for ArNi compound will be >>300 GPa. (b) Experimental XRD pattern of Ar-Ni compound from ref. [44] compared with the proposed *R*-3*m*-ArNi and *P*4/*mmm*-ArNi structures at 140 GPa. The XRD pattern was calculated using Mercury software [156].

Supplementary Material for Chapter 5

Table A5.1: Optimized structural information of predicted thermodynamically stable K-Fe compound that are not considered further due to dynamic instability.

P (GPa)	SG	*a* (Å)	*b* (Å)	*c* (Å)	α	β	γ	Atom	Fractional atomic coordinates			
									x	*y*	*z*	Site
30	*P2₁/m*	10.26	3.77	2.44		96.33		K1	0.923	0.250	0.212	2*e*
								Fe1	0.470	0.250	0.735	2*e*
								Fe3	0.730	0.750	0.844	2*e*
								Fe5	0.332	0.750	0.658	2*e*
60	*P4/nmm*	2.41	2.41	10.97				K1	0.000	0.500	0.601	2*c*
								Fe1	0.000	0.500	0.207	2*c*
								Fe3	0.000	0.500	0.926	2*c*
90	*P-1*	2.32	2.33	9.85	92.25	96.00	60.12	K1	0.000	0.500	0.500	1*g*
								Fe1	0.202	0.349	0.725	2*i*
								Fe3	0.378	0.327	0.092	2*i*
120	*P-1*	2.29	2.29	9.63	92.71	95.73	95.73	K1	0.500	0.500	0.500	1*h*
								Fe1	0.873	0.332	0.093	2*i*
								Fe3	0.714	0.334	0.722	2*i*
150	P-1	2.25	2.26	9.47	93.11	95.80	60.22	K1	0.500	0.500	0.000	1*e*
								Fe1	0.872	0.335	0.593	2*i*

								Fe3	0.718	0.323	0.221	2*i*
200	*P-1*	2.21	2.22	9.22	93.79	94.64	60.38	K1	0.000	0.000	0.000	1*a*
								Fe1	0.642	0.153	0.406	2*i*
								Fe3	0.254	0.791	0.218	2*i*

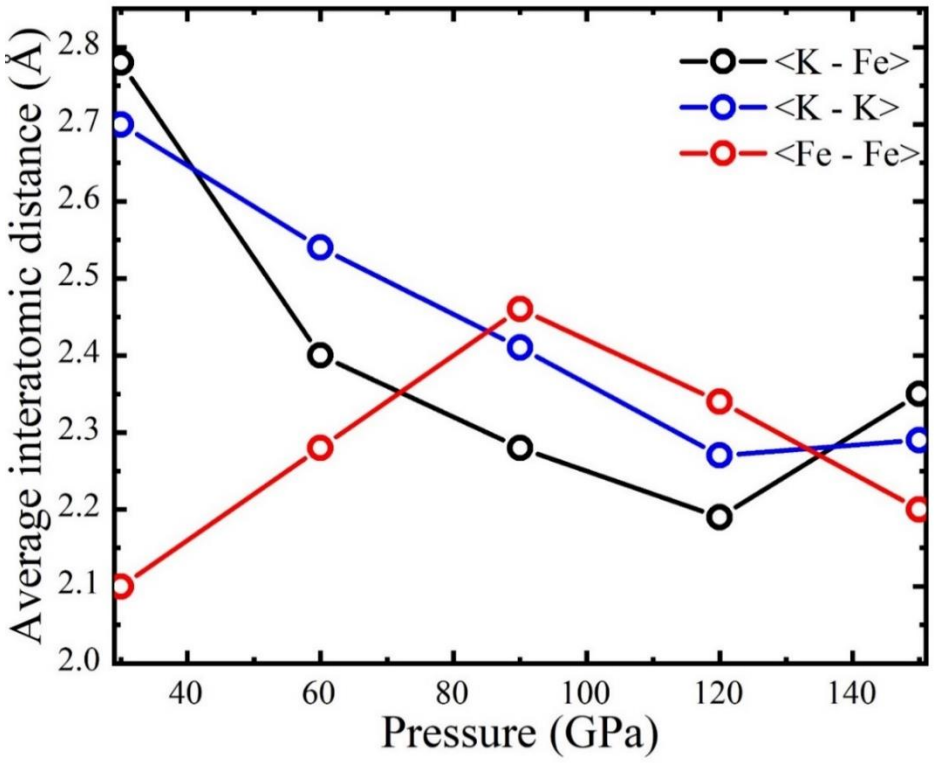

Figure A5.1. Interatomic distance (bondlength) evolution with pressure for various units in the K-Fe candidate crystal structures studied at 0 K.

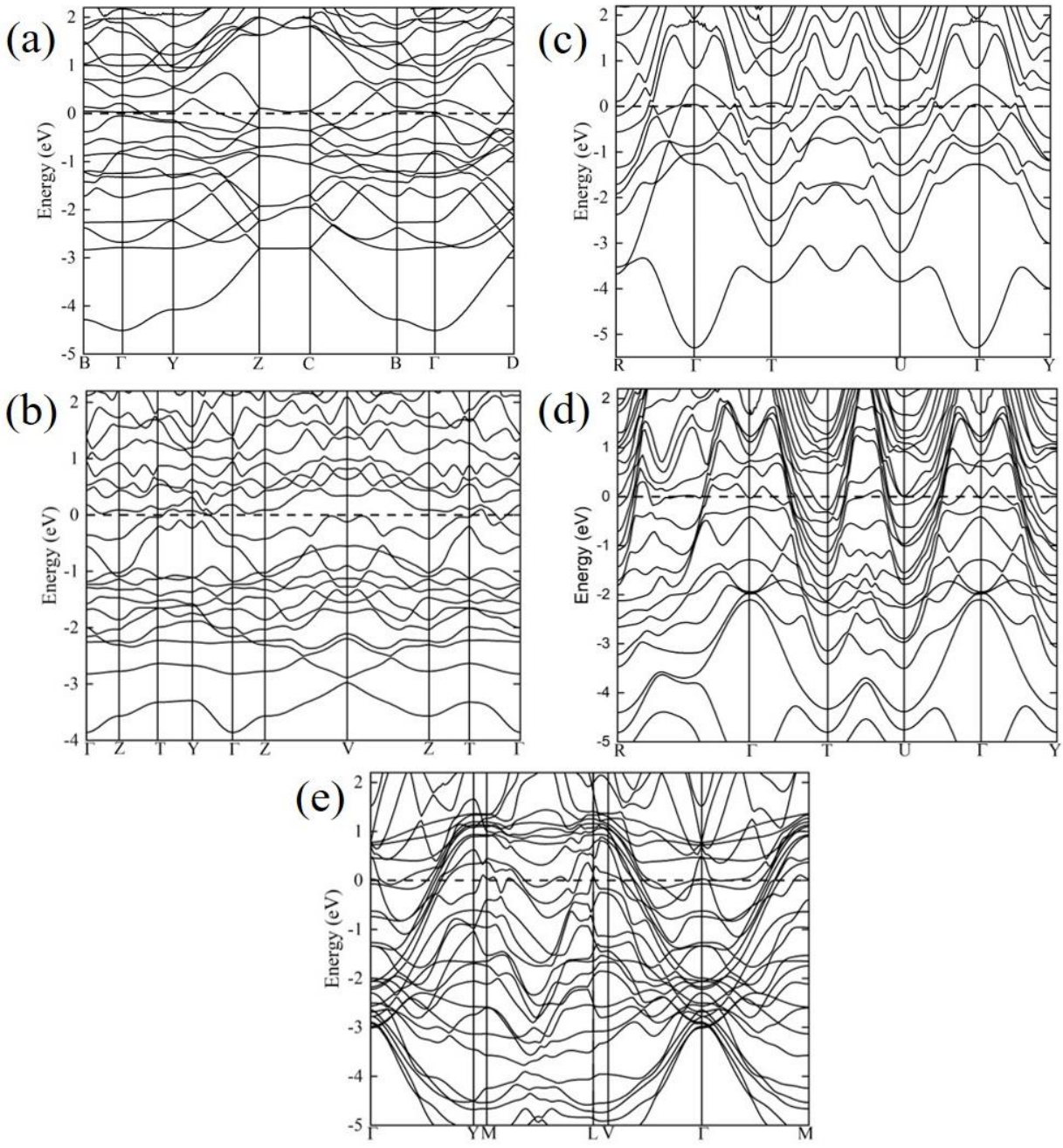

Figure A5.2. Calculated nonmagnetic electronic band structure for the (a) K_4Fe in $P2_1/m$ structure at 30 GPa (b) K_4Fe in P-1 structure at 60 GPa (c) K_4Fe (1 f.u.) in *P1* structure at 90 GPa (d) K_4Fe (2 f.u.) in *P1* structure at 120 GPa (e) KFe_3 in $C2/m$ structure at 150 GPa. The dash horizontal line is the Fermi energy level.

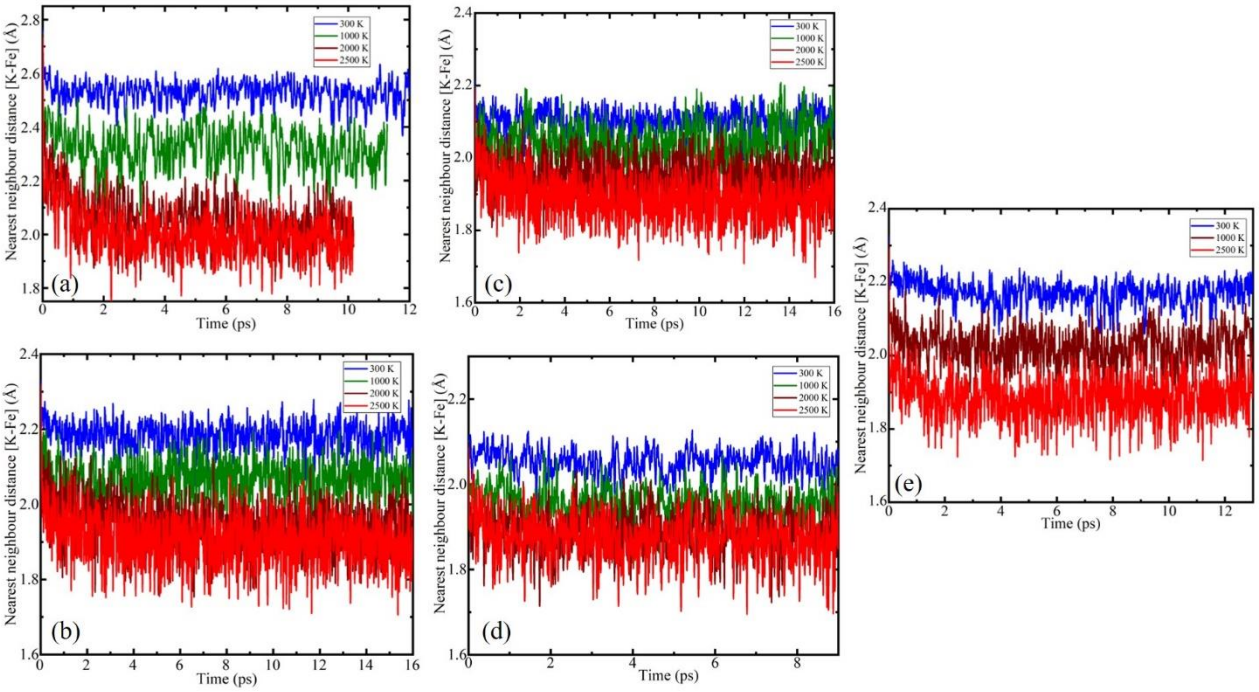

Figure A5.3. Temporal evolution of the nearest neighbor distance of the (a) K_4Fe in $P2_1/m$ structure at 30 GPa (b) K_4Fe in P-1 structure at 60 GPa (c) K_4Fe (1 f.u.) in *P1* structure at 90 GPa (d) K_4Fe (2 f.u.) in *P1* structure at 120 GPa (e) KFe_3 in $C2/m$ structure at 150 GPa. The plots are shown for temperatures 300 K, 1000 K, 2000 K and 2500 K.

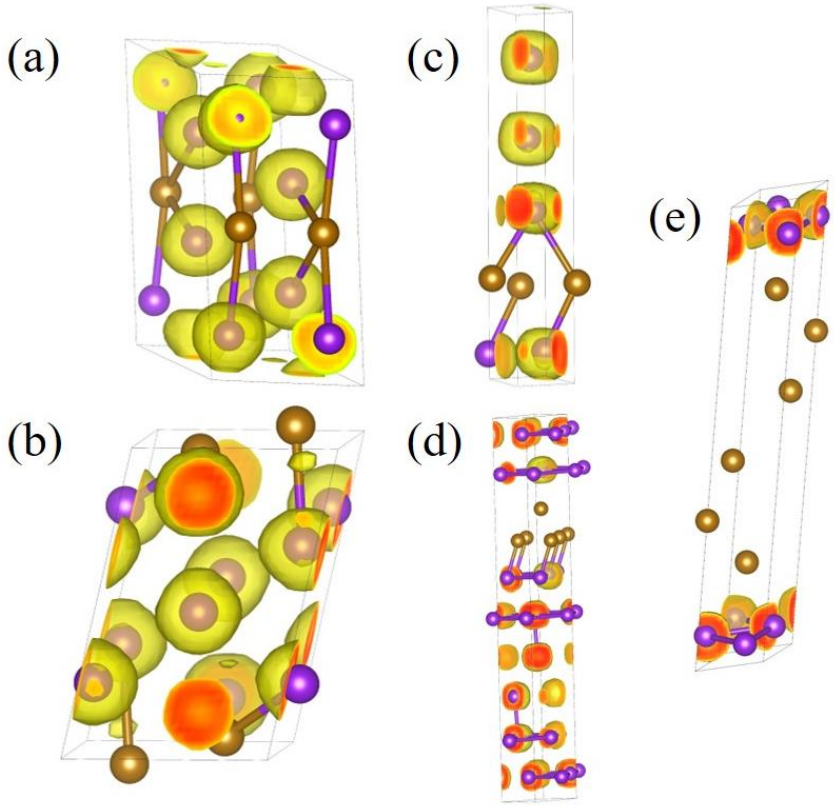

Figure A5.4. Calculated electron localization function of the (a) K_4Fe in $P2_1/m$ structure at 30 GPa (b) K_4Fe in P-1 structure at 60 GPa (c) K_4Fe (1 f.u.) in $P1$ structure at 90 GPa (d) K_4Fe (2 f.u.) in $P1$ structure at 120 GPa (e) KFe_3 in $C2/m$ structure at 150 GPa. An isovalue = 0.65 was used.

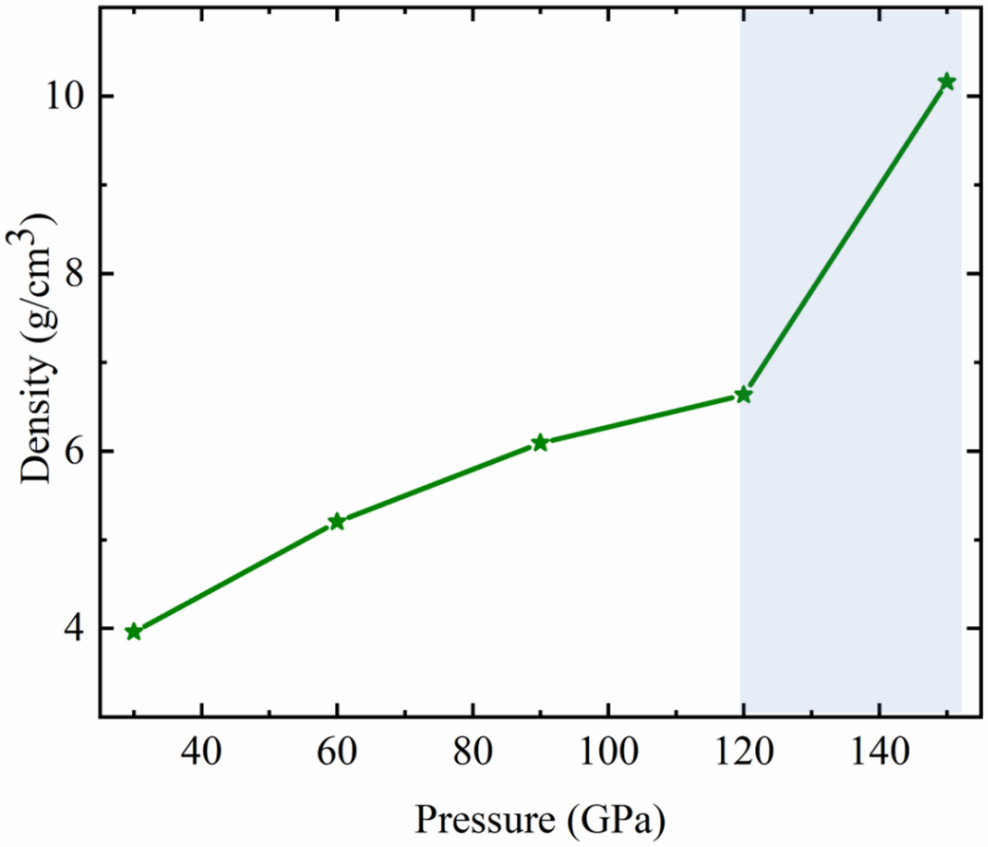

Figure A5.5. Evolution of density under pressure for K-Fe candidate structures. The region marked blue indicate the region where density jump was observed due to change in composition.

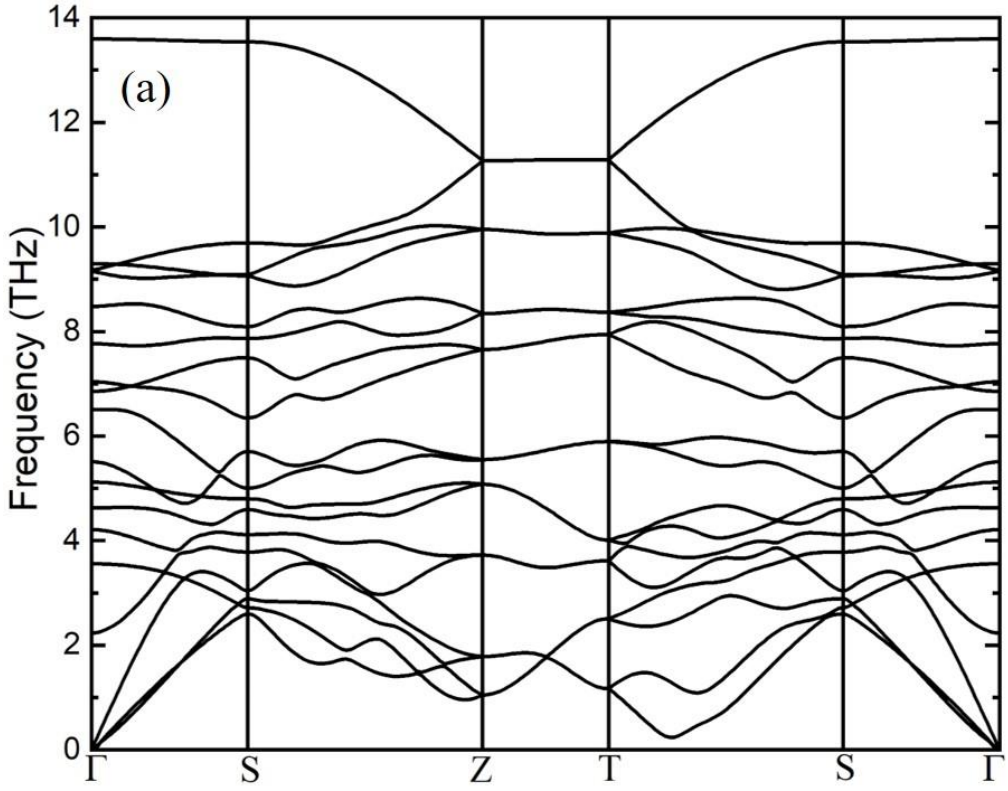

Figure A5.6. (a) Phonon dispersion relations for the *Cmcm*-K_2Ni (thermodynamic ground state) structure at 37 GPa.

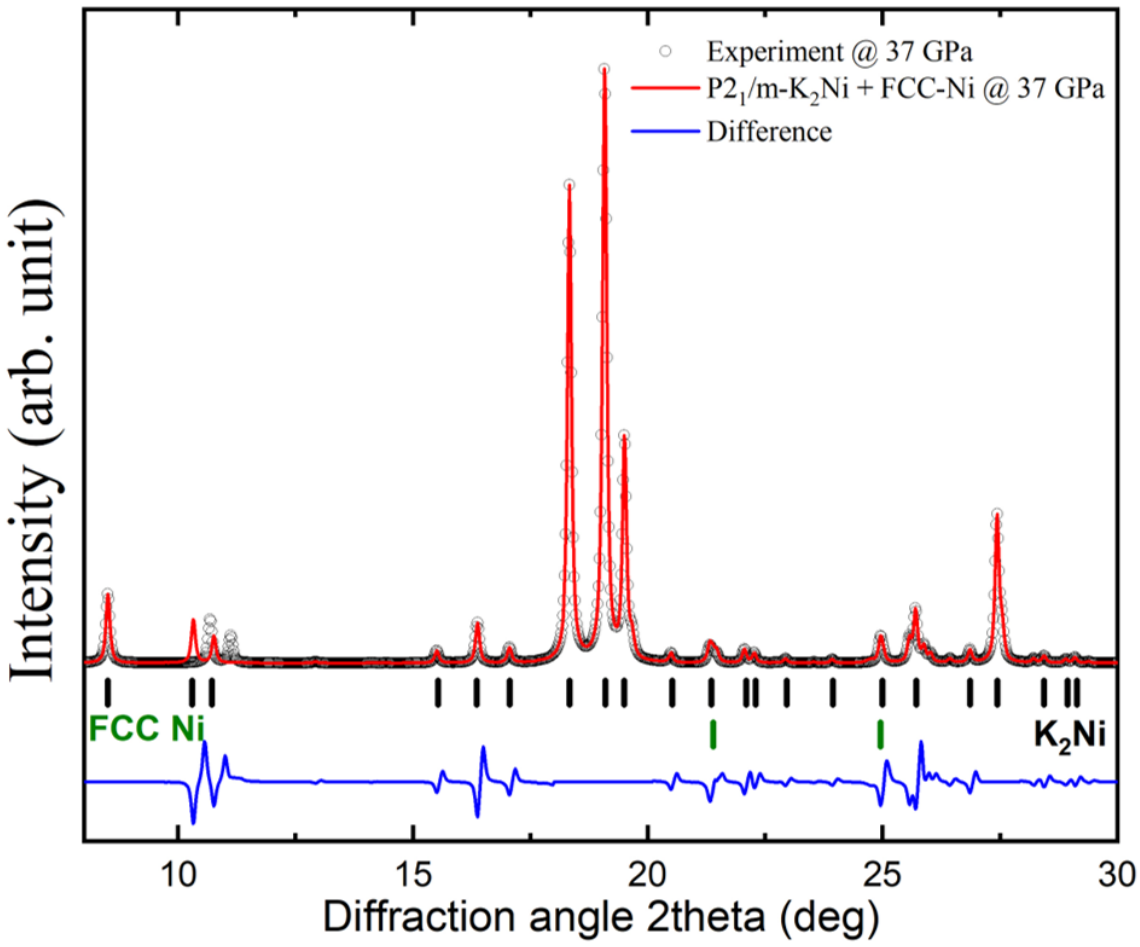

Figure A5.7. Refinement of the XRD pattern of K_2Ni compound at 37 GPa using Fullprof suite [268]. The Bragg peaks of the $P2_1/m$ K_2Ni and FCC Ni structures are marked with black and green vertical lines, respectively. Experimental data were extracted from ref. [236].

Table A5.2: Elastic constants of the $P2_1/m$ K_2Ni at 37 GPa.

C_{ij}	C_{11}	C_{22}	C_{33}	C_{12}	C_{13}	C_{23}	C_{44}	C_{55}	C_{66}
	106.18	161.18	128.30	101.03	87.96	62.33	18.79	36.90	50.48
C_{ij}	C_{15}	C_{25}	C_{35}	C_{46}					
	-9.53	27.72	-12.51	21.78					

The elements of C_{ij} are in the unit of GPa. The C_{ij} matrix is symmetric and has all-positive eigenvalues: $(301.21 \quad 5.32 \quad 30.85 \quad 95.18 \quad 7.70 \quad 61.57)$, indicating elastic stability.

A5.1 Understanding why the gap opened

Structurally, the creation of the band gap in the semiconducting $P2_1/m$-K_2Ni involves modifications in the geometric configuration of a parent *Cmcm*-K_2Ni polymorph. The opening of band gap thus involves a "two steps" distortion of the high symmetric *Cmcm*-K_2Ni. First, there is cell distortion followed by distortion in the staking of the honeycomb K layer and the Ni atoms sandwiched between two K layers (this induces Peierls distortion). One can argue that a combination of the cell distortion and the simultaneous shift in the layered honeycomb K and interspersing Ni atoms open a band gap in the $P2_1/m$-K_2Ni. Since each layers of the honeycomb K are metallic and Ni atoms are also metallic, one will expect staking them on top of each other (with no translation) to produce a metallic layered structure [269]. Significantly translating every other layer in one direction should therefore open a gap.

To verify this argument, we created a model system. The system is a high symmetric *Cmcm*-K_2Ni in which the first K-Ni layers is placed directly over the second K-Ni layers without displacement in both K and Ni layers, thereby forming linear-chained Ni. The electronic density of states of the model (Fig. 5.18(a)) was calculated and compared with the electronic density of states of the $P2_1/m$-K_2Ni (Fig. 5.18(b)) using HSE functional. The result of the calculation confirms the argument that the displacement of the honeycomb K layer and the formation of zig-zag Ni chains open a band gap in the $P2_1/m$-K_2Ni structure.

REFERENCES

[1] J. I. Goldstein, E. R. D. Scott, and N. L. Chabot, Chemie der Erde–Geochemistry **69** 293 (2009).

[2] L. Stixrude and B. Karki, Science **310** 297 (2005).

[3] A. Lopez-Noriega, D. Arcos, I. Izquierdo-Barba, Y. Sakamoto, O. Terasaki, and M. Vallet-Regi, Chem. Mater. **18** 3137 (2006).

[4] H. H. Kim, F. Miyaji, T. Kokubo, C. Ohtsuki, and T. Nakamura, J. Am. Ceram. Soc. **78** 2405 (1995).

[5] R. E. Schenker and W. G. Oldham, J. Appl. Phys. **82** 1065 (1997).

[6] F. P. Bundy, H. T. Hall, H. M. Strong, R. H. Wentorf, Nature **176** 51 (1955).

[7] R. H. Wentorf, J. Chem. Phys. **26** 956 (1957).

[8] Y. Yao and D. D. Klug, Phys. Rev. B **88** 014113 (2013).

[9] M. Born, and R. Oppenheimer, Annalen der Physik **389** 457 (1927).

[10] N. Dubrovinskaia et al., Sci. Adv. **2** e1600341 (2016).

[11] T. Ogitsu, E. Schwegler, and G. Galli, Chem. Rev. **113** 3425 (2013).

[12] S. Kirkpatrick, C. D. Gelatt, and M. P. Vecchi, Science **220** 671 (1983).

[13] S. Goedecker, J. Chem. Phys. **120** 9911 (2004).

[14] R. Car and M. Parrinello, Phys. Rev. Lett. **55** 2471 (1985).

[15] J. S. Tse, Annu. Rev. Phys. Chem. **53** 249 (2002).

[16] A. Laio and M. Parrinello, Proc. Natl Acad. Sci. U S A **99** 12562 (2002).

[17] C. J. Pickard and R. J. Needs, J. Phys. Condens. Matter **23** 053201 (2011).

[18] G. Trimarchi and A. Zunger, Phys. Rev. B **75** 104113 (2007).

[19] D. C. Lonie and E. Zurek, Comput. Phys. Commun. **182** 372 (2011).

[20] A. R. Oganov and C. W. Glass, J. Chem. Phys. **124** 244704 (2006).

[21] Y. Wang and Y. Ma, Comput. Phys. Commun. **183** 2063 (2012).

[22] E. Stavrou, Y. Yao, A. F. Goncharov, S. S. Lobanov, J. M. Zaug, H. Liu, E. Greenberg, and V. Prakapenka, Phys. Rev. Lett. **120** 096001 (2018).

[23] K. H. J. Buschow, Phys. Stat. Sol. (a) **7** 199 (1971).

[24] L. J. Swartzendruber, V. P. Itkin, and C. B. Alcock, J. Phase Equilibria **12** 288 (1991).

[25] L. J Parker, T. Atou, and J. V. Badding, Science **273** 95 (1996).

[26] K. K. M. Lee, and R. Jeanloz, Geo. Res. Lett. **30** 2212 (2003).

[27] K. K. M. Lee, G. Steinle-Neumann, and R. Jeanloz, Geo. Res. Lett. **31** 11603 (2004).

[28] https://brainly.in/question/24223387 (retrieved on the 21st January, 2021).

[29] S. Tateno, K. Hirose, Y. Ohishi, and Y. Tatsumi, Y. Science **330** 359 (2010).

[30] C. J. Allegre, J. P. Poirier, E. Humler, A. W. Hofmann, Earth Planet. Sci. Lett., **134** 515 (1995).; L. Vocadlo Treatise on Geophysics: Mineral Physics **2** 91 (2007).

[31] G. L. Weerasinghe, C. J. Pickard, R. J. Needs, J. Phys.: Condens. Matter. **27** 455501 (2015).

[32] W. McDonough and S. Sun, Chem. Geol., **120** 223 (1995).

[33] C. A. Norris, and B. J. Wood, Nature, **549** 507 (2017).

[34] B. J. Wood, M. J. Walter, and J. Wade, Nature **441** 825 (2006).

[35] C. Frondel and U. B. Marvin, Nature **214** 587 (1967).

[36] H. W. Kroto, J. R. Heath, S. C. O'Brien, R. F. Curl and R. E. Smalley, Nature **318** 162 (1985).

[37] S. Iijima and T. Ichihashi, Nature **363** 603 (*1993*).

[38] D. S. Bethune, C. H. Klang, M. S. De Vries, G. Gorman, R. Savoy, J. Vazquez and R. Beyers, Nature **363** 605 (1993).

[39] A. F. Goncharov, E. Gregoryanz, H. K. Mao, Z. X. Liu, and R. J. Hemley, Phys. Rev. Lett. **85** 1262 (2000).

[40] M. I. Eremets, A. G. Gavriliuk, I. A. Trojan, D. A. Dzivenko, and R. Boehler, Nat. Mater. **3** 558 (2004).

[41] A. A. Adeleke, A. O. Adeniyi, H. Tang, H. Gou, and Y. Yao, J. Phys.: Condens. Matter. **32** 395401 (2020).

[42] C. Ji, A. A. Adeleke, L. Yang, B. Wan, H. Gou, Y. Yao, B. Li, Y. Meng, J. S. Smith, V. B. Prakapenka, et. al. Sci. Adv., **6** eaba9206 (2020).

[43] A. A. Adeleke, and Y. Yao, Phys. Chem. Chem. Phys., **21** 7508-7517 (2019).

[44] A. A. Adeleke, M. Kunz, E. Greenberg, V. B. Prakapenka, Y. Yao and E. Stavrou, ACS Earth Space Chem., **3** 2517-2524 (2019).

[45] A. A. Adeleke, and Y. Yao, J. Phys. Chem. A **124** 4752-4763 (2020).

[46] A. A. Adeleke, E. Stavrou, A. O. Adeniyi, B. Wan, H. Gou, and Y. Yao, Phys. Rev. B. **102** 134120 (2020).

[47] P. A. M Dirac, Proc. R. Soc. Lond. A **123** 714 (1929).

[48] W. Kohn and L.J. Sham, Phys. Rev. **140** A1133 (1965).

[49] B. Delley, "Modern density functional theory: a tool for chemistry, vol. 2 of theoretical and computational chemistry." Elsevier Science Publ., Amsterdam (1995).

[50] D. Sholl, and J. A. Steckel. Density functional theory: a practical introduction. John Wiley & Sons, (2011).

[51] P. Hohenberg and W. Kohn, Phys. Rev. **136** B864 (1964).

[52] L. H. Thomas, Proc. Camb. Philos. Soc. **23** 542 (1927).

[53] J. C. Slater, Physical Review **81** 385 (1951).

[54] M. Born, and R. Oppenheimer, Annalen der Physik **389** 457 (1927).

[55] A. A. Adeleke MSc. Thesis, University of Saskatchewan (2017).

[56] J. P. Perdew and A. Zunger, Phys. Rev. B **23**, 5048 (1981).

[57] D. M. Ceperley and B. J. Alder, Phys. Rev. Lett., **45**, 566 (1980).

[58] A. D. Becke, Phys. Rev. A **38** 3098 (1988).

[59] A. D. Becke, J. Chem. Phys. **88** 1053 (1988).

[60] K. Burke, J. P. Perdew, Y. Wang, Electronic Density Functional Theory. Springer US, **81** (1998).

[61] J. P. Perdew, K. Burke, M. Ernzerhof, Phys. Rev. Lett. **77** 3865 (1996).

[62] J. P. Perdew, Phys. Rev. Lett. **55** 1665 (1985).

[63] J. P. Perdew, J. A. Chevary, S. H. Vosko, K. A. Jackson, M. Pederson, D. J. Singh, C. Fiolhais, Phys. Rev. B **46** 6671 (1992).

[64] J. S. Tse, Y. Yao, D. D. Klug, S. Desgreniers, J. Phys. Conf. Series **121** 012006 (2008).

[65] W. J. Evans, M. J. Lipp, C. S. Yoo, H. Cynn, J. L. Herberg, R. S. Maxwell, and M. F. Nicol, Chem. Mater. **18** 2520 (2006).

[66] A. D. Becke, J. Chem. Phys. **98** 1372 (1993).

[67] K. Kim, and K. D. Jordan, J. Phys. Chem. **98** 10089 (1994).

[68] P. J. Stephens, F. J. Devlin, C. F. Chabalowski, and M. J. Frisch, J. Phys. Chem. **98** 11623 (1994).

[69] C. Adamo, and B. Vincenzo, J Chem. Phys. **110** 6158 (1999).

[70] J. Heyd, G. E. Scuseria and M. Ernzerhof , J. Chem. Phys. **118** 8207 (2003).

[71] M. A. L. Marques, J. Vidal, M. J. T. Oliveira, L. Reining, and S. Botti Phys. Rev. B **83** 035119 (2011).

[72] V. I. Anisimov and O. Gunnarsson, Phys. Rev. B, **43** 7570 (1991).

[73] I. V. Solovyev and P. H. Dederichs, Phys. Rev. B, **49** 6736 (1994).

[74] T. L. Gilbert, Phys. Rev. B **12** 2111 (1975).

[75] R. Orlando, R. Dovesi, C. Roetti, and V. R. Saunders, J. Phys. Condens. Matter **2**, 7769 (1990).; J. C. Phillips, Phys. Rev. **112** 685 (1958).; M. L. Cohen and V. Heine, Solid State Physics **24** 37 (1970).

[76] J. M. Soler, E. Artacho, J. D. Gale, A. Garcia, J. Junquera, P. Ordejon, and D. Sanchez-Portal, J. Phys. Condens. Matter **14** 2745 (2002).; J. C. Phillips and L. Kleinman, Phys. Rev. **116** 287 (1959).; J. S. Lin, A. Qteish, M. C. Payne, and V. Heine. Phys. Rev. B **47** 4174 (1993).

[77] P.E. Blöchl, Phys. Rev. B **50** 17953 (1994).; G. Kresse and D. Joubert, Phys. Rev. B **59** 1758 (1999).

[78] This figure is taken from Yansun Yao's PhD Thesis (Department of Physics and Engineering Physics, University of Saskatchewan, 2008) or supplied directly by Prof. Yansun Yao.

[79] S. Baroni, S. de Gironcoli, A. D. Corso, P. Giannozzi, Rev. Mod. Phys. **73** 515 (2001).

[80] D. J. Singh, and L. Nordstrom, Planewaves, Pseudopotentials, and the LAPW method. Springer Science & Business Media. (2006).

[81] O. K. Andersen, Phys. Rev. B **12**, 3060 (1975).

[82] P. Blaha, K. Schwarz, G. Madsen, D. Kvasnicka, and J. Luitz,WIEN2k, an Augmented Plane Wave Plus Local Orbitals Program for Calculating Crystal Properties (Vienna University of Technology, Vienna, 2001).

[83] C. J. Pickard, and R. J. Needs, J. Phys.: Condens. Matter **23** 053201 (2011).

[84] S. Y. Chen, F. Zheng, S. Q. Wu, and Z. Z. Zhu, Current Appl. Phys. **17** 454 (2017).

[85] Y. Wang, J. Lv, L. Zhu, and Y. Ma, Phys. Rev. B **82** 094116 (2010).

[86] B. J. Alder and T. E. Wainwright, J. Chem. Phys. **27** 1208 (1957).

[87] B. J. Alder and T. E. Wainwright, J. Chem. Phys. **31** 459 (1959).

[88] M. P. Allen and D. J. Tildesley, Computer simulation of liquids, REP ed. (Clarendon Press, Wotton-under-Edge, 1989).

[89] K. Mizushima, S. Yip, and E. Kaxiras, Phys. Rev. B **50** 14952 (1994).

[90] A. Laio and M. Parrinello, Proc. Natl. Acad. Sci. **99** 12562 (2002).

[91] A. Barducci, M. Bonomi, and M. Parrinello, Wiley Interdiscip. Rev. Comp. Mol. Sci. **1** 826 (2011).

[92] R. Martoňák, A. Laio, and M. Parrinello, Phys. Rev. Lett. **90** 075503 (2003).; Y. Yao and D. D. Klug, Phys. Rev. B **85** 214122 (2012).

[93] G. Kresse and J. Hafner, Phys. Rev. B **47** 558 (1993).

[94] M. Born and K. Huang, Dynamical Theory of Crystal Lattices (Clarendon Press, Oxford, 1956).

[95] F. Mouhat, and F. X. Coudert, Phys. Rev. B **90** 224104 (2014).

[96] R. Hill, Proc. Phys. Soc. (London) **65** 349 (1952).

[97] D. M. Teter, MRS Bull **23** 22 (1998).

[98] X-Q. Chen, H. Niu, D. Li, and Y. Li, Intermetallics **19** 1275 (2011).

[99] https://phonopy.github.io/phonopy/

[100] Y. Wang, J. Lv, L. Zhu, and Y. Ma, Phys. Rev. B **82** 094116 (2010).

[101] Y. Wang, J. Lv, L. Zhu, and Y. Ma, Computer Phys. Commun. **183** 2063 (2012).

[102] A. Togo, F. Oba and I. Tanaka, Phys. Rev. B: Condens. Matter Mater. Phys. **78** 134106 (2008).

[103] P. S. DeCarli and J. C. Jamieson, Science **133** 1821 (1961).

[104] R. Z. Khaliullin, H. Eshet, T. D. Kühne, J. Behler, and M. Parrinello, Nat. Mater. **10** 693 (2011).

[105] H. Xie, F. Yin, T. Yu, et *al.*, Sci Rep **4** 5930 (2014).

[106] Y. Omata, *Y.* Yamagami, K. Tadano, T. Miyake and S. Saito, Physica E **29** 454 (2005).

[107] M. J. Allen, V. C. Tung and R. B. Kaner, Chem. Rev. **110** 132 (2010).

[108] S. Yamanaka, N. S. Kini, A. Kubo, S. Jida and H. Kuramoto, J. Am. Chem. Soc. **130** 4303 (2008).

[109] R. S. Kumar, M. G. Pravica, A. L. Cornelius, M. F. Nicol, M. Y. Hu and P. C. Chow, Diamond Relat. Mater. **16** 1250 (2007).

[110] J. Robertson, Mater. Sci. Eng. R Rep. **37** 129 (2002).

[111] M. Núñez-Regueiro, L. Marques, J-L. Hodeau, O. Béthoux and M. Perroux, Phys. Rev. Lett. **74** 278 (1995).

[112] M. Álvarez-Murga, P. Bleuet, G. Garbarino, A. Salamat, M. Mezouar and J L. Hodeau, Phys. Rev. Lett. **109** 025502 (2012).

[113] Y. Guo, L. Cui, D. Zhao, T. Song, X. Cui and Z. Liu, J. Phys.: Condens. Matter **32** 165701 (2020).

[114] X. Shi, C. He, C. J. Pickard, C. Tang and J. Zhong, Phys. Rev. B **97** 014104 (2018).

[115] C. He, X. Shi, S. J. Clark, J. Li, C. J. Pickard, T. Ouyang, C. Zhang, C. Tang and J. Zhong, Phys. Rev. Lett. **121** 175701 (2018).

[116] G. Kresse and D. Joubert, Phys. Rev. B **59** 1758 (1999).

[117] A. D. Becke and K. E. Edgecombe, J. Chem. Phys. **92** 5397 (1990).

[118] P. Giannozzi et al, J. Phys.: Condens. Matter **21** 395502 (2009).

[119] Y. Yao and D. D. Klug, Phys. Rev. B **85** 214122 (2012).

[120] B. Sundqvist, in Fullerenes, edited by K. M. Kadish and R. S. Rudorff (Wiley, New York, 2000), Chap. 15.

[121] T. Miyake and S. Saito, Chem. Phys. Lett. **380**, 589 (2003).

[122] S. Yamanaka, A. Kubo, K. Inumaru, K. Komaguchi, N. Kini, T. Inoue and T. Irifune, Phys. Rev. Lett. **96** 076602 (2006).

[123] D. Krishnamurti, Proc. Indian Acad. Sci. **40,** 211 (1954).

[124] F. Tian, X. Dong, Z. Zhao, J. He and H-T. Wang, J. Phys.: Condens. Matter **24** 165504 (2012).

[125] F. Delodovici, N. Manini, R. Wittman, D. Choi, M. Fahim and L. Burchfield, Carbon **126** 574 (2018).

[126] C. He, L. Sun, C. Zhang, X. Peng, K. Zhang and J. Zhong, Solid State Commun. **152** 1560 (2012).

[127] D. Fan, S. Lu, A. A. Golov, A. A. Kabanov and X. Hu, J. Chem. Phys. **149** 114702 (2018).

[128] Q. Wei, C. Zhao, M. Zhang, H. Yan, Y. Zhou and R. Yao, Phys. Lett. A, **382** 1685 (2018).

[129] N. García, P. Esquinazi, J. Barzola-Quiquia, and S. Dusari, New J. Phys. **14** 053015 (2012).

[130] D. M. Teter, MRS Bull. **23** 22-27 (1998).

[131] B. Xu and Y. Tian, J. Phys. Chem. C **119** 5633 (2015).

[132] Q. Wei, Q. Zhang, H. Yan and M. Zhang, J. Mater. Sci. **52** 2385 (2017).

[133] Z. N Ding, S. J. Zhou and Y. S. Zhao, Phys. Rev. B **70** 184117 (2004).

[134] D. He, Y. Zhao, L. Daemen, J. Qian, T. D. Shen and T. W. Zerda, Appl. Phys. Lett. **81** 643 (2002).

[135] M. Grimsditch, E. S. Zouboulis and A. Polian, J. Appl. Phys **76** 832 (1994).

[136] Q. Wei, C. Zhao, M. Zhang, H. Yan, Y. Zhou and R. Yao, Phys. Lett. A, **382** 1685 (2018).

[137] G. B. Ghorbal, A. Tricoteaux, A. Thuault, G. Louis, G., and D. Chicot, J. Euro Ceramic Soc. **37** 2531 (2017).

[138] X-Q. Chen, H. Niu, D. Li and Y. Li, Intermetallics **19** 1275 (2011).

[139] V. L, Solozhenko, O. O. Kurakevych, D. Andrault, Y. Le Godec and M. Mezouar, Phys. Rev. Lett. **102** 015506 (2009).

[140] A. G. Kvashnin, H. A. Zakaryan, C. Zhao, Y. Duan, Y. A. Kvashnina, C. Xie, H. Dong and A. Oganov, J. Phys. Chem. Lett. **9** 3470 (2018).

[141] H. Niu, S. Niu and A. R. Oganov, J. Appl. Phys. **125** 065105 (2019).

[142] W. J. Nellis, N. C. Holmes, A. C. Mitchell, and M.Vanthiel, Phys. Rev. Lett. **53** 1661 (1984).

[143] C. S. Yoo, AIP Conf. Proc. **1195** 11 (2009).

[144] M. I. Eremets, A. G. Gavriliuk, N. R. Serebryanaya, I. A. Trojan, D. A. Dzivenko, R. Boehler, H. K. Mao, and R. J. Hemley, J. Chem. Phys. **121** 11296 (2004).

[145] M. Frost, R. T. Howie, P. Dalladay-Simpson, A. F. Goncharov, and E. Gregoryanz, Phys. Rev. B **93** 024113 (2016).

[146] D. Tomasino, M. Kim, J. Smith, and C.-S. Yoo, Phys. Rev. Lett. **113** 205502 (2014).

[147] D. Laniel, G. Geneste, G. Weck, M. Mezouar, and P. Loubeyre, Phys. Rev. Lett. **122** 066001 (2019).

[148] A. A. Adeleke, M. J. Greschner, A. Majumdar, B. Wan, H. Liu, Z. Li, H. Gou, and Y. Yao, Phys. Rev. B **96** 224104 (2017).

[149] Y. Ma, A. R. Oganov, Z. Li, Y. Xie, and J. Kotakoski, Phys. Rev. Lett. **102** 065501 (2009).

[150] U. Müller, *Inorganic Structural Chemistry* (John Wiley & Sons, Ltd., Chichester, UK, 2006).

[151] X. Ling, H. Wang, S. Huang, F. Xia, and M. S. Dresselhaus, Proc. Nat. Acad. Sci., **112** 4523 (2015).

[152] D. Laniel, B, Winkler, T Fedotenko, A. Pakhomova, S. Chariton, V. Milman, V. Prakapenka, L. Dubrovinsky and N. Dubrovinskaia Phys. Rev. Lett. **124** 216001 (2020).

[153] A. Carvalho, M. Wang, X. Zhu, A. S. Rodin, H. Su, A. H. Castro Neto, Nat. Rev. Mater. **1** 16061 (2016).

[154] M. Pumera, Z. Sofer, Adv. Mater. **29** 1605299 (2017).

[155] A. Majumdar, X. Yang, W. Luo, S. Chowdhury, S. Chakraborty, R. Ahuja, Appl. Surf. Sci. **529** 146552, (2020).

[156] C. F. Macrae, I. Sovago, S. J. Cottrell, P.T. Galek, P. McCabe, E. Pidcock, and P. A. Wood, J. App. Cryst. **53** 226 (2020).

[157] D. Porezag, and M. R. Pederson, Phys. Rev. B **54** 7830 (1996).

[158] A. Fonari and S. Stanffer, *VASP Raman* https://github.com/raman-sc/VASP/ (2013).

[159] H. B. Ribeiro, M. A. Pimenta, and C. J. de Matos, J. Raman Spectro., **49** 76-90 (2018).

[160] A. Brown and S. Rundqvist, Acta Crystallogr. **19** 684 (1965).

[161] Y. Chen *et al.*, Adv. Mater. **30** 1800754 (2018).

[162] P. Pavone, S. Baroni, and S. de Gironcoli, Phys. Rev. B **57** 10421 (1998).

[163] F. I. Mopsik, J. Res. Natl. Bur. Stand. A **77** 407 (1973).

[164] A. Jain and A. J. H. McGaughey, J. Appl. Phys. **116** 073503 (2014).

[165] L. Kleinman, Phys. Rev. **128**, 2614 (1962).

[166] W. A. Harrison, *Electronic structure and the properties of solids: the physics of the chemical bond*. Courier Corporation (2012).

[167] B. Deng, V. Tran, Y. Xie, H. Jiang, C. Li, Q. Guo, X. Wang, H. Tian, S. J. Koester, H. Wang, J. J. Cha, Q. Xia, L. Yang, and F. Xia, Nat. Commun. **8** 4 (2017).

[168] H. Kalai, B. Khelifa, N. Badi, H. Abid, N. Amrane, B. Soudini, and H. Aourag, Mater. Chem. Phys. **39** 180 (1995).

[169] F. Xia, H. Wang, Y. Jia, Nat. Commun. **5** 4458 (2014).

[170] A. Pasturel, C. Colinet, D. N. Manh, A. T. Paxton, and M. Van Schilfgaarde, Phys. Rev. B **52** 15176 (1995).

[171] X. Huang, C. Bungaro, V. Godlevsky, and M. R, Karin, Phys. Rev. B **65** 014108 (2001).

[172] X. Huang, J. A. Graeme, and M. R. Karin, Nat. Mat. **25** 307 (2003).

[173] D. Stöckel, Min. Invas. Ther. and Allied Technol. **9** 81 (2000).

[174] T.G. Frank, W. Xu, and A. Cuschieri, Proceedings of the International Conference on Shape Memory and Superelastic Technologies, 549 (2000).

[175] T. Duerig and M. Wholey, Min. Invas. Ther. & Allied Technol. **11** 173 (2002).

[176] J. H. Carreau, C. L. Farnsworth, D. A. Glaser, J. D. Doan, T. Bastrom,N. Bryan,and P. O. Newton, J. Child. Ortho. **6** 241 (2012).

[177] T. W. Duerig and A. R. Pelton, Materials Properties Handbook: Titanium Alloys ASM International, New York, 1035 (1994).

[178] J. S. Tse, and D. D. Klug, Science **255** 1559 (1992).

[179] A. A. Golestaneh, and J. M. Carpenter, Acta metall. Mater. **38** 1291 (1990).

[180] J. A. Shaw, and S. Kyriakides, J. Mech. Phys. Solids, **43** 1243 (1995).

[181] O. Benafan, S. A. Padula, R. D. Noebe, T. A. Sisneros, and R. Vaidyanathan, J. App. Phys. **112** 093510 (2012).

[182] X. M. Zeng, Z. Du, N. Tamura, Q. Liu, C. A. Schuh, and C. L. Gan, Acta Materialia, **134** 257 (2017).

[183] G. Liu, H. Liu, X. Feng, and S. A. Redfern, Phys. Rev. B **97** 140104 (2018).

[184] F. M. Bickelhaupt, E. J. Baerends, Rev. in Comp. Chem. **15** 1 (2007).

[185] R. Martoňák et al., Nat. Mater. **5** 623 (2006).

[186] W. Tang, E. Sanville, and G. Henkelman J. Phys.: Condens. Matter **21**, 084204 (2009).

[187] B. Leimkuhler, E. Noorizadeh, F. A. Theil, J. Stat. Phys. **135** 261 (2009).

[188] A. A. Adeleke, and Y. Yao, J. Chem. Phys. **148** 104503 (2018).

[189] N. Hatcher, O. Y. Kontsevoi, and A. J. Freeman, Phys. Rev. B **80** 144203 (2009).

[190] T_c is the highest temperature in which it is still possible to stress- or heat-induce the formation of martensite and reproduce the martensite → austenite (parent) → martensite transformation cycle.

[191] X. Zhang, B. Grabowski, F. Körmann, C. Freysoldt, and J. Neugebauer, Phys. Rev. B **95** 165126 (2017).

[192] See supplemental materials for chapter 3 (A3.1) in the Appendix for details of mathematical and physical justification of Eq. (3.3).

[193] Y. Yao, R. Marto˘nák, S. Patchkovskii, and D. D. Klug, Phys. Rev. B **82** 094107 (2010).

[194] The B33 is the base centred orthorhombic (BCO) phase with space group Cmcm and feature twinning effect in which two orthogonal unit cells doubled along the b direction.

[195] X. Q. Wang, Phys. Rev. B, **78** 092103 (2008).

[196] X. Wang, A. A. Adeleke, W. Cao, Y. Luo, M. Zhang, Y. Yao, J. Phys. Chem. C **120** 25588 (2016).

[197] B. J. Wood, M. J. Walter, and J. Wade, Nature, **441** 825 (2006).

[198] A. M. Dziewonski, and D. L. Anderson, D. L. Phys. Earth and Planet. Interiors, **25** 297 (1981).

[199] H. Tkalčić, and T. S. Phạm, Science, **362** 329 (2018).

[200] A. Dewaele, P. Loubeyre, F. Occelli, M. Mezouar, P. I. Dorogokupets, M. Torrent, Phys. Rev. Lett. **97** 215504 (2006).; T. Sakamaki, E. Ohtani, H. Fukui, S. Kamada, S. Takahashi, T. Sakairi, et al., Sci. Adv. **2** e1500802 (2016).; G. Steinle-Neumann, L. Stixrude, R. E. Cohen, and O. Gülseren, Nature, **413**, 57 (2001).

[201] J. P. Poirier, Phys. Earth Planet. Inter. **85** 319 (1994).

[202] L. Dubrovinsky, N. Dubrovinskaia, W. A. Crichton, A. S. Mikhaylushkin, S. I Simak,I. A. Abrikosov, et al., Phys. Rev. Lett., **98** 045503 (2007).

[203] R. Ahuja, S. Rekhi, and B. Johansson, Phys. Rev. B **63** 212101 (2001).

[204] R. Briggs, F. Coppari, M. G. Gorman, R. F. Smith, S. J. Tracy, A. L. Coleman, et al., Phys. Rev. Lett. **123** 045701 (2019).

[205] L. P. Nielsen, F. Besenbacher, I. Stensgaard, E. Lægsgaard, C. Engdahl, P. Stoltze, et al., Phys. Rev. Lett. **71** 754 (1993).

[206] S. Mehendale, Y. Girard, V. Repain, C. Chacon, J. Lagoute, S. Rousset, et al., Phys. Rev. Lett., **105** 056101 (2010).

[207] W. Tang, E. Sanville, G. Henkelman, J. Phys.: Condens. Matter, **21** 084204 (2009).

[208] M. Cococcioni, and S. De Gironcoli, Phys. Rev. B **71** 035105 (2005).

[209] A. Majumdar, J. S. Tse, M. Wu, and Y. Yao, Phys. Rev. B **96** 201107 (2017).

[210] A. Stamatelatos, P. Poulopoulos, A. Goschew, P. Fumagalli, E. Sarigiannidou, L. Rapenne, et al., Sci. Rep. **9** 1 (2019).

[211] J. X. Zheng-Johansson, O. Eriksson, B. Johansson, L. Fast, and R. Ahuja, Phys. Rev. B **57** 10989 (1998).

[212] W. Biltz and F. Weibke, Z. Anorg. Allg. Chem. **236** 12 (1938).

[213] R. A. Sperling, P. R. Gil, F. Zhang, M. Zanella, W. J. Parak, Chem Soc Rev. **37** 1909 (2008).

[214] B. A. Buffett, Science **288** 2007 (2000).

[215] M. Humayun, and R. N. Clayton, Geochim. Cosmochim. Acta **59** 2131 (1995).

[216] C. J. Allègre, A. Hofmann, and K. O'Nions, Geophys. Res. Lett. **23** 3555 (1996).

[217] J. C. Lassiter, Geochem. Geophys. Geosyst. **5** Q11012 (2004).

[218] T. Lyubetskaya, and J. Korenaga, J. Geophys. Res. **112** B03212 (2007).

[219] M. -s. Miao, X. -l. Wang, B. Brgoch, F. Spera, M. G. Jackson, G. Kresse, and H. -q. Lin, J. Am. Chem. Soc. **137** 14122 (2015).

[220] X. Li, A. Hermann, F. Peng, J. Lv, Y. Wang, H. Wang, and Y. Ma, Sci. Rep. **5** 16675 (2015).

[221] L. Zhu, H. Liu, C. J. Pickard, G. Zou, and Y. Ma, Nat. Chem. **6** 644 (2014).

[222] X. Dong, A. R. Oganov, A. F. Goncharov, E. Stavrou, S. Lobanov, G. Saleh, G. -R-. Qian, Q. Zhu, C. Gatti, et al., Nat. Chem. **9** 440 (2017).

[223] H. Liu, Y. Yao, and D. D. Klug, Phys. Rev. B **91** 014102 (2015).

[224] Z. Liu, J. Botana, A. Hermann, S. Valdez, E. Zurek, D. Yan, H. -q. Lin, and M. -s. Miao, Nat. Commun. **9** 951 (2018).

[225] http://butane.chem.uiuc.edu/pshapley/GenChem1/L6/3.html (retrieved on 21st January, 2021).

[226] V. S. Bhadram, D. Y. Kim, and T. A. Strobel, Chem. Mater. **28** 1616 (2016).

[227] M. Bykov, E. Bykova, G. Aprilis, K. Glazyrin, E. Koemets, I. Chuvashova, et al., Nat. Commun. **9** 2756 (2018).

[228] K. Watanabe, E. Ohtani, S. Kamada, T. Sakamaki, M. Miyahara, Y. Ito, Phys. Earth Planet. Inter. **237** 65 (2014).; C. K. Gessmann and B. J. Wood, Earth Planet. Sci. Lett., **200** 63 (2002).

[229] D. Alfé, M. J. Gillan, G. D. Price, Earth Planet. Sci. Lett. **195** 91 (2002).

[230] B. J. Wood, Earth Planet. Sci. Lett. **117** 593 (1993).

[231] D. M. Sherman, Geophys. Res. Lett. **17** 693 (1990).

[232] E. Ito, K. Morooka, and O. Ujike, Geophys. Res. Lett. **20** 1651 (1993).

[233] K. K. M. Lee, and R. Jeanloz, Geophys. Res. Lett. **30** 2212 (2003).

[234] K. K. M. Lee, G. Steinle-Neumann, and R. Jeanloz, Geophy. Res. Lett. **31** L11603 (2004).

[235] M. Hasegawa, T. Atou, and J. V. Badding, J. Sol. State Chem. **130** 311 (1997).

[236] L. J. Parker, T. Atou, and J. V. Badding, Science, **273** 95 (1996).

[237] J. W. Morgan, and E. Anders, Proc. Nat. Acad. Sci. **77** 6973 (1980).

[238] M. S. T. Bukowinsky, Geophys. Res. Lett. **3** 491 (1976).

[239] S. L. Dudarev, G. A. Botton, S. Y. Savrasov, C. J. Humphreys, and A. P. Sutton, Phys. Rev. B **57** 1505 (1998).

[240] L. F. Lundegaard, M. Marqués, G. Stinton, G. J. Ackland, R. J. Nelmes, and M. I. McMahon, Phys. Rev. B **80** 020101 (2009).

[241] S. Cottenier, M. I. Probert, T. van Hoolst, V. van Speybroeck, and M. Waroquier, Earth Planet. Sci. Lett. **312** 237 (2011).

[242] A. Anelli, E. A. Engel, C. J. Pickard, and M. Ceriotti, Phys. Rev. Mat. **2** 103804 (2018).

[243] S. M. Walley, and J. E. Field, Elastic wave propagation in materials. Encyclopedia of Materials: Science and Technology', (ed. KHJ Buschow et al.) 2435 (2001).

[244] O. L. A. Anderson, J. Phys. Chem. Solids **24** 909 (1963).

[245] E. Schreiber, O. L. Anderson, and N. Soga, Elastic Constants and their Measurements; McGraw-Hill: New York (1973).

[246] I. Johnston, G. Keeler, R. Rollins, and S. Spicklemire, Solid State Physics Simulation; Wiley: New York (1996).

[247] A. A. Pawlicki, A. Vilan, M. Jurow, C. M. Drain, J. D. Batteas, Faraday discuss. **204** 349 (2017).

[248] X. Dong, A. R. Oganov, G. Qian, X-F. Zhou, Q. Zhu, and H.-T. Wang, arXiv:1503.00230.

[249] A. R. Miedema, P. F. de Chatel, and F. R. de Boer, Physica B **100** 1 (1980).

[250] D. G. Pettifor Solid State Phys. **40** 4392 (1987).

[251] Y. Liu, C. Wang, P. Lv, H. Sun, D. Duan, X. Wang, Solid State Commun. **287** 77 (2019).

[252] J. Zhao, B. Ao, S. Li, T. Gao, X. Ye, J. Phys. Chem. C **124** 7361 (2020).

[253] D. A. Young, Phase Diagram of the Elements (Univ. of California Press, Berkeley, 1991).

[254] T. Atou, M. Hasegawa, L. J. Parker, J. V. Badding, J. Am. Chem. Soc. **118** 12104 (1996).

[255] M. Hasegawa, T. Atou, J. V. Badding, J. Sol. State Chem. **130** 311(1997).

[256] Y. Liu, C. Wang, P. Lv, H. Sun, D. Duan, X. Wang, Sol. State Comm. **287** 77 (2019).

[257] Y. Yao, J. S. Tse, and K. Tanaka, Phys. Rev. B **77** 052103 (2008).

[258] Y. Yao, R. Martoňák, S. Patchkovskii, and D. D. Klug, Phys. Rev. B **82** 094107 (2010).

[259] G. W. Mann, K. Lee, M. Cococcioni, B. Smit, B., and J. B. Neaton, J. Chem. Phy. **144** 174104 (2016).

[260] M. Winzenick, V. Vijayakumar, W. B. Holzapfel, Phys. Rev. B **50** 12381 (1994).

[261] O. T. Lord, I. G. Wood, D. P. Dobson, L. Vočadlo, W. Wang, A. R. Thomson, and M. J. Walter, Earth and Planet. Sci. Lett. **408** 226 (2014).

[262] A. Anelli, E. A. Engel, C. J. Pickard, M. Ceriotti, Phys. Rev. Mat. **2** 103804 (2018).

[263] A. F. Wells, Structural Inorganic Chemistry. 3rd ed. Oxford University Press, London. 1962.

[264] A. A. Pawlicki, A. Vilan, M. Jurow, C. M. Drain, J.D. Batteas, Faraday discussions **204** 349 (2017).

[265] E. B. Wilson, J. C. Decius, and P. C. Cross, *Molecular Vibrations* (McGraw-Hill, New York, 1955).

[266] D. Steele, *Theory of Vibrational Spectroscopy* (Saunders, Philadelphia, 1971).

[267] Y. Li, L. Vočadlo, and J. P. Brodholt, Earth and Planet. Sci. Lett. **493** 118 (2018).

[268] J. Rodríguez-Carvajal, Physica B: Condensed Matter **192** 55 (1993).

[269] Y. Yao and D. D. Klug, Phys. Rev. B **81** 140104 (2010).

PERMISSIONS

The figure 1.4 in Chapter 1 have been adapted with permission from Chen S. Y., Zheng F., Wu S. Q., and Zhu Z. Z. An improved genetic algorithm for crystal structure prediction. Current Appl. Phys. *17,* **2017** 454. Copyright 2017 Elsevier B.V. (see below)

ELSEVIER LICENSE
TERMS AND CONDITIONS
Nov 25, 2020

This Agreement between Mr. Adebayo Adebayo ("You") and Elsevier ("Elsevier") consists of your license details and the terms and conditions provided by Elsevier and Copyright Clearance Center.

License Number	4956070115750
License date	Nov 25, 2020
Licensed Content Publisher	Elsevier
Licensed Content Publication	Current Applied Physics
Licensed Content Title	An improved genetic algorithm for crystal structure prediction
Licensed Content Author	S.Y. Chen,F. Zheng,S.Q. Wu,Z.Z. Zhu
Licensed Content Date	Apr 1, 2017
Licensed Content Volume	17
Licensed Content Issue	4
Licensed Content Pages	7
Start Page	454
End Page	460
Type of Use	reuse in a thesis/dissertation
Portion	figures/tables/illustrations
Number of figures/tables/illustrations	1
Format	electronic
Are you the author of this Elsevier article?	No
Will you be translating?	No

Title	STRUCTURES, STRUCTURAL TRANSFORMATIONS AND PROPERTIES OF SELECTED ELEMENTAL AND EXTENDED SOLIDS
Institution name	University of Saskatchewan
Expected presentation date	Mar 2021
Portions	Figure 1
Requestor Location	Mr. Adebayo Adebayo 1217, 15th St. E Saskatoon, SK S7N 0R6 Canada Attn: Mr. Adebayo Adebayo
Publisher Tax ID	GB 494 6272 12
Total	0.00 USD

Terms and Conditions

INTRODUCTION

1. The publisher for this copyrighted material is Elsevier. By clicking "accept" in connection with completing this licensing transaction, you agree that the following terms and conditions apply to this transaction (along with the Billing and Payment terms and conditions established by Copyright Clearance Center, Inc. ("CCC"), at the time that you opened your Rightslink account and that are available at any time at http://myaccount.copyright.com).

GENERAL TERMS

2. Elsevier hereby grants you permission to reproduce the aforementioned material subject to the terms and conditions indicated.

3. Acknowledgement: If any part of the material to be used (for example, figures) has appeared in our publication with credit or acknowledgement to another source, permission must also be sought from that source. If such permission is not obtained then that material may not be included in your publication/copies. Suitable acknowledgement to the source must be made, either as a footnote or in a reference list at the end of your publication, as follows:

"Reprinted from Publication title, Vol /edition number, Author(s), Title of article / title of chapter, Pages No., Copyright (Year), with permission from Elsevier [OR APPLICABLE SOCIETY COPYRIGHT OWNER]." Also Lancet special credit - "Reprinted from The Lancet, Vol. number, Author(s), Title of article, Pages No., Copyright (Year), with permission from Elsevier."

4. Reproduction of this material is confined to the purpose and/or media for which permission is hereby given.

5. Altering/Modifying Material: Not Permitted. However figures and illustrations may be altered/adapted minimally to serve your work. Any other abbreviations, additions, deletions and/or any other alterations shall be made only with prior written authorization of Elsevier Ltd. (Please contact Elsevier's permissions helpdesk here). No modifications can be made to any Lancet figures/tables and they must be reproduced in full.

6. If the permission fee for the requested use of our material is waived in this instance, please be advised that your future requests for Elsevier materials may attract a fee.

7. Reservation of Rights: Publisher reserves all rights not specifically granted in the combination of (i) the license details provided by you and accepted in the course of this licensing transaction, (ii) these terms and conditions and (iii) CCC's Billing and Payment terms and conditions.

8. License Contingent Upon Payment: While you may exercise the rights licensed immediately upon issuance of the license at the end of the licensing process for the transaction, provided that you have disclosed complete and accurate details of your proposed use, no license is finally effective unless and until full payment is received from you (either by publisher or by CCC) as provided in CCC's Billing and Payment terms and conditions. If full payment is not received on a timely basis, then any license preliminarily granted shall be deemed automatically revoked and shall be void as if never granted. Further, in the event that you breach any of these terms and conditions or any of CCC's Billing and Payment terms and conditions, the license is automatically revoked and shall be void as if never granted. Use of materials as described in a revoked license, as well as any use of the materials beyond the scope of an unrevoked license, may constitute copyright infringement and publisher reserves the right to take any and all action to protect its copyright in the materials.

9. Warranties: Publisher makes no representations or warranties with respect to the licensed material.

10. Indemnity: You hereby indemnify and agree to hold harmless publisher and CCC, and their respective officers, directors, employees and agents, from and against any and all claims arising out of your use of the licensed material other than as specifically authorized pursuant to this license.

11. No Transfer of License: This license is personal to you and may not be sublicensed, assigned, or transferred by you to any other person without publisher's written permission.

12. No Amendment Except in Writing: This license may not be amended except in a writing signed by both parties (or, in the case of publisher, by CCC on publisher's behalf).

13. Objection to Contrary Terms: Publisher hereby objects to any terms contained in any purchase order, acknowledgment, check endorsement or other writing prepared by you, which terms are inconsistent with these terms and conditions or CCC's Billing and Payment terms and conditions. These terms and conditions, together with CCC's Billing and Payment terms and conditions (which are incorporated herein), comprise the entire agreement between you and publisher (and CCC) concerning this licensing transaction. In the event of any conflict between your obligations established by these terms and conditions and those established by CCC's Billing and Payment terms and conditions, these terms and conditions shall control.

14. Revocation: Elsevier or Copyright Clearance Center may deny the permissions described in this License at their sole discretion, for any reason or no reason, with a full refund payable to you. Notice of such denial will be made using the contact information provided by you. Failure to receive such notice will not alter or invalidate the denial. In no event will Elsevier or Copyright Clearance Center be responsible or liable for any costs, expenses or damage incurred by you as a result of a denial of your permission request, other than a refund of the amount(s) paid by you to Elsevier and/or Copyright Clearance Center for denied permissions.

LIMITED LICENSE

The following terms and conditions apply only to specific license types:

15. **Translation**: This permission is granted for non-exclusive world **English** rights only unless your license was granted for translation rights. If you licensed translation rights you may only translate this content into the languages you requested. A professional translator must perform all translations and reproduce the content word for word preserving the integrity of the article.

16. **Posting licensed content on any Website**: The following terms and conditions apply as follows: Licensing material from an Elsevier journal: All content posted to the web site must maintain the copyright information line on the bottom of each image; A hyper-text must be included to the Homepage of the journal from which you are licensing at http://www.sciencedirect.com/science/journal/xxxxx or the Elsevier homepage for books at http://www.elsevier.com; Central Storage: This license does not include permission for a scanned version of the material to be stored in a central repository such as that provided by Heron/XanEdu.

Licensing material from an Elsevier book: A hyper-text link must be included to the Elsevier homepage at http://www.elsevier.com . All content posted to the web site must maintain the copyright information line on the bottom of each image.

Posting licensed content on Electronic reserve: In addition to the above the following clauses are applicable: The web site must be password-protected and made available only to

bona fide students registered on a relevant course. This permission is granted for 1 year only. You may obtain a new license for future website posting.

17. **For journal authors:** the following clauses are applicable in addition to the above:

Preprints:

A preprint is an author's own write-up of research results and analysis, it has not been peer-reviewed, nor has it had any other value added to it by a publisher (such as formatting, copyright, technical enhancement etc.).

Authors can share their preprints anywhere at any time. Preprints should not be added to or enhanced in any way in order to appear more like, or to substitute for, the final versions of articles however authors can update their preprints on arXiv or RePEc with their Accepted Author Manuscript (see below).

If accepted for publication, we encourage authors to link from the preprint to their formal publication via its DOI. Millions of researchers have access to the formal publications on ScienceDirect, and so links will help users to find, access, cite and use the best available version. Please note that Cell Press, The Lancet and some society-owned have different preprint policies. Information on these policies is available on the journal homepage.

Published journal article (JPA): A published journal article (PJA) is the definitive final record of published research that appears or will appear in the journal and embodies all value-adding publishing activities including peer review co-ordination, copy-editing, formatting, (if relevant) pagination and online enrichment.

Policies for sharing publishing journal articles differ for subscription and gold open access articles:

Subscription Articles: If you are an author, please share a link to your article rather than the full-text. Millions of researchers have access to the formal publications on ScienceDirect, and so links will help your users to find, access, cite, and use the best available version.

Theses and dissertations which contain embedded PJAs as part of the formal submission can be posted publicly by the awarding institution with DOI links back to the formal publications on ScienceDirect.

If you are affiliated with a library that subscribes to ScienceDirect you have additional private sharing rights for others' research accessed under that agreement. This includes use for classroom teaching and internal training at the institution (including use in course packs and courseware programs), and inclusion of the article for grant funding purposes.

Gold Open Access Articles: May be shared according to the author-selected end-user license and should contain a CrossMark logo, the end user license, and a DOI link to the formal publication on ScienceDirect.

Please refer to Elsevier's posting policy for further information.

18. **For book authors** the following clauses are applicable in addition to the above: Authors are permitted to place a brief summary of their work online only. You are not allowed to download and post the published electronic version of your chapter, nor may you scan the printed edition to create an electronic version. **Posting to a repository:** Authors are permitted to post a summary of their chapter only in their institution's repository.

19. **Thesis/Dissertation**: If your license is for use in a thesis/dissertation your thesis may be submitted to your institution in either print or electronic form. Should your thesis be published commercially, please reapply for permission. These requirements include permission for the Library and Archives of Canada to supply single copies, on demand, of the complete thesis and include permission for Proquest/UMI to supply single copies, on demand, of the complete thesis. Should your thesis be published commercially, please reapply for permission. Theses and dissertations which contain embedded PJAs as part of the formal submission can be posted publicly by the awarding institution with DOI links back to the formal publications on ScienceDirect.

Figure 1.8 in Chapter 1 have been adapted with permission from A. Barducci, M. Bonomi, and M. Parrinello, Wiley Interdiscip. Rev. Comp. Mol. Sci., **1**, 826 (2011). Copyright 2011 John Wiley and Sons (see below).

JOHN WILEY AND SONS LICENSE
TERMS AND CONDITIONS
Jan 29, 2021

This Agreement between Mr. Adebayo Adebayo ("You") and John Wiley and Sons ("John Wiley and Sons") consists of your license details and the terms and conditions provided by John Wiley and Sons and Copyright Clearance Center.

License Number	4998380091626
License date	Jan 29, 2021
Licensed Content Publisher	John Wiley and Sons
Licensed Content Publication	WILEY INTERDISCIPLINARY REVIEWS: COMPUTATIONAL MOLECULAR SCIENCE
Licensed Content Title	Metadynamics
Licensed Content Author	Alessandro Barducci, Massimiliano Bonomi, Michele Parrinello
Licensed Content Date	Feb 18, 2011
Licensed Content Volume	1
Licensed Content Issue	5
Licensed Content Pages	18
Type of use	Dissertation/Thesis
Requestor type	University/Academic
Format	Electronic
Portion	Figure/table
Number of figures/tables	1

Will you be translating?	No
Title	STRUCTURES, STRUCTURAL TRANSFORMATIONS AND PROPERTIES OF SELECTED ELEMENTAL AND EXTENDED SOLIDS
Institution name	University of Saskatchewan
Expected presentation date	Mar 2021
Portions	Fig. 1
Requestor Location	Mr. Adebayo Adebayo 1217, 15th St. E Saskatoon, SK S7N 0R6 Canada Attn: Mr. Adebayo Adebayo
Publisher Tax ID	EU826007151
Total	0.00 USD
Terms and Conditions	

TERMS AND CONDITIONS

This copyrighted material is owned by or exclusively licensed to John Wiley & Sons, Inc. or one of its group companies (each a"Wiley Company") or handled on behalf of a society with which a Wiley Company has exclusive publishing rights in relation to a particular work (collectively "WILEY"). By clicking "accept" in connection with completing this licensing transaction, you agree that the following terms and conditions apply to this transaction (along with the billing and payment terms and conditions established by the Copyright Clearance Center Inc., ("CCC's Billing and Payment terms and conditions"), at the time that you opened your RightsLink account (these are available at any time at http://myaccount.copyright.com).

WILEY OPEN ACCESS TERMS AND CONDITIONS

Wiley Publishes Open Access Articles in fully Open Access Journals and in Subscription journals offering Online Open. Although most of the fully Open Access journals publish open access articles under the terms of the Creative Commons Attribution (CC BY) License only, the subscription journals and a few of the Open Access Journals offer a choice of Creative Commons Licenses. The license type is clearly identified on the article.

The Creative Commons Attribution License

The Creative Commons Attribution License (CC-BY) allows users to copy, distribute and transmit an article, adapt the article and make commercial use of the article. The CC-BY license permits commercial and non-

Creative Commons Attribution Non-Commercial License

The Creative Commons Attribution Non-Commercial (CC-BY-NC)License permits use, distribution and reproduction in any medium, provided the original work is properly cited and is not used for commercial purposes.(see below)

Creative Commons Attribution-Non-Commercial-NoDerivs License

The Creative Commons Attribution Non-Commercial-NoDerivs License (CC-BY-NC-ND) permits use, distribution and reproduction in any medium, provided the original work is properly cited, is not used for commercial purposes and no modifications or adaptations are made. (see below)

Use by commercial "for-profit" organizations

Use of Wiley Open Access articles for commercial, promotional, or marketing purposes requires further explicit permission from Wiley and will be subject to a fee.

Further details can be found on Wiley Online Library
http://olabout.wiley.com/WileyCDA/Section/id-410895.html

All the figures and tables in Chapter 2 have been adapted with permission from Adeleke A. A., Adeniyi O. A., Tang H., Gou H., and Yao Y., *o*-C_{240}: A new sp^3-dominated allotrope of Carbon, *J. Phys.: Condens. Matter*. 32, **2020** 395401. Copyright 2020 Institute of Physics (IOP) publishing and Ji, C., Adeleke, A. A., Yang, L., Wan, B., Gou, H., Yao, Y., Li, B., Meng, Y., Smith, J. S., Prakapenka, V. B. *et. al*. Nitrogen in black phosphorus structure. *Sci. Adv.*, *6*, **2020** eaba9206. Copyright 2020 American Association for the Advancement of Science (see below)

Journal of Physics : Condensed Matter

General Information
Request ID: 600028589
Request Status: Accepted
Request Date: 16 Nov 2020
Price: 0.00 USD?

All Details
ISSN: 0953-8984
Type of Use: Republish in a thesis/dissertation
Publisher: IOP Publishing
Portion: Chapter/article

Licensed Content
Publication Title: Journal of Physics : Condensed Matter
Author/Editor: Institute of Physics (Great Britain)
Date: 12/31/1988
Language: English
Country: United Kingdom of Great Britain and Northern Ireland
Rightsholder: IOP Publishing, Ltd
Publication Type: Journal

Request Details

Portion Type: Chapter/article
Page range(s): 395401-395408
Total number of pages: 8
Format (select all that apply): Electronic
Who will republish the content?: Author of requested content
Duration of Use: Life of current and all future editions
Lifetime Unit Quantity: Up to 499
Rights Requested: Main product
Distribution
Canada
Translation

Original language of publication
Copies for the disabled?
No
Minor editing privileges?
No
Incidental promotional use?
No
Currency
USD

New Work Details

Title
STRUCTURES, STRUCTURAL TRANSFORMATIONS AND PROPERTIES OF SELECTED ELEMENTAL AND EXTENDED SOLIDS
Instructor name
Adebayo Adeleke
Institution name
University of Saskatchewan
Expected presentation date
2021-02-28

Additional Details

The requesting person / organization to appear on the license
Adebayo A. Adeleke

Reuse Content Details

Title, description or numeric reference of the portion(s)
Adebayo A Adeleke et al 2020 J. Phys.: Condens. Matter 32 395401
Editor of portion(s)
N/A
Volume of serial or monograph
N/A
Page or page range of portion
N/A
Title of the article/chapter the portion is from
o-C240: a new sp3-dominated allotrope of carbon
Author of portion(s)
Institute of Physics (Great Britain)
Publication date of portion
2020-06-23

Nitrogen in black phosphorus structure

Cheng Ji[1,2,*], Adebayo A. Adeleke[3,*], Liuxiang Yang[1,*], Biao Wan[1], Huiyang Gou[1,†], Yansun Yao[3,†], Bing...
+ See all authors and affiliations

Science Advances 03 Jun 2020:
Vol. 6, no. 23, eaba9206
DOI: 10.1126/sciadv.aba9206

Article Information

vol. 6 no. 23

DOI: https://doi.org/10.1126/sciadv.aba9206

Published By: American Association for the Advancement of Science

Online ISSN: 2375-2548

History: Received for publication January 15, 2020

Accepted for publication April 10, 2020

回复：Permission to use Experimental data in my thesis

Some content in this message has been blocked because the sender isn't in your Safe senders list. I trust content from ch

Cheng Ji_吉诚 <cheng.ji@hpstar.ac.cn>
Tue 2/2/2021 8:19 PM
To: Adeleke, Adebayo
Cc: Yao, Yansun; Cheng Ji_吉诚 <cheng.ji@hpstar.ac.cn>

CAUTION: External to USask. Verify sender and use caution with links and attachments. Forward suspicious emails to

Dear Adebayo,

Sorry for the delayed response.
I have no problem, please feel free to use your attached data in your thesis.

Best,

Cheng

发件人：Adeleke, Adebayo <adebayo.adeleke@usask.ca>
发送时间：2021年2月3日(星期三) 09:18
收件人：Cheng Ji_吉诚 <cheng.ji@hpstar.ac.cn>
主　题：Permission to use Experimental data in my thesis

Hello Dr. Ji,
My name is Adebayo Adeleke, Prof. Yao's PhD student. I am presently writing my thesis and will like to request your permission to include the attached experimental data in my thesis write-up. The data is the raw Raman spectra data for Nitrogen at the early days of the project. Please, let me know if you approve of this request.

I look forward to your prompt and positive response.

--
Many thanks.

---

cid:image001.gif@01CCEB2A.F7D0C5B0**Adeleke, Adebayo Abayomi (MSc).**
PhD Candidate
Department of Physics and Engineering Physics
University of Saskatchewan

All the figures and tables in Chapter 3 have been adapted with permission from Adeleke, A. A., and Yao, Y. High-temperature shape memory loss in nitinol: a first principles study. *Phys. Chem. Chem. Phys.*, *21*, **2019** 7508-7517. Copyright 2019 Royal Society of Chemistry (see below)

- For reproduction of material from NJC:
  [Original citation] - Reproduced by permission of The Royal Society of Chemistry (RSC) on behalf of the Centre National de la Recherche Scientifique (CNRS) and the RSC
- For reproduction of material from PCCP:
  [Original citation] - Reproduced by permission of the PCCP Owner Societies
- For reproduction of material from PPS:
  [Original citation] - Reproduced by permission of The Royal Society of Chemistry (RSC) on behalf of the European Society for Photobiology, the European Photochemistry Association, and RSC
- For reproduction of material from all other RSC journals:
  [Original citation] - Reproduced by permission of The Royal Society of Chemistry

If you are the author of this article you still need to obtain permission to reproduce the whole article in a third-party publication with the exception of reproduction of the whole article in a thesis or dissertation.

Information about reproducing material from RSC articles with different licences is available on our Permission Requests page.

All the figures and tables in Chapter 4 have been adapted with permission from Adeleke A. A., Kunz M., Greenberg E., Prakapenka V. B., Yao Y. and Stavrou E., High-pressure compound of argon and nickel: noble gas in the Earth's core? *ACS Earth Space Chem.,* 3, **2019** 2517-2524. Copyright 2019 American Chemical Society (see below)

A High-Pressure Compound of Argon and Nickel: Noble Gas in the Earth's Core?

Author:

Adebayo A. Adeleke, Martin Kunz, Eran Greenberg, et al

Publication:

ACS Earth & Space Chemistry

Publisher:

American Chemical Society

Date:

Nov 1, 2019

All the figures and tables in Chapter 5 have been adapted with permission from Adeleke A. and Yao Y. Formation of Stable Compounds of Potassium and Iron under Pressure. *J. Phys. Chem. A 124*, **2020** 4752-4763. Copyright 2020 American Chemical Society and Adeleke A. A., Stavrou E., Adeniyi O. A., Wan B., Gou H., and Yao Y. Two good metals make a semiconductor: A potassium-nickel compound under pressure. *Phys. Rev. B.* 102 **2020** 134120. Copyright 2020 American Physical Society (see below)

Formation of Stable Compounds of Potassium and Iron under Pressure

Author:

Adebayo A. Adeleke, Yansun Yao

Publication:

The Journal of Physical Chemistry A

Publisher:

American Chemical Society

Date:

Jun 1, 2020

PERMISSION/LICENSE IS GRANTED FOR YOUR ORDER AT NO CHARGE

This type of permission/license, instead of the standard Terms & Conditions, is sent to you because no fee is being charged for your order. Please note the following:

- Permission is granted for your request in both print and electronic formats, and translations.
- If figures and/or tables were requested, they may be adapted or used in part.
- Please print this page for your records and send a copy of it to your publisher/graduate school.
- Appropriate credit for the requested material should be given as follows: "Reprinted (adapted) with permission from (COMPLETE REFERENCE CITATION). Copyright (YEAR) American Chemical Society." Insert appropriate information in place of the capitalized words.

- One-time permission is granted only for the use specified in your request. No additional uses are granted (such as derivative works or other editions). For any other uses, please submit a new request.

SciPris

Scientific Publishing and Remittance Integration services

APS physics

Rights and Permissions Request Details

Article Information

Title: Two good metals make a semiconductor: A potassium-nickel compound under pressure
Author: Adebayo A. Adeleke et al.
Publication: Physical Review B
DOI: 10.1103/PhysRevB.102.134120
Publisher: American Physical Society
Date: 23-Nov-2020

Reuse Information

Reuse Category: Reuse in a thesis/dissertation
Reuse By: Author of requested content
Items for Reuse: Whole Article
Format for Reuse: Electronic

Information about New Publication

Does your reuse require significant modifications of the original content?: No
University/Publisher: University of Saskatchewan
Title of dissertation/thesis: STRUCTURES, STRUCTURAL TRANSFORMATIONS AND PROPERTIES OF SELECTED ELEMENTAL AND EXTENDED SOLIDS
Expected completion date: Mar. 2021
Author(s) Adebayo Adeleke
Specify intended distribution locations: Canada

License Requester Information

Name: Adebayo Adeleke
Email ID: aaa238@mail.usask.ca
Country: Canada
Request Id: RNP/20/NOV/033305

Rights and Permissions request status

Status: Complete

23-Nov-2020
T his license agreement between the American Physical Society ("APS") and Adebayo Adeleke ("You") consists of your license
details and the terms and conditions provided by the American Physical Society and SciPris.
Licensed Content Information
Lice nse Numbe r: RNP/20/NO V/033305
Lice nse date : 23-Nov-2020
DO I: 10.1103/PhysRevB.102.134120
Title : Two good metals make a semiconductor: A potassium-nickel
compound under pressure
Author: Adebayo A. Adeleke et al.
Publication: Physical Review B
Publishe r: American Physical Society
Cost: USD $ 0.00
Request Details
Does your re use re quire significant modifications: No
Spe cify inte nde d distribution
locations:
Canada
Re use Cate gory: Reuse in a thesis/dissertation
Re que stor Type : Author of requested content
Ite ms for Re use : Whole Article
Format for Re use : Electronic
Information about New Publication:
Unive rsity/Publishe r: University of Saskatchewan
Title of disse rtation/the sis: ST RUCT URES, ST RUCT URAL T RANSFORMAT IONS AND
PROPERT IES OF SELECT ED ELEMENTAL AND EXT ENDED
SOLIDS
Author(s): Adebayo Adeleke
Expe cte d comple tion date : Mar. 2021
License Requestor Information
Name : Adebayo Adeleke
Affiliation: Individual
Email Id: aaa238@mail.usask.ca
Country: Canada

TERMS AND CONDITIONS
The American Physical Society (APS) is pleased to grant the Requestor of this license a non-exclusive, non-transferable permission, limited to Electronic format, provided all criteria outlined below are followed.
1. You must also obtain permission from at least one of the lead authors for each separate work, if you haven’t done so already. The author's name and affiliation can be found on the first page of the published Article.

2. For electronic format permissions, Requestor agrees to provide a hyperlink from the reprinted APS material using the source material's DOI on the web page where the work appears. The hyperlink should use the standard DOI resolution URL, http://dx.doi.org/{DOI}. The hyperlink may be embedded in the copyright credit line.
3. For print format permissions, Requestor agrees to print the required copyright credit line on the first page where the material appears: "Reprinted (abstract/excerpt/figure) with permission from [(FULL REFERENCE CITAT ION) as follows: Author's Names, APS Journal T itle, Volume Number, Page Number and Year of Publication.] Copyright (YEAR) by the American Physical Society."
4. Permission granted in this license is for a one-time use and does not include permission for any future editions, updates, databases, formats or other matters. Permission must be sought for any additional use.
5. Use of the material does not and must not imply any endorsement by APS.
6. APS does not imply, purport or intend to grant permission to reuse materials to which it does not hold copyright. It is the requestor 's sole responsibility to ensure the licensed material is original to APS and does not contain the copyright of
another entity, and that the copyright notice of the figure, photograph, cover or table does not indicate it was reprinted by APS with permission from another source.
7. The permission granted herein is personal to the Requestor for the use specified and is not transferable or assignable without express written permission of APS. This license may not be amended except in writing by APS.
8. You may not alter, edit or modify the material in any manner.
9. You may translate the materials only when translation rights have been granted.
10. APS is not responsible for any errors or omissions due to translation.
11. You may not use the material for promotional, sales, advertising or marketing purposes.
12. The foregoing license shall not take effect unless and until APS or its agent, Aptara, receives payment in full in accordance with Aptara Billing and Payment Terms and Conditions, which are incorporated herein by reference.
13. Should the terms of this license be violated at any time, APS or Aptara may revoke the license with no refund to you and
seek relief to the fullest extent of the laws of the USA. Official written notice will be made using the contact information.
provided with the permission request. Failure to receive such notice will not nullify revocation of the permission.
14. APS reserves all rights not specifically granted herein.
15. This document, including the Aptara Billing and Payment Terms and Conditions, shall be the entire agreement between the parties relating to the subject matter hereof.

Figure 2.5 in Chapter 2 have been adapted with permission from D. Laniel, B, Winkler, T Fedotenko, A. Pakhomova, S. Chariton, V. Milman, V. Prakapenka, L. Dubrovinsky and N. Dubrovinskaia Phys. Rev. Lett. **124** 216001 (2020). Copyright 2020 American Physical Society (see below).

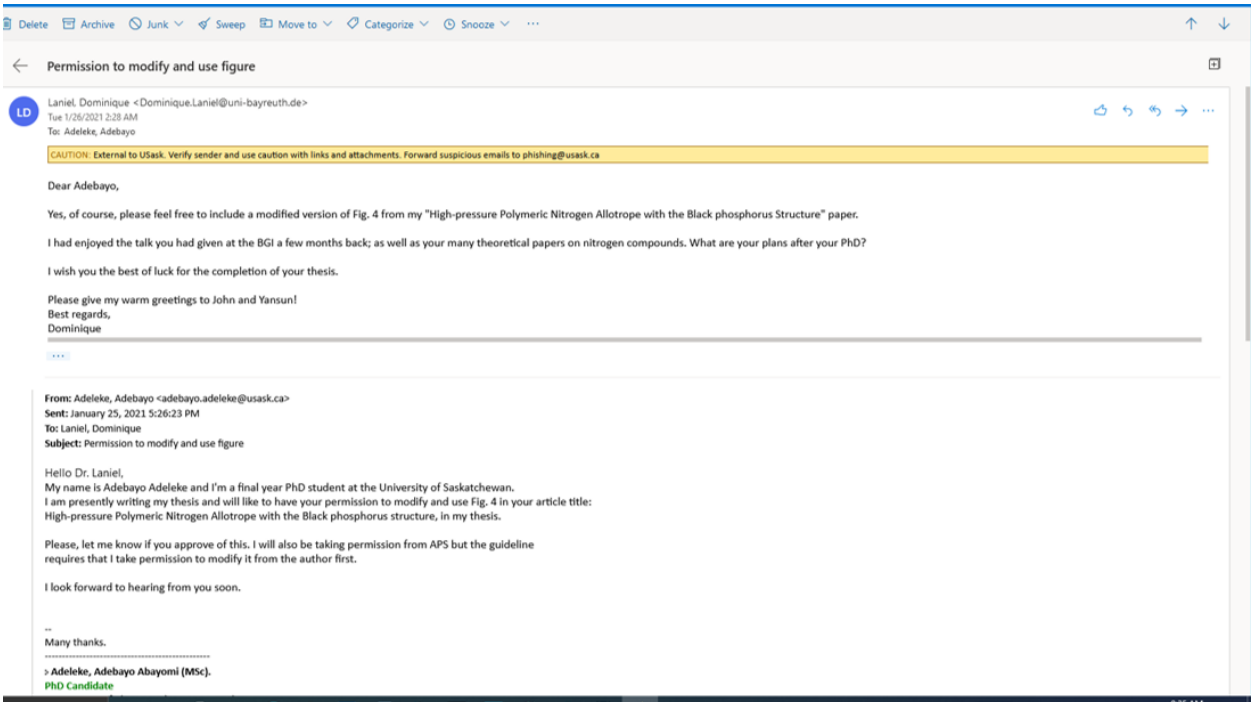

Delete Archive Junk Sweep Move to Categorize Snooze

Permission to modify and use figure

Laniel, Dominique <Dominique.Laniel@uni-bayreuth.de>
Tue 1/26/2021 2:28 AM
To: Adeleke, Adebayo

CAUTION: External to USask. Verify sender and use caution with links and attachments. Forward suspicious emails to phishing@usask.ca

Dear Adebayo,

Yes, of course, please feel free to include a modified version of Fig. 4 from my "High-pressure Polymeric Nitrogen Allotrope with the Black phosphorus Structure" paper.

I had enjoyed the talk you had given at the BGI a few months back; as well as your many theoretical papers on nitrogen compounds. What are your plans after your PhD?

I wish you the best of luck for the completion of your thesis.

Please give my warm greetings to John and Yansun!
Best regards,
Dominique

From: Adeleke, Adebayo <adebayo.adeleke@usask.ca>
Sent: January 25, 2021 5:26:23 PM
To: Laniel, Dominique
Subject: Permission to modify and use figure

Hello Dr. Laniel,
My name is Adebayo Adeleke and I'm a final year PhD student at the University of Saskatchewan.
I am presently writing my thesis and will like to have your permission to modify and use Fig. 4 in your article title:
High-pressure Polymeric Nitrogen Allotrope with the Black phosphorus structure, in my thesis.

Please, let me know if you approve of this. I will also be taking permission from APS but the guideline requires that I take permission to modify it from the author first.

I look forward to hearing from you soon.

--
Many thanks.

› **Adeleke, Adebayo Abayomi (MSc).**
PhD Candidate

SciPris

Scientific Publishing and Remittance Integration services

APS physics

Rights and Permissions Request Details

Article Information

Title: High-Pressure Polymeric Nitrogen Allotrope with the Black Phosphorus Structure
Author: Dominique Laniel et al.
Publication: Physical Review Letters
DOI: 10.1103/PhysRevLett.124.216001
Publisher: American Physical Society
Date: 26-Jan-2021

Reuse Information

Reuse Category: Reuse in a thesis/dissertation
Reuse By: Student
Items for Reuse: Figures/Tables
Number of figures/tables: 1
Figures and tables description: Figure 4
Format for Reuse: Electronic

Information about New Publication

Does your reuse require significant modifications of the original content?: Yes
Significant modifications details
I will like to modify Fig. 4 from the above paper for illustration in my thesis. I have the permission of the Author (e-mail correspondence) to modify and use Fig 4.
University/Publisher: University of Saskatchewan
Title of dissertation/thesis: STRUCTURES, ST RUCTURAL TRANSFORMATIONS AND PROPERTIES OF SELECTED ELEMENTAL AND EXTENDED SOLIDS
Expected completion date: Mar. 2021
Author(s): Adebayo Abayomi Adeleke
Specify intended distribution locations: Canada

License Requester Information

Name: Adebayo Adeleke
Email ID: aaa238@mail.usask.ca
Country: Canada
Request Id: RNP/21/JAN/035628

Rights and Permissions request status

Status: Complete

TERMS AND CONDITIONS

The American Physical Society (APS) is pleased to grant the Requestor of this license a non-exclusive, non-transferable permission,
limited to Electronic format, provided all criteria outlined below are followed.

1. You must also obtain permission from at least one of the lead authors for each separate work, if you haven't done so already. The author's name and affiliation can be found on the first page of the published Article.
2. For electronic format permissions, Requestor agrees to provide a hyperlink from the reprinted APS material using the source material's DOI on the web page where the work appears. The hyperlink should use the standard DOI resolution URL, http://dx.doi.org/{DOI}. The hyperlink may be embedded in the copyright credit line.
3. For print format permissions, Requestor agrees to print the required copyright credit line on the first page where the material appears: "Reprinted (abstract/excerpt/figure) with permission from [(FULL REFERENCE CITAT ION) as follows: Author's Names, APS Journal T itle, Volume Number, Page Number and Year of Publication.] Copyright (YEAR) by the American Physical Society."
4. Permission granted in this license is for a one-time use and does not include permission for any future editions, updates, databases, formats or other matters. Permission must be sought for any additional use.

5. Use of the material does not and must not imply any endorsement by APS.
6. APS does not imply, purport or intend to grant permission to reuse materials to which it does not hold copyright. It is the requestor ’s sole responsibility to ensure the licensed material is original to APS and does not contain the copyright of another entity, and that the copyright notice of the figure, photograph, cover or table does not indicate it was reprinted by APS with permission from another source.
7. The permission granted herein is personal to the Requestor for the use specified and is not transferable or assignable without express written permission of APS. This license may not be amended except in writing by APS.
8. You may not alter, edit or modify the material in any manner.
9. You may translate the materials only when translation rights have been granted.
10. APS is not responsible for any errors or omissions due to translation.
11. You may not use the material for promotional, sales, advertising or marketing purposes.
12. The foregoing license shall not take effect unless and until APS or its agent, Aptara, receives payment in full in accordance with Aptara Billing and Payment Terms and Conditions, which are incorporated herein by reference.
13. Should the terms of this license be violated at any time, APS or Aptara may revoke the license with no refund to you and seek relief to the fullest extent of the laws of the USA. Official written notice will be made using the contact information provided with the permission request. Failure to receive such notice will not nullify revocation of the permission.
14. APS reserves all rights not specifically granted herein.
15. This document, including the Aptara Billing and Payment Terms and Conditions, shall be the entire agreement between the parties relating to the subject matter hereof.

Figure 2.10a in Chapter 2 have been adapted with permission from D. Laniel, G. Geneste, G. Weck, M. Mezouar, and P. Loubeyre, Phys. Rev. Lett. **122** 066001 (2019). Copyright 2019 American Physical Society (see below).

22-Jan-2021

T his license agreement between the American Physical Society ("APS") and Adebayo Adeleke ("You") consists of your license

details and the terms and conditions provided by the American Physical Society and SciPris.

Licensed Content Information

License Number: RNP/21/JAN/035505

License date : 22-Jan-2021

DO I: 10.1103/PhysRevLett.122.066001

Title : Hexagonal Layered Polymeric Nitrogen Phase Synthesized near 250

GPa

Author: D. Laniel et al.

Publication: Physical Review Letters

Publisher: American Physical Society

Cost: USD $ 0.00

Request Details

Does your re use re quire significant modifications: No

Specify intended distribution

locations:

Canada

Reuse Category: Reuse in a thesis/dissertation

Requestor Type: Student

Items for Reuse: Figures/Tables

Number of Figure /Table s: 1

Figure /Tables Details: Fig. 4

Format for Reuse: Electronic

Information about New Publication:

University/Publisher: University of Saskatchewan

Title of dissertation/thesis: STRUCTURES, ST RUCTURAL TRANSFORMATIONS AND PROPERTIES OF SELECTED ELEMENTAL AND EXTENDED SOLIDS

Author(s): Adebayo Abayomi Adeleke

Expected completion date : Mar. 2021

License Requestor Information

Name: Adebayo Adeleke

Affiliation: Individual

Email Id: aaa238@mail.usask.ca

Country: Canada

TERMS AND CONDITIONS

The American Physical Society (APS) is pleased to grant the Requestor of this license a non-exclusive, non-transferable permission, limited to Electronic format, provided all criteria outlined below are followed.

1. You must also obtain permission from at least one of the lead authors for each separate work, if you haven't done so already. The author's name and affiliation can be found on the first page of the published Article.
2. For electronic format permissions, Requestor agrees to provide a hyperlink from the reprinted APS material using the source material's DOI on the web page where the work appears. The hyperlink should use the standard DOI resolution URL, http://dx.doi.org/{DOI}. The hyperlink may be embedded in the copyright credit line.
3. For print format permissions, Requestor agrees to print the required copyright credit line on the first page where the material appears: "Reprinted (abstract/excerpt/figure) with permission from [(FULL REFERENCE CITAT ION) as follows: Author's Names, APS Journal T itle, Volume Number, Page Number and Year of Publication.] Copyright (YEAR) by the American Physical Society."
4. Permission granted in this license is for a one-time use and does not include permission for any future editions, updates, databases, formats or other matters. Permission must be sought for any additional use.
5. Use of the material does not and must not imply any endorsement by APS.
6. APS does not imply, purport or intend to grant permission to reuse materials to which it does not hold copyright. It is the requestor 's sole responsibility to ensure the licensed material is original to APS and does not contain the copyright of another entity, and that the copyright notice of the figure, photograph, cover or table does not indicate it was reprinted by APS with permission from another source.
7. The permission granted herein is personal to the Requestor for the use specified and is not transferable or assignable without express written permission of APS. This license may not be amended except in writing by APS.
8. You may not alter, edit or modify the material in any manner.

9. You may translate the materials only when translation rights have been granted.
10. APS is not responsible for any errors or omissions due to translation.
11. You may not use the material for promotional, sales, advertising or marketing purposes.
12. The foregoing license shall not take effect unless and until APS or its agent, Aptara, receives payment in full in accordance with Aptara Billing and Payment Terms and Conditions, which are incorporated herein by reference.
13. Should the terms of this license be violated at any time, APS or Aptara may revoke the license with no refund to you and
seek relief to the fullest extent of the laws of the USA. Official written notice will be made using the contact information.
provided with the permission request. Failure to receive such notice will not nullify revocation of the permission.
14. APS reserves all rights not specifically granted herein.
15. This document, including the Aptara Billing and Payment Terms and Conditions, shall be the entire agreement between the parties relating to the subject matter hereof.

Figure 2.10a in Chapter 2 have been adapted with permission from D. Tomasino, M. Kim, J. Smith, and C.-S. Yoo, Phys. Rev. Lett. **113** 205502 (2014). Copyright 2014 American Physical Society (see below).

22-Jan-2021

This license agreement between the American Physical Society ("APS") and Adebayo Adeleke ("You") consists of your license
details and the terms and conditions provided by the American Physical Society and SciPris.

Licensed Content Information

License Numbe r: RNP/21/JAN/035506

License date : 22-Jan-2021

DOI: 10.1103/PhysRevLett.113.205502

Title : Pressure-Induced Symmetry-Lowering Transition in Dense Nitrogen
to Layered Polymeric Nitrogen (LP-N) with Colossal Raman Intensity

Author: Dane Tomasino et al.

Publication: Physical Review Letters

Publisher: American Physical Society

Cost: USD $ 0.00

Request Details

Does your re use re quire significant modifications: No

Specify intended distribution
locations:
Canada

Reuse Category: Reuse in a thesis/dissertation

Requestor Type: Student

Items for Reuse: Figures/Tables

Number of Figure /Table s: 1

Figure /Tables Details: Fig. 4

Format for Reuse: Electronic

Information about New Publication:

University/Publisher: University of Saskatchewan

Title of dissertation/thesis: ST RUCTURES, STRUCT URAL TRANSFORMAT IONS AND PROPERTIES OF SELECTED ELEMENTAL AND EXTENDED SOLIDS

Author(s): Adebayo Abayomi Adeleke

Expected completion date : Mar. 2021

License Requestor Information

Name: Adebayo Adeleke

Affiliation: Individual

Email Id: aaa238@mail.usask.ca

Country: Canada

TERMS AND CONDITIONS

The American Physical Society (APS) is pleased to grant the Requestor of this license a non-exclusive, non-transferable permission, limited to Electronic format, provided all criteria outlined below are followed.

1. You must also obtain permission from at least one of the lead authors for each separate work, if you haven't done so already. The author's name and affiliation can be found on the first page of the published Article.
2. For electronic format permissions, Requestor agrees to provide a hyperlink from the reprinted APS material using the source material's DOI on the web page where the work appears. The hyperlink should use the standard DOI resolution URL, http://dx.doi.org/{DOI}. The hyperlink may be embedded in the copyright credit line.
3. For print format permissions, Requestor agrees to print the required copyright credit line on the first page where the material appears: "Reprinted (abstract/excerpt/figure) with permission from [(FULL REFERENCE CITAT ION) as follows: Author's Names, APS Journal T itle, Volume Number, Page Number and Year of Publication.] Copyright (YEAR) by the American Physical Society."
4. Permission granted in this license is for a one-time use and does not include permission for any future editions, updates, databases, formats or other matters. Permission must be sought for any additional use.
5. Use of the material does not and must not imply any endorsement by APS.
6. APS does not imply, purport or intend to grant permission to reuse materials to which it does not hold copyright. It is the requestor 's sole responsibility to ensure the licensed material is original to APS and does not contain the copyright of another entity, and that the copyright notice of the figure, photograph, cover or table does not indicate it was reprinted by APS with permission from another source.
7. The permission granted herein is personal to the Requestor for the use specified and is not transferable or assignable without express written permission of APS. This license may not be amended except in writing by APS.
8. You may not alter, edit or modify the material in any manner.
9. You may translate the materials only when translation rights have been granted.
10. APS is not responsible for any errors or omissions due to translation.

11. You may not use the material for promotional, sales, advertising or marketing purposes.
12. The foregoing license shall not take effect unless and until APS or its agent, Aptara, receives payment in full in accordance with Aptara Billing and Payment Terms and Conditions, which are incorporated herein by reference.
13. Should the terms of this license be violated at any time, APS or Aptara may revoke the license with no refund to you and
seek relief to the fullest extent of the laws of the USA. Official written notice will be made using the contact information.
provided with the permission request. Failure to receive such notice will not nullify revocation of the permission.
14. APS reserves all rights not specifically granted herein.
15. This document, including the Aptara Billing and Payment Terms and Conditions, shall be the entire agreement between the parties relating to the subject matter hereof.

Figure 1.9 in Chapter 1 have been adapted with permission from X-Q. Chen, H. Niu, D. Li, and Y. Li, Intermetallics **19** 1275 (2011). Copyright 2011 Elsevier Ltd (see below).

ELSEVIER LICENSE
TERMS AND CONDITIONS
May 21, 2021

This Agreement between Mr. Adebayo Adebayo ("You") and Elsevier ("Elsevier") consists of your license details and the terms and conditions provided by Elsevier and Copyright Clearance Center.

License Number	5073660736884
License date	May 21, 2021
Licensed Content Publisher	Elsevier
Licensed Content Publication	Intermetallics
Licensed Content Title	Modeling hardness of polycrystalline materials and bulk metallic glasses
Licensed Content Author	Xing-Qiu Chen,Haiyang Niu,Dianzhong Li,Yiyi Li
Licensed Content Date	Sep 1, 2011
Licensed Content Volume	19
Licensed Content Issue	9
Licensed Content Pages	7
Start Page	1275
End Page	1281
Type of Use	reuse in a thesis/dissertation
Portion	figures/tables/illustrations
Number of figures/tables/illustrations	1
Format	electronic
Are you the author of this Elsevier article?	No
Will you be translating?	No
Title	STRUCTURES, STRUCTURAL TRANSFORMATIONS AND PROPERTIES OF SELECTED ELEMENTAL AND EXTENDED SOLIDS
Institution name	University of Saskatchewan
Expected presentation date	May 2021
Portions	Fig. 2

Mr. Adebayo Adebayo
1217, 15th St. E

Requestor Location

Saskatoon, SK S7N 0R6
Canada
Attn: Mr. Adebayo Adebayo

Publisher Tax ID	GB 494 6272 12
Total	0.00 USD

Terms and Conditions

INTRODUCTION

1. The publisher for this copyrighted material is Elsevier. By clicking "accept" in connection with completing this licensing transaction, you agree that the following terms and conditions apply to this transaction (along with the Billing and Payment terms and conditions established by Copyright Clearance Center, Inc. ("CCC"), at the time that you opened your Rightslink account and that are available at any time at http://myaccount.copyright.com).

GENERAL TERMS

2. Elsevier hereby grants you permission to reproduce the aforementioned material subject to the terms and conditions indicated.

3. Acknowledgement: If any part of the material to be used (for example, figures) has appeared in our publication with credit or acknowledgement to another source, permission must also be sought from that source. If such permission is not obtained then that material may not be included in your publication/copies. Suitable acknowledgement to the source must be made, either as a footnote or in a reference list at the end of your publication, as follows:

"Reprinted from Publication title, Vol /edition number, Author(s), Title of article / title of chapter, Pages No., Copyright (Year), with permission from Elsevier [OR APPLICABLE SOCIETY COPYRIGHT OWNER]." Also Lancet special credit - "Reprinted from The Lancet, Vol. number, Author(s), Title of article, Pages No., Copyright (Year), with permission from Elsevier."

4. Reproduction of this material is confined to the purpose and/or media for which permission is hereby given.

5. Altering/Modifying Material: Not Permitted. However figures and illustrations may be altered/adapted minimally to serve your work. Any other abbreviations, additions, deletions and/or any other alterations shall be made only with prior written authorization of Elsevier

Ltd. (Please contact Elsevier's permissions helpdesk here). No modifications can be made to any Lancet figures/tables and they must be reproduced in full.

6. If the permission fee for the requested use of our material is waived in this instance, please be advised that your future requests for Elsevier materials may attract a fee.

7. Reservation of Rights: Publisher reserves all rights not specifically granted in the combination of (i) the license details provided by you and accepted in the course of this licensing transaction, (ii) these terms and conditions and (iii) CCC's Billing and Payment terms and conditions.

8. License Contingent Upon Payment: While you may exercise the rights licensed immediately upon issuance of the license at the end of the licensing process for the transaction, provided that you have disclosed complete and accurate details of your proposed use, no license is finally effective unless and until full payment is received from you (either by publisher or by CCC) as provided in CCC's Billing and Payment terms and conditions. If full payment is not received on a timely basis, then any license preliminarily granted shall be deemed automatically revoked and shall be void as if never granted. Further, in the event that you breach any of these terms and conditions or any of CCC's Billing and Payment terms and conditions, the license is automatically revoked and shall be void as if never granted. Use of materials as described in a revoked license, as well as any use of the materials beyond the scope of an unrevoked license, may constitute copyright infringement and publisher reserves the right to take any and all action to protect its copyright in the materials.

9. Warranties: Publisher makes no representations or warranties with respect to the licensed material.

10. Indemnity: You hereby indemnify and agree to hold harmless publisher and CCC, and their respective officers, directors, employees and agents, from and against any and all claims arising out of your use of the licensed material other than as specifically authorized pursuant to this license.

11. No Transfer of License: This license is personal to you and may not be sublicensed, assigned, or transferred by you to any other person without publisher's written permission.

12. No Amendment Except in Writing: This license may not be amended except in a writing signed by both parties (or, in the case of publisher, by CCC on publisher's behalf).

Figure 3.1 in Chapter 3 have been adapted with permission from X. M. Zeng, Z. Du, N. Tamura, Q. Liu, C. A. Schuh, and C. L. Gan, Acta Materialia, **134** 257 (2017). Copyright 2017 Elsevier Ltd (see below).

ELSEVIER LICENSE
TERMS AND CONDITIONS
May 21, 2021

This Agreement between Mr. Adebayo Adebayo ("You") and Elsevier ("Elsevier") consists of your license details and the terms and conditions provided by Elsevier and Copyright Clearance Center.

License Number	5073811093464
License date	May 21, 2021
Licensed Content Publisher	Elsevier
Licensed Content Publication	Acta Materialia
Licensed Content Title	In-situ studies on martensitic transformation and high-temperature shape memory in small volume zirconia
Licensed Content Author	Xiao Mei Zeng,Zehui Du,Nobumichi Tamura,Qing Liu,Christopher A. Schuh,Chee Lip Gan
Licensed Content Date	Aug 1, 2017
Licensed Content Volume	134
Licensed Content Issue	n/a
Licensed Content Pages	10
Start Page	257
End Page	266
Type of Use	reuse in a thesis/dissertation
Portion	figures/tables/illustrations
Number of figures/tables/illustrations	1
Format	electronic
Are you the author of this Elsevier article?	No
Will you be translating?	No
Title	STRUCTURES, STRUCTURAL TRANSFORMATIONS AND PROPERTIES OF SELECTED ELEMENTAL AND EXTENDED SOLIDS

Institution name	University of Saskatchewan
Expected presentation date	May 2021
Portions	Graphical abstract
	Mr. Adebayo Adebayo 1217, 15th St. E
Requestor Location	
	Saskatoon, SK S7N 0R6 Canada Attn: Mr. Adebayo Adebayo
Publisher Tax ID	GB 494 6272 12
Total	0.00 USD